The University Of Sheffield.

Multi-Scale Analysis of Deformation and Damage Development in DP1000 Automotive Steel

By: Asim Alsharif

A thesis submitted in partial fulfilment of the requirements for the degree of Doctor of Philosophy

The University of Sheffield
Faculty of Engineering
Department of Mechanical Engineering

Submission Date

30/06/2021

This research is done under the supervision of

Dr Christophe Pinna

in the department of Mechanical Engineering

ACKNOWLEDGEMENTS

I would like to express my sincere gratitude to my supervisor, Dr Christophe Pinna, who has shown me a generous level of support in the completion of this research. I would like further to thank Tata Steel Europe, in IJmuiden, The Netherlands, for providing the material for this study. My thanks also to those of my colleagues and associates who have provided valuable guidance on technical issues and questions as they have arisen. Finally, I would like to acknowledge the generous financial support of Taibah University in Saudi Arabia, without which my doctoral studies would not be possible.

ABSTRACT

The use of dual-phase (DP) steels in the automotive industry is rising due to their light weight and ability to enhance safety. The development of next generation DP steels requires better understanding of their microstructure deformation and damage propagation to help predict their mechanical properties. The formability and damage development in DP1000 steels are studied in this research using a multiscale method for better understanding of these phenomena.

An in-situ tensile test, in combination with digital image correlation, was performed inside the chamber of a scanning electron microscope to evaluate the microstructure deformation. Martensite fracture and ferrite void localisation were observed and studied in relation to local strain measurements. Further finite element simulation–based damage modelling was developed to analyse damage nucleation in relation to mechanical stress strain fields. The Gurson-Tvergaard-Needleman damage modelling approach was adopted to predict the load-displacement curves of notched tensile samples by calibrating damage parameters. Validation was conducted through the prediction of load-displacement curves of the bespoke tensile geometry of specimens tested inside the Scan electron microscope . The formability of DP1000 was further examined through a punch test with validation of the finite element model using 3 dimension digital image correlation . Damage propagation at the scale of the microstructure was then studied through the development of a new micro punch test. Although short cracks could be observed in the microstructure with strain values at the onset of fracture measured using 3 dimensions digital imagine correlation, this test geometry showed some limitations in terms of analysing damage propagation in the two-phase steel. A new in-situ bending test with a bespoke specimen geometry was then used to study extensive damage propagation in dual phase1000 in relation to strain distributions for the first time. Results show that despite early damage taking place through martensite cracking, deformation and final fracture of dual phase1000 are controlled by the ferrite phase with cracks following a path mainly located along

ferrite islands. The original experimental procedure developed in this work combining various test geometries therefore provides the means to generate news physical insight into the development of deformation and damage up to fracture in advanced high strength steels under conditions representative of forming operations. These experimental results can also be used for the future development of more robust multi-scale damage models as results also showed the limitations of the Gurson model when transferred to the punch test geometry.

Table of contents

Acknowledgements III

Abstract IV

Table of contents VI

List of figures: XI

Appendix list of figures XVII

List of tables: XX

Appendix list of table: XXI

List of equations XXII

Abbreviations XXIV

Nomenclature XXV

1. Introduction 1

1.1 Aim and novelty 4

1.2 Thesis structure 4

2. Literature review 6

2.1 DP 1000 steel 6

2.2 Formability characterization 12

2.2.1 Deformation modes during forming operations 12

2.2.2 Formability tests 13

2.2.3 Small Punch (SP) tests review 16

2.3 Deformation and damage mechanisms 20

2.4 Damage and microstructure modelling 28

2.4.1 Marciniak-Kuczynski (MK) model 29

2.4.2 Constitutive damage modelling 33

2.4.3 Microstructure-based modelling of RVE of DP steel 38

2.5 Summary 43

3. EXPERIMENTAL PROCEDURES 44

3.1 Chemical components and microstructure contained in DP1000 45

3.2 Uniaxial tensile testing of DP1000 46

3.3 Microscale SEM tensile test using DIC 48

3.3.1 In-situ uniaxial tensile tests of DP1000 utilizing a tensile stage 48

3.3.2 DIC setup for strain measurement 50

3.4. Formability test of DP1000 52

3.4.1 Macro punch test using 3D DIC 52

3.4.2 Small Punch test 56

3.5 Bending test of DP1000 utilizing a micro bending stage 66

4. FE simulation procedure of DP1000 68

4.1 FE simulation of standard and notched tensile test 68

4.2 SEM tensile test modelling 69

4.3 Microstructure modelling 71

4.4 Punch test modelling 74

4.4.1 Macroscale punch test modelling 74

4.4.2 Small Punch modelling 75

4.5 Bending test modelling 76

5. Experimental results 78

5.1 Uniaxial tensile testing results of DP1000 78

5.1.1 Plastic stress strain curve of uniaxial tensile test 78

5.1.2 Load displacement curves of uniaxial notched specimens 80

5.2 In situ uniaxial tensile test of DP1000 utilizing a tensile stage 81

5.2.1 Localized plastic deformation of DP1000 observation using SEM 82

5.2.2 Inspection of martensite cracks and ferrite voids of DP1000 using SEM 86

5.2.3 Plastic deformation strain measurement of DP1000 microstructure using Micro scale DIC 94

5.2.4 Strain analyses of the onset of martensite microcracking and ferrite void nucleation using DIC 100

5.3 Formability tests for DP1000 106

5.3.1 Punch test using optical 3D DIC 106

5.3.2 Small punch test analysis using micro scale SEM and 3D DIC 111

5.3.3 Small punch test study using 3D DIC 114

5.3.4 Small punch test using 3D DIC for crack propagation analysis 116

5.4 Bending test of DP1000 using micro bending stage results 119

5.4.1 Bending test strain analysis using micro DIC 126

5.4.2 Bending test using micro bending stage to investigate Crack Propagation 129

5.4.2.1 Crack formation during first micro stage bending test 130

5.5 Summary 139

6. FE simulation analysis of DP1000 141

6.1 Continuum damage Modelling of DP1000 141

6.1.1 Tensile damage modelling: Effect of GTN parameters 142

6.2 Microstructure based modelling results of DP1000 149

6.3 Macro-scale modelling to analysis the fracture of DP1000 158

6.3.1 Formability punch test FE simulation 158

6.3.2 Small punch test 161

6.3.3 Bending Test 166

6.4 Conclusion: 168

7. Discussion 170

7.1 Plastic deformation 170

7.2 Martensite damage 171

7.3 Damage initiation in the Ferrite 173

7.4 Damage propagation in DP1000 174

7.5 Damage modelling 179

8. Conclusion and future work 181

8.1 Conclusion 181

8.2 Future work 183

References 184

Appendices 189

Appendix I 189

Appendix II 190

Appendix III 192

Appendix IV 192

Appendix V 193

Appendix VI 194

APPENDIX VII 195

Appendix VIII 201

Appendix IX 204

Appendix X 208

Appendix XI 212

Appendix XII 214

Appendix XIII 218

Appendix XIV 222

Appendix XV 223

LIST OF FIGURES:

Fig.1. 1 The formability graph of AHSS and other kinds of steel (Keeler & Kimchi, 2015). 2

Fig. 2. 1 UTS and elongation of DP steels, plain carbon steels and ferrite-pearlite steels (Rashid, 1981). 7

Fig. 2. 2 Engineering stress-strain curve of DP steels and other AHSSs (Tasan et al., 2015). 8

Fig. 2. 3 Left: TTT diagram of heat treatment performed to form ferrite and martensite phases. Right: iron-carbon equilibrium phase diagram (Tasan et al., 2015). 9

Fig. 2. 4 SEM image of DP1000 steel microstructure; brighter sections are martensite, darker sections, ferrite (Zhao et al., 2014). 10

Fig. 2. 5 Strain paths on a forming limit diagram (ISO, 2008) 14

Fig. 2. 6 Erichsen cupping test (Kamikawa & Morino, 2019) 17

Fig. 2. 7 (a): Computed displacement of the tube and flat specimens against a force (b): Flat and curved tube before and after the fracture (Simonovski et al., 2017). 18

Fig. 2. 8 Simulation and experimental results of SP test showing load-displacement curves (Abendroth & Kuna, 2003) 19

Fig. 2. 9 (a) Void nucleation on inclusion; (b) and (c) cracks on martensite; (d) and (e) decohesion of ferrite-martensite interface and crack propagation through ferrite phase; (f) void coalescence near to surface fracture (Avramovic-Cingara, Ososkov, et al., 2009). 21

Fig. 2. 10 Void creation in narrow ferrite areas between two adjacent martensite islands(Saeidi et al., 2014). 22

Fig. 2. 11 Voids inside the strain localisation band, between the martensite particles (Alaie, Kadkhodapour, et al., 2015) 23

Fig. 2. 12 (a) Void following diffused necking; (b) Void after necking but before fracture; (c) Void after specimen fracture (Kadkhodapour et al., 2011) 24

Fig. 2. 13 (a) A non-metallic inclusion void; (b) Void formation following the martensite fractur (Alharbi et al., 2015) 25

Fig. 2. 14 Test on microstructure of DP600 steel, identifying damage initiation process due to ferrite-martensite failure (left); crack propagation before final damage (right) (Ghadbeigi et al., 2013). 27

Fig. 2. 15 Bending test, with load-displacement curve showing the visibility of cracks in the martensite initiating at 5 mm displacement (Ramazani et al., 2014). 28

Fig. 2. 16 Schema for M-K modelling. 30

Fig. 2. 17 FE simulation of DP steel microstructure (Abid et al., 2015). 39

Fig. 2. 18 FE simulation of SEM image with strain distribution (Alaie, Rad, et al., 2015) 40

Fig. 2. 19 FE simulation for micro-structure-based damage modelling of martensite cracks (Alharbi et al., 2015). 42

Fig. 3. 1 Reference image of microstructure. 45

Fig. 3. 2 (a) Geometries of standard and notched samples (Saeidi et al., 2014); (b) specimens after failure; and (c) the sample in the machine with 3D DIC. 47

Fig. 3. 3 Sample of micro tensile test (Ghadbeigi et al., 2010). 50

Fig. 3. 4 (a) Deben tensile stage. (b) Camscan SEM. 50

Fig. 3. 5 Reference image for DIC. The blue arrows provide an example of the subset's size. 51

Fig. 3. 6 Strain map resulting from an investigation of the distorted region of interest. 52

Fig. 3. 7 Drawing of the Sample with 90-mm diameter. 53

Fig. 3. 8 Illustration of the macro punch test (Rohaizat, 2018) 54

Fig. 3. 9 3D DIC setting with punch rig for experiment. 55

Fig. 3. 10 (a) Camera setup for 3D DIC measurement (Rohaizat, 2018); (b) Plate calibration for 3D DIC. 56

Fig. 3. 11 Small punch test sample geometry (dimensions in mm). 57

Fig. 3. 12 Sample geometry to explain variables in equation 28. 58

Fig. 3. 13 Top and side views of top die. 59

Fig. 3. 14 Geometry of the bottom die. 60

Fig. 3. 15 Geometry of the punch guide. 61

Fig. 3. 16 New bottom die after manufacture. 61

Fig. 3. 17 Geometry of punch. 62

Fig. 3. 18 (a) SP sample geometry and (b) Specimen holder geometry in the Inspect F SEM. 64

Fig. 3. 19 Sample affixed to the SEM instrument base with two pins. 64

Fig. 3. 20 Sample in the Inspect F machine (left) with the first image of the microstructure before the application of displacement (right). 66

Fig. 3. 21 Bending test specimen geometry (mm). 67

Fig. 3. 22 Sample on the bending stage (left); stage fixed on SEM chamber (right). 67

Fig. 4. 1 Modelling of notched geometries (engineering drawing see fig 3.2 a). 69

Fig. 4. 2 Finite element model of the SEM tensile sample geometry (drawing 3.3). 70

Fig. 4. 3 Undeformed microstructure of DP1000; the ferrite is darker, and the martensite is brighter. 71

Fig. 4. 4 Flowchart detailing the production of stress maps over the deformed microstructure. 73

Fig. 4. 5 Models of sample and punch tool (see figures.3.7 and 3.8 for dimensions). 74

Fig. 4. 6 Models of the small sample and punch tool (see figures 3.11 and 3.17 for dimensions). 76

Fig. 4. 7 FE simulation via Abaqus (engineering drawing see fig. 3.21) 77

Fig. 5. 1 Engineering and true stress–strain curves for standard tensile tests, conducted using optical 3D DIC. This curve is used to simulate notched SEM and punch test samples. 79

Fig. 5. 2 The load displacement curves for notched samples in (a) R= 7.5 mm and (b) R= 1.5 mm. 81

Fig. 5. 3 Load displacement and engineering stress strain curves produced using the SEM tensile test. ... 82

Fig. 5. 4 (a), (b) Images captured at 0.11 strain; (c), (d) images captured after the application of 0.18 strain. 84

Fig. 5. 5 The progressive deformation up to failure (from (a) to (b)). Images (c) and (d) captured after the application of 0.30 and 0.35 strain respectively. 85

Fig. 5. 6 Example of the damage mechanism for the void initiation in the ferrite phase, which caused the martensite to crack after significant deformation. 86

Fig. 5. 7 Strain distribution at the first point of plastic deformation. 94

Fig. 5. 8 The deformed microstructure at UTS after the application of 0.13 global strain. The image shows the tensile strain component distribution measured with DIC. 95

Fig. 5. 9 Map distribution for 0.11 global strain. 97

Fig. 5. 10 Distribution of microstructure strain: (a) 0.18 global strain; (b) 0.33 global strain. 98

Fig. 5. 11 Comparative histograms for strain values for ferrite and martensite. 99

Fig. 5. 12 Evolution of strain partitioning between ferrite and martensite throughout an in-situ tensile test. 100

Fig. 5. 13 (a) shows the global strain value against local DIC strain values on the left curve and (b) the global stress value (MPa) against the local DIC strain value on the right curve. 106

Fig. 5. 14 (a) Sample after failure, with black arrows indicating cracks; (b) load–displacement curve for the macro punch test. 107

Fig. 5. 15 3D DIC results of the out-of-plane displacement in the Z direction, through the beginning of the deformation process and before the appearance of a crack. 108

Fig. 5. 16 2D plot of maximum displacement in the Z direction, before and after the appearance of the crack on the surface. 108

Fig. 5. 17 Lagrangian strain distribution results (Exx) for the punch test deformation. 109

Fig. 5. 18 Maximum principal strain e1 against minimum principal strain, e2 showing biaxial loading as it applied during the punch test. 110

Fig. 5. 19 Load–displacement curve for SPT. Points of interruption during the test are shown. 113

Fig. 5. 20 (a) 3D DIC results of plan deformation before crack appearance test; (b) Maximum displacement in Z direction after the crack appearance on the surface. 115

Fig. 5. 21 Strain results of SPT using 3D DIC, before the emergence of crack at the sample of the surface. 116

Fig. 5. 22 Images of (a) area cut around the crack, (b) second cut through the crack and (c) samples mounted after cutting for the purpose of observation using the inspect F SEM. 117

Fig. 5. 23 Results of crack inspection in the areas of the first of the SPT after the 3D DIC sample was fractured throughout its depth. 119

Fig. 5. 24 (a) Bending test geometry with (b), (c) and (d) cracks appearing following a large deformation. The black rectangle highlights the region where the cracks appeared (blue arrows), with the blue rectangle in (b) highlighting the region of the microstructure analysed using DIC. 120

Fig. 5. 25 Micrographs showing (a) the expected deformation of lines X and Y; (b) initial deformation of both lines (black and red arrows), early deformation in the ferrite phase (blue rectangle and circles) and the continuation of deformation (black squares); (c) continuation of deformation mechanism; (d) stage prior to final fracture. 122

Fig. 5. 26 Images of the (a) deformation lines (indicated by ovals), and (b) force analysis of the deformation lines X and Y. 123

Fig. 5. 27 Load displacement curve from the bending test; the black numbered show the order in which the martensite cracks were initiated. 124

Fig. 5. 28 (a) the maximum strain value appeared early in the ferrite phase. The arrows point to the maximum value appearing along the deformation lines in the black ovals. (b) shows the maximum region was within the ferrite. (c) shows the most affected region is at the same location in the ferrite phase. 128

Fig. 5. 29 Location of large cracks in the sample, with details provided in Fig. 5.30. 131

Fig. 5. 30 Cracks in the samples after the material became damaged; images b and d provide magnifications of images (see blue squares) a and c respectively. 133

Fig. 5. 31 Bending sample after damage; the crack propagation is clearly visible. 134

Fig. 5. 32 (a) to (h) results in the development of crack propagation. Figs. (a) and (b) show the crack pathway and early ferrite deformation, respectively. Displacement values for all images: fig. (a) at 0.225 mm, figs. (b) and (c) at 2.027 mm, fig. (d) at 2.475mm, fig.(e) at 2.98 mm, fig. (f) at 3.504 mm, and fig. (g) at 4.041 mm. (h) Measurement length of the crack once the sample has been damaged. 136

Fig. 5. 33 (a) to (l) shows crack number 2, from the start of the ferrite deformation until the final propagation. Displacement values for all images: fig. (a) and (b) at 2.027 mm, figs. (c) at 2.475 mm, fig.at (d) 2.98 mm, fig.(e) at 3.28 mm, figs (f) at 3.504 mm, (g) at 3.685mm, fig (h) at 4.041 mm, fig (i) at 4.784 mm, fig.(j) at 5.03 mm, and fig.(k) at 5.515 mm. (l) Measurement length of the crack after the sample was damaged..... 139

Fig. 6. 1 Modelled plastic deformation curve. 143

Fig. 6. 2 Effect of q parameters on curve. 144

Fig. 6. 3 Void volume fraction effect on the simulation curve. 145

Fig. 6. 4 Influence of void volume fraction on the curve. 145

Fig. 6. 5 Influence of standard deviation on the curve. 146

Fig. 6. 6 Best fitted simulation results compared to the experimental curve. 146

Fig. 6. 7 Load displacement curves for the second notch, with the same GTN parameters as those applied to first notch. 147

Fig. 6. 8 Simulation curve with GTN parameters compared with experimental results. 148

Fig. 6. 9 Effect of the subset size on the image resolution: (a) 8 x 8 pixels, (b) 5 x 5 pixels and (c) 1 square pixel. 150

Fig. 6. 10 (a) Area of the microstructure highlighted by the red rectangle in Fig.6.9 (c), (b) Mesh corresponding to a 5 x 5 pixels subset size and (c) 1 pixel subset size. 150

Fig. 6. 11 (a) Adjusted stress-strain curves for both phases from finite simulations of the microstructure, (b) Applied strain values selected for calculated errors reported in Table 6.2. 151

Fig. 6. 12 Strain distributions for (a) experimental and (b) modelling result. 153

Fig. 6. 13 Maximum principal stress distribution in the two-phase microstructure (in MPa) at 0.048 global strain. 154

Fig. 6. 14 Results on von Mises stress distribution (in MPa). 155

Fig. 6. 15 Results on von Mises stress frequency distribution for both martensite and ferrite. 155

Fig. 6. 16 Strain results for the area where six cracks occurred in martensite. The black lines indicate their locations (the X direction is horizontal). 156

Fig. 6. 17 Maximum principal stress distribution (MPa) in the martensite phase. Highlights on martensite phase: black circles indicate maximum principal values located in crack region and other areas where cracks could occur. 157

Fig. 6. 18 Maximum principal stress distribution before the first void appeared in the microstructure in the tensile test (0.26 global strain). 158

Fig. 6. 19 Load-displacement curves comparing the punch test experimental results with the FE punch simulation analyses. 159

Fig. 6. 20 (a) comparison between LE11 strain distributions in the simulation and Exx in the experiment, at displacement of 9.95. (b) distribution of computed LE22 compared to experimental Eyy. 161

Fig. 6. 21 Maximum strain value obtained for small punch model with mesh element sizes 2, 4, 6 and 8. 162

Fig. 6. 22 Experimental results compared with the results of the modelling. 163

Fig. 6. 23 (a) and (b) LE11 and LE22 Strain distributions from Abaqus compared to Exx and Eyy experimental results respectively 164

Fig. 6. 24 Equivalent plastic strain distributions through the thickness: (a) maximum value of about 7% at the surface in contact with the tool, (b) maximum value of about 8%, moving to the top surface of the sample, and (c) Prior to final fracture with a maximum value of 66%. 165

Fig. 6. 25 Comparison between GTN simulations with different q parameters and experimental results. 166

Fig. 6. 26 Load-displacement curve for experimental bending test compared to simulation results. 167

Fig. 6. 27 Top and front views of the equivalent plastic strain distribution on both the edge and the top surfaces of the specimen prior to the appearance of a crack. 168

Fig. 7. 1 Distributions of strain values at the onset of the martensite cracking phase. Left: in-situ tensile test; and Right: in-situ bending test. 172

APPENDIX LIST OF FIGURES

Fig. I. 1 More details for setup of tensile test with 3D 189

Fig. II. 1 Specimen on die 190

Fig. II. 2 Macro punch tool 190

Fig. II. 3 3D DIC setting with punch rig for experiment. 191

Fig. III. 1 Top and bottom views of top die. 192

Fig. IV. 1 New punch design. 192

Fig. V. 1 Sample with rig of SP test with 3D DIC. 193

Fig. VI. 1 Setup of punch rig. 194

Figs. VIII. 1 Figures (a) to (f) explain Lagrangian strain distribution results (Exx) of punch test deformation 202

Figs. VIII. 2 Figures (a) to (f) Clarify strain distribution results before crack appearance. 204

Fig. IX. 1 Sample after application of 2.6 mm displacement. Red square shows lack of visible crack on surface. 204

Fig. IX. 2 First image of microstructure before application of load in small punch test. 205

Fig. IX. 3 Deformation of microstructure after application of 1.12 mm displacement. The black arrows show the initiation of microcracks. 206

Fig. IX. 4 Microstructure damage before appearance of crack on surface 207

Fig. X. 1 (a) to (f) Strain Exx results of micro punch test with 3D DIC, from beginning of test until before emergence of crack. 209

Fig. X. 2 Strain distribution results before development of crack. 210

Fig. X. 3 Results of crack inspection in the areas of the first and second parts of the small punch test after the 3D DIC sample was fractured through its thickness. 211

Fig. XII. 1 Location of large cracks in the sample, which are explained in detail Fig. (5.30) is section 5.4.2.1. 214

Fig. XII. 2 (b) to (k) explain cracks in samples after the material became damaged; images (c), (f), (g), and (k) are magnifications of images (see blue squares) (b),(d), (f), and (h), respectively. 217

Figs. XIV. 1 (a) Maximum principal stress distribution in the martensite phase, and (b) Highlights on martensite phase; black circles indicate maximum principal values located in crack region and other areas where cracks could occur. 222

Fig. XV. 1 Max. principal stress distribution before the second void appeared in the ferrite phase (0.26 global strain). 223

Fig. XV. 2 Max. principal stress distribution before the third ferrite void formed (0.3 global strain). 223

Fig. XV. 3 Max. principal stress distribution before the fourth ferrite void appeared (0.3 global strain). 224

LIST OF TABLES:

Table 3. 1 Chemical composition weight ratio (wt%) of DP1000 45

Table 4. 1 Material properties for conventional sample modelling. 68

Table 4. 2 Show the original values of GTN parameters 71

Table 5. 1 Details of global stress–strain values just prior to the appearance of damage in the martensite. Image number 1 indicates the crack location in the reference microstructure capture, and image 2 indicates the martensite fracture just before the crack appears in image 3. 88

Table 5. 2 Explanation of the formation of ferrite voids through deformation under the stress–strain curve. Image 1 is the reference microstructure. Image 2 indicates the ferrite void location just before it appeared, as shown at image 3. 93

Table 5. 3 Strain distributions in relation to the onset of the martensite cracking, as measured by DIC. Red arrows indicate the martensite fracture location. Black arrows indicate the DIC measurement strain localisation value before each crack appeared. Blue arrows indicate the maximum ferrite value located close to the martensite fracture. 101

Table 5. 4 Ferrite voids measured by DIC. Red circles indicate the ferrite void location in the microstructure. Black arrows indicate the ferrite strain localisation value just prior to void formation. 104

Table 5. 5 Maximum Lagrangian strain results before surfacing of crack. 110

Table 5. 6 Three locations of microstructures damaged through the SEM SPT. 114

Table 5. 7 Maximum Lagrangian strain results before the surfacing of cracks. 116

Table 5. 8 Martensite cracks and ferrite voids present throughout the deformation. 125

Table 5. 9 Strain distributions measured by DIC in relation to the fracture mechanism in table 5.8. 129

Table 6. 1 Show the damage parameters for all geometries. 148

Table 6. 2 Percentage error between the experimental true stress and averaged simulation stress for applied displacements selected before the appearance of the first crack. 152

Table 6. 3 Error between experimental and simulation strain values 153

Table 6. 4 Summary of results for ferrite voids initiation. 158

APPENDIX LIST OF TABLE:

Table XI. 1 Martensite cracks and ferrite voids throughout the deformation. 212

List of equations

Equation 1 $f^0 = e_b^0 / e_a^0$ 28

Equation 2 $\overline{\sigma}^a = f_{HR}(\overline{\varepsilon}^a)$ 29

Equation 3 $\overline{\sigma}_{YF} = f_{YF}(\sigma_{xx}, \sigma_{yy}, \sigma_{xy})$ 30

Equation 4 $\alpha = \sigma_2 / \sigma_1.$ 30

Equation 5 $d\varepsilon_{ij} = d\overline{\varepsilon}(\partial \overline{\sigma}_{YF} / \partial \sigma_{ij})$ 30

Equation 6 $[\sigma]_{ntz}^a = [T]^T \cdot [\sigma]_{xyz}^a \cdot [T]$ 30

Equation 7 $[\sigma]_{ntz}^a = [T]^T \cdot [\sigma]_{xyz}^a \cdot [T]$ 30

Equation 8 $[T] = \begin{bmatrix} \cos\varphi & -\sin\varphi & 0 \\ \sin\varphi & \cos\varphi & 0 \\ 0 & 0 & 1 \end{bmatrix}$ 30

Equation 9 $tan(\varphi) = tan\,\varphi^0 \,(1 + d\varepsilon_x^a) / (1 + d\varepsilon_y^a)$ 30

Equation 10 $\sigma_{nn}^a e_a = \sigma_{nn}^b e_b$ 31

Equation 11 $\sigma_{nt}^a e_a = \sigma_{nt}^b e_b$ 31

Equation 12 $d\varepsilon_{tt}^a = d\varepsilon_{tt}^b$ 31

Equation 13 $\begin{cases} f\sigma_{nn}^b = \sigma_{nn}^a \\ f\sigma_{nt}^b = \sigma_{nt}^a \end{cases}$ 31

Equation 14 $f = f^0 \cdot exp(\varepsilon_{zz}^b - \varepsilon_{zz}^a)$ 31

Equation 15 $\begin{cases} F_1(d\overline{\varepsilon}_b, \sigma_{tt}^b) = \overline{\sigma}^b - \overline{\sigma}_{YF}^b = 0 \\ F_1(d\overline{\varepsilon}_b, \sigma_{tt}^b) = d\varepsilon_{tt}^a - d\varepsilon_{tt}^b = 0 \end{cases}$ 31

Equation 16 $\Phi = \Phi = \frac{\sigma_{eq}^2}{\sigma_y^2} + 2f cosh\left(\frac{1}{2}\frac{\sigma_{kk}}{\sigma_y}\right) - 1 - f^2 = 0$ 33

Equation 17 $\sigma kk = \sigma 1 + \sigma 2 + \sigma 3$ 33

Equation 18 $\sigma_{eq} = \sqrt{\frac{1}{2}}[(\sigma_1 - \sigma_2)^2 + (\sigma_2 - \sigma_3)^2 + (\sigma_3 - \sigma_1)^2]$ 33

Equation 19 $f = 1 - r$ 33

Equation 20 $r = Vm/Vt$ *33*

Equation 21 $\Phi = (\frac{\sigma_{eq}}{\sigma_y})^2 - 1 = 0$ *33*

Equation 22 $\Phi = \frac{\sigma_{\bar{e}q}^2}{\sigma_y^2} + 2fq_1\, f\, cosh\left(\frac{q_2}{2}\frac{\sigma_{kk}}{\sigma_y}\right) - 1 - q_3 f^2 = 0$ *34*

Equation 23 $\dot{f}_n = A_n\, \dot{p}$ *34*

Equation 24 $An = \frac{f_n}{s_n\sqrt{2\pi}} \exp\left(-\frac{1}{2}\left(\frac{p-\varepsilon_n}{s_n}\right)^2\right)$ *34*

Equation 25 $f *= f \qquad , f < fcfc + \delta f - fc$ *35*

Equation 26 $\Phi = \frac{\sigma_{\bar{e}q}^2}{\sigma_y^2} + 2fq_1\, f^*\, cosh\left(\frac{q_2}{2}\frac{\sigma_{kk}}{\sigma_y}\right) - 1 - q_3 f^{*^2} = 0$ *35*

Equation 27 $\sigma T = \sigma m/\sigma eq$ *45*

Equation 28 $A \geq D + 2t$ *57*

Equation 29 $\sigma = 1V \int V\ \sigma\, dV$ *72*

Equation 30 $\sigma A = F/A$ *76*

Equation 31 $\varepsilon_e = {}^{\Delta l}/_{l}$ *76*

Equation 32 $\sigma t = \sigma e\,(1 + \varepsilon e)$ *77*

Equation 33 $\varepsilon t = \int_{l_o}^{l} l\, dl = ln(1 + \varepsilon e)$ *77*

ABBREVIATIONS

AHSS	Advanced High Strength Steels
DP	Dual Phase
DIC	Digital Image Correlation
SEM	Scanning Electron Microscope
GTN	Gurson-Tvergaard-Needleman
UTS	Ultimate Tensile Strength
Ys	Yield Strength
TTT	Time Temperature Transformation
M	Martensite
F	Ferrite
Ms	Martensite Start Temperature
A	Austenite
SP	Small Punch
SPT	Small Punch Test
FE	Finite Element

NOMENCLATURE

In this thesis, abbreviations and symbols were applied. The explanation specified in the script and the synopsis is as follows:

Φ	Plastic yield surface of the material
σ_{kk}	The trace stress tensor (σ1 + σ2 + σ3)
σ_y	The yield stress
σ_{eq}	Von Mises equivalent $\sigma_{eq} = \sqrt{\frac{1}{2}}[(\sigma_1 - \sigma_2)^2 + (\sigma_2 - \sigma_3)^2 + (\sigma_3 - \sigma_1)^2]$
V_m	The matrix volume
V_t	The material total volume
f	Value of porosity
f_0	The initial volume fraction of voids
q_1, q_2, q_3	Gurson model parameters
A_n	The strain controlled
f_n	The volume fraction of the second phase particles where voids can be nucleated
f^*	The effective porosity at failure introduced by Tvergaard and Needleman to Gurson model

f_c	The critical porosity at which the void begins to coalesce.
δ	The multiplication factor presented by Tvergaard and Needleman to accelerate void growth
$c\,(x, y)$	The cross-correlation coefficient for the subset at a specified location
$c'(\Delta x, \Delta y)$	The normalized correlation coefficient for the DIC subset at a certain location
$I1$	The pixel intensity of the reference image for the DIC analysis
$I2$	The pixel intensity of the deformed image for the DIC analysis

1. INTRODUCTION

Steel is a vital structural material in the field of engineering, and of particular value for infrastructure and transportation. Researchers and automotive companies seeking greater fuel efficiency and tensile strength have developed this material, thereby reducing the weight of cars and enhancing crash-resistance.

Two different methods are employed to classify automotive steels: evaluation of metallurgical properties and strength. Metallurgical assessment provides information designating lower-strength, high strength, which includes high-strength low-allow steels (HSLA), and advanced high-strength steels (AHSS). In addition, designs focusing on enhanced steel strength are combined with applications that seek to improve edge stretching and bending characteristics. The strength technique is especially important for the designers of parts and is the primary focus of this article. HSLA and AHSS are the commonest terms applied when developing higher strength steels.

This paper discusses orthodox HSLA steels and AHSS modifications in their microscopic structure, where the former consists of one-layered ferritic steels with potential for carbon-manganese (C-Mn) steels (or pearlite). Meanwhile, AHSS has a multiphase microstructure containing multiple phases; for example, martensite, bainite, and/or (retained) austenite are essential when producing steel with exclusively tolerable mechanical properties. Some AHSS types have a high strain hardening capacity, balancing ductility and strength, while some have superior output on terms of tensile strength, exhibiting a bake hardening behaviour. AHSS contains martensitic steels with a minimum tensile strength value of 440 MPa. Any steels rated above the minimum assigned value are designated ultra-high-strength steels (UHSS), where several industries choose 980 MPa as a threshold, and others use 1180 or 1270 MPa; which represents a much higher threshold relative to others. However, microstructurally, both AHSS

and UHSS are essentially the same products, only characterized by steel grade, thickness, and mechanical properties. The third-generation type of AHSS builds on previously designed first-generation and second-generation AHSS, with third generation engineered multi-phase steels enhancing formability, as gauged in tensile, sheared edge, and bending tests. Usually, specific proportions and distributions of retained austenite in a bainite or martensite matrix, with a fair sum of ferrite and precipitates, are included to augment their respective properties (Keeler & Kimchi, 2015).

Originally, AHSS were defined using the metallurgical approach and referring to minimum tensile strength. Prior to their commercialization, HSLA steels were described by their minimum yield strength, with units being region-specific; i.e., MPa, with AHSS frequently presented as the only option available for a given metallurgical method and tensile strength. As an example, AHSS DP590 was described as a dual-phase steel with 590 MPa tensile strength. Today, however, multiple dual-phase grades, with a minimum 980 MPa tensile strength are available. The different characteristics are identified as either cold rolled or hot rolled, minimum yield strength, minimum tensile strength and metallurgical type; for example, CR-500Y780T-DP describes the cold rolled (CR) dual phase (DP), with a 500 MPa yield strength of (500Y) with a tensile strength of 780 MPa (780T) (Keeler & Kimchi, 2015).

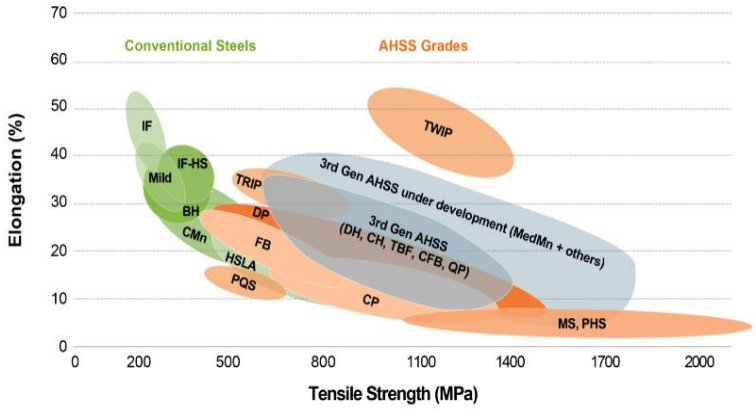

Fig.1. 1 The formability graph of AHSS and other kinds of steel (Keeler & Kimchi, 2015).

New-generation automotive steels include DP steels, because they are an ideal choice for automobile complexes due to their low yield point, high strength and high work hardening (Sarwar & Priestner, 1996). These properties lend DP steel excellent capability for ductility and strengthening.

Several studies have been published in previous decades to understand the deformation and damage in DP steels, and the scale of their microstructure. Despite the development of new experimental capabilities, such as mechanical testing carried out inside scanning electron microscopes, and advanced microstructure-based modelling, which can afford useful insights into local deformation and damage initiation, the majority of studies have focused on tensile testing. The results are therefore limited to this type of testing geometry, and do not represent the large deformations that can be arise during forming operations. Furthermore, damage propagation is too limited to the understanding of conditions leading to final failure. Studies conducted on formability have so far been insufficiently broad to deliver meaningful results concerning damage localisation and crack propagation. The deformation behaviour in the early stages of microstructural damage in DP steels has yet to be fully explored, with statistical results being unable to predict damage initiation. Damage development, leading to failure under conditions that are representative of forming conditions remains an open field of research.

To address current lack of understanding, a new research methodology will be adopted in this study. Tensile tests carried out inside a scanning electron microscope will be conducted with digital image correlation (DIC) to determine the localisation of deformation in the microstructure, and the formation of damage in relation to local strain distributions. The DIC results will also be used to develop a microstructure model to clarify the conditions leading to damage development. Further multi-scale mechanical tests will also be developed to investigate damage development, specifically by applying a small punch test (SPT), under

deformation conditions closer to forming operations. The work will also assess the capacity of the commonly used Gurson damage model to predict the overall response of DP1000 for the various test geometries.

1.1 Aim and novelty

The aim of this work is to provide a new understanding of deformation and damage development in the microstructure of DP 1000 steel. Particular emphasis will be placed on the damage propagation up to failure which has not been studied adequately to date, especially under deformation conditions more representative of industrial forming operations for automotive components. It is anticipated that this new insight will facilitate the development of predictive multi-scale models of the mechanical responses of next generation automotive steels.

1.2 Thesis structure

This thesis is structured as follows:

1. The next chapter reviews literature previously published concerning the deformation, formability and damage mechanism in DP steels. Damage modelling based on constitutive equation modelling for continuum damage will also be reviewed, alongside microstructure-based damage modelling, to define the study context and identify gaps in knowledge.

2. Chapter 3 describes the material investigated, and the specific experimental procedures used in this study.

3. Chapter 4 explains the techniques used for the simulations performed in this work.

4. Chapters 5 and 6 present the experimental and simulation results.

5. Chapters 7 and 8 identify the chief areas of discussion and a give a brief summary, with suggestions for future work.

2. LITERATURE REVIEW

DP steels are generally used in automotive manufacturing because they possess high ductility, superior strength, and good formability. They are also known for their exceptional material qualities, which are derived from their innovative microstructures and a mixture of attributes such as martensite and ferrite deformability, martensite volume fraction, grain size, and crystallographic orientation. Under displacement the microscale connections amongst these functions result in suitable macroscale deformation properties. Nevertheless, the mechanism of damage in these structures is not fully understood. Accordingly, this thesis begins with a comprehensive review of the relevant literature concerning DP steels, their formability, and their deformation mechanisms, together with an explanation of damage modelling based on constitutive equations and microstructure-based damage.

2.1 DP 1000 steel

This type of steel was discovered in 1970 and named after the material's microstructure, which is processed for its superior drawability (ability of the material to deform under plastic deformation without being damaged) over ferrite-pearlite steels. DP steels have indeed a high ratio of yield strength (Ys) to ultimate tensile strength (UTS) ratio while the Ys/UTS ratio for ferrite-pearlite steels is low. The stress-strain for DP steels is continuous, as shown in Figure 2.1, is typically different to that for ferrite-pearlite steels, plain carbon steels, high-strength low-alloy (HSLA) steels, and micro-alloyed steels, among others (Rashid, 1981).

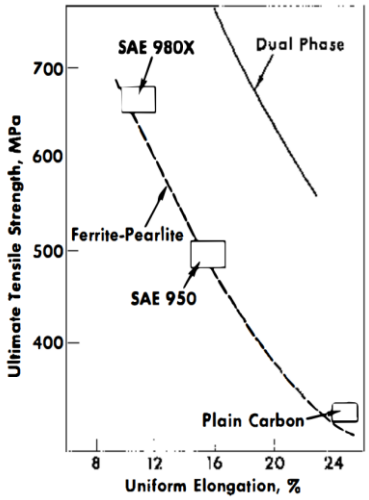

Fig. 2. 1 UTS and elongation of DP steels, plain carbon steels and ferrite-pearlite steels (Rashid, 1981).

In 1960 the British Iron and Steel Research Association (BISRA; United Kingdom) and the Inland Steel Corporation (ISC; United States) improved the properties of ferrite and martensite simultaneously. The objective of the BISRA was to improve the annealing procedure to create steels with a tensile strength of approximately 500 MPa, whilst the goal of the ISC was to achieve 1000 MPa. The BISRA used a method for quenching either liquid metal, with low tempered salt or water, post tempering. The ISC, by contrast, focused their experiments on a completely quenched martensite product. Both studies aimed to develop the formability of steel and thereby reduce its weight (Rashid, 1981).

This research focuses on the formability and ductility of steel. Formability is measured via stress, temperature, Ys, and ductility. The most important of these is ductility (or drawability), because it concerns the plastic deformation of the material to the point of fracture. Specifically, during the tensile test for a material, the length and area change. The percentage of length is $(l_f/l_0 - 1)$ *100, and any reduction in area is represented by (1- A_f/A_0) *100; in these equations, l_0 and A_0 denote the initial length and the initial area of the specimen, respectively, and the final length and final area of the specimen are denoted by l_f and A_f, respectively. The

mechanism of damage can be divided into the following phases: void nucleation, growth, and coalescence (Callister & Rethwisch, 2007).

High-quality DP steel materials offer the advantage of high elongation with regard to failure and strength. The mechanical attributes of DP steels are compared with those of other steels in Fig. 2.2. Their combined microstructure indicates that these steels would be comparable to ferrite-pearlite steels. However, under similar uniform stretching, DP steels typically have a higher UTS than pearlite steels. The malleability of DP steels can be contrasted with that of ferrite-pearlite steels. In similar assembly processes, DP steels of the preferred quality show cost advantages over ferrite-pearlite steel; it is therefore conceivable that weight can be reduced, which is desirable to automobile manufacturing companies (Tasan et al., 2015).

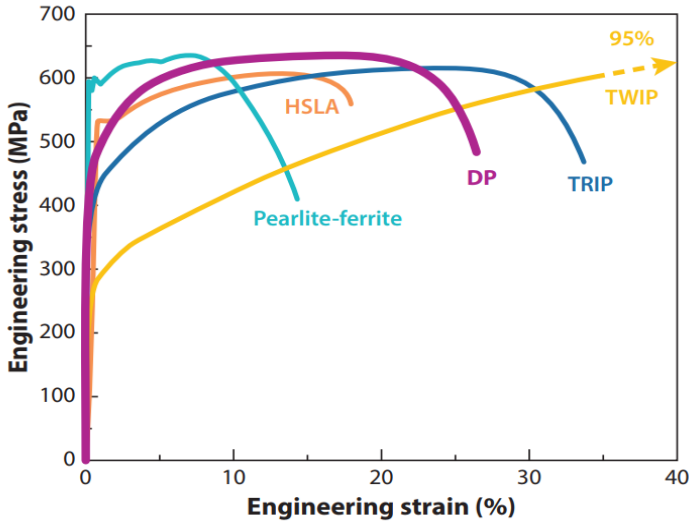

Fig. 2. 2 Engineering stress-strain curve of DP steels and other AHSSs (Tasan et al., 2015).

The microstructure of dual-phase steel is normally formed via a process of intercritical annealing, followed by quenching. Fig. 2.3 shows both the phases and Time-Temperature-Transformation (TTT) diagrams for carbon steels with the heat treatments that are relevant to DP steels. The steel is first heat treated to a temperature that falls within the intercritical regime, where a mixture of austenite and ferrite form. Annealing is then followed by quenching with

austenite transforming into martensite. The volume fraction for these phases is controlled by both the steel composition and the annealing temperature (Rashid, 1981; Tasan et al., 2015).

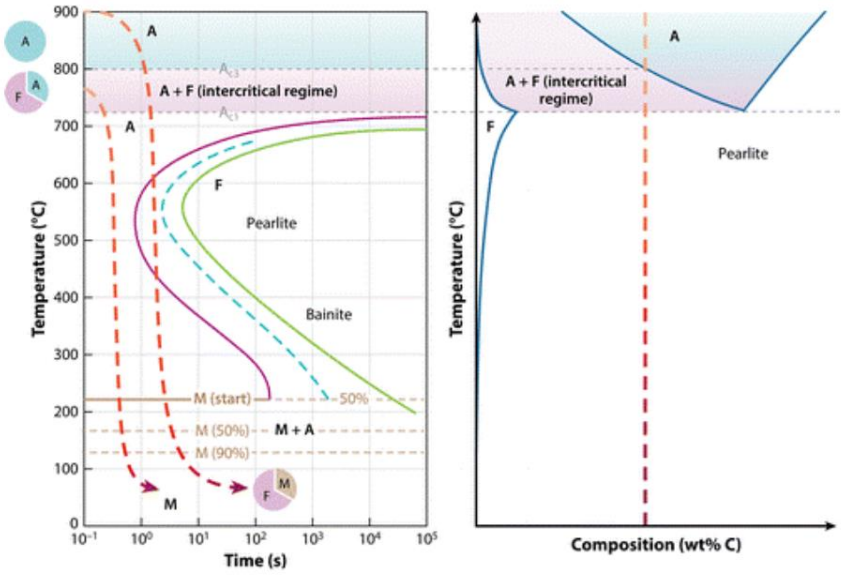

Fig. 2. 3 Left: TTT diagram of heat treatment performed to form ferrite and martensite phases. Right: iron-carbon equilibrium phase diagram (Tasan et al., 2015).

The microstructure of DP 1000 steel contains two phases: ferrite and martensite (see Fig. 2.4). Ferrite is a soft phase and can enhance ductility, whilst martensite is a hard phase and can enhance the material's strength. Increasing the volume fraction of the martensite increases strength, but often also reduces ductility.

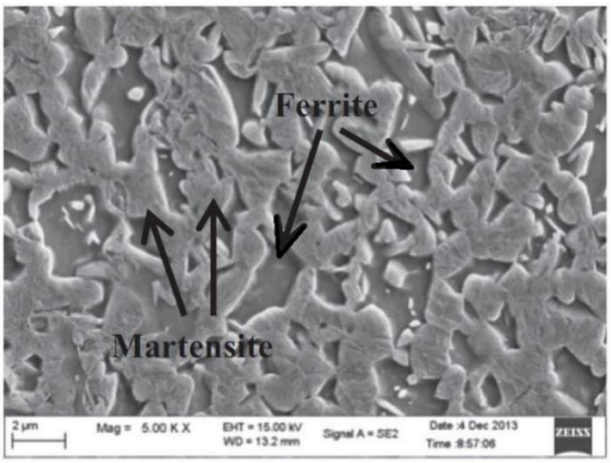

Fig. 2. 4 SEM image of DP1000 steel microstructure; brighter sections are martensite, darker sections, ferrite (Zhao et al., 2014).

A controlled manufacturing procedure can improve the formability of DP steels and delay the formation of damage at the microstructure scale.

The use of distinctive process conditions can result in the production of different DP steels with unique mechanical properties. Some specialists have attempted to connect the production methods to the mechanical properties of DP steels. (Zhao et al., 2014) examined the impact of temperature strengthening on the DP steels produced. Elsewhere, (Ramazani, Mukherjee, Prahl, & Bleck, 2012) considered the impact of banding of DP steels on their mechanical properties. Banding refers to the arrangement of martensite particles in the microstructure into layers, instead of having a uniform or arbitrary martensite distribution. In their study, a distinctive heat process was utilised to create DP steel products. The rising temperature and rapid heating prompted the emergence of a banded microstructure. The findings indicated that banding produced a reduction in hardening, together with a decrease in tensile strength and Ys. Likewise, microstructural deformation became evident, causing failure during the initial periods of deformation and limiting the uniform stretching of the steel.

A separate work by (Park, Nishiyama, Nakada, Tsuchiyama, & Takaki, 2014) examined the impact of microstructure morphology on DP steels, with focus on the martensite deformation . They examined samples in which martensite surrounded ferrite. The results showed that this morphology could decrease necking deformation and develop hardenability without influencing the overall elongation.

Coarse- and ultra-fine-grained DP steels with an average grain size of 2µm and an approximate microstructure volume fraction of 50% martensite were evaluated in (Saeidi, Ashrafizadeh, Niroumand, Forouzan, & Barlat, 2014). They found that grain morphology has little effect on yield point or UTS but a perceptible effect on strain and total elongation to fracture. In addition, ultra-fine-grained DP steels exhibit superior uniform stretchability and ductile properties than coarse-grained steels. According to the results of an analysis by (Livatyali, Firat, Gurler, & Ozsoy, 2010), enlarging the volume fraction of martensite with a consistent carbon content reduced the ferrite grain size and raised the strength of the interface; this was attributed to the separation of the interface during the austenite change process. Similarly, the martensite volume portion expands with a reduction in carbon content. The microstructures with higher carbon content exhibit better hardening and enhanced UTS; moreover, they deliver increasingly uniform elongation, with no effect on the yield stress. This is because the interface strengthening improves as dislocation occurs close to the interface. This section has dealt primarily with the characterisation of DP steel; the following subsections will discuss its formability and mechanisms of damage.

A study by (Saeidi et al., 2014) evaluated coarse- and ultra-fine-grained DP steels with an approximately 50% volume fraction of martensite. They found that the grain morphology had little effect on yield point or UTS, but there was a perceptible impact on the strain and total elongation to break. Ultra-fine-grained DP steels have a better uniform stretchability and ductile properties in comparison with coarse-grained ones. In the analysis of (Wagoner, Wang,

& Sriram, 1994), increasing the volume fraction of martensite with a consistent carbon content reduced the ferrite grain size and raised strength between the boundaries. Microstructures with a high carbon content exhibited better hardening, enhanced UTS, and increasingly uniform elongation. This was due to an improvement of the interface strength between ferrite and martensite.

2.2 Formability characterization

2.2.1 Deformation modes during forming operations

Forming operations are very common in the automotive industry for producing high-quality car body parts, with the desired final shape achieved after the application of complex forming loads. The demand for cost-effective part manufacturing processes is increasing and this has driven the development of the recent deformation and damage models. Predicting material behaviour during metal forming applications with accuracy requires the correct application of material deformation modes and knowledge of the most favourable deformation mode. Similarly, the application of advanced high-strength for reducing the weight of the vehicle has increased in the automotive industry. These materials should be adequately ductile and their forming behaviour should also be quantifiable. Here damage modelling methods are essential for providing critical information about material behaviour in metal forming processes.

The evolution of the structure occurs due to severe plastic deformation and is dependent upon the deformation mode. Common forming operations are differentiated from severe plastic deformation techniques according to the principal characteristic of the deformation mode. The deformation mode can vary between simple shear and pure shear. The optimal mode for grain refinement and structure modification is simple shear, whereas the optimal mode for forming operations is pure shear (Segal, 2002). The objective of several plastic deformation (SPD)

techniques is to manufacture lightweight parts through fine-grain modification, and these can find application in the automotive industry (Azushima et al., 2008). SPD techniques include equal channel angular extrusion, high-pressure torsion, twist extrusion, and simple sheer extrusion; all of these have the simple shear deformation mode. By contrast, accumulative roll bonding, repetitive corrugation, straightening multi-directional forging, and cyclic expansion extrusion involve total or partial pure shear as the deformation mode (Rahimi & Eivani, 2015).

The next section reviews the different tests that have been performed to characterise the formability of metals. Particular attention will be paid to the punch test used in the present study.

2.2.2 Formability tests

Given the ongoing competition between automotive manufacturers to develop materials with improved properties, there is general acceptance regarding experimental techniques for testing the properties of these materials.

Formability refers to the ability of the material to undergo plastic deformation without the formation of defects (necking, buckling, flaws, etc…) and is characterised by formability tests. Tensile and compression testing is one example of formability tests used to measure behaviour under axial tensile loading and to determine the behaviour of materials. The tensile test is a mechanical test that is widely adopted to examine the properties of materials. It gives data about the tensile strength, Ys and ductile behaviour of materials. A downside of the tensile test is that it is only uniaxial. Whilst this is sufficient for identifying the tensile properties of a material, additional information might be needed to characterise the formability of the material under more complex loading conditions.

The forming limit diagram (FLD), used in sheet metal forming, shows the forming limit curve defined as the transition between safety and failure in a graph plotting the true major strain on

the Y-axis against true minor strain on the X-axis (ISO, 2008) (see Fig. 2.5). To calculate the forming limit, the strain paths are plotted between major strain ε_1 and minor strain ε_2. The paths are drawn across the strain range from uniaxial tension to biaxial tension. The forming limit curve is plotted for different strain states, and the FLD is expressed as a function of true major and minor strain on the surface of the sheet.

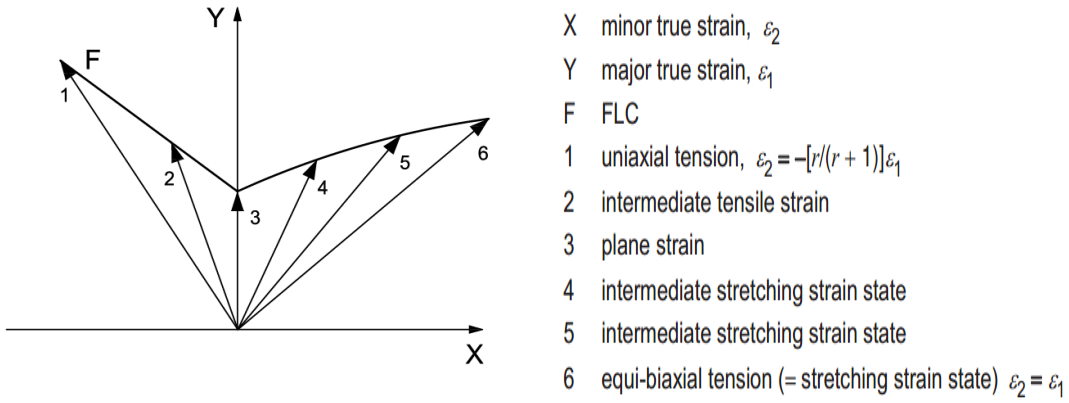

Fig. 2. 5 Strain paths on a forming limit diagram (ISO, 2008) .

Various tests can be used to characterise the formability of sheet metals with standards developed for the determination of forming limit curves in the laboratory (e.g. BS EN ISO 12004-2:2008) (ISO, 2008). Different types of experiment have been conducted to understand formability. Fig. 2.6 illustrates two contrasting examples: the swift cup test, which uses a flat punch tool to evaluate the drawability fraction for flat cups, and the Fukui conical cup experiment, which uses a ball to form and draw the material (Fig. 2.7). The limiting dome height (LDH) test also uses a ball tool to estimate the ability of the material to deform (Hosford & Caddell, 2011).

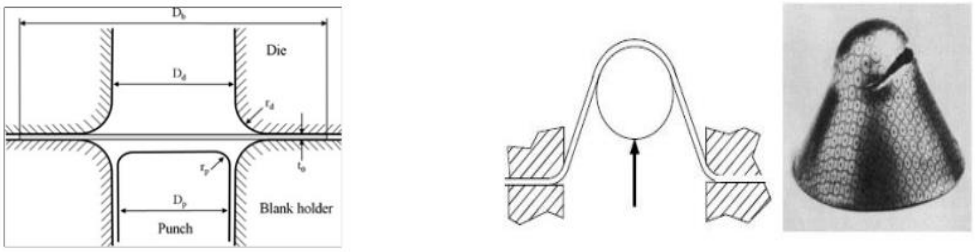

Fig. 2. 6 The left diagram shows the swift and cup drawing for testing a flat-bottom cup (Yoon, Cazacu, Yoon, & Dick, 2010). The figure on the right shows the Fukui test conducted with a damaged cup (Hosford & Caddell, 2011).

Standards for the ball punch test have also been developed (e.g. E643 – 15, 2015) to evaluate the formability of the material (ASTM, 2015). The ball punch test was developed to standardise many of the test parameters of other punch tests such as the Olsen and Erichsen cupping tests (Fig. 2.7).

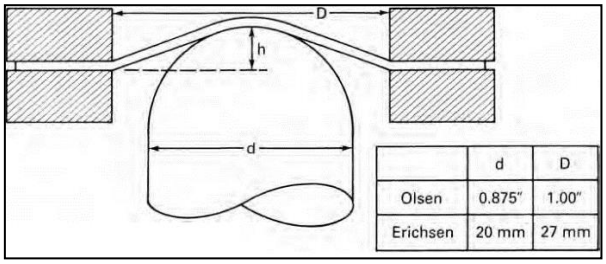

Fig. 2.7 Olsen and Erichsen tests using a hemispherical tool (Hosford and Caddell, 2011)

A further formability test was designed by Ohio State University (OSU) to measure the point in a sheet forming operation where the punch height is taken ‘to failure’. It has performed well in numerous industrial applications (Wagoner et al., 1994). However, this test reveals limited information about microstructure deformability. Fig. 2.8 shows the OSU formability test conducted with three types of punch tests.

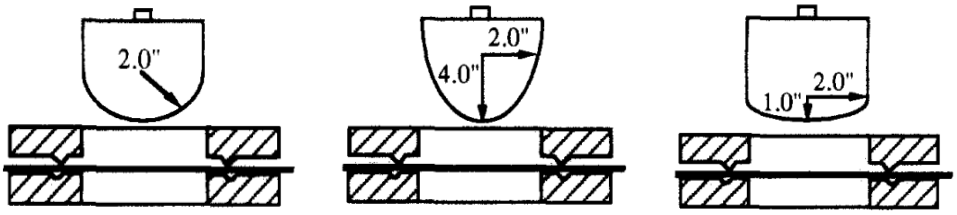

Fig. 2. 8 OSU punch tests (Azushima et al., 2008).

The formability of DP1000 produced using several heat treatments was studied by conducting a punch test in (Kamikawa & Morino, 2019), where 90-mm-diameter samples were tested to failure. 3D Digital Image Correlation was used to measure full-field strain distributions at the surface of the sample. A comparison of the load displacement curves of all treatment samples indicated that DP 1000 treatment at 240 °C yields the best formability.

The formability punch test used in this research is based on the standard ball test but has been adapted to focus on the analysis of the deformation and damage of the material, especially at the scale of the microstructure with details reported in Chapter 3. One significant difference is therefore the sample diameter which is far smaller than the recommended sample diameter for the standard ball punch test (ASTM, 2015). The next section reviews studies carried out using small punch (SP) tests.

2.2.3 Small Punch (SP) tests review

The small punch (SP) test has undergone numerous iterations since it was first used during the 1980s. Tests such as the Erichsen cupping test (Kamikawa & Morino, 2019), which uses a cup with a diameter moderately greater than that in a strong punch test, were initially viewed as the worldwide standard. The Erichsen experiment examines the material's forming behaviour, including its reaction to the extended forming and drawing process, as shown in Fig. 2.8.

A past distortion experiment utilised a ball to deform the material. This method is now preferred to the typical SP test because the ball can be replaced after each test.

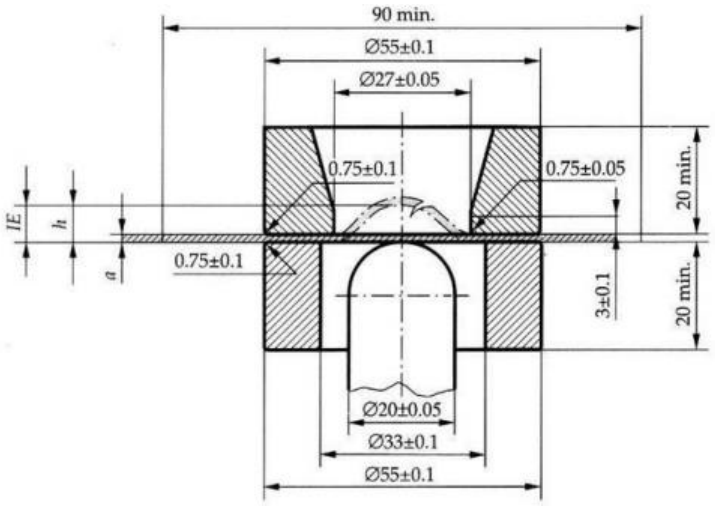

a = the test piece thickness.

IE = Erichsen cupping index.

h = Indentation depth through running the experiment.

Fig. 2. 6 Erichsen cupping test (Kamikawa & Morino, 2019)

.

Finite element (FE) models were developed by (Simonovski, Holmström, & Bruchhausen, 2017) to support the parametric analysis of the SP test. The SP technique was used to characterise irradiated materials and when the quantity of the tested material was small. The application of FE analysis demonstrated that there were no significant differences between rectangular flat specimens (6.55 × 11 mm, 0.45 thickness) and circular flat specimens (ø = 8 mm, 0.5 mm thickness). Due to the curvature of the tube specimen (0.45 mm), as shown in Fig. 2.9, a high maximal force (Fm) was achieved at significantly lower displacements. FE analysis also showed that, because the UTS was kept constant, the Fm was unaffected by hardening and yield stress. At a small punch deflection (0.1 mm), the likelihood of substantial specimen deformation restricted the further application of the SP technique to ductile materials. To limit the scatter in the yield stress estimates, a suitable amount of clamping was ensured. The authors concluded that the simulation and experimental results were in agreement with each other at a friction coefficient of 0.2.

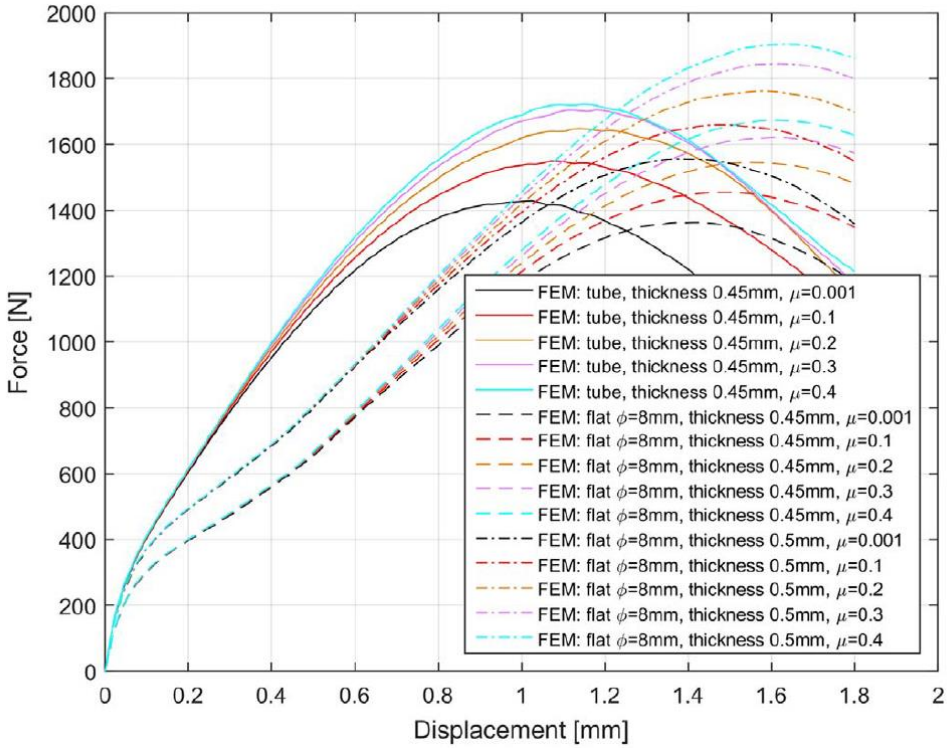

(a)

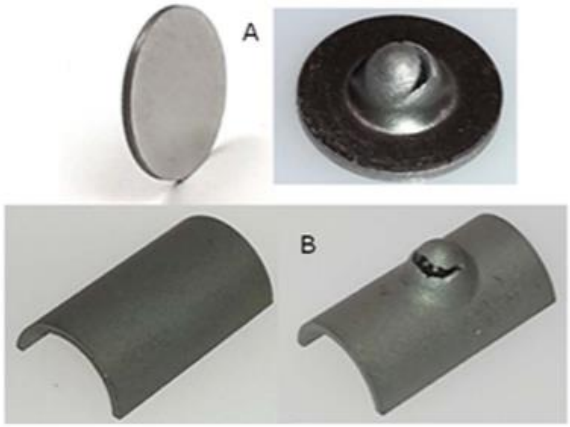

(b)

Fig. 2. 7 (a): Computed displacement of the tube and flat specimens against a force (b): Flat and curved tube before and after the fracture (Simonovski et al., 2017).

A novel method was developed by (Abendroth & Kuna, 2003) by exploiting the experimental results of the SP test to recognise the deformation properties of ductile materials. According to the authors, for material parameters, neural networks are able to generate estimated functions based on the load-displacement curve. The estimated function was obtained by coupling the Gurson-Tvergaard-Needleman (GTN) model with numerical simulations. Due to the

complexity of using all twelve GTN parameters, the authors emphasised the importance of preselecting parameters on the basis of material type (Fig 2.10). Furthermore, the void volume fraction was considered a damage variable, as the GTN model assumes that damage is only caused by nucleation and spherical void growth. Lastly, the research demonstrated that the damage model can adequately predict failure and deformation for multiple stress states.

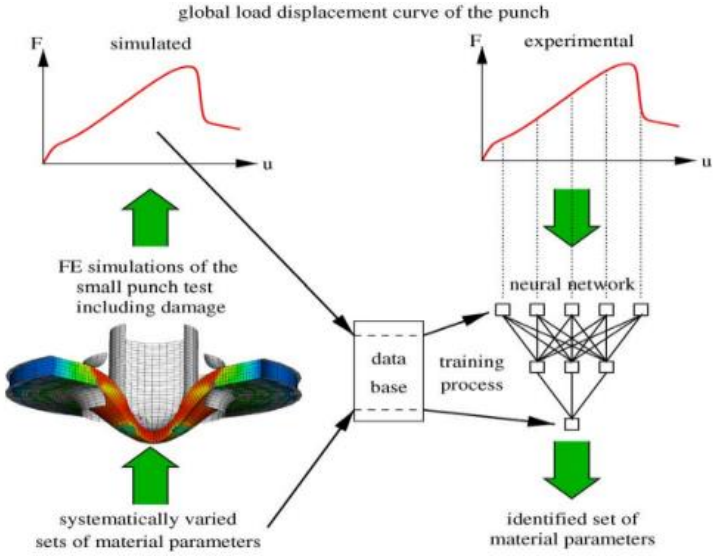

Fig. 2. 8 Simulation and experimental results of SP test showing load-displacement curves (Abendroth & Kuna, 2003)

The formability of DP steels needs to be better understood as findings of experimental work with 3D DIC are incomplete. Yet, taken together, the above sources indicate that novel ideas, such as using the SP test in combination with DIC to study the material formability, can be developed to observe the damage that occurs in steel. The SP test has also been applied to analyse the strain distribution in a specimen during the formability test. Accordingly, in the present research, DIC will be used to further understand strain localisation and damage mechanisms in the steel's microstructure.

2.3 Deformation and damage mechanisms

The mechanisms of damage through ductile plastic deformation are discussed in this section. Plastic deformation is the first sign of fracture, the inspection of which is crucial to understanding the strain localisation damage which leads to the final failure. The damage could be initiated in martensite or ferrite phases, then propagated in ferrite to create voids; the voids then nucleate and coalescence to form the micro cracks, which in turn lead to macro cracks (!!! INVALID CITATION !!!). Accordingly, this section presents a summary of findings on the plastic deformation mechanisms of DP steels.

In a study of DP600 detailed in (Avramovic-Cingara, Saleh, Jain, & Wilkinson, 2009), a micro crack in the martensite phase began at a low strain of 0.029 and propagated immediately after initiation. Void nucleation is the first mechanism of damage, and was observed at the ferrite martensite interface at a strain value of 0.09. A second specimen showed another mechanism of damage decohesion at the ferrite-martensite interface, and the void grew along the ferrite phases. Furthermore, a smaller number of voids nucleation followed the cracking of the martensite particles, and a very small number of large voids were nucleated at inclusions.

A further study described in (Avramovic-Cingara, Ososkov, Jain, & Wilkinson, 2009) reported mechanisms of damage of DP600-B steel in martensite islands and ferrite matrixes, one of which was related to void formation at inclusions as shown in Fig. 2.11. A few cracks in martensite particles were nucleated at 13% strain. Decohesion at the interface was also observed at the ferrite and martensite phases as well as coalescence of voids shown in Fig. 2.11.

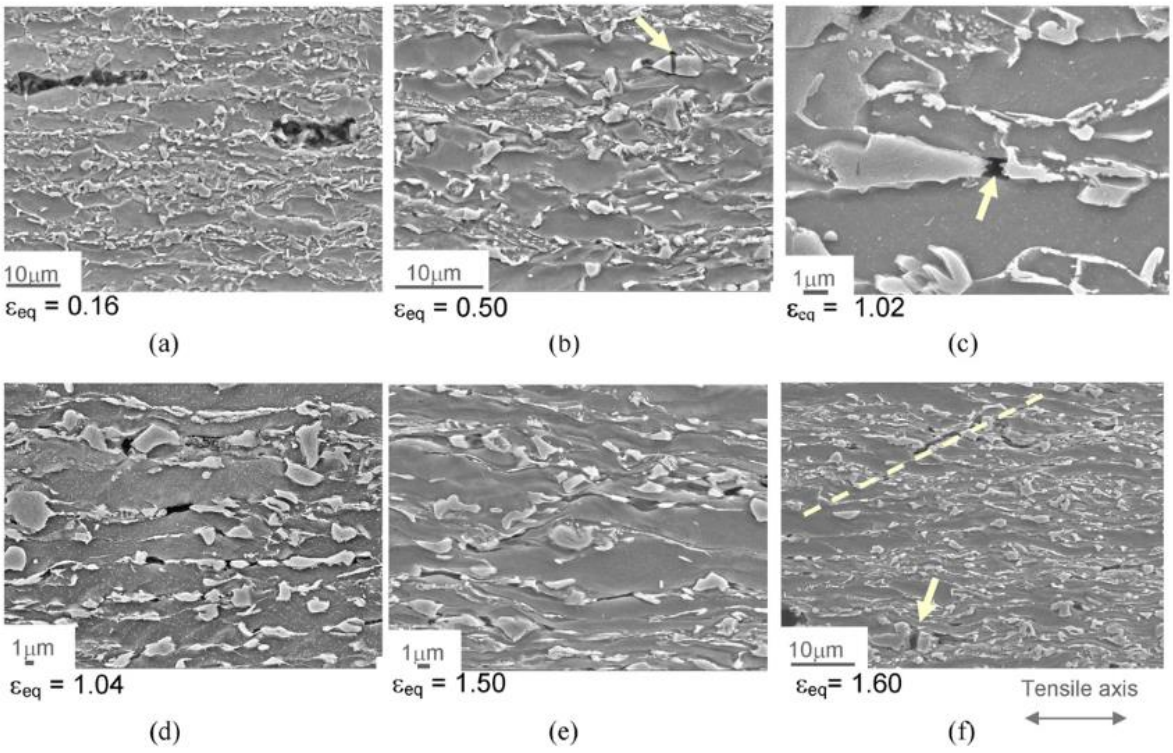

Fig. 2. 9 (a) Void nucleation on inclusion; (b) and (c) cracks on martensite; (d) and (e) decohesion of ferrite-martensite interface and crack propagation through ferrite phase; (f) void coalescence near to surface fracture (Avramovic-Cingara, Ososkov, et al., 2009).

The damage initiation and growth behaviour of DP780 using smooth and notched specimens was studied by (Saeidi et al., 2014), and quantified the void nucleation and growth using SEM. This work revealed that the main void nucleation procedure in both the standard and notched samples showed void development at the triple junctions (ferrite-ferrite-martensite grains) and narrow ferrite areas between two martensite islands (Fig. 2.12). The reported results, which agreed with those of (Erdogan, 2002; Nicolaou & Semiatin, 2001), stated that the majority of void nucleation in the DP steel was at the tip of the martensite-located ferrite grains along the direction of loading. They also observed that void nucleation was a continuous process until fracture, and the mechanism of void nucleation was the same in the notched and smooth specimens. Finally, the SEM analyses showed that the kinetics of void development was faster in specimens with low triaxiality than that in specimens with high triaxiality.

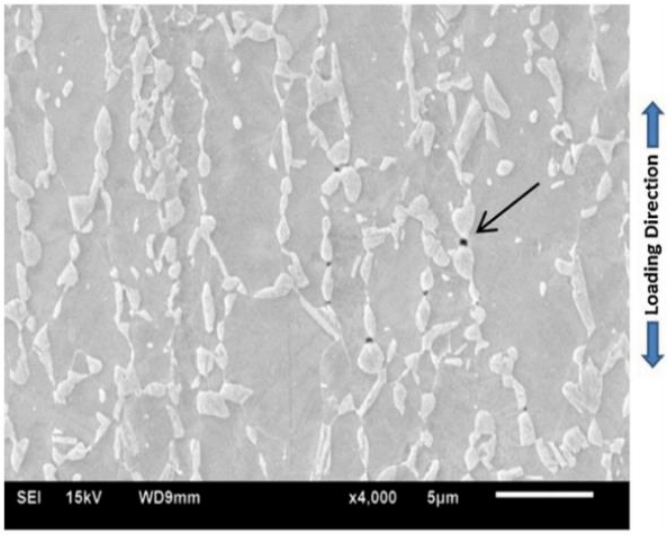

Fig. 2. 10 Void creation in narrow ferrite areas between two adjacent martensite islands(Saeidi et al., 2014).

Further contributions to this field of study were made in (Alaie, Kadkhodapour, Rad, Asadabad, & Schmauder, 2015), which used SEM to examine the important factors impacting formation and coalescence of deformation bands in the ferrite matrix of DP600. They also discussed the phenomenon of strain localisation and examined the appearance of voids and cracks in the localisation band. Before necking occurred, the local slip band was located in three ferrite regions: the centre of the large ferrite grains, between the martensite islands, and close to the cracks. This finding validated the results of previous studies (Azuma, Goutianos, Hansen, Winther, & Huang, 2012; Ghassemi-Armaki et al., 2014).

In addition, (Alaie, Kadkhodapour, et al., 2015) investigated formation and coalescence of the strain band at several locations in a specimen; SEM images were captured by selecting an area inside necking regions. Two cracks were observed inside the martensite grains, with a small crack also appearing in the ferrite phase. Another type of crack was detected where the slip band in the ferrite crossed the martensite grains, which caused it to break up. Furthermore, due to the necking inside the deformation band, the voids between the particles in the ferrite became

elongated (see Fig. 2.13). In the final phase of deformation, microcracks appeared inside the strain band due to the high triaxiality.

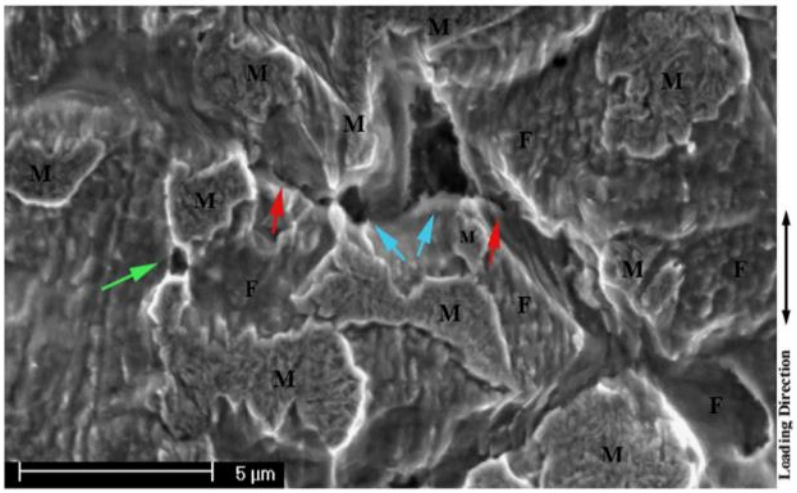

Fig. 2. 11 Voids inside the strain localisation band, between the martensite particles (Alaie, Kadkhodapour, et al., 2015)

SEM tensile tests have been used (Kadkhodapour, Butz, & Rad, 2011) to observe the process of void nucleation, growth, and coalescence in DP800 throughout diffused necking, after necking but before fracture, and after failure (see Fig. 2.14). Following diffused necking, some voids nucleated between two martensite particles, with some voids being located between two ferrite grains. Separation between the martensite and ferrite was also observed in the first test.

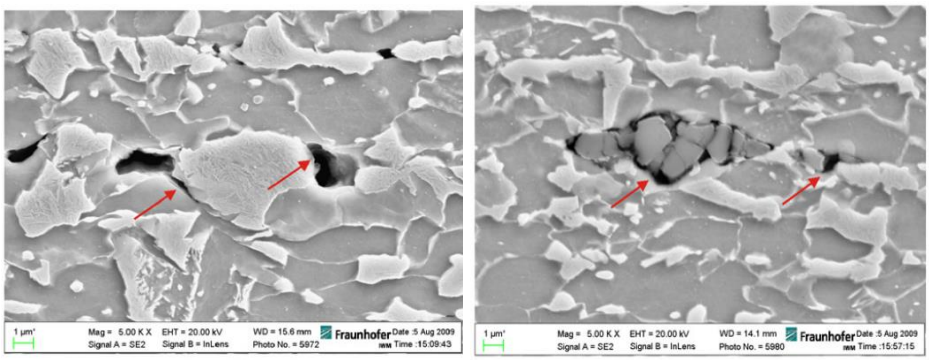

(a) (b)

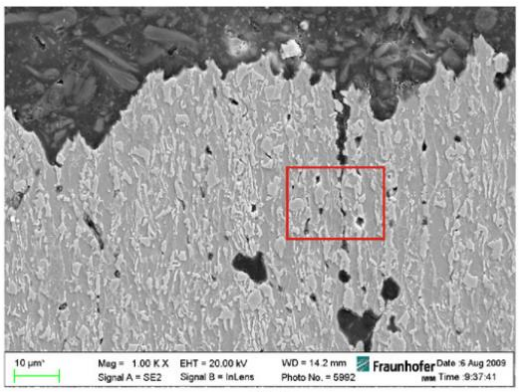

(c)

Fig. 2. 12 (a) Void following diffused necking; (b) Void after necking but before fracture; (c) Void after specimen fracture (Kadkhodapour et al., 2011)

In (Alharbi et al., 2015) a combination of tensile tests and SEM, DIC, and FE modelling were used to observe damage in DP1000. The main aim of this paper was to investigate the initiation of martensite fractures. The first void was observed around non-metallic inclusion, and was broken before the test began, as shown in Fig. 2.15 (a). A second void was generated at the interface of the martensite and ferrite and appeared at 32% global strain value. At this value, the martensite fracture initiated, and a void in the ferrite formed when the global strain value reached 52%. Finally, the damage increased (propagated) into the ferrite, where the martensite island became separated, as shown in Fig. 2.15 (b).

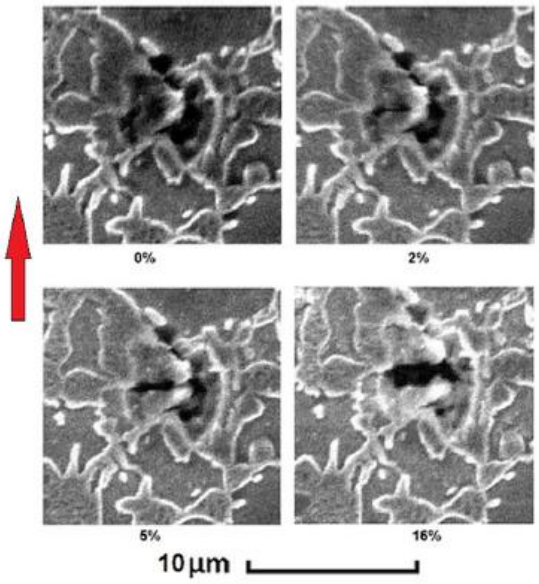

(a)

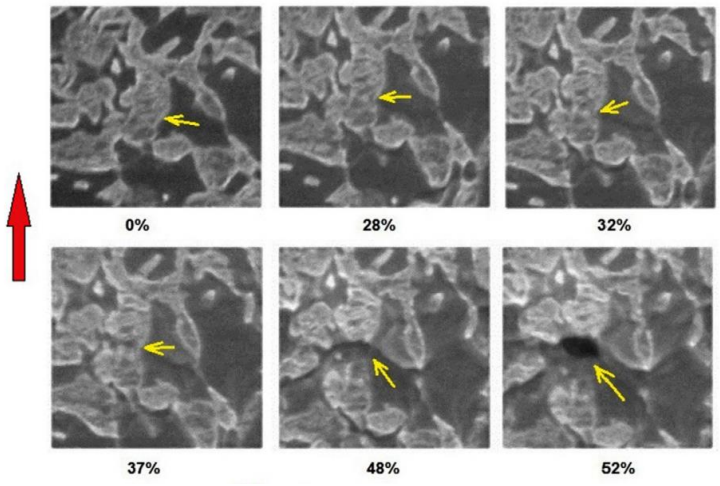

(b)

Fig. 2. 13 (a) A non-metallic inclusion void; (b) Void formation following the martensite fractur (Alharbi et al., 2015).

DIC was adopted by (Ososkov, Wilkinson, Jain, & Simpson, 2007) to analyse the strain partitioning within DP600 steels. The analysis explored local strain values at martensite-rich locations, with minimum and maximum ferrite strain values of 30% and 70%, respectively. Similarly, (Kang, Ososkov, Embury, & Wilkinson, 2007) utilised DIC for assessing DP600 steel strain partitioning under varied tempering conditions, which reduced the strength differential between the martensite and ferrite, hence decreasing the strain partitioning. Their finding was that 0.4 was the local strain value for void initiation amid two different martensite islands. However, the resulting local strain maps could not be linked to the previously recognised damage mechanisms of DP steels (Avramovic-Cingara, Saleh, et al., 2009; Erdogan, 2002).

In situ tensile tests using SEM were utilised by (Ghadbeigi, Pinna, Celotto, & Yates, 2010), who also adopted DIC to assess the strain fields of DP1000 during deformation. Constant interruptions were made during the tests to capture SEM images of the deformed microstructure. DIC was then used to examine the captured images to assess the local plastic

strain evolution of the ferrite and martensite. Two distinct mechanisms were observed, with the more prevalent one being a lack of cohesion at the interface between the ferrite and martensite, and the other being the fracturing of the martensite. Essentially, the study found that the voids observed in the ferrite phase only nucleated in the areas subjected to a 120% local strain.

To inspect the behaviour of ferrite phases at the microstructure scale, (Alaie, Rad, et al., 2015) established a dislocation-based constitutive equation. They used a combination of analyses of in situ experiments, DIC strain calculations, and numerical simulations. The material examined was DP600 steel. The authors used the model detailed in (Estrin & Mecking, 1984), which focuses on strain hardening behaviour during hot deformation rather than softening at high strain values. Results indicated that the strain localisation in the ferrite was much higher than that in the martensite and the dimensions of the martensitic grains directly affected the amount of strain localisation in the ferrite phase.

Implementing a tensile test conducted with SEM and DIC, (Ghadbeigi, Pinna, & Celotto, 2013) analysed local deformation and damage initiation in DP600 steels. They observed that fracture initiation occurred at the micro level in the martensite phase following a 13.5% macroscopic elongation. Moreover, the paper proposed a new gauge geometry for studying material's damage evolution mechanisms. The findings showed that damage evolution took place due to void coalescence and a microcrack formation in the microstructure. The ferrite matrix inclusions and decohesion of sub-micron carbide particles caused sub-micron voids to be created in the large ferrite grains. In these large grains, sub-micron voids were created due to Mn-S inclusions and decohesion of the carbide particles (Fig. 2.16). Observation of the crack mechanisms during test interruptions suggested that the crack propagated though the ferrite phase.

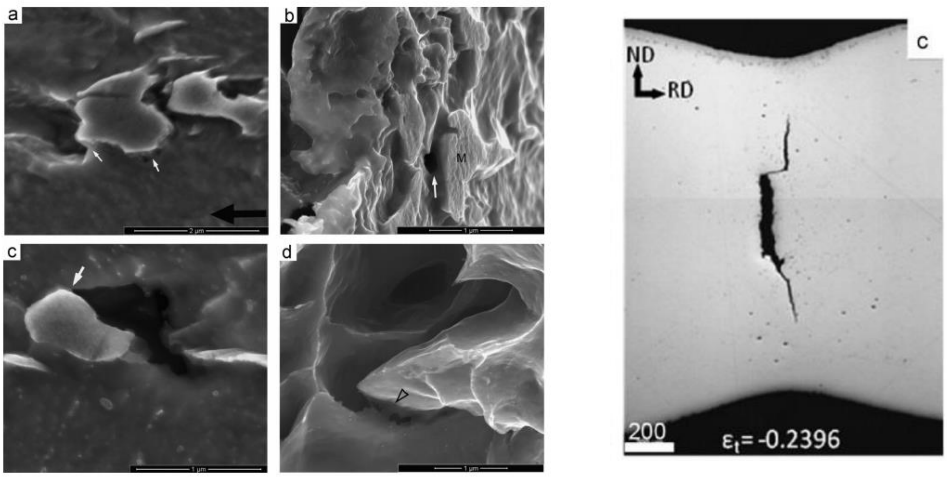

Fig. 2. 14 Test on microstructure of DP600 steel, identifying damage initiation process due to ferrite-martensite failure (left); crack propagation before final damage (right) (Ghadbeigi et al., 2013).

DP steels are high-strength steels with high ductility, but some reports show void initiation in the martensite particles of DP steels when the material is deformed or pressured. Damage initiation in the martensite particles of DP steel through a mini tensile test was investigated in (Ramazani, Ebrahimi, & Prahl, 2014) .The DIC technique was used in the mini tensile test to analyse microscopic damage initiation. Furthermore, bending tests were performed on equiaxed and banded DP steel to identify martensite cracking (see Fig. 2.17). The result of the test showed that failure initiation in the banded DP microstructure occurred at a lower pressure than in the equiaxed DP microstructure. Hence, the equiaxed microstructure had superior failure behaviour. The predicted results matched the experimental findings on cracking in the DP steel martensite particles.

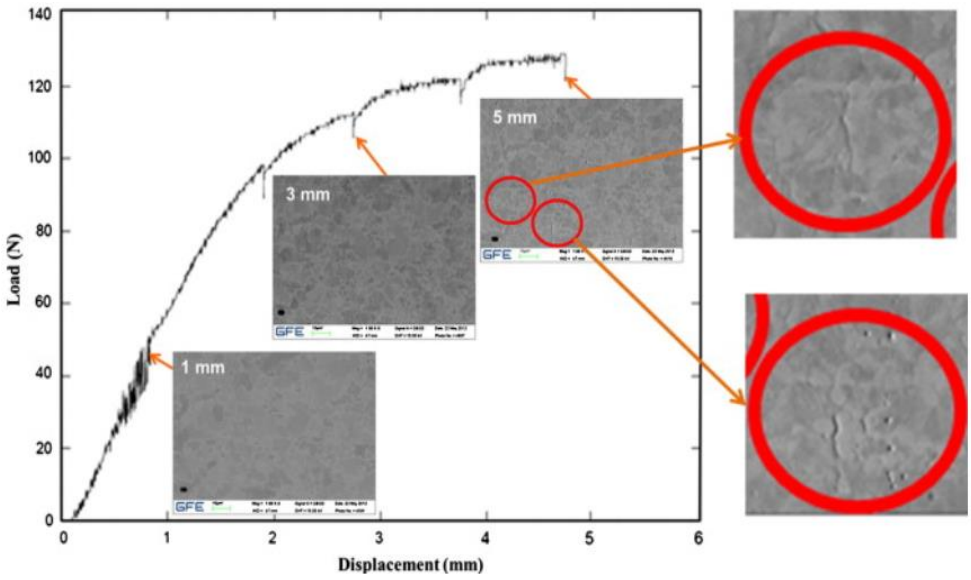

Fig. 2. 15 Bending test, with load-displacement curve showing the visibility of cracks in the martensite initiating at 5 mm displacement (Ramazani et al., 2014).

The various studies presented above have identified different mechanisms of damage in DP steels. Voids have been observed to form at the ferrite martensite interface, followed by martensite cracking. Voids also form in the ferrite phase through the failure of inclusions or nucleate along the ferrite grain boundaries. Decohesion close to the interface between the martensite particles and the ferrite matrix occurs due to microcracks propagating in the ferrite phase. Although damage mechanisms have been clearly identified during the early stages of deformation, there is still a significant lack of understanding of how damage development leads to final failure of the material. Therefore, the present project aims to improve the physical understanding of damage initiation and growth in DP steels.

2.4 Damage and microstructure modelling

Modelling has become an essential part of most studies to better understand damage development and to predict the failure properties of DP steels. Both continuum-scale damage models and microstructure-based models have been used to predict the behaviour of DP steels. This section begins by introducing the Marciniak-Kuczynski (M-K) model and Gurson damage

model which are commonly reported in the literature, the Gurson model also being used in this study to predict the overall mechanical response of the DP steel. Microstructure-based models, also used in this work, are then reviewed.

2.4.1 Marciniak-Kuczynski (MK) model

To properly predict the FLD curve, (Yue, 2014) introduced the forming limit curve by discussing the uncertainty in prior research over how to establish an effective way to relate major principal strain $\underline{\varepsilon_1}$ to the minor principal strain $\underline{\varepsilon_2}$, which can be fitted to the structure of forming limit diagram (FLD). Moreover, FLDs are stress path-dependent, therefore a forming limit stress diagram is put forward in the stress space which is insensitive to the strain paths. As such, two classes of theoretical models have been established for calculating forming limit curves: 1) (on the assumption of homogeneous sheet metal) the necking theory, bifurcation theory, and linearised perturbation theory, and 2) (on the assumption of inhomogeneous sheet metal) the MK theory/model. Therefore, the author proposed a Marciniak-Kuczynski (or MK) model which is based on initial defect growths regarded as inhomogeneities, with assumptions of rigid plasticity, plane stress condition, and isotropic work hardening.

The MK model is used on a two-zone material with an initial perturbation of insignificant thickness, of indefinite length, and with minor strain direction orientation to predict monotonic strain path limits on the forming limit diagram (FLD), with sheet inhomogeneity characterised by the imperfection parameter. The author further demonstrates the theoretical MK analysis by expressing various thicknesses of a two-zone material separately, consisting of zone a and zone b, respectively (see Fig. 2.18). The thickness ratio:

$$f^0 = e_b^0 / e_a^0 \tag{1}$$

characterises the geometry defect in zone b, where e_b^0 and e_a^0 represent initial thickness in zone b and zone a, respectively.

The material is subjected to plastic deformation by stretching the homogeneous part in increments. However, the plastic evolution is not uniform. A critical strain occurs in the homogeneous region, and the values corresponding to major and minor strains are plotted on a forming limit diagram. The same values are later used for a forming limit stress diagram, independent of pre-strain deformation.

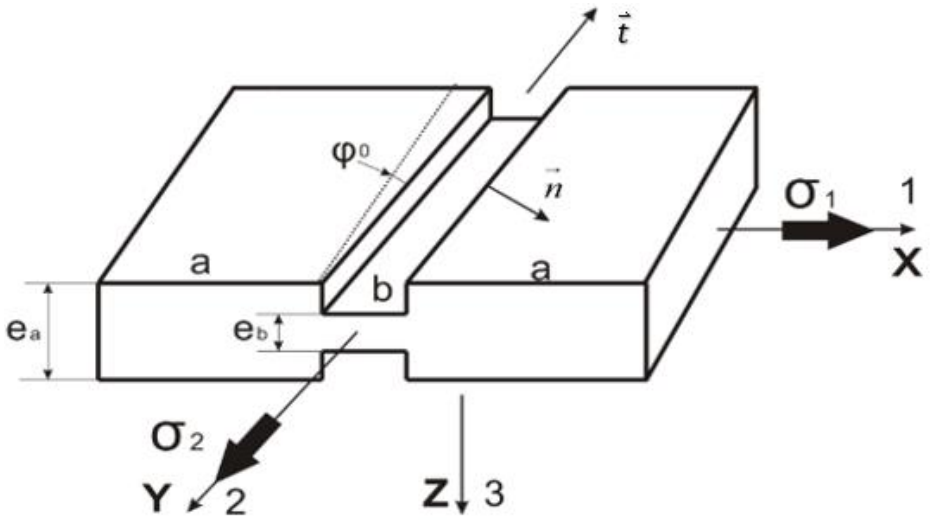

Fig. 2. 16 Schema for M-K modelling.

For zone a, the hardening rule determines equivalent stress flow

$$\overline{\sigma}^a = f_{HR}(\overline{\varepsilon}^a) \tag{2}$$

by imposing equivalent strain increment $d\overline{\varepsilon}^a$. The stress matrix $[\sigma^a]_{xyz}$ is determined by coupling yield function

$$\overline{\sigma}_{YF} = f_{YF}(\sigma_{xx}, \sigma_{yy}, \sigma_{xy}) \tag{3}$$

with stress ratio

$$\alpha = \sigma_2 / \sigma_1 \tag{4}$$

The relationship among strain increments is described by the flow rule

$$d\varepsilon_{ij} = d\overline{\varepsilon}(\partial\overline{\sigma}_{YF} / \partial\sigma_{ij}) \tag{5}$$

which also determines strain increment matrix $[d\varepsilon^a]_{xyz}$. The changes in axes define the states of stress and strain in the groove reference frame by:

$$[\sigma]^a_{ntz} = [T]^T \cdot [\sigma]^a_{xyz} \cdot [T] \tag{6}$$

$$[\sigma]^a_{ntz} = [T]^T \cdot [\sigma]^a_{xyz} \cdot [T] \tag{7}$$

where:

$$[T] = \begin{bmatrix} \cos\varphi & -\sin\varphi & 0 \\ \sin\varphi & \cos\varphi & 0 \\ 0 & 0 & 1 \end{bmatrix} \tag{8}$$

with defection band rotation (during loading) defined as:

$$\tan(\varphi) = \tan\varphi^0 \, (1 + d\varepsilon^a_x) / (1 + d\varepsilon^a_y) \tag{9}$$

By proposing compatibility equations and force equilibrium conditions, increment strain and stress value along longitudinal direction of groove are determined.

The equilibrium condition indicating force balance:

$$\sigma_{nn}^{a} e_a = \sigma_{nn}^{b} e_b \tag{10}$$

$$\sigma_{nt}^{a} e_a = \sigma_{nt}^{b} e_b \tag{11}$$

The compatibility condition (assuming identical stretching of necking band direction):

$$d\varepsilon_{tt}^{a} = d\varepsilon_{tt}^{b} \tag{12}$$

This reduces the equilibrium equations to:

$$\begin{cases} f\sigma_{nn}^{b} = \sigma_{nn}^{a} \\ f\sigma_{nt}^{b} = \sigma_{nt}^{a} \end{cases} \tag{13}$$

where $f = e_b / e_a$ is the non-homogeneity factor and can be expressed as:

$$f = f^{0} \cdot exp\left(\varepsilon_{zz}^{b} - \varepsilon_{zz}^{a}\right) \tag{14}$$

Now that the conditions have been established, flow stress value in normal direction of groove and its respective flow shear stress can be calculated. The transposition of stress matrix to the principal referential frame, equivalent flow stress, can be evaluated through the yield function. The strain matrix is also determined through the hardening rule and flow rule.

The two invariables $d\bar{\varepsilon}_b$ and σ_{tt}^{b} are calculated by the two nonlinear equations:

$$\begin{cases} F_1\left(d\bar{\varepsilon}_b, \sigma_{tt}^{b}\right) = \bar{\sigma}^{b} - \bar{\sigma}_{YF}^{b} = 0 \\ F_1\left(d\bar{\varepsilon}_b, \sigma_{tt}^{b}\right) = d\varepsilon_{tt}^{a} - d\varepsilon_{tt}^{b} = 0 \end{cases} \tag{15}$$

2.4.2 Constitutive damage modelling

In the study of ductile fracture, the Gurson model is one of the most common micromechanical models used to analyse the outcomes from nucleation, growth, and coalescence (Gurson, 1977). The original study was based on a unit cell model examination of a single void within a finite matrix. The void volume fraction f is given by the ratio of the volume of the void to that of the unit cell. Gurson established a yield criterion that was separate from the effective von Mises stress σ_{eq} (as in classical plasticity theory), and which depended on the hydrostatic stress σ_{kk} and the void volume fraction f. Modification of the original Gurson model was undertaken in (Tvergaard, 1989) to better agree with FE analyses of void growth and elucidate the effect of plastic work hardening.

Micro-void damage in relation to macroscopic material behaviour has been widely studied using the Gurson-Tvergaard plasticity model. Many have used the GTN model (such as (Abbasi, Ketabchi, Izadkhah, Fatmehsaria, & Aghbash, 2011)) to predict the micromechanical damage of DP steels by calculating the evolution of voids in the matrix as a result of mechanical loadings. This model explains the behaviour of macroscopic plastic material with regard to microstructural phenomena. The void volume fraction also plays a significant role as a softening parameter in the GTN model; it enables the modelling of the decrease in the material load bearing capacity before fracture. As many sources have indicated, the GTN model predicts the material behaviour directly prior to failure much more effectively than continuum-based models do (Wcislik, 2016).

The GTN model represents the growth of voids in DP steels; it describes these voids as hollow spheres in a rigid perfectly plastic matrix. The failure is signified by the porosity *f*, which corresponds to the ratio of the voids' volume to the total volume. The plastic yield surface is defined as a function of porosity (see equation 16) (Alharbi, 2015; Besson, 2009).

$$\Phi = \frac{\sigma_{eq}^2}{\sigma_y^2} + 2f cosh\left(\frac{1}{2}\frac{\sigma_{kk}}{\sigma_y}\right) - 1 - f^2 = 0 \quad (16)$$

where σ_{kk} is the stress-tensor trace, σ_y is the yield strength, and σ_{eq} is the von Mises equivalent stress (see equations 17, 18, 19, and 20).

$$\sigma_{kk} = \sigma_1 + \sigma_2 + \sigma_3 \quad (17)$$

$$\sigma_{eq} = \sqrt{\frac{1}{2}[(\sigma_1 - \sigma_2)^2 + (\sigma_2 - \sigma_3)^2 + (\sigma_3 - \sigma_1)^2\ ]} \quad (18)$$

$$f = 1 - r \quad (19)$$

$$r = \frac{V_m}{V_t} \quad (20)$$

where V_m is the matrix volume and V_t is the total volume of the material. The failure model must effectively define the material behaviour up to the point of fracture. In the case of $f = 1$, the material is made up of voids only, and rupture will occur. For $f = 0$, the material is completely dense, and equation 6 of the yield can be redrafted as:

$$\Phi = (\frac{\sigma_{eq}}{\sigma_y})^2 - 1 = 0 \quad (21)$$

which shows that the undamaged material is a von Mises material. The Gurson model is limited to describing the growth stage, but the nucleation and coalescence stages of material damage also need to be understood. Based on the damage parameters q_1, q_2 and q_3, Tvergaard and

Needleman (Tvergaard, Needleman, & Lo, 1981) further developed the Gurson model. They determined the yield surface as follows:

$$\Phi = \frac{\sigma_{eq}^2}{\sigma_y^2} + 2f q_1 f \cosh\left(\frac{q_2}{2}\frac{\sigma_{kk}}{\sigma_y}\right) - 1 - q_3 f^2 = 0 \quad (22)$$

In most materials, the constant q_1 ranges from 1.0 to 1.5, and q_2 equals 1.0.

Void nucleation corresponding to damage during plastic deformation can occur due to decohesion occurring between the particles and the martensite at the interface, or as a result of martensitic cracking. A simple phenomenological foundation can be presented for void nucleation in strain-controlled nucleation and can be expressed as equation 23.

$$\dot{f}_n = A_n \dot{p} \quad (23)$$

where A_n is the strain-controlled nucleation and depends on the parameter *p*, which denotes the plastic strain as equation 24.

$$A_n = \frac{f_n}{s_n\sqrt{2\pi}} \exp\left(-\frac{1}{2}\left(\frac{p-\varepsilon_n}{s_n}\right)^2\right) \quad (24)$$

This relationship illustrates certain parameters. f_n denotes the inclusion volume fraction of void which can be nucleated; ε_n denotes the strain where 50% of the particles are broken; s_n denotes the standard deviation of the nucleation strain.

Needleman and Tvergaard (Needleman & Tvergaard, 1984) studied void coalescence and introduced the multiplicative fraction δ, which predicts the acceleration rate of the void growth through the effective porosity. The effective porosity f^* can be defined as follows:

$$f^* = \begin{cases} f & , f < f_c \\ f_c + \delta\,(f - f_c) & , \quad otherwise \end{cases} \tag{25}$$

where f_c is the critical porosity at which the void begins to coalescence; f_c and δ can be identified through experimentation. The yield in the last stage of ductile fracture can be expressed as follows:

$$\Phi = \frac{\sigma_{eq}^2}{\sigma_y^2} + 2fq_1\, f^*\, cosh\left(\frac{q_2}{2}\frac{\sigma_{kk}}{\sigma_y}\right) - 1 - q_3 f^{*^2} = 0 \tag{26}$$

GTN parameters are ascertained by adjusting the results of numerical simulations and experimental data (such as stress-strain curves). Conversely, the following GTN model parameters can be assessed experimentally: the void nucleation strain ε_n, the critical void volume fraction at the moment of failure f, and the critical void volume fraction at the onset of void coalescence f_c. Using quantitative image analysis and microscopic observation, the current study aims to evaluate the stress-strain curve on the basis of Gurson parameters (Wcislik, 2016).

To explain the plastic work hardening effect, and enhance the prediction of the Gurson model relative to FE investigations of void growth, Tvergaard (Tvergaard, 1981, 1982) introduced the parameters q_1 and q_2, in what is commonly called the Gurson-Tvergaard (GT) model. With a change in the dependency of the void volume fraction or the damage parameter, the parameter q_1 affects the yield region. A high q_1 plays a major role in reducing the plastic limit and lowering the strength of porous materials.

Initially, Tvergaard assumed q_1 = 1.5 to be the optimal value, i.e., a value that can create a good relationship between the experimental and numerical results on porous solids. Indeed, q_2

was known to influence the hydrostatic component of the present elastic domain. However, an increase in the value of q_2 will trigger a significant decrease in the yield limit. (Corigliano, Mariani, & Orsatti, 2000) verified that at a high q_2 value, the strain hardening properties of the matrix material can almost be removed by softening because of the improved void growth induced by a decrease in the porous material's total strength.

Therefore, not all materials can be subject to a fixed set of q parameters. The q parameters and other parameters, such as triaxiality, typically vary with material properties. By analysing the effect of stress triaxiality and void volume fraction on void growth and coalescence, (Kim, Gao, & Srivatsan, 2004) distinctly showed how q_1 and q_2 depended on the stress triaxiality and the initial void volume fraction.

In summary, the GTN model is used to define the growth of microcavities as a constitutive equation and simulate the propagation that generates ruptures using numerical modelling. For these reasons, the GTN model will be applied in this work using Abaqus software (Manual; Simulia, 2010; Smith, 2009) to understand the criteria for void nucleation, growth, and coalescence in DP steels.

A major limitation of the model is that the effects caused by the shear mode are not taken into account in the constitutive equation. Therefore, under conditions of low-stress triaxiality, it may not be possible to predict fracture and shear localisation. In a loading condition that is shear dominated, the distortion of voids is essential for predicting the degradation evolution of the material. Thus, under these conditions, the predictive capability of GTN requires improvement (Achouri, Germain, Dal Santo, & Saidane, 2013). Similarly, another limitation of the GTN model derives from its assumption that the evolution of voids can be divided into a nucleation stage and a growth stage, with fractures occurring when the void volume fraction reaches the critical value (Wang, Daniel, Lu, Liu, & Meehan, 2017). Furthermore, the

coalescence parameters, especially the void volume fraction and critical porosity which are the two key coalescence parameters for the GTN model, have to be properly identified for accurate predictions of localised flow (Mansouri, Chalal, & Abed-Meraim, 2014).

2.4.3 Microstructure-based modelling of RVE of DP steel

The microstructure of DP steels contains martensite islands distributed within a soft ferrite matrix. The properties of martensite and ferrite, coupled with their volume fraction and morphology, influence the steel's behaviour. Microstructure modelling is conducted to inspect the damage occurring in the steel and can determine stress localisation that cannot be evaluated by experimental work.

According to (Abid, Al-Rub, & Palazotto, 2015), two main phases are distributed heterogeneously inside the microstructure of DP steels. A study was conducted to examine the computational modelling of the effect of equiaxed heterogeneous microstructures on the strength and ductility of these steels. The microstructure-based modelling was used to analyse the strain by FE simulation is shown in Fig. 2.19. The focus of the study was the martensite (equiaxed morphology) and ferrite phases. Certain studies analysed the micromechanical properties of DP steels, and the effects of the elongation and banding of the martensite within them. The results of the above works verified that the Ys of DP steels inversely follows the aspect ratio of the banded martensite.

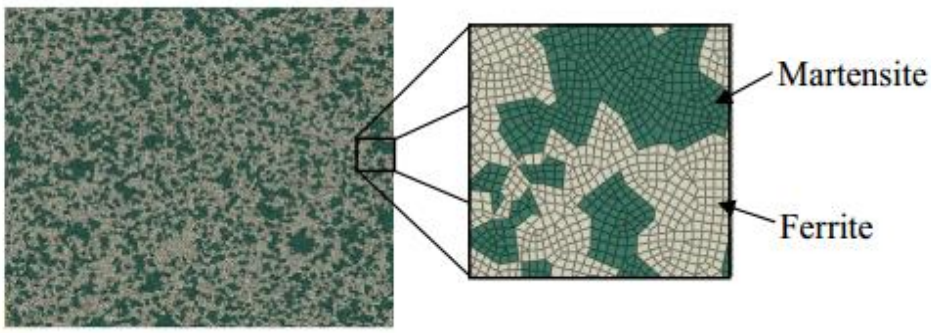

Fig. 2. 17 FE simulation of DP steel microstructure (Abid et al., 2015).

The microstructures in modern materials are usually composite, and according to (Perzyński, Wrożyna, Kuziak, Legwand, & Madej, 2017) such microstructures provide enough in-use properties. Local interaction has been observed between microscale features and the matrix that surrounds them. DP steels are subjected to thermochemical operations to obtain such highly sophisticated microstructures. An understanding of the behaviour of such microstructures is essential for design engineers working in the automotive industry, especially those in vehicle chassis design and fabrication. The behaviour of these microstructures determines the stability, UTS, and endurance of the chassis.

In (Alaie, Rad, et al., 2015) it emerged that the primary reason for fracture in DP steels is strain localisation. A study was conducted to investigate this phenomenon in the ferrite phase by performing in situ tensile tests. Findings showed that the strain in the ferrite is a function of the change in the strengths of the martensite and ferrite, and that it increases when the strength ratio increases. This study analysed not only strain calculation but also in situ experiments through image processing of the test outcomes. An SEM image of the microstructure that was generated through the in situ tensile experiment was additionally used in FE analysis, as shown in Fig. 2.20. This analysis was performed to examine the dislocation density model in the steel microstructures.

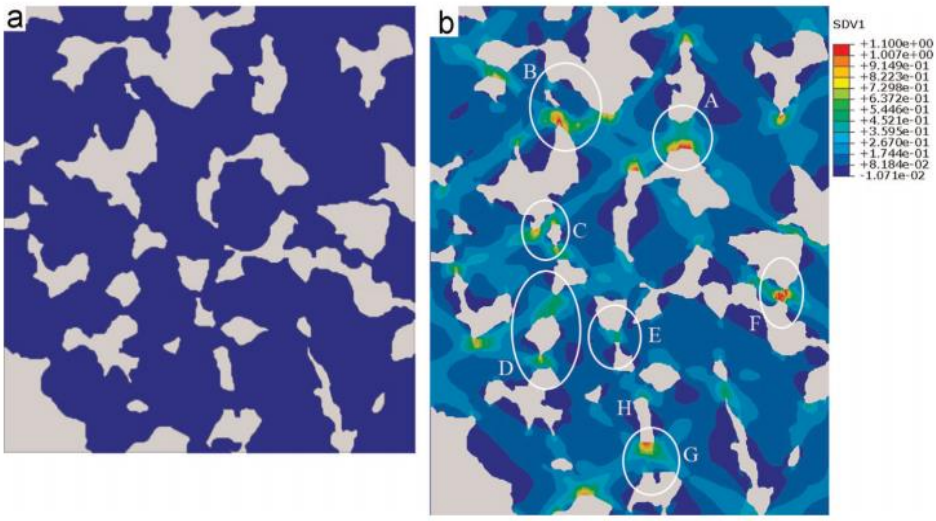

Fig. 2. 18 FE simulation of SEM image with strain distribution (Alaie, Rad, et al., 2015)

A study by (Perzyński et al., 2017) regarding the influence of the martensite volume fraction on the deformation behaviour and stress triaxiality of DP steels showed strain incompatibility arises during the tensile straining within the hardened martensite phase and the ferrite matrix. Such incompatibility in tensile straining is due to the differences between the two phases (Paul, 2013). Moreover, the study revealed that local stress triaxiality developed due to local deformation in the ferrite phase, which was constrained by adjacent martensite islands. There were variations in the martensite distribution within the microstructure and in the local stress triaxiality within it. In addition, owing to the composite effect of the martensite and ferrite, the steel exhibited a combination of strength, ductility, and strain hardening. The research was conducted using microstructure-based micromechanical modelling to study the deformation behaviour of the steel along with its tensile behaviour. The initial imperfections that triggered strain incompatibility in the steel was microstructure-level inhomogeneity. Furthermore, adjacent islands of martensite constrained the local deformation in the ferrite phase, which resulted in the occurrence of stress triaxiality. Finally, the material inhomogeneity caused an inhomogeneous strain and stress distribution within the softer ferrite phase.

The strain rate evolution of the ferrite and martensite in DP steels was investigated using FE simulations by (Ha, Lee, Kim, Lee, & Barlat, 2017). The rate investigated was that of transient plastic strain, which was analysed during strain path changes using micromechanics-based simulation or FE analysis. Sequential polishing of the small material volume enabled three-dimensional reconstruction of the microstructure images, through which a representative volume element was created. The influence of large and small deformation on the mechanical behaviour was detected using FE simulation analyses.

Preferable combinations between the formability and strength of multiphase steels have been observed by (Uthaisangsuk, Prahl, & Bleck, 2008). These combinations are due to the coexistence of distinct microstructural components and their interactions; the spatial distribution and number of different phases within multiphase steels can be utilised to great advantage in industrial applications.

In (Alharbi et al., 2015) a combination of DIC and FE analyses were used to develop a microstructure-based damage model of DP1000. This model was used to study the microstructure deformation and calculate the stress distribution before a martensite crack was initiated. The results indicated that damage was initiated in martensite at a stress value of 1700 MPa, as shown in Fig. 2.21. However, the model only focused fully on a small number of damage locations.

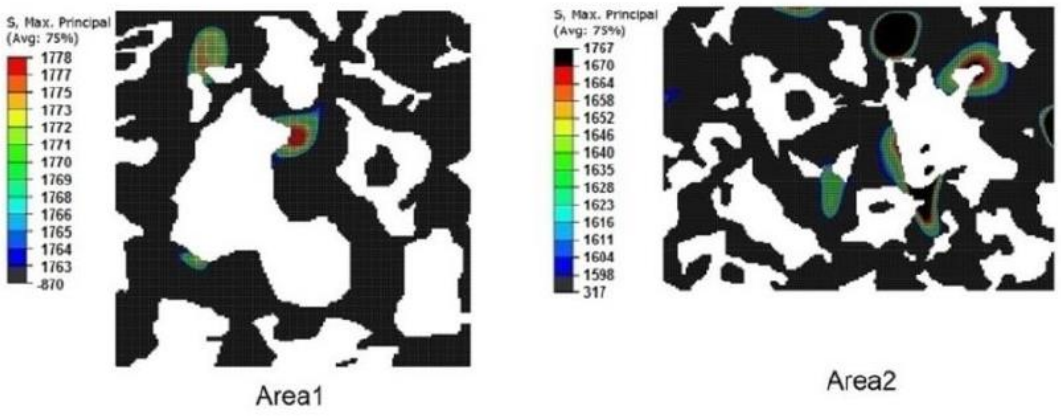

Fig. 2. 19 FE simulation for micro-structure-based damage modelling of martensite cracks (Alharbi et al., 2015).

Micromechanics-based modelling of DP steels shows that they behave like a material containing distributed soft ferrite and hard martensite in its matrix (Paul, 2012). The plastic instability, flow behaviour, and plastic strain localisation of such steels have also been predicted; a microstructure-based approach was applied to predict such modalities (Hosseini-Toudeshky, Anbarlooie, Kadkhodapour, & Shadalooyi, 2014). Several deformation mechanisms during tensile straining in steels have been distinguished by assuming different particle sizes. (Hosseini-Toudeshky et al., 2014) reported that uniform strain decreased and strength increased as the martensite volume fraction rose. As previously highlighted, the microstructure of DP steels comprises hard martensite islands embedded in a soft ferrite matrix. At the microscopic level, this combination of hard and soft phases causes strain partitioning (Alharbi et al., 2015). The morphology of the intrinsic mechanical properties of martensite, coupled with its volume fraction, influences the ductility and strength of the steel.

However, the stress results from the microstructure modelling of DP1000 conducted to understand damage are incomplete in the literature. In the current research, FE simulation of the microstructure will be performed to predict the crack initiation in the martensite phase.

Consequently, the stress distribution will be calculated, and the strain results compared with the experimental work.

2.5 Summary

The mechanical performance and formability of DP steels can be improved by obtaining a clearer understanding of the deformation and damage mechanisms at the scale of their microstructures. This literature review has shown that early damage of the martensite phase has been successfully analysed in several studies, whereas statistically meaningful criteria for initiation have yet to be found. Such criteria will therefore be investigated in this work by combining in-situ mechanical testing inside a SEM, micro-scale strain measurements using DIC, and microstructure-based finite element modelling. Furthermore, insight into damage initiation in the ferrite phase is even more limited, with no quantitative information about damage propagation found anywhere in the literature.

This work will therefore focus on developing new knowledge for these two types of mechanism, both of which are key to understanding the formability of DP1000. The next chapter will introduce the testing methodology which has been developed accordingly, including punch test geometries to simulate deformation conditions closer to forming operations. The experimental results, in combination with the physically based models reported in Chapter 5, are also expected to lead to more reliable predictions of the mechanical response of DP1000.

3. EXPERIMENTAL PROCEDURES

Following macro-scale tensile testing on DP1000, a damage initiation and development study was performed applying a multiscale method to understand crack initiation and propagation. First, an in situ tensile test was conducted within a SEM, to make it possible to observe the damage through the microstructure. Due to the limitations affecting this test in terms of observing damage propagation, a macro-scale punch test was used initially to deform the DP steel up to the point of failure, followed by the design and manufacture of a SPT, which was created to examine the crack initiation and damage development at the scale of the microstructure. Limitations with the SPT led to the development of a new experimental procedure, using a new bending test (conducted inside the SEM) which became available at a late stage in the work, and which was developed to study the crack propagation path within the microstructure.

Therefore, this section describes the materials, experiments and specimen dimensions for this study. In addition, with the help of in situ tensile tests conducted inside an SEM chamber, the processes of deformation and the recording of the deformation history of the microstructure is explained. Subsequently, a strain measurement procedure using DIC is introduced, in combination with in situ tensile test images. This methodology was employed to study strain distribution over the surface of DP1000 steel.

In addition, a conventional tensile test was performed to measure the load-displacement curve, and new macro and SPTs applied to track the path of the crack within the microstructure. Finally, an in situ bending test was developed to study the crack propagation path. The following subsections detail all the experimental methods.

3.1 Chemical components and microstructure contained in DP1000

DP steel DP1000 was selected for investigation. This steel is comprised of two primary phases: (1) martensite islands embedded in (2) a ferrite matrix. The material for investigation was procured in the form of a 1.5 mm thick uncoated steel sheet, manufactured by Tata Steel (IJmuiden, Netherlands).

Table 3.1 presents the chemical composition of the material utilised in the study. The martensite matrix accounts for nearly 51% of the total volume. Figure 3.1 depicts the microstructure.

Table 3. 1 Chemical composition weight ratio (wt%) of DP1000

Ni	Si	Mn	V	Cr	C	Nb
0.0325	0.473	1.522	0.012	0.0271	0.153	0.0135

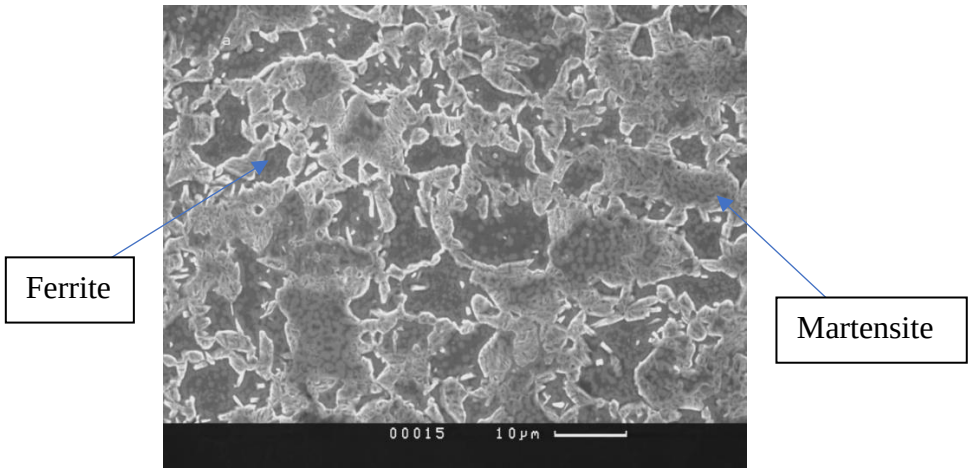

Fig. 3. 1 Reference image of microstructure.

3.2 Uniaxial tensile testing of DP1000

Convectional tensile tests were used to evaluate the deformation and understand the damage behaviour of DP1000 by comparing experimental results with those from the GTN simulation, as shown in Chapters 4 and 6. Standard samples (Saeidi et al., 2014; Testing & Materials, 1990) were tested to determine the stress-strain response for DP1000. Specimens with different notch geometries (Saeidi et al., 2014) were used to measure the load-displacement curve of the DP1000 for different levels of stress triaxiality (see equation 27).

$$\sigma_T = \sigma_m/\sigma_{eq} \tag{27}$$

Where σ_m is the hydrostatic stress, and σ_{eq} is von Mises equivalent stress. A 25 kN electric machine (Tinius Olsen) was used to conduct the tensile tests. A displacement control of about 1 mm was applied to run the experiments. The procedure implemented for the standard and notched samples was the same.

3D DIC (see following section for details) was applied to the gauge section to determine total strain and extension, meanwhile, deformation along the gauge length was followed from the start until the point where the sample fractured. A speckle pattern was created by painting the surface of the samples, which assisted in obtaining the DIC measurement. The standard and notched geometries are shown in Figure 3.2, where the sample thickness is 1.5 mm. Additional details concerning Fig.3.2 (c) setup is given in the Appendix I.

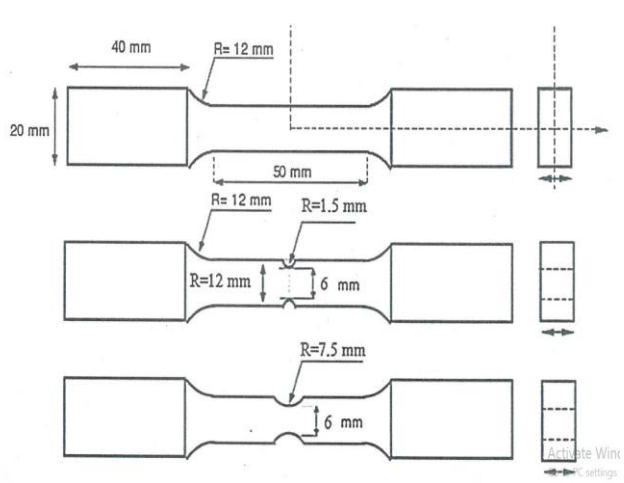

(a)

(b)

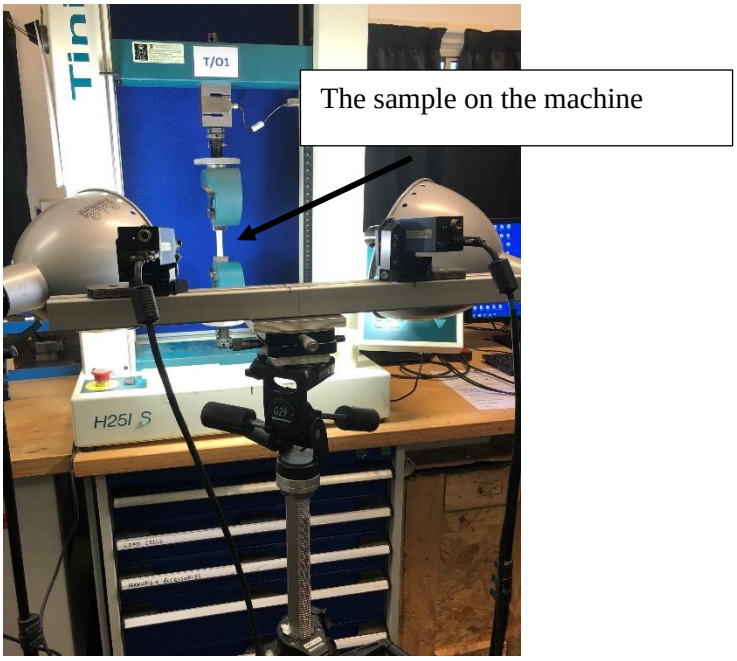

(c)

Fig. 3. 2 (a) Geometries of standard and notched samples (Saeidi et al., 2014); (b) specimens after failure; and (c) the sample in the machine with 3D DIC.

3.3 Microscale SEM tensile test using DIC

This section explains the in situ tensile microstructure tests conducted in the SEM chamber to examine how damage develops in DP1000. Subsequently, the DIC principle, and strain as measured from the SEM images using DIC are explained.

3.3.1 In-situ uniaxial tensile tests of DP1000 utilizing a tensile stage

A Deben Microtest tensile stage, with a maximum load capacity of 5 kN was used. The specimen geometry employed for these tests is shown in Figure 3.3, and was designed based on the maximum load capacity for that stage. The primary benefit of such experiments is their capacity to observe and measure any instant distortion that occurs affecting the microstructure of a DP1000 sample surface when a load is applied. The specimen geometry used for these tests is set out in Figure 3.4, and was designed based on the maximum load capacity for that stage (Ghadbeigi et al., 2010). A CamScan SEM was used to obtain the images for the steel microstructure. Figure 3.4 shows the tensile stage, as situated within the CamScan SEM chamber. Additionally, a 2 mm gauge section was selected to localise the deformation and observe the development of damage.

To prepare the sample for SEM observations the microstructure of DP1000 must be revealed. Furthermore microstructural features are used to track the deformation of the microstructure and produce strain maps using DIC during the in-situ tensile test. To reveal the microstructure, grinding and polishing are first used followed by etching. Grinding was carried out using abrasive silicon carbide papers of varying roughness to progressively reduce the size of scratches at the surface of the specimen. The coarser paper P120 was first used followed by P400, to P800, and P12000 papers. Each grinding step takes about 3 to 5 minutes. Polishing was then used to remove scratches left by the grinding process. The process started with a 6 µm diamond suspension followed by a 1 µm diamond suspension to produce a mirror-like

finish. The DP1000 microstructure was then revealed through etching using a 2% Nital solution for 4–12 s. The sample should be swiftly cleaned between each step using an Isopropanol solution, to prevent the surface from over etching. Over etching would damage the specimen's microstructure. An optical microscope was then used to check the microstructure and etching quality.

The tensile test was completely automated, and involved running an experiment in the SEM chamber. Initially, the sample was secured on a tensile stage, and then loaded in the chamber under vacuum conditions, to obtain SEM images. Subsequently, an area of interest was selected prior to applying a displacement. To acquire the SEM images, it was vital to interrupt the test regularly to take images of the microstructure as it deformed. After acquiring each image, the test was resumed, and the same process repeated for all subsequent deformation steps until the specimen failed.

The experiment was controlled by displacement and run at a minimum speed rate of 0.1 mm/min. This velocity ensured successful correlation of the SEM images could be achieved. Executing the test at low velocity made it possible to check the deformation, so the test could be paused should any remarkable event occur affecting the microstructure, such as damage initiation.

The test was interrupted after every 0.05 mm displacement increment, so as to take SEM pictures of the microstructure distortion until fracture occurred. The captured images were subsequently set aside for examination under quantitative distortion using DIC, as described in the following section.

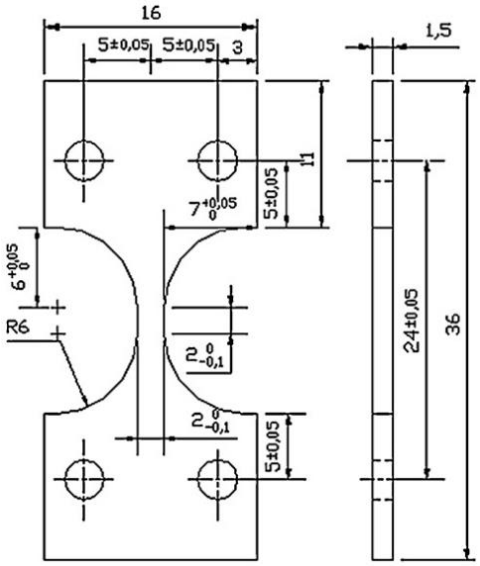

Fig. 3. 3 Sample of micro tensile test (Ghadbeigi et al., 2010).

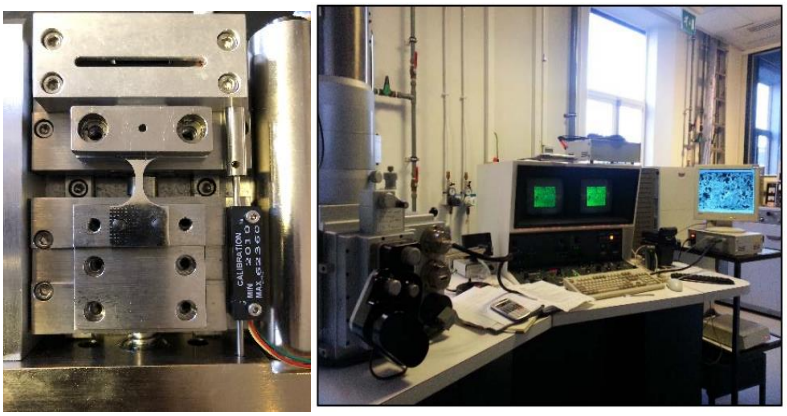

(a) (b)

Fig. 3. 4 (a) Deben tensile stage. (b) Camscan SEM.

3.3.2 DIC setup for strain measurement

Digital image correlation was used to measure strain distributions within the microstructure. The SEM pictures acquired showed the two phases: ferrite (dark) and martensite (bright). This explained the speckled appearance. The undistorted (reference) image was discretised into minor subsets, called interrogation windows. This is shown in Figure 3.5, where the extent of each subset is expressed in pixels. For instance, the size can range from 8 or 16 to 32 in

LaVision (Davis, 2010), with duplication increasing to a maximum of 512 pixels. The form in this case can then be a sphere, oval or square.

In the DIC procedure, the subsets may overlap across different ranges: 0% indicates no overlap, 50% signifies a half overlap, and 75% represents a three-quarter overlap. The pictures are discretised into smaller windows by choosing the subset. Consequently, this supports the calculation of displacement values for each subset, using a correlation algorithm to determine the displacement by identifying irregular patterning in the microstructure. Correspondingly, Figure 3.6 demonstrates the strain map, which results from the investigated distorted region of interest.

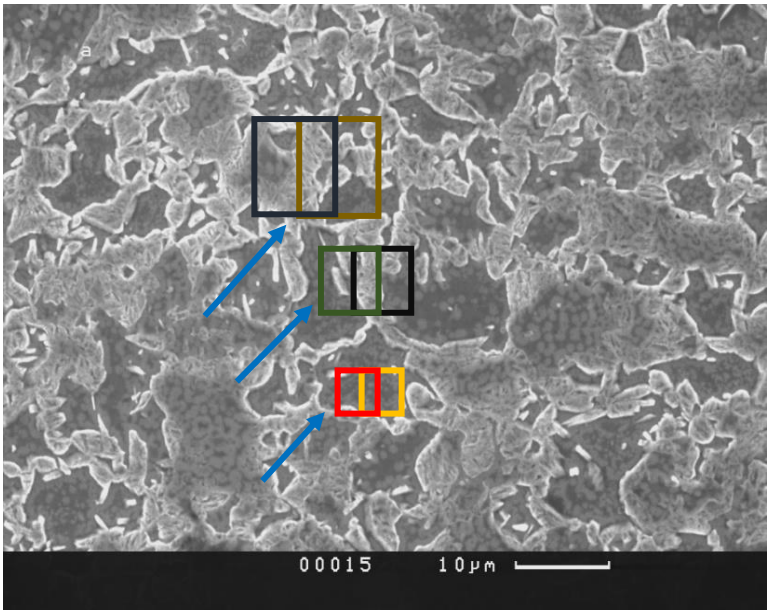

Fig. 3. 5 Reference image for DIC. The blue arrows provide an example of the subset's size.

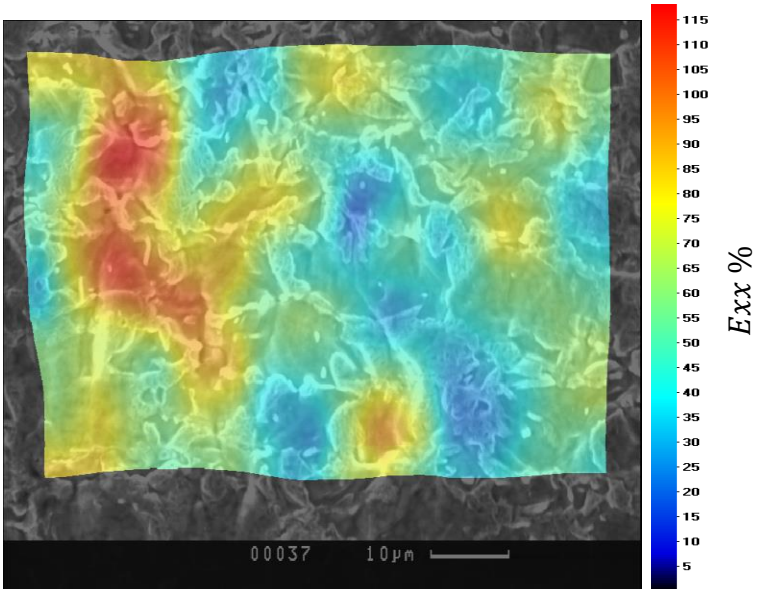

Fig. 3. 6 Strain map resulting from an investigation of the distorted region of interest.

3.4. Formability test of DP1000

3.4.1 Macro punch test using 3D DIC

The aim of this laboratory-scale punch test is to apply sizeable deformation to samples to induce damage to the point of failure. This was performed to measure the deformation capacity of DP1000. The sample geometry corresponds to a 1.5mm thick circular disk with a 90mm diameter (Rohaizat, 2018). For the punch test with the 3D DIC, the sample surface must initially be uniformly coated with white paint and this then allowed to harden. The speckle pattern should then be applied evenly with black paint. The dotting must be performed carefully to avoid smudging, and to allow the subsequent DIC analysis to measure strain.

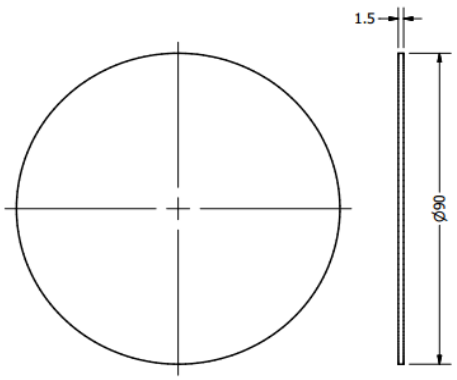

Fig. 3. 7 Drawing of the Sample with 90-mm diameter.

During testing, a unique die must be produced to constrain the entire outer area of the blank safely, as shown in Figure II.1 (see Appendix II). Six bolts are used to secure the die, ensuring the provision of ample restraint to effectively secure the blank. The die must have a circular drawbead feature to prevent blank flanges from being pulled in, thereby providing the necessary downward force during punching without causing the blank to experience significant deformation. Moreover, this ensures that only the material within the die aperture will be damaged during the process of stretch forming.

The punch tool is expected to play a vital role in the testing process, by causing considerable deformation on the sample. Therefore, as shown in fig. II.2 (Appendix II), a circular-headed, cone-shaped punch was produced that matched the requisite characteristics (Rohaizat, 2018).

A factor that relates to the punch for the purpose of prediction is the amount of friction at the tip. If the friction is high, then the sample will not fracture; instead it may shred due to the bond at the tip which is sharp and would pull the material into contact as the punch moves upwards. Thus, the tip had to be smoothed to remove any sharpness and then hardened. This guarantees the tip is strong enough, and that no material will flow and wear out upon contact with the sample. Fig. 3.8 illustrates the components of the macro punch test (Rohaizat, 2018).

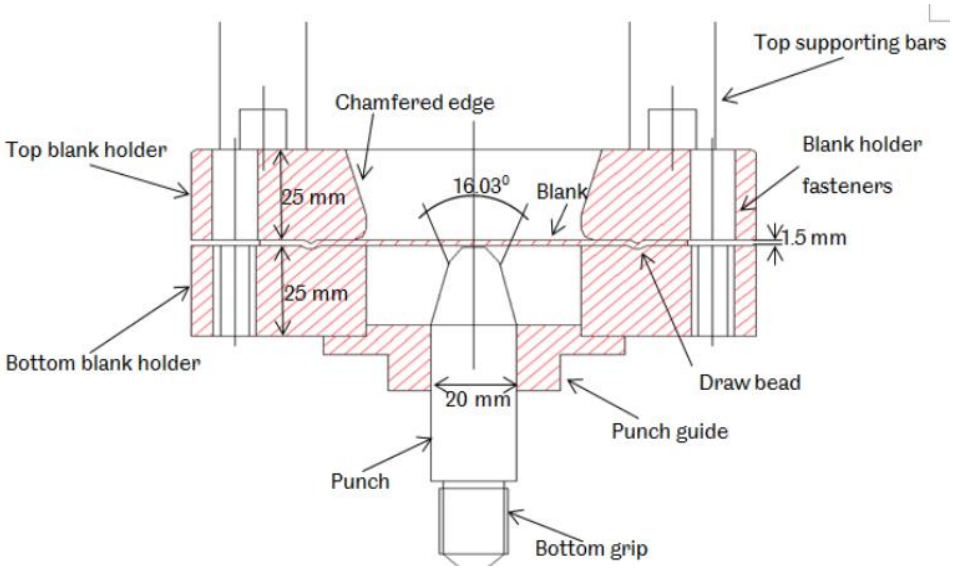

Fig. 3. 8 Illustration of the macro punch test (Rohaizat, 2018)

The rig for the punch test was set on a 100 kN electric Mayes test machine, as shown in Figure 3.9, and more details shown in the Appendix II fig. II.3. The entire rig was then assembled in the usual manner, which involved fastening the blanks between the dies, and then securing them before then loading the rig onto the punch. A pair of stands was then used to provide leeway between the punch tip and the sample, thereby supporting the die set. This prevented the punch from deforming the sample prior to commencing the experiment. After this, bars were placed on top of the die set to supply the downward force during the test. These were secured with screws at the point of connection, fastening both the top and bottom bars of the Mayes machine. All the experiments were conducted using graphite grease for lubrication to reduce resistance when connecting the punch tip and the material; this option was chosen due to the low friction of graphite.

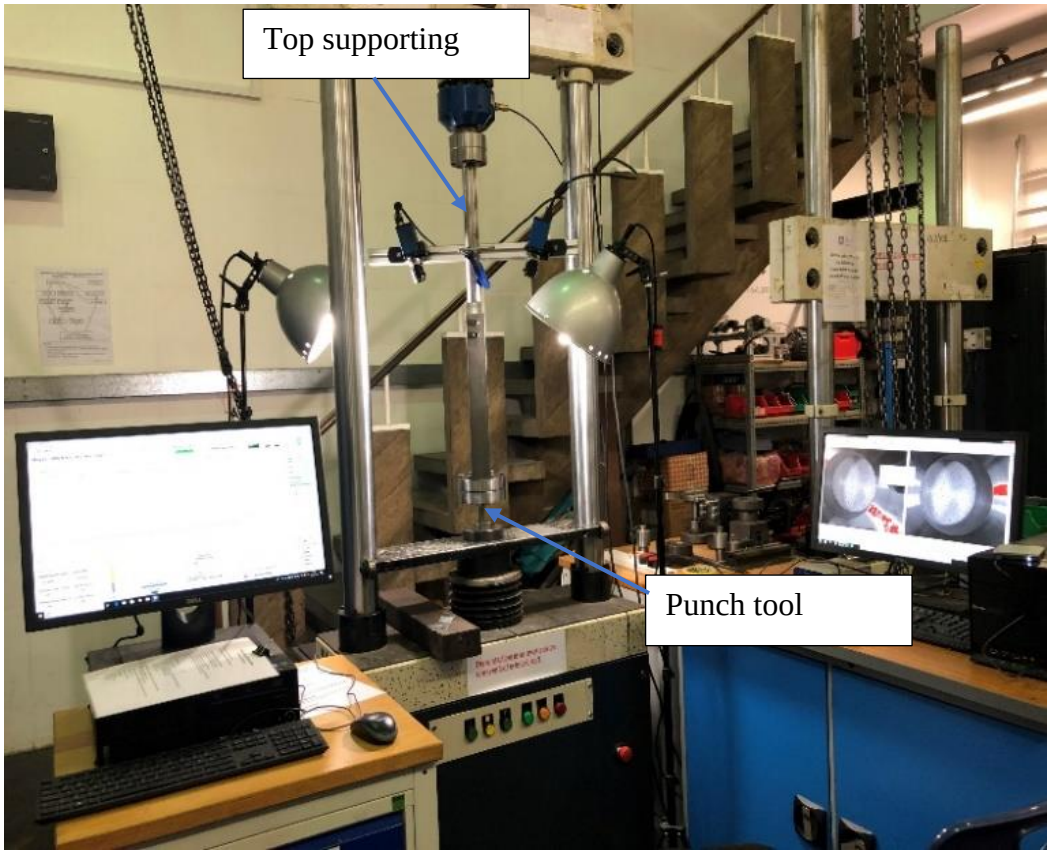

Fig. 3. 9 3D DIC setting with punch rig for experiment.

The 3D DIC setup was created by placing two photographic cameras on the bar, on top of the rig. Both cameras were connected to the computer, showing the sample area of interest in the field of vision. The software VIC-3D (Correlated Solutions) was used for DIC. Both cameras photographed pairs of images continuously, and these were later processed into stereo images. The placement of both cameras was fixed with the point of interest in the centre. The prime focal length was determined after modifying the lenses.

Figure 3.10 (a) depicts the location of the cameras, and shows how the cameras should be fixed. When both cameras were in focus, the calibration was performed using a predetermined dot-pattern plate, as depicted in Figure 3.10 (b). A minimum of 25 photos were taken to assist in this process; of which 15 had satisfactory calibration scores, and were thus selected. This was done to maintain the calibration error of the two cameras below 0.03. Whilst the photos were

being captured for calibration purposes, the plate was kept within the camera's range of view to procure images with rotation, in-and-out-of-plane and translation movements. The punch experiment was later initiated once the 3D DIC setup was complete.

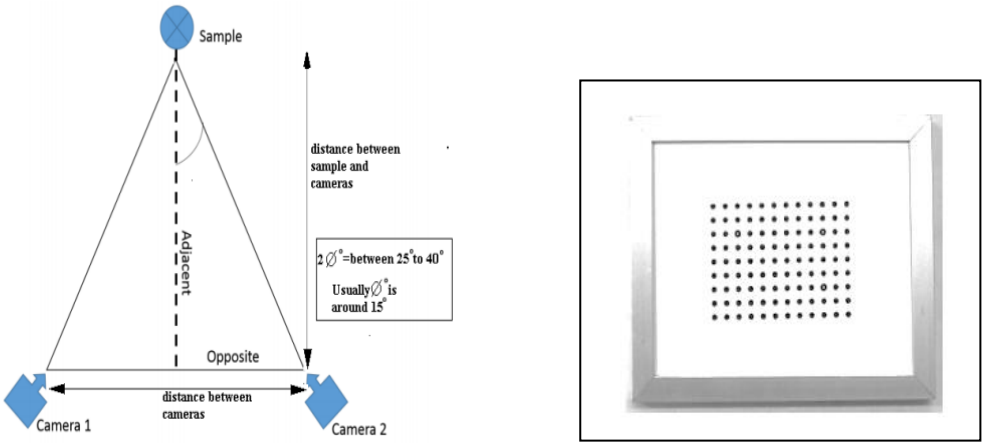

Fig. 3. 10 (a) Camera setup for 3D DIC measurement (Rohaizat, 2018); (b) Plate calibration for 3D DIC.

3.4.2 Small Punch test

The small punch (SP) test was set up to incorporate DIC measurements with the specimen's dimensions, to enable the sample to be regularly transferred to a SEM chamber to image the microstructure and review any damage as it develops. Furthermore, the SP test design requires tests be conducted in accordance with the testing equipment at the University of Sheffield's Lea Lab.

This experiment requires certain specifications, as the punch needs to be suited to equipment that is available in the laboratory and can meet the dimensions of the specific samples. Therefore, the standards generally followed when designing the SP tests were not considered while preparing this design, even though the SP had features that conform to standard practice.

Even though the precise measurements within existing standards do not correspond with the current project's requirements, valuable data has previously been obtained (especially by (Bruchhausen et al., 2017)) regarding the design of functional SP tests and their requisite features. Nevertheless, American standards (Matocha, 2015) require the diameter to be at least 89 mm; a small diameter can be 8 mm or 3 mm, with a required thicknesses of 0.5 mm and 0.25 mm, respectively (Brumovsky & Kopriva, 2018). When developing the test, the sample should have a radius of 30 mm and a thickness of 1.5 mm, as detailed in Figure 3.11. The design of the test is further explained in the next subsection. The SP test had to be designed to facilitate the transference of specimens to the SEM chamber to monitor damage as it develops in the microstructure. The following subsections explain the SPT design in detail.

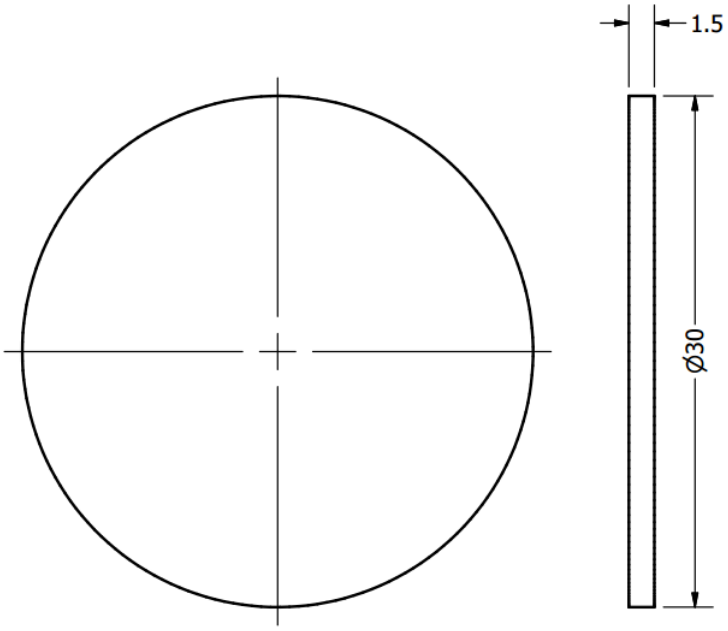

Fig. 3. 11 Small punch test sample geometry (dimensions in mm).

3.4.2.1 Design of the top die

The dimensions of the top die have to be reviewed closely, as its diameter will have a direct impact on the characteristics of the force-displacement curve. A chamfer can be used (flat or curved (Rohaizat, 2018),(Altstadt et al., 2016)) to prevent the specimen from shearing. In this

experiment, it will be beneficial to affix the top die to the ‘top supporting bars’, as with the macro punch design (Rohaizat, 2018) (see Figure 3.12).

In the University of Sheffield’s Lea Lab, punch tests are typically conducted using the Mayes 100 kN machine. The radius at the top of the die must be greater than the critical radius, so that an opening can be made through which the DIC cameras will photograph the sample, as explained above with regard to the macro punch test using 3D DIC. Furthermore, in line with (Habibi, Ziadi, & Megueni, 2014), the top die diameter must adhere to equation 28:

$$A \geq D + 2t \tag{28}$$

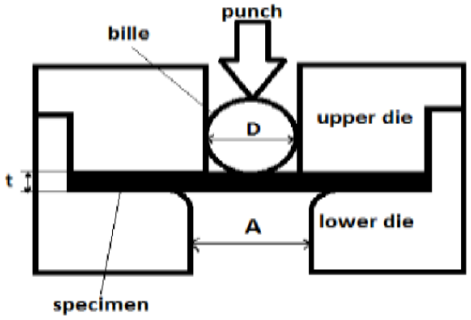

Fig. 3. 12 Sample geometry to explain variables in equation 28.

Equation 28 will avoid too much movement from occurring, due to the connection between the sample and the bottom die (Habibi et al., 2014).

A curved chamfer with a 1-mm radius was chosen, in line with that used for the macro punch test (Rohaizat, 2018). The top structure was be positioned via the holes, which are shown in Figure 3.13. Another chamfer is introduced in the upper position of the die, so as to improve the visibility of the sample. This will enable mounting of the DIC cameras.

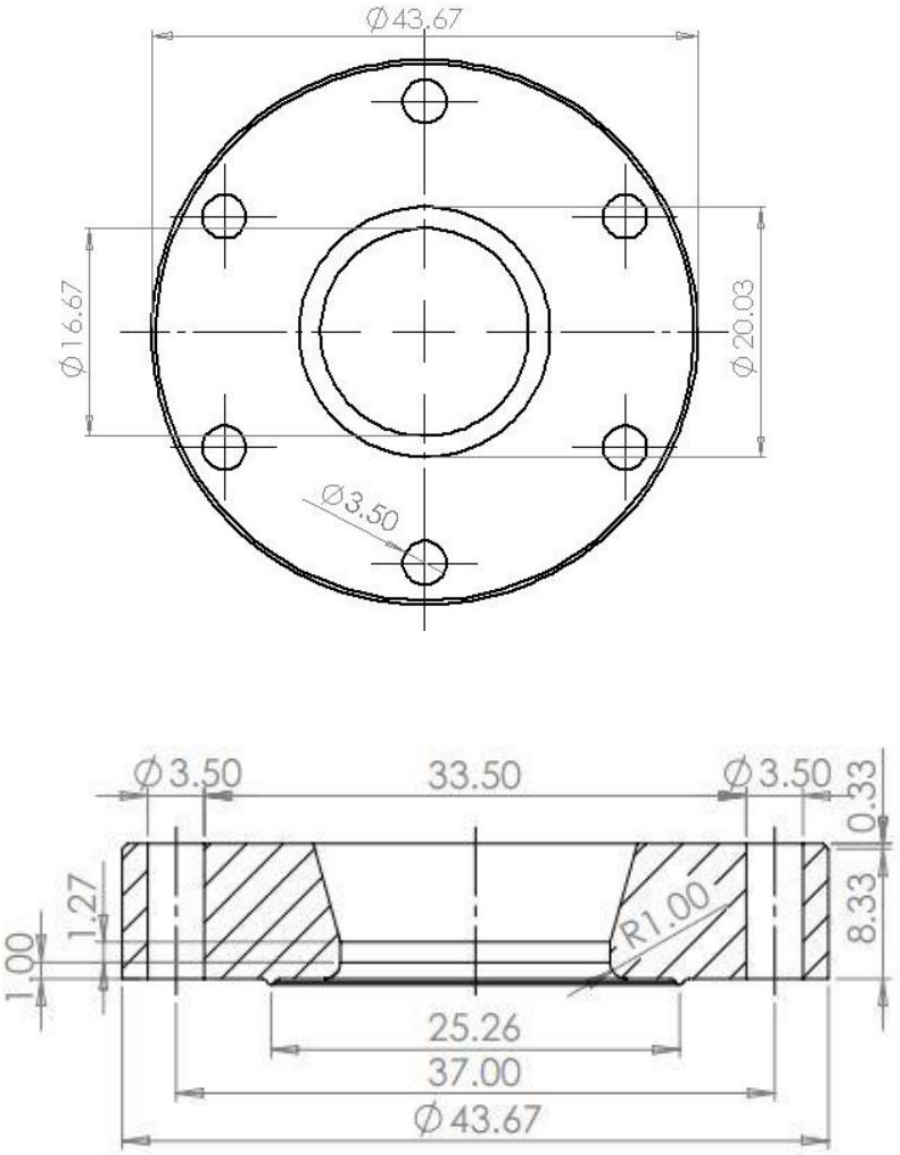

Fig. 3. 13 Top and side views of top die.

The top die was designed with a 1 mm radius chamfer in which the original setup was retained (Fig. III.1 of Appendix III). The chamfered edge diameter was altered, however, which meant the ultimate force displacement would be affected. Nonetheless, the design continued to comply with the requirements in Equation 28.

The SP test rig can still connect to the supporting bars located on top of the Mayes machine. The attachments for the conduct of DIC remain the same, because the diameter of the top hole

is much greater than that at the bottom. This ensures the sample will be located in view of all the cameras used for DIC.

3.4.2.2 Design of the bottom die

The bottom die is meant to ensure that the specimen is secured properly (Bruchhausen et al., 2017). The top die pattern can be adjusted according to the punch shape; however, this is not essential. The die must be large and sturdy enough to minimise the likelihood of it twisting or deforming during the experimental process, which will also affect the force displacement.

Figure 3.14 illustrates the shape and dimensions of the bottom die. Figure 3.15 shows the punch guide. Although the bottom die and the punch guide are separate parts, they are joined during the testing process, by connecting threads on the latter. The adapted shape of the punch guide ensures the punch will be in contact with the specimen at the desired angle. In this way, the testing process will proceeds satisfactorily. Figure 3.16 shows the new bottom die after manufacturing this design for 30 mm diameter sample. The advantage of the new design is that the punch guide can be changed to align with the future geometry reducing costs.

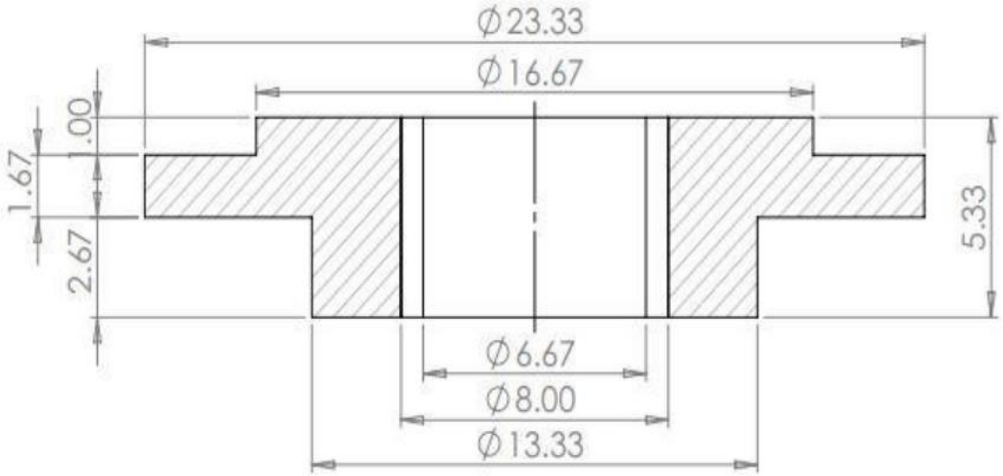

Fig. 3. 14 Geometry of the bottom die.

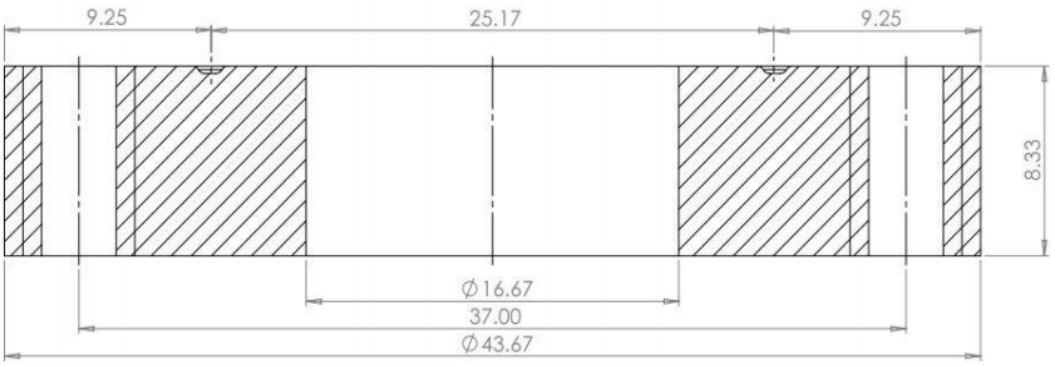

Fig. 3. 15 Geometry of the punch guide.

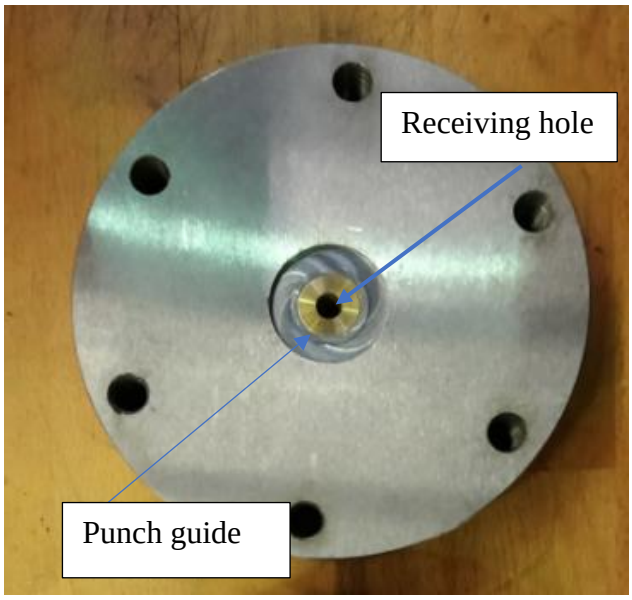

Fig. 3. 16 New bottom die after manufacture.

A hole at the receiving end will allow the punch to contact the centre of the sample. Therefore, a sample will always be deformed at the same point; even if, for example, it is detached during an experiment for assessment and then returned for continuation of the test. The inner threads of the bottom die are used to fasten it to the top die. The punch guide's diameter is 6.67 mm, which keep it closely aligned, and guarantees that it will contact the sample at the proper angle. This limits the probability of damage being caused to the punch tool, and promotes the

repeatability of the test. At the lower point the die has a chamfered edge at the point of entry to the punch guide.

3.4.2.3 Design of the punch tool

A single solid punch with a hemispherical end was selected according to (Bruchhausen et al., 2017), because this is the option frequently selected by researchers (Cuesta, Rodríguez, García, & Alegre, 2015; Rodríguez, Cárdenas, Belzunce, & Betegón, 2013). Another alternative was to insert a solid sphere through the sample, using a punch with a flat or concave tip (Lucas, 1983). This could be beneficial, as it would allow for the ball to be changed after each test, and avoid the possible use of a defective punch. However, this option was not selected because use of a normal single solid punch was already in line with the project requirements, and a sphere would have hindered the design and testing processes.

The measurements and requirements for making the punch can be seen in Figure 3.17. These dimensions were chosen to replicate the design of both the top and bottom dies; thereby ensuring a workable punch.

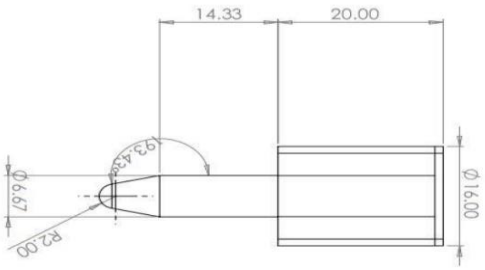

Fig. 3. 17 Geometry of punch.

The radius of the punch tip was set to 2 mm, and would easily satisfy the requirements of future users. The top part has an M16 × 1.5 screw thread (metric system), which is in line with the Mayes 100 kN machine utilised for the experiment. Figure IV.1 in the Appendix IV shows the

new punch after its manufacture. The pin makes it possible to change the punch tool if damage occurs, or if a new design is selected in the future.

3.4.3.4 Small punch test procedure

3.4.3.4.1 SP test using 3D DIC

The aim of this work is to understand the deformation, damage initiation and propagation in DP1000. As mentioned in the previous sections, the suggested diameter of the sample is 30 mm. The SP test procedure is the same as that for the macro punch test process (Section 3.4.1), but with a different sample geometry. Figure V.1 depicts the sample with the test rig as shown in the Appendix V.

3.4.3.4.2 SP test with microstructure observation using inspect F SEM

Results from the tensile test carried out in the SEM only revealed how damage initiate in the two-phase microstructure of DP1000 steel but did not show any significant propagation. The SP test offers a new opportunity to not only study this propagation but also under deformation conditions closer to forming operations.

The sample was designed to fit on the stage of the Inspect F scanning electron microscope; hence, damage development in the microstructure that resulted from the punch test could be inspected at regular intervals of deformation. Figure 3.18 shows how the geometry of the sample along with that of the Inspect F SEM specimen holder. Figure 3.19 shows how the sample was affixed to the SEM specimen holder with two pins after manufacture. This ensures the sample will return to the same location after the strain is applied, and allows the same area to be inspected by SEM. The microstructure was then prepared following the same method as that for the SEM tensile test sample, as explained in Section 3.3.2.

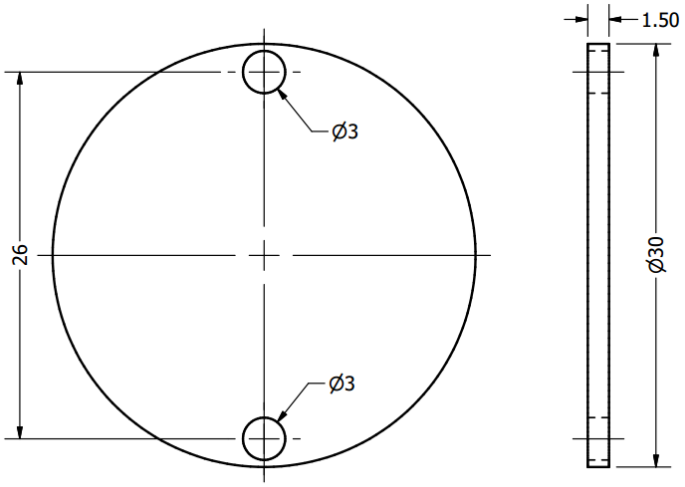

(a)

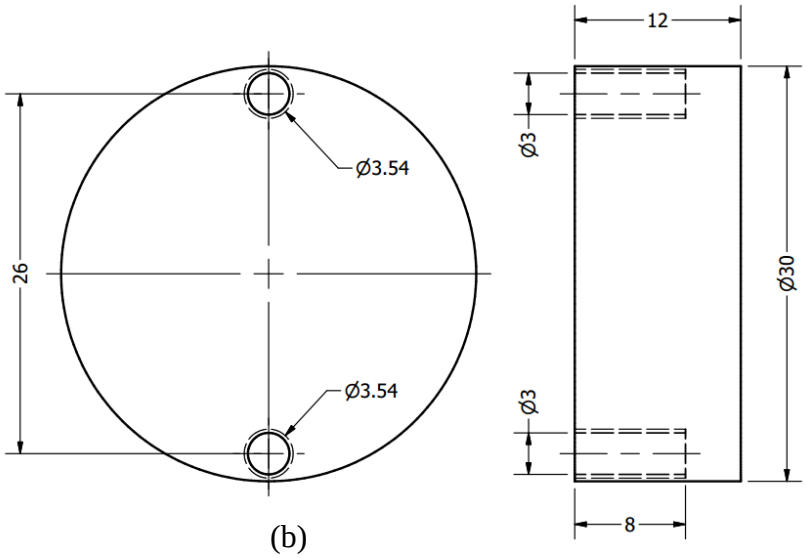

(b)

Fig. 3. 18 (a) SP sample geometry and (b) Specimen holder geometry in the Inspect F SEM.

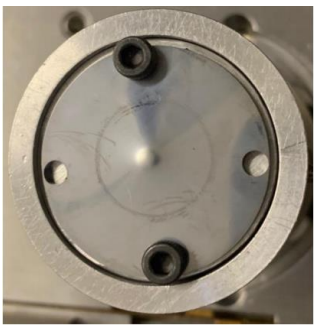

Fig. 3. 19 Sample affixed to the SEM instrument base with two pins.

Figure VI.1 in the Appendix VI shows the SP test rig. The sample was fixed on holes between the bottom and top dies with a key, and six bolts were used to tighten the specimen. The punch tool was then moved on the machine to deform the sample through a hole in the die. The machine used for this experiment was the 100 kN Mayes electric machine located at the Lea Lab, University of Sheffield. The bottom die was supported by two bars and blocks, whilst the top die was supported by the top bars.

The test was set at displacement control, and the rate of the punch movement set to 1 mm/min so the test could be stopped at any displacement level, and the microstructure observed before the sample became damaged. Prior to starting the test, SEM images of the sample microstructure were taken (Fig. 3.20). The images were captured at different magnification levels, as well as at different locations. The sample was then taken out of the SEM machine and transferred to the Mayes electric machine for testing. The punch tool later began to deform the sample, and the test was ended at the 1mm level. The sample was then carefully removed to keep the surfaces clean and it was then again placed in the SEM. An image of the microstructure was captured and investigated for damage initiation. This procedure was repeated until the sample failed.

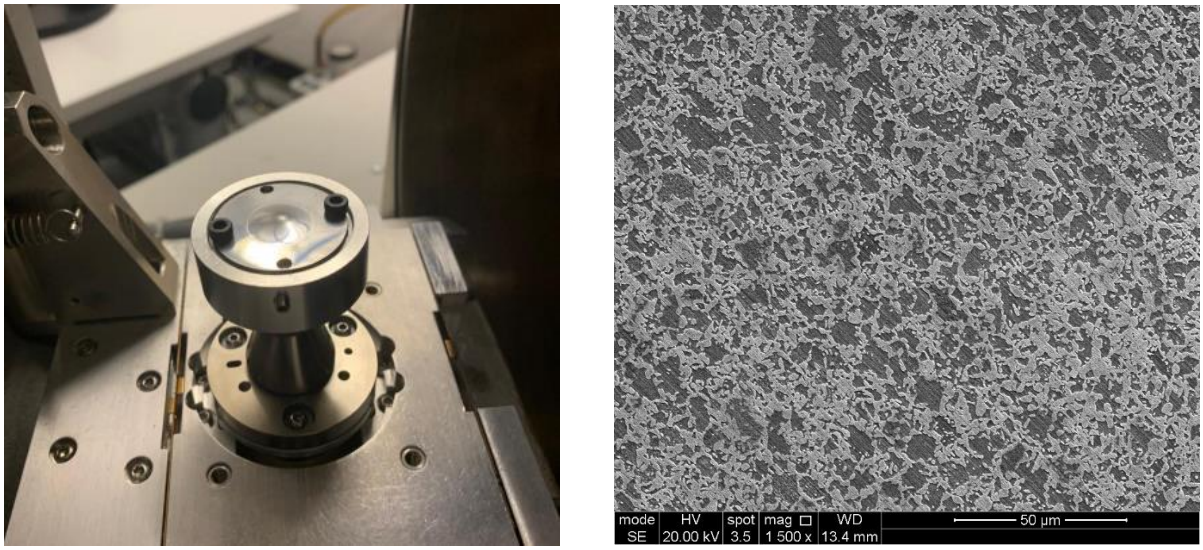

Fig. 3. 20 Sample in the Inspect F machine (left) with the first image of the microstructure before the application of displacement (right).

3.5 Bending test of DP1000 utilizing a micro bending stage

SP tests provided more insight into damage development in DP1000 in comparison with the in-situ tensile tests but damage propagation remained limited. Furthermore the tests could not continuously analyse the evolution of deformation and damage in the microstructure as the specimen had to be transferred from the punch test rig to the SEM at particular limited intervals.

An in-situ bending test was then carried out inside the CamScan SEM using a rig which became available late in the work. A new bending geometry based on (Dowding, Pinna, Ghadbeigi, & Farrugia, 2020) was implemented in the SEM, and the specimen geometry redesigned to fit the purpose of this research, as illustrated in Figure 3.21. The bespoke geometry of the specimen was designed to localise damage at the surface observed in the SEM. This sample design was selected chiefly based on studies of crack propagation in microstructures observed in a SEM, and was associated with the finite element calculations presented in Chapter 6. First, the top surface (see figure 3.21) of the sample was ground, polished and nital-etched. Then, the sample was placed by the bending test machine and loaded into the SEM chamber to obtain the SEM

images (Fig. 3.22). After the correct vacuum was reached the following day, the best focus and location were selected to analyse any deformation in the microstructure. A Deben micro bending stage, with a maximum loading capacity of 5 kN was utilised. The experimental displacement was controlled to a minimum of 0.001 mm. The setting of the in situ bending test was similar to that of the in situ tensile test (Section 3.3.1). For the SEM, combined with DIC analysis, the setting was the same as that used in Suction 3.3.2.

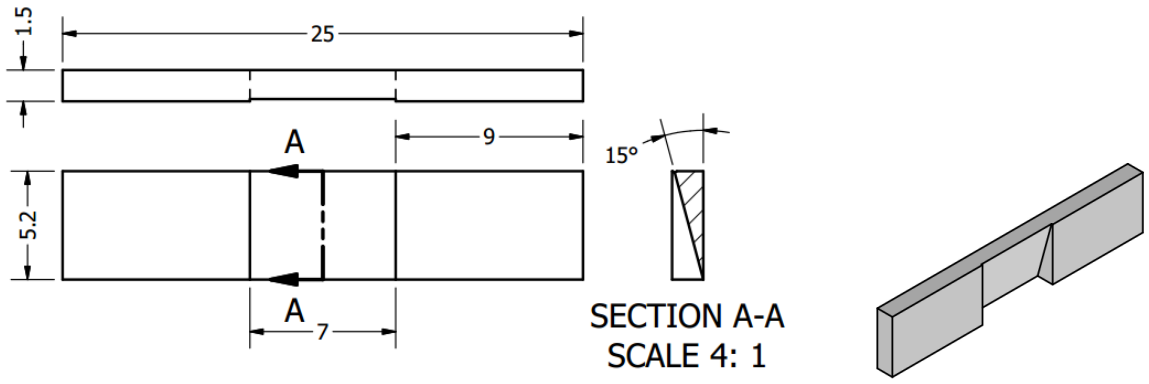

Fig. 3. 21 Bending test specimen geometry (mm).

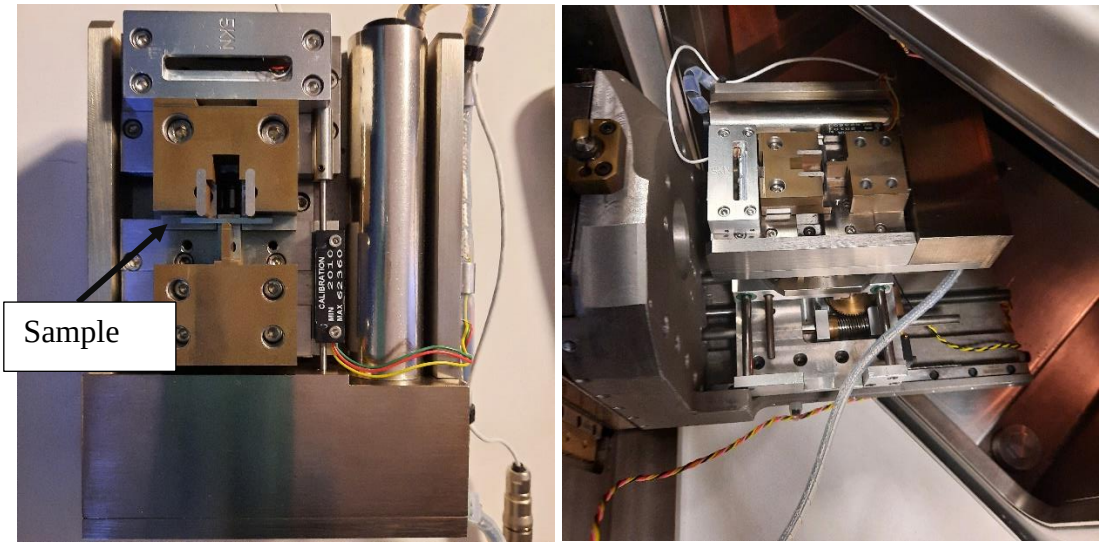

Fig. 3. 22 Sample on the bending stage (left); stage fixed on SEM chamber (right).

4. FE SIMULATION PROCEDURE OF DP1000

Abaqus software was utilised to simulate the experimental work, with the objective of obtaining accurate results from the modelling. Modelling was used for several purposes in this work. First, it was used to design the specimens, especially the bespoke bending specimen geometry reported in the previous chapter. It was also used to analyse the experimental work carried out at the micro-scale, to predict micro-scale stress distributions which could not be obtained experimentally. The aim of this modelling activity was to discover the damage initiation criterion in the two-phase microstructure of DP steel. Finally, damage modelling using the Gurson model was conducted to link the investigative scales in this work, and to predict the overall macroscopic response of DP1000, when tested for various test geometries.

4.1 FE simulation of standard and notched tensile test

To simulate standard and notched tensile tests with Abaqus (Simulia, 2010), a stress-strain curve was needed for the standard geometry, to be used to determine the material properties of the modelling. The conventional tensile tests of DP1000 were simulated at the macroscale, and the dimensions of the geometry were set to align with those of the actual samples (Fig. 4.1). Plastic deformation and damage was simulated using the Gurson damage model, and the linear C3D8R element type was implemented for the meshing. Table 4.1 lists the material property data of DP1000.

Table 4. 1 Material properties for conventional sample modelling.

Mass density	Young's modulus	Poisson's ratio
7.85E-006 Kg/mm^3	18 0000 MPa	0.3

The boundary conditions generated needed to match those of the clamp holder of the machine being used for the real test; thus, the bottom face was fixed in all directions, with the X and Z directions constrained for the top surface. The parameters of the Gurson model were calibrated to obtain the best stress-strain curve for DP1000. Displacement speed in the Y direction was set to 0.1 mm/s to match the displacement rate in the experimental test.

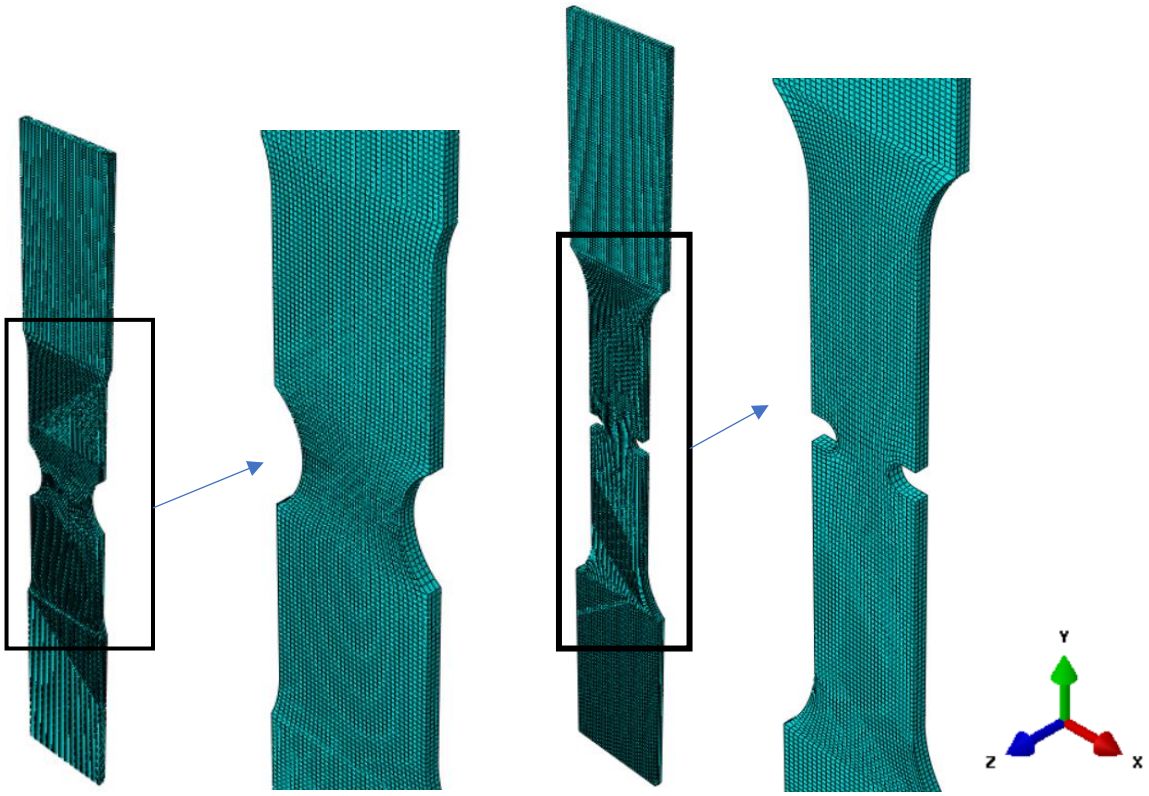

Fig. 4. 1 Modelling of notched geometries (engineering drawing see fig 3.2 a).

4.2 SEM tensile test modelling

Continuum damage modelling involves modelling the deformation of a macroscopic specimen until the point of fracture is reached. Figure 4.2 depicts the model of the specimen used for in-situ tensile tests. This was designed with dimensions matching those of the real specimen (Fig. 3.3).

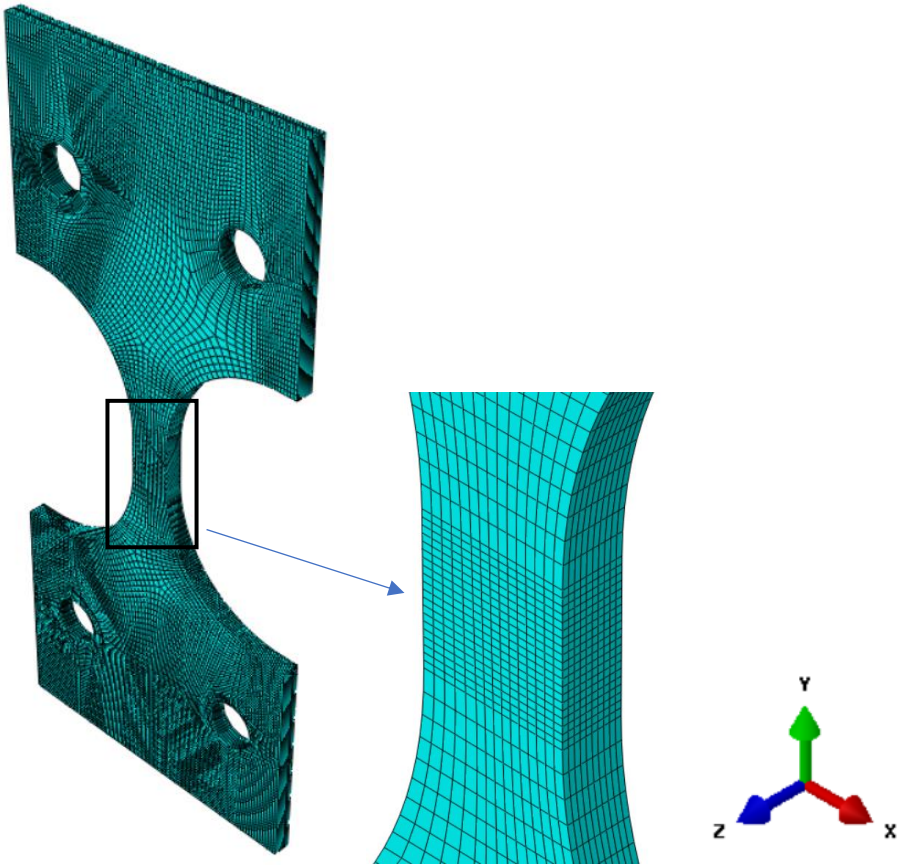

Fig. 4. 2 Finite element model of the SEM tensile sample geometry (drawing 3.3).

For in situ tensile specimen modelling, the boundary conditions were such that the two bottom holes were fixed in all directions except for the rotation around the Z axis (because it is an out-of-plane axis), which was designed to stimulate boundary conditions in the application of a real test through an experiment, whereas the two top holes were fixed in the horizontal and out-of-plane directions (X and Z axes). Afterwards, a linear speed (0.001 mm/s) was utilised in the Y direction to recreate the conditions in the actual experiment. As the speed was low, the model could be run in a quasi-static state. Therefore, to model the material behaviour of the softening part, the static analysis was also used in Abaqus/CAE. The parameters of the Gurson model, q_1 and q_2 , were recommended by (Tvergaard et al., 1981) to obtain the best match for the experimental load-displacement curves of the typical materials. The void nucleation parameters f_n, ε_n and s_n were selected according to the Abaqus manual for typical materials

(Simulia, 2010). Table 4.2 provides the base values for all the parameters. The Results section will explain the calibrated parameters in detail.

Table 4. 2 Show the original values of GTN parameters

q_1	q_2	f_n	ε_n	s_n
1.5	1	0.04	0.3	0.05

4.3 Microstructure modelling

The microstructure of DP1000, with 51% martensite (brighter phase) and 49% ferrite (darker phase), is shown in Fig. 4.3.

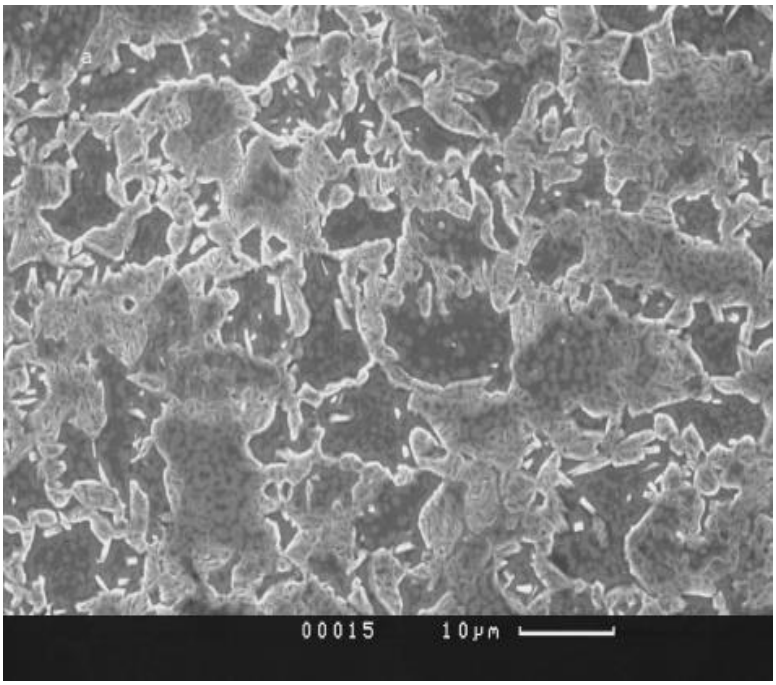

Fig. 4. 3 Undeformed microstructure of DP1000; the ferrite is darker, and the martensite is brighter.

Figure 4.4 shows the methodology developed to produce stress maps of the microstructure of DP steel, as a way to study damage initiation. The image of an undeformed microstructure was then converted into a meshed microstructure for FE simulations using Abaqus. First, a Matlab

script (Alharbi, 2015) was used to convert the microscope images into black and white, applying a thresholding method (Chalon, 2004). The images were then subdivided into rectangular elements, and the phases (ferrite and martensite) allocated on the basis of the pixel distribution intensities of each element. The element type CPS4R was selected for Abaqus modelling.

The script was extended to map the displacement vectors measured using DIC onto the microstructural mesh, and these were then applied as the boundary conditions to force the microstructure to deform, as in the experiment. Linear interpolation was adopted to map the DIC data onto the nodes of the FE mesh. To analyse conditions leading to nucleation, the deformation of the microstructure was simulated under plane stress conditions until deformation was achieved, but prior to the emergence of a damage event in the martensite.

Two Matlab codes were used to develop the finite element model of the microstructure based on the SEM images (Alharbi et al., 2015; Davis, 2010; Manual). The first code, as developed by Chalon (Chalon, 2004), converted the SEM image into a finite element mesh depicting the microstructure. A threshold process was applied to change the original SEM image of DP1000 into a black and white image, according to the level of grey in the SEM picture. The image was then subdivided into square elements, with the user controlling the element size. Elements were then assigned a phase number, according to whether they belonged to the ferrite or martensite phase. An input file for Abaqus was then generated, with the appropriate format to generate the mesh. The quadratic linear element CPS4R was then used for modelling purposes. Using the second Matlab code developed by Alharbi (Alharbi, 2015), the displacement vectors measured by DIC over the entire microstructure were imported into the Abaqus input file, and implemented as boundary conditions at every node. The model was then expected to depict the actual deformation of the microstructure, as measured experimentally. The model was also applied to some SEM images, which were captured through the process of plastic deformation

around the point of ultimate tensile strength. The average stress present in the microstructure was then calculated using the following equation 29:

$$\bar{\sigma} = \frac{1}{V}\int_V \sigma \, dV \tag{29}$$

where σ is average stress, V is the volume of the analysed microstructure in the model, and σ is the stress within each element of the model.

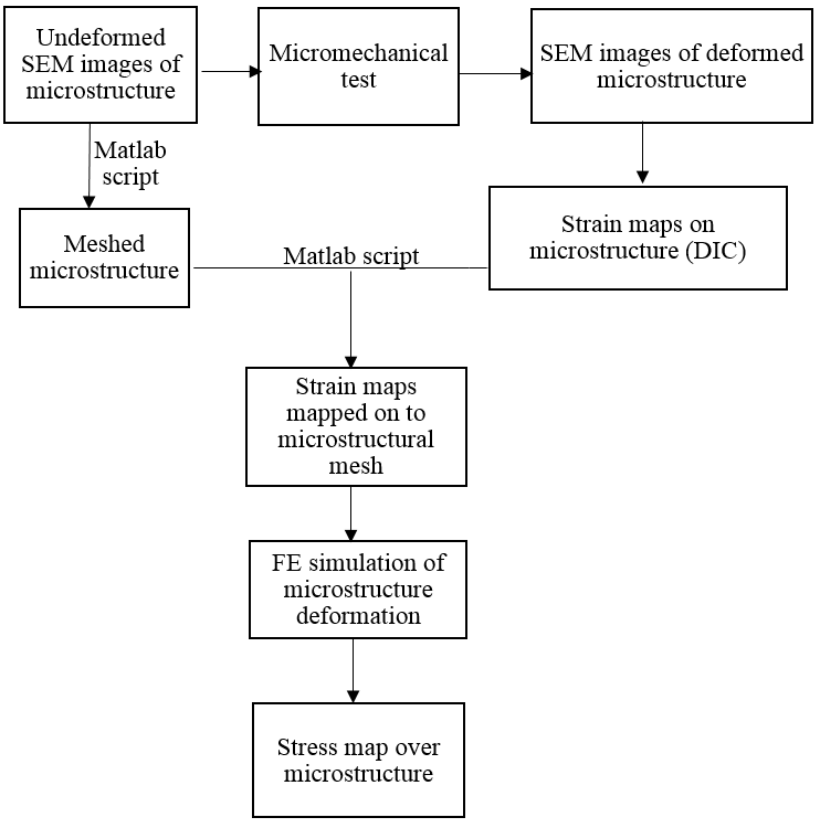

Fig. 4. 4 Flowchart detailing the production of stress maps over the deformed microstructure.

4.4 Punch test modelling

This section presents the macro- and micro-scale simulations of plastic deformation and the damage from the punch tests. The modelling procedures performed using Abaqus are also discussed further.

4.4.1 Macroscale punch test modelling

As was the case with the previous modelling procedure, this simulation required a true stress-strain curve; that is, the curve obtained from the experimental results of the standard geometry, as shown in fig.5.1.1. The macro punch test modelling was carried out with the specimen dimensions, which were designed to match those of the real experimental sample. Figure 4.5 shows the sample geometry, with the punch tool being a rigid body designed using Abaqus. The material properties reported in Table 4.1.1, along with the tensile stress strain data were inputted to the model.

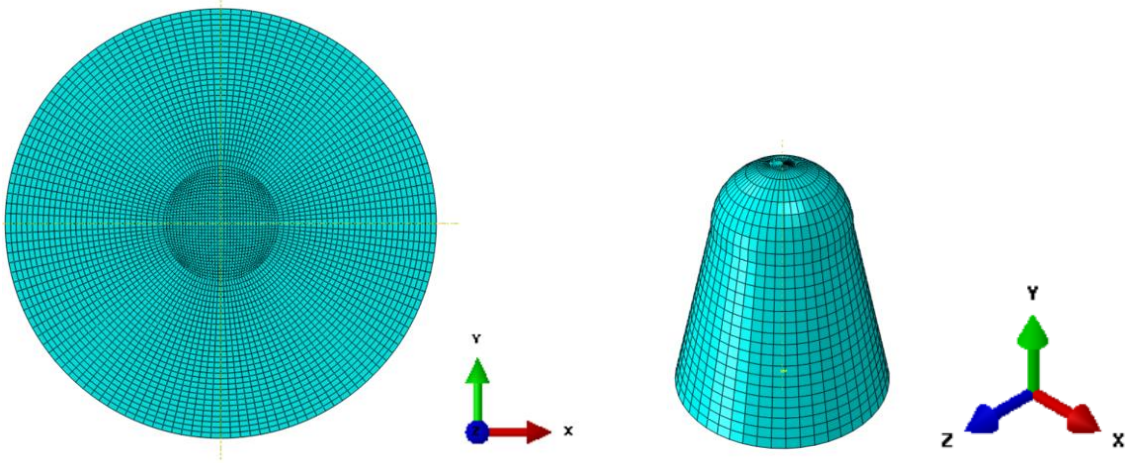

Fig. 4. 5 Models of sample and punch tool (see figures.3.7 and 3.8 for dimensions).

With reference to the experimental work, a clamp was placed around the sample, and the outer diameter of the sample fixed in every direction. This meant that the boundary conditions of the outer circle of the sample were zero. The value of the maximum displacement was 9.93 mm

when applied in the Y direction, as measured from the results of the 3D DIC experiment during the macro punch test. This was applied to move the punch tool towards the sample. The other directions of the punch (X and Z) resulted in zero rotations.

Contact between the punch and the specimen was modelled using the penalty method with a coefficient for the friction value of 0.35. The element used for the simulation was the standard linear type C3D8R. This value was selected via a parametric study, with 0.35 providing the best match to the experimental results.

4.4.2 Small Punch modelling

Simulations of the SP tests were also carried out, with comparisons against experimental data including strain measurements using 3D DIC. Figure 4.6 shows the modelling dimensions of the specimen, and the punch designed using Abaqus. This was the same procedure as that applied to the macro punch modelling, although the diameter of the specimen was 30 mm. The maximum displacement value applied in the Y direction was 4 mm.

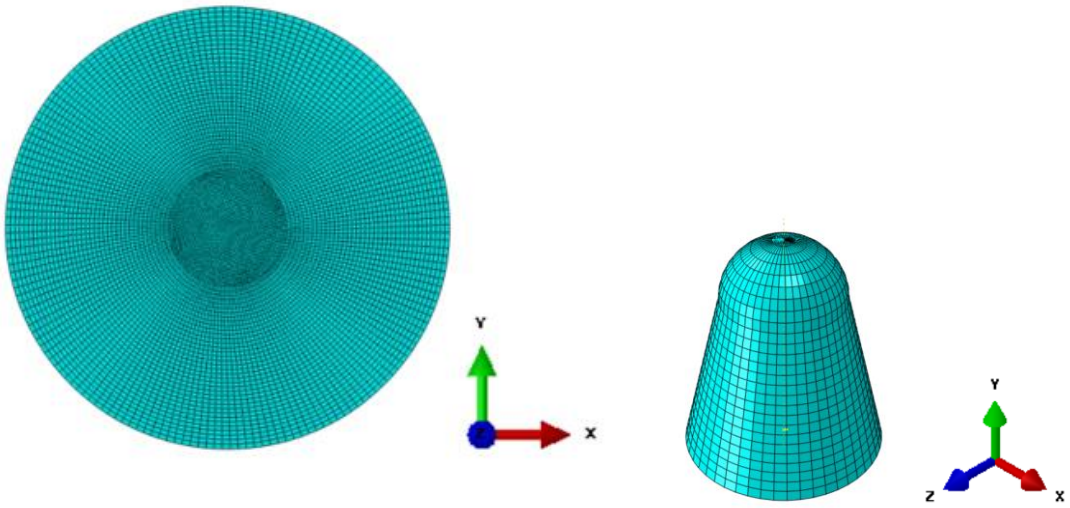

Fig. 4. 6 Models of the small sample and punch tool (see figures 3.11 and 3.17 for dimensions).

4.5 Bending test modelling

The same approach employed for continuum modelling in the tensile test and carried out inside the SEM was adopted here. Abaqus was used to simulate the bending test to infer the damage criterion leading to crack propagation. Figure 4.7 shows the complete model, which was designed with dimensions matching those of the real specimen (Fig.3.21); and the rollers were designed as a rigid body. Material properties were reported in Table 4.1; along with the true tensile stress-strain curve, these were also used to model plastic deformation in the specimen. The boundary conditions were such that the first and second points at the centre of the bottom rollers (see Fig. 4.7) were fixed in all directions, whilst the third point at the centre of the top roller was moved vertically. The maximum displacement of the third point matched the full extension, and was applied experimentally (6.25 mm). For the contact procedure, as explained in Section 4.4.1, a value of 0.35 was used to establish the friction coefficient.

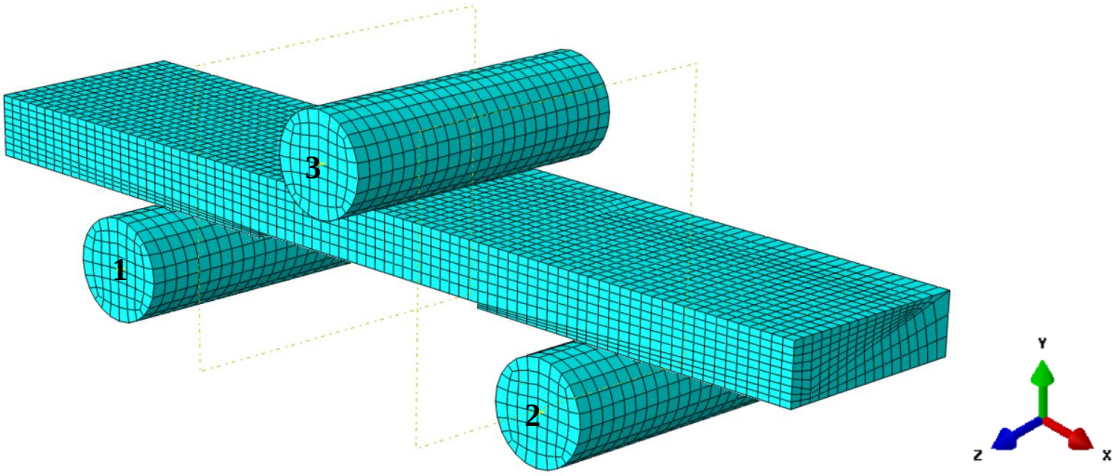

Fig. 4. 7 FE simulation via Abaqus (engineering drawing see fig. 3.21).

5. EXPERIMENTAL RESULTS

The main goal of this work is to study the deformability of DP1000, and evaluate the material's behaviour by observing damage as it occurs, from its initial development to the point of final fracture. In this chapter, experimental work, performed at different scales is analysed to understand the deformation and damage of DP1000 at both the macro- and micro-scale. The first subsection focuses on stress–strain curves for DP1000, which were obtained through standard tensile tests. The second subsection analyses the in situ tensile test inside a scanning electron microscope (SEM), in combination with 2D digital image correlation (DIC). The third part focuses on the macro punch test, and the new small punch test (SPT) evaluated with 3D DIC. Crack propagation analysis in the SPT for the fractured sample has also been added here. The last subsection discusses the in situ bending test with SEM in combination with 2D DIC, as well as the crack initiation and propagation analyses throughout this test.

5.1 Uniaxial tensile testing results of DP1000

5.1.1 Plastic stress strain curve of uniaxial tensile test

To study the material deformability and damage process, including through modelling, the stress strain curve needs to be obtained by testing standard specimens. The load-displacement curve can first be converted into an engineering stress–strain curve, from which the yield point can be determined as 662 MPa, and the UTS as 1109 MPa. This curve can then be calculated based on equations 30 and 31.

$$\sigma_e = f/A \tag{30}$$

$$\varepsilon_e = \Delta l/l \tag{30}$$

The σ_e indicates engineering stress and ε_e indicates engineering strain. *F* is the load, and *A* is the area of the gauge length. The Δl denotes change of gauge length, and l_o is the original gauge length. Poisson's ratio and modulus of elasticity values were 0.3 and 200 GPa, respectively. The true stress–strain curve required for the modelling work was then obtained, and is shown in Fig. 5.1. The plastic true stress strain curve can be calculated based on the equations 32 and 33.

$$\sigma_{t=}\, \sigma_e\, (1 + \varepsilon_e) \tag{31}$$

$$\varepsilon_t = \int_{l_o}^{l} \frac{dl}{l} = \ln(1 + \varepsilon_e) \tag{32}$$

Were σ_t refers to the true stress, and ε_t the true strain.

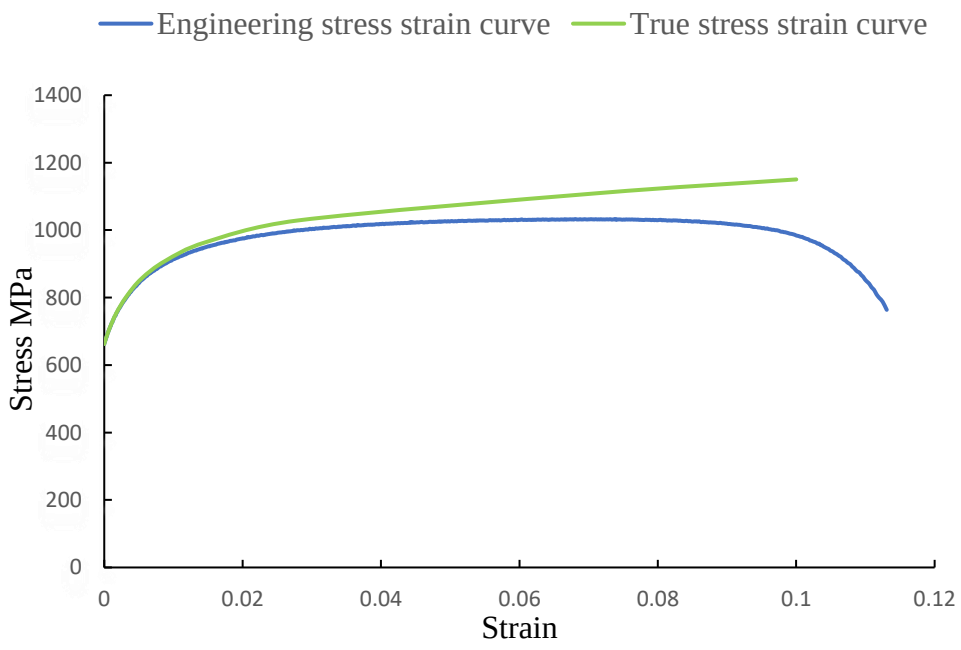

Fig. 5. 1 Engineering and true stress–strain curves for standard tensile tests, conducted using optical 3D DIC. This curve is used to simulate notched SEM and punch test samples.

5.1.2 Load displacement curves of uniaxial notched specimens

Notched samples can be used to predict fracture mechanics as a result of differing stress triaxiality. The notched load displacement curve can be used to study the formability of DP1000. Fig. 5.2 shows the experimental load displacement results for the notched samples. In the current research, the notches are used to predict and calibrate the GTN parameters, as the next chapter explains.

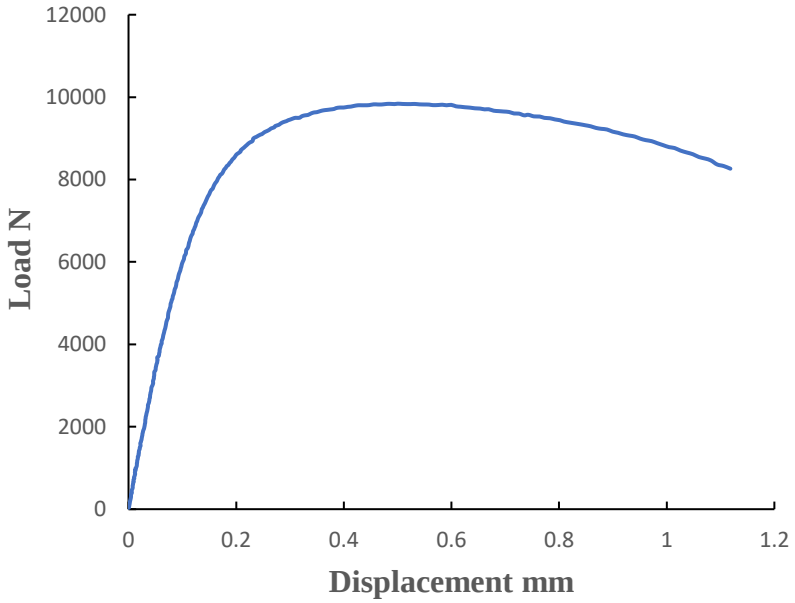

(a)

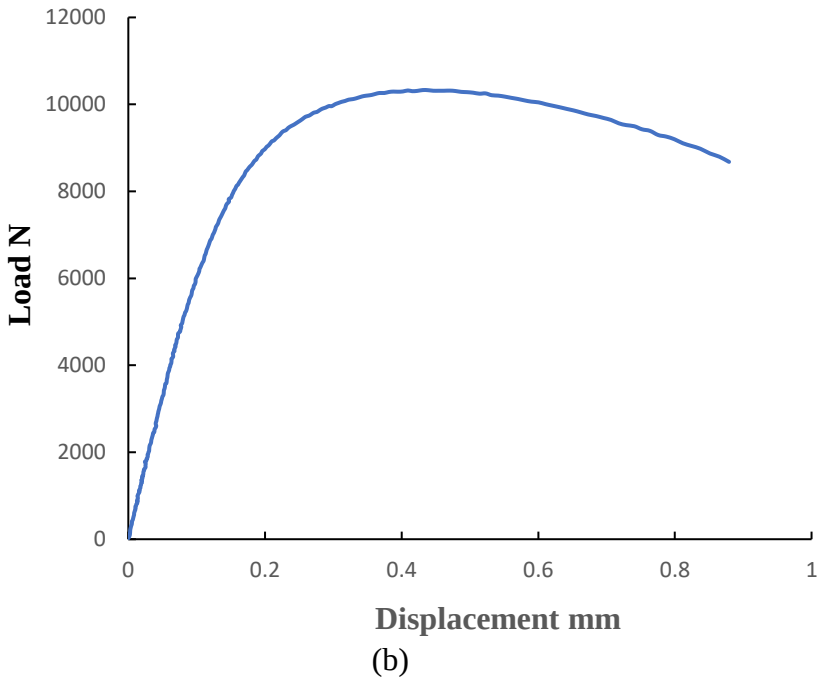

(b)

Fig. 5. 2 The load displacement curves for notched samples in (a) R= 7.5 mm and (b) R= 1.5 mm.

5.2 In situ uniaxial tensile test of DP1000 utilizing a tensile stage

This section presents the results of the in situ tensile test, which was conducted within the SEM in combination with DIC measurements. The load–displacement and engineering stress–strain curves recorded in the in-situ tensile test are shown in Fig. 5.3 The small decreases in the stress values along the curve correspond to instances when the test was interrupted to capture images of the microstructure for subsequent DIC analysis. The strain value at the plastic deformation started at 0.01, and this value increased to 0.35 by final fracture. Large post-uniform deformation is ideal for studying damage development in the microstructure, and is attributed to special specimen geometry, where stress triaxiality levels differ from those of standard geometry.

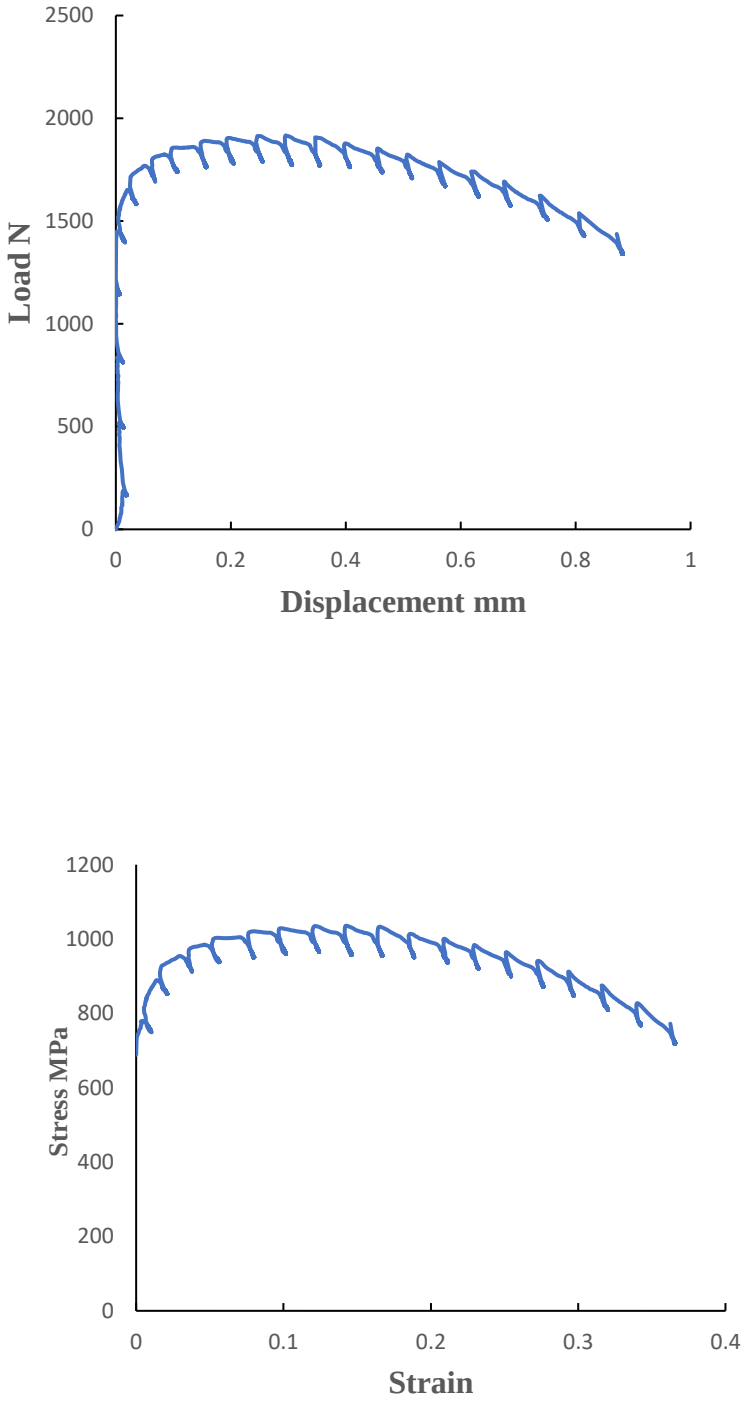

Fig. 5. 3 Load displacement and engineering stress strain curves produced using the SEM tensile test.

5.2.1 Localized plastic deformation of DP1000 observation using SEM

Localised deformation's of the plastic develop in the specimen, and were analysed using in-situ SEM images, which were captured during the tensile test by interrupting the extension

every 0.05 mm. The micrographs recorded were utilized to examine the enhancement of local deformations, this included damage initiation and propagation to the point of specimen fracture. Fig. 5.4 provides examples of micrographs, which were captured during the early stages of the plastic's deformation. The initial manifestation of non-uniform deformation can be seen on these micrographs with an applied strain value of 0.18. Localised deformation bands were observed within large ferrite grains (Figs. 5.4 (b) and 5.4 (d)), in contrast to smaller ferrite areas, which were trapped between the islands of martensite. Therefore, the ferrite had already started to deform before any cracks appeared in the martensite.

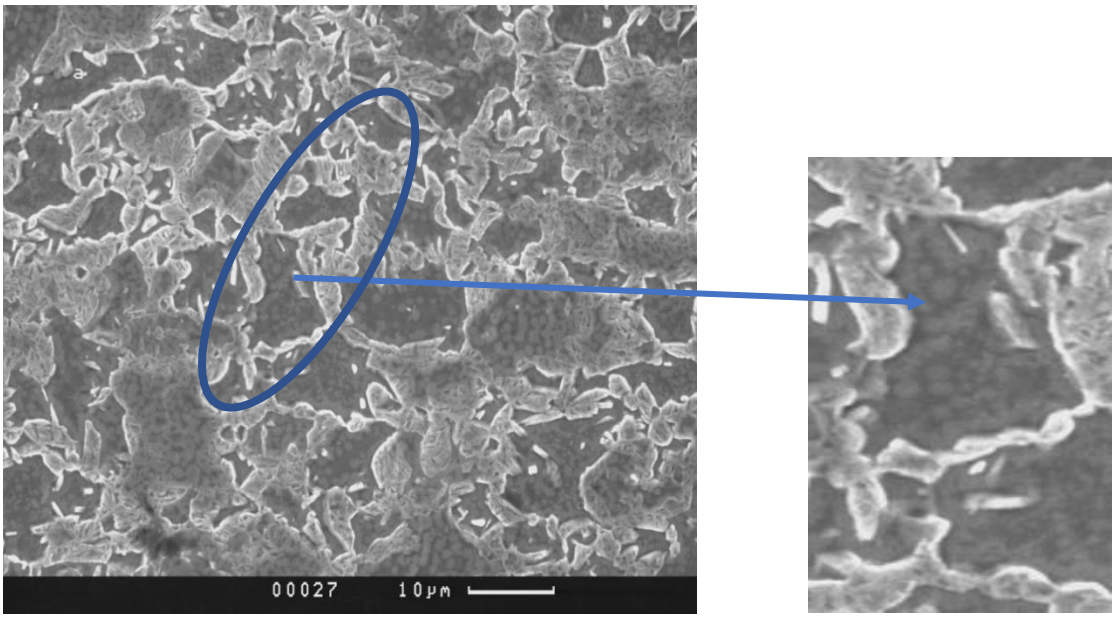

a b

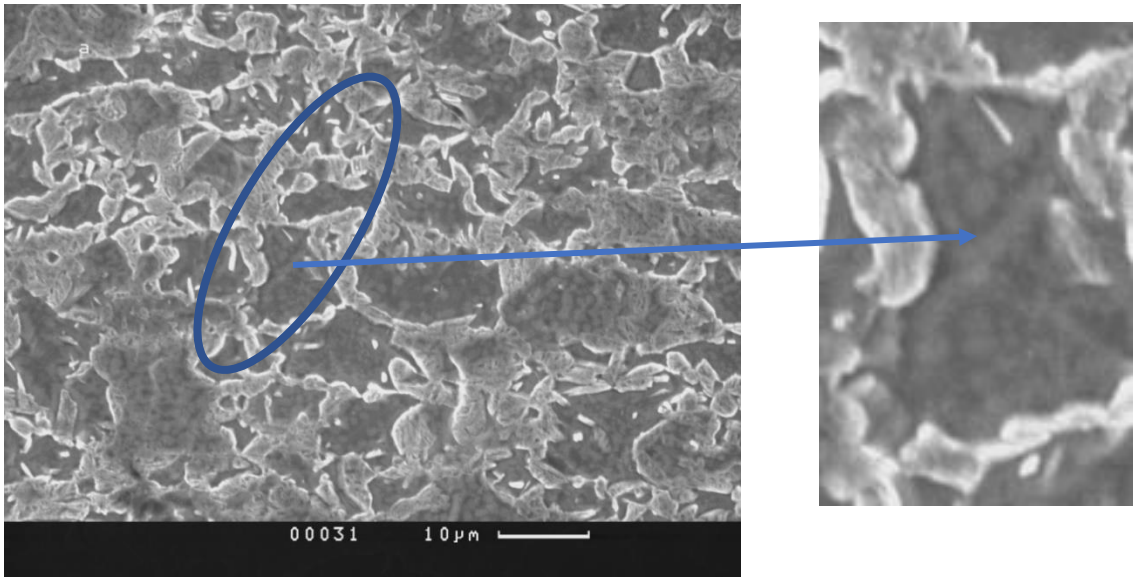

c d

Fig. 5. 4 (a), (b) Images captured at 0.11 strain; (c), (d) images captured after the application of 0.18 strain.

The plastic deformation's localisation in the ferrite and martensite phases was seen in the early stages of strain. As shown in Fig. 5.5, such localisation resulted in progressive damage, as the test progressed, up to the point of failure at a strain value of about 0.35. These areas were enlarged in the figure, and clearly depict the proliferation of plastic deformation in both the ferrite and martensite phases. The (localised) deformation bands situated within the big ferrite phases (within the ovals in Figs. 5.4 and 5.5(c) and (d)) were more intense, and led to the separation of two martensite islands, due to localised deformation within the ferrite phase (e.g., see the rectangle and oval in Fig. 5.5).

The SEM microstructure analysis of the samples shows void nucleation in DP1000 steel: the void initiation occurred in the ferrite near to the ferrite martensite interface following significant plastic deformation. After this point, damage propagation caused the martensite to crack. Typical instances of these mechanisms are shown in Fig. 5.6 and table 5.1 (crack 12), detailing the progression in void development close to the martensite islands, with an increase in the applied strain. An example of void initiation is visible in Fig. 5.6, where the value of the

specimen strain reached 0.3. The damage spread into the adjacent ferrite phase, where the currently divided martensite island was situated, as a rectangular shape shown in the figure. The next subsections explain these mechanisms in detail.

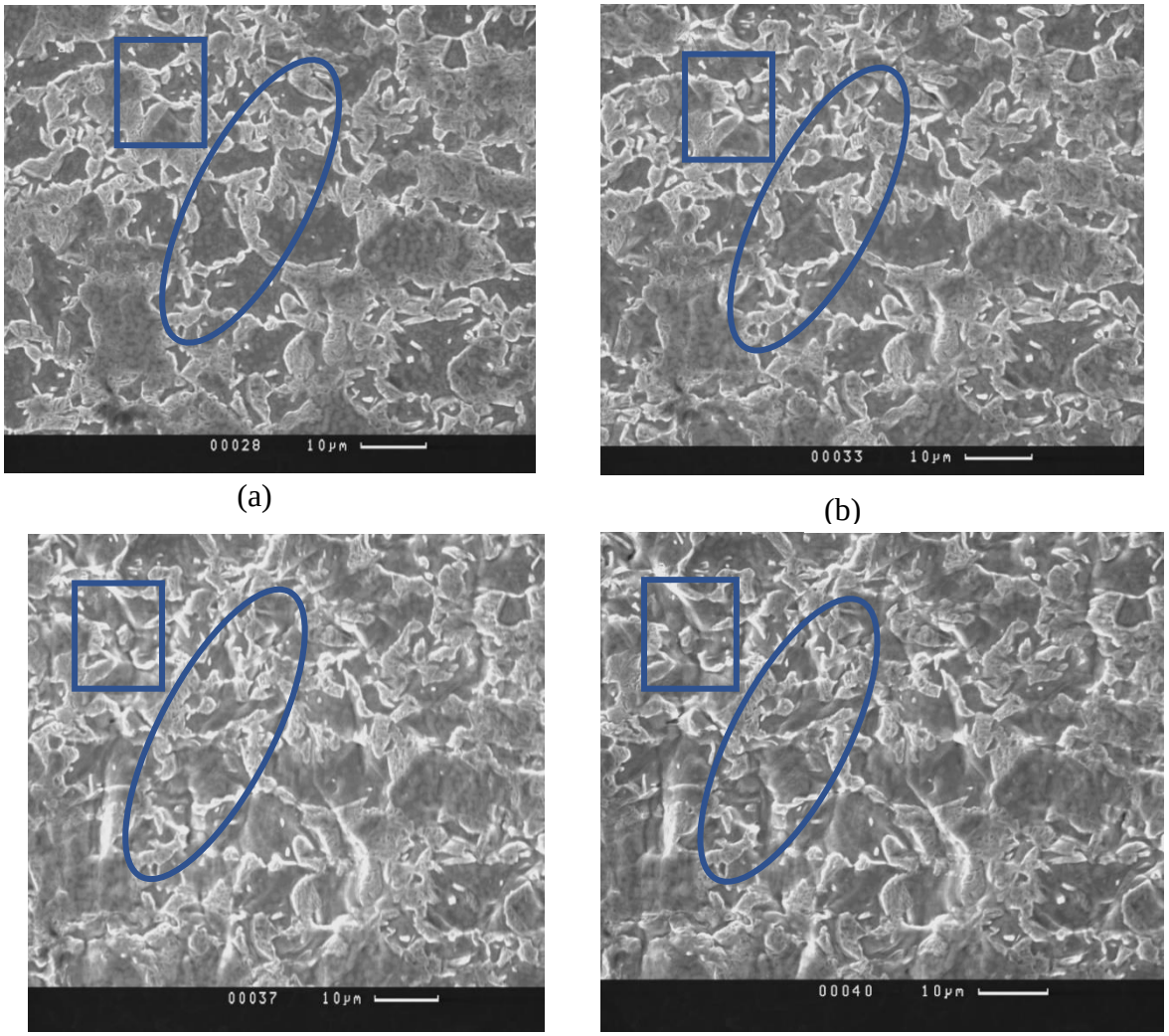

Fig. 5. 5 The progressive deformation up to failure (from (a) to (b)). Images (c) and (d) captured after the application of 0.30 and 0.35 strain respectively.

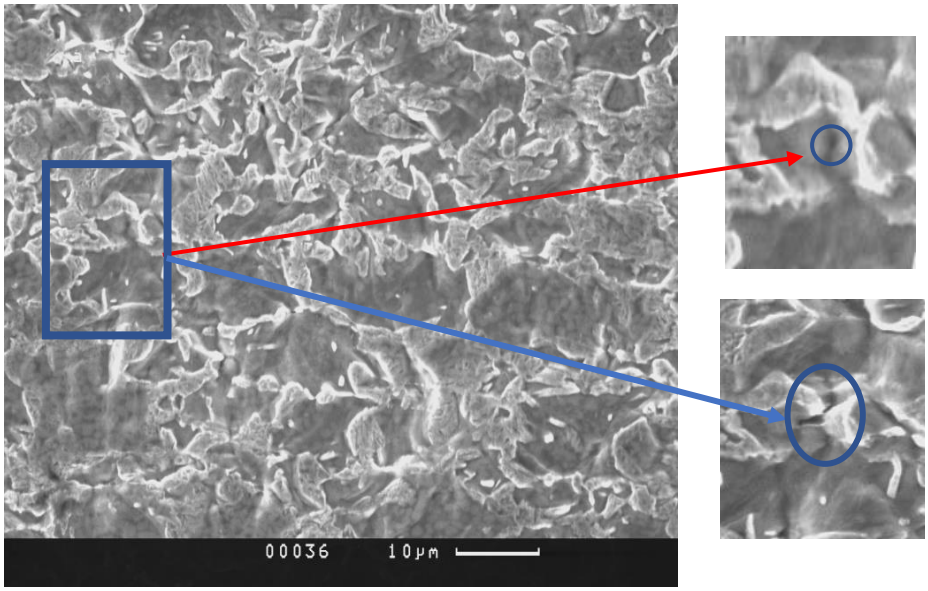

Fig. 5. 6 Example of the damage mechanism for the void initiation in the ferrite phase, which caused the martensite to crack after significant deformation.

5.2.2 Inspection of martensite cracks and ferrite voids of DP1000 using SEM

According to (Rashid, 1981; Tasan et al., 2015), damage in the martensite phase can arise as a result of the high stress value, whereas damage in the ferrite can happen as a result of a high the strain value. The results from the present analysis show that martensite cracking occurred in different regions of the microstructure. Table 5.1 shows the figures for the stress–strain curve. There is an interruption every 0.05 mm of extension when observing the microstructure deformation and martensite cracking from beginning of the test until the failure. This table also reports the global stress and strain values just prior to the crack appearing in the martensite to deliver more in depth insights into the processes of deformation and damage behaviour. Table 5.1 shows microcrack tracking at each step of the loading stage. These cracks are arranged in the table in ascending order of the stress and strain values throughout the test.

The first mechanism observed was the martensite cracking. For example, in cracks 1 and 5 the martensite deformed until cracks separated the martensite. Crack 1 appeared before the UTS point, with a global strain value of 0.0486, and a global stress value of 1020.5 MPa just prior

to the formation of the crack. Cracks 5 can be detected immediately after the UTS, where the strain value was 0.13 and the stress value 1053 MPa; that is, before the crack initiated.

A second mechanism involved the martensite cracking following deformation, as observed in the ferrite phase, where this deformation occurred close to the martensite crack. Cracks 2, 3, 4, 6 ,8, 9,10.11, and 13 illustrate this mechanism. In crack 2, the ferrite deformed close to the martensite at 0.11 global strain and 1050.8 MPa global stress, which was before the UTS. Then, the ferrite continued to deform, causing crack 4. This happened after the UTS; the strain value before the crack appeared in the martensite was 0.13, and the stress value was 1053 MPa. For cracks 7 and 8, the global strain reached 0.18 and the global stress 1030 MPa prior to initiating these cracks. Crack number 10 started after the ferrite deformed at the red arrow. Then, the crack propagated to the martensite as shown in the figure. The strain value before the crack started to appear was 0.22, and the stress was 998 MPa. The strain value prior to crack 9 forming was 0.2, and the corresponding stress value was 1013 MPa, whereas the respective values for crack 11 were 0.24 and 981 MPa. For crack number 13 the strain value was 0.3, and the stress was 892 MPa.

A third mechanism observed was void formation in ferrite close to the ferrite martensite interface, after large deformation with damage propagation cracked the martensite. For example, for crack number 12 the ferrite void was propagated, cracking the martensite once the stress value was 892 MPa and the strain 0.3.

This shows that martensite cracking can occur at low strain levels (mechanism 1), but mostly after significant strain localisation, at or close to the interface (mechanism 2) with the third mechanism being rarely observed and corresponding to martensite cracking after very large strain values were obtained in the ferrite close to the interface.

To understand the process of deformation through the martensite cracks, we measured the different strain values between the first and last cracks. The cracks started to form between strain values of 0.05 and 0.3, and the highest level of strain was reached triggering failure at 0.35.

Table 5. 1 Details of global stress–strain values just prior to the appearance of damage in the martensite. Image number 1 indicates the crack location in the reference microstructure capture, and image 2 indicates the martensite fracture just before the crack appears in image 3.

Crack	Interruptions for microstructure observation	Global stress/strain curves
1	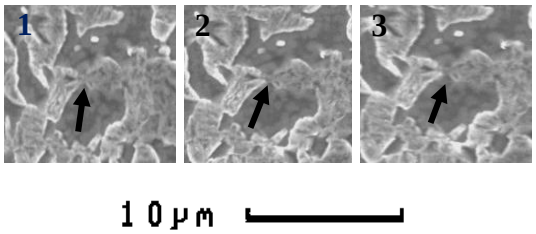 The black arrows indicate the location of crack appearance.	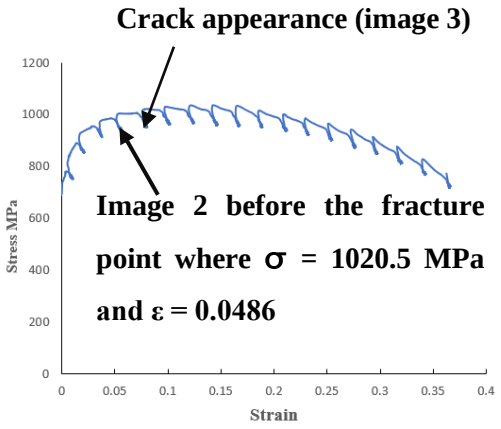
2	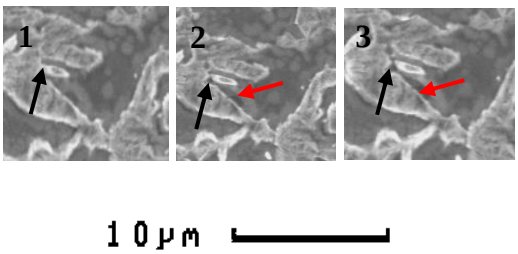 The ferrite deformed at the red arrow, and cracking happened at the black arrow.	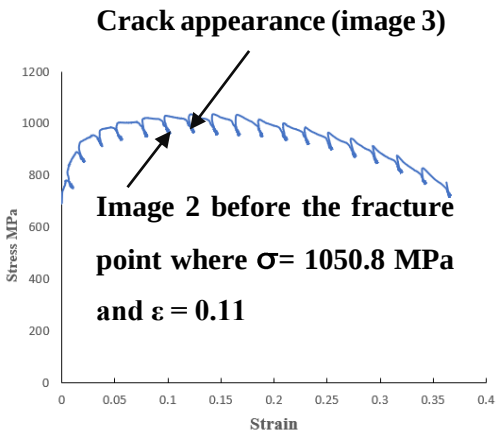

3	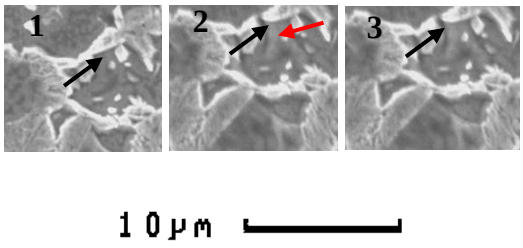 The ferrite deformed at the red arrow, and cracking happened at the black arrow.	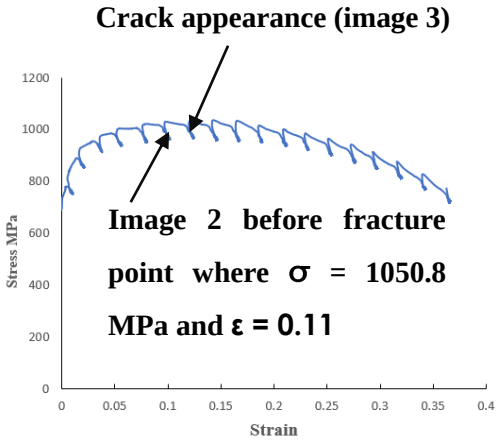
4	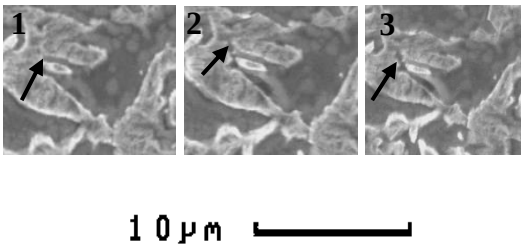 The ferrite deformed at the red arrow, and cracking happened at the black arrow.	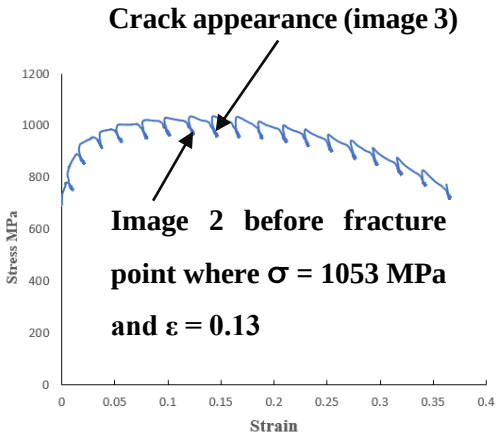
5	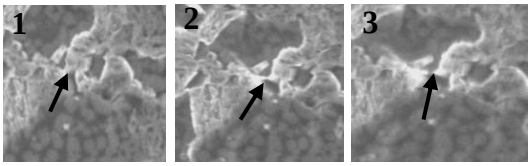 The black arrows indicate the crack.	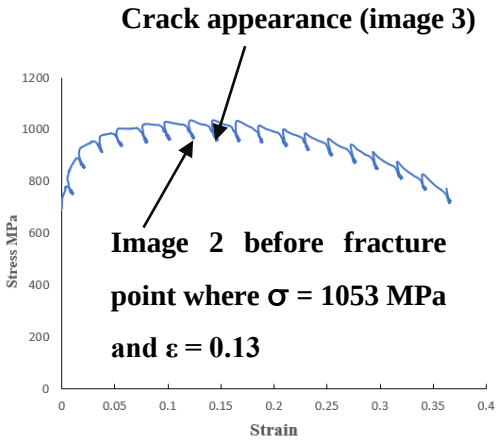

6	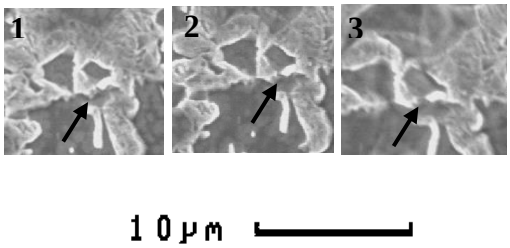 The black arrow indicate the crack.	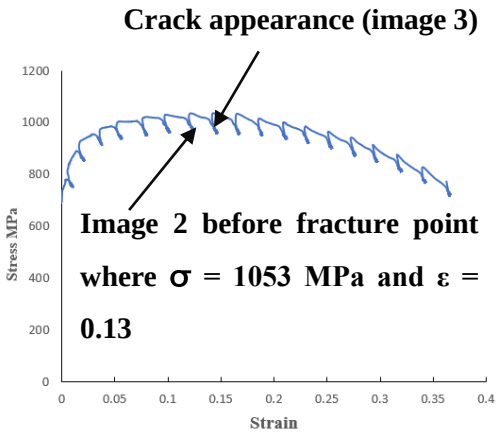
7 and 8	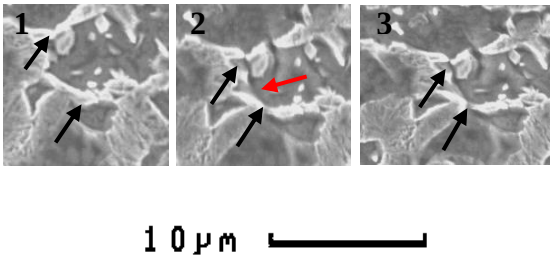 The ferrite deformed at the red arrow, and cracking happened at the black arrow.	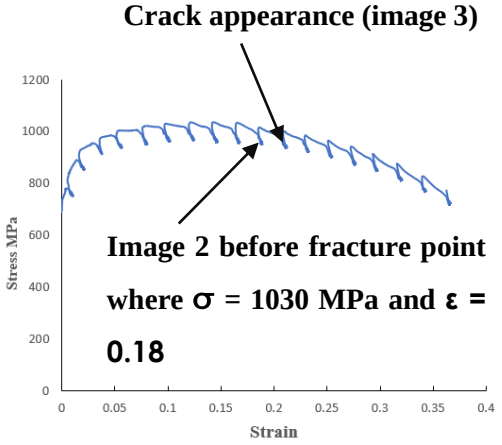
9	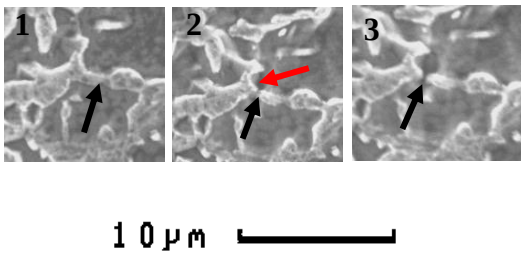 Plastic deformation in the ferrite, as the red arrow shows, leads to martensite cracking (black arrow).	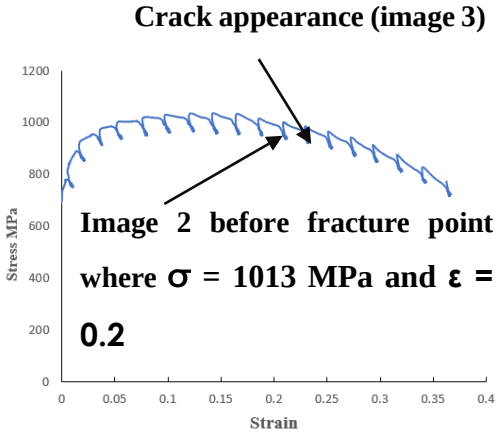

10	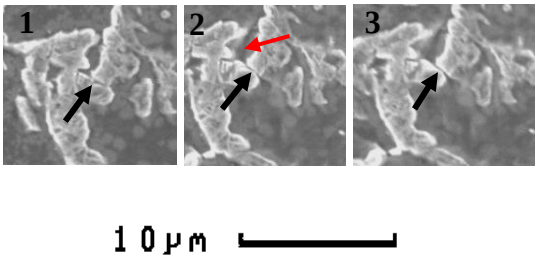 Deformation of the ferrite (red arrow), and martensite cracking (black arrow).	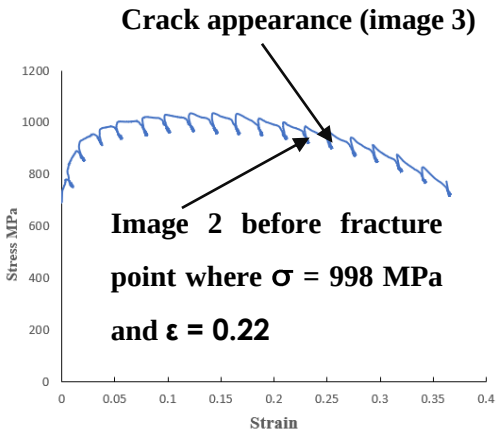
11	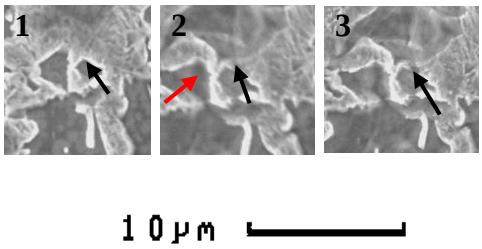 Deformation of ferrite (red arrow), and the black arrows indicate the crack.	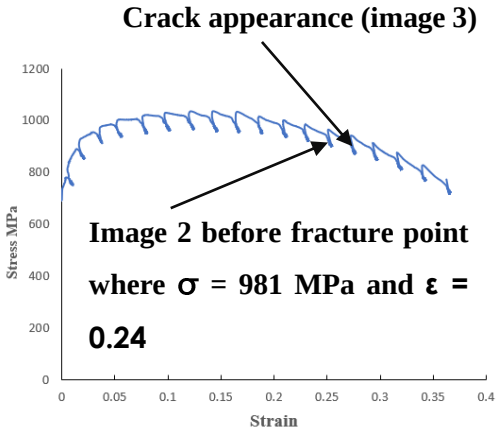
12	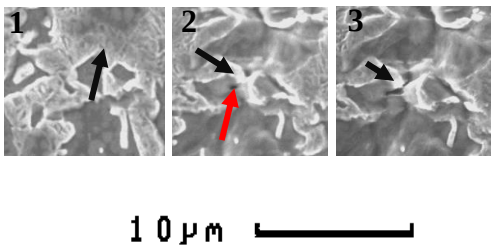 Void initiated in the ferrite, as shown by the red arrow, then propagated to crack the martensite, as shown by the black arrow.	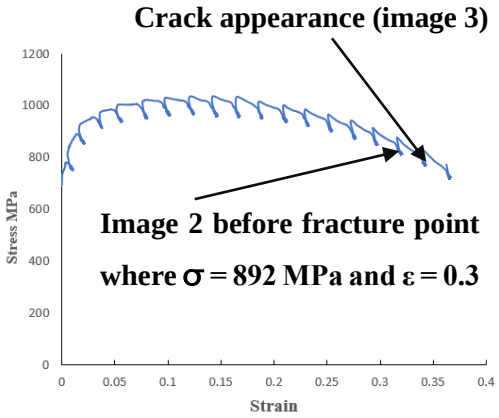

13	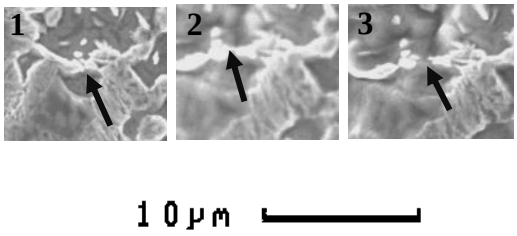 The black arrows indicate the crack.	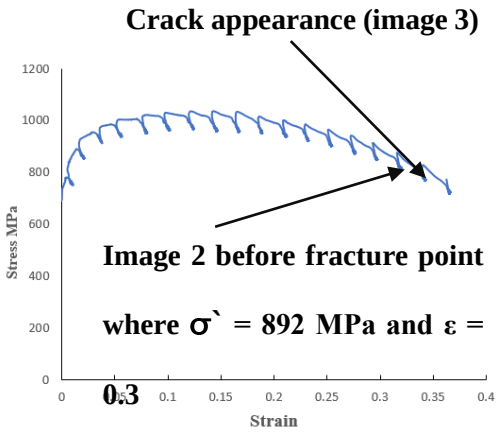

Voids in the ferrite phase have very rarely been reported in the literature involving tensile testing. Several voids were observed in this study. Continuous observations of the damage to the microstructure revealed that voids formed in the ferrite phase under high rates of global strain. Large plastic deformations at such a locations eventually lead to the formation of voids in the ferrite phase. The stress–strain curve in Table 5.2 shows the global strain values before the voids are nucleated. The first void appeared in the ferrite phase, and was surrounded by the martensite phase, and propagated to cause a martensite crack, as explained in Table 5.1 (crack 12). The second void was initiated in the ferrite phase, with limited growth to the final fracture. Both voids were initiated under a global strain rate of 0.26. Furthermore, the third and fourth voids were nucleated along the ferrite grain boundaries, where the strain value at initiation was 0.3.

Table 5. 2 Explanation of the formation of ferrite voids through deformation under the stress–strain curve. Image 1 is the reference microstructure. Image 2 indicates the ferrite void location just before it appeared, as shown at image 3.

Voids	Interruptions for microstructure observation	Global stress/strain curves
1	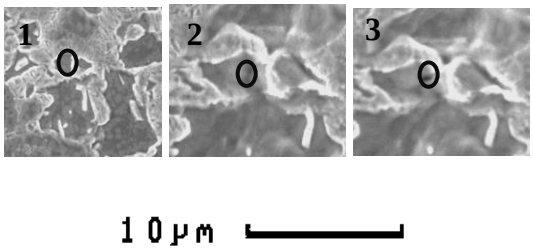	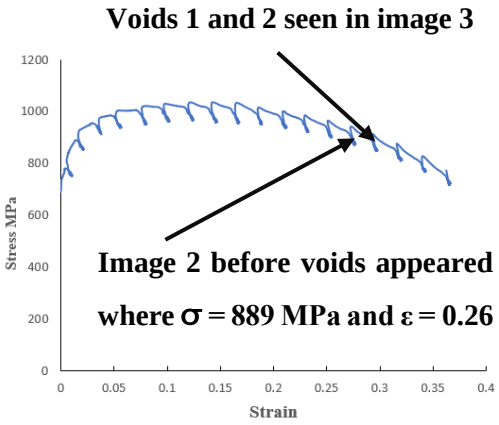
2	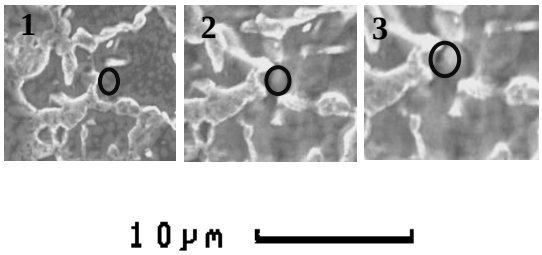	
3	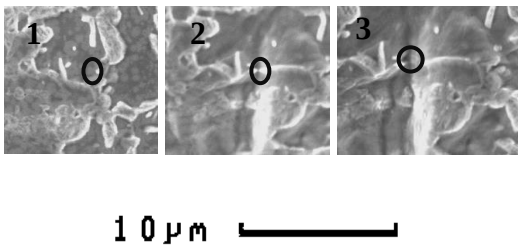	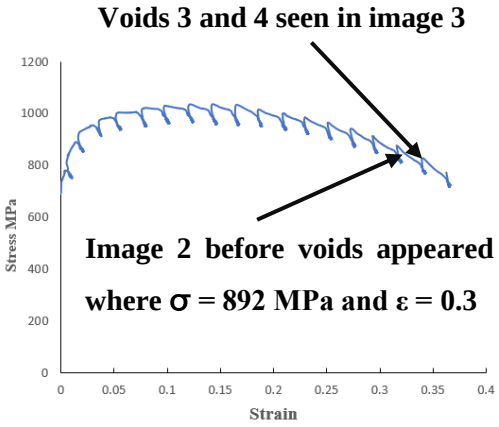
4	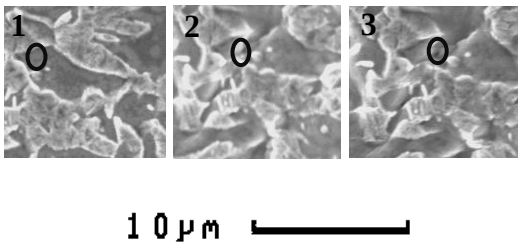	

5.2.3 Plastic deformation strain measurement of DP1000 microstructure using Micro scale DIC

It was necessary to continuously study the occurrence deformation and damage to the microstructures using DIC. The contrasting strain evolutions in the ferrite and martensite phases are shown in this section, with the strain in both phases being analysed in different specific areas, in addition to the overall microstructure. E_{xx} corresponds to the Lagrangian strain component along the tensile axis, which is horizontal in terms of its images.

As seen in Fig. 5.7, the highest strain localisation value started appearing early in the ferrite region, and the global strain rate of 0.01 was the first point in the plastic region corresponding to the deformation band in the ferrite, as seen in Fig. 5.4.

The strain map in this figure is superimposed on the deformed microstructure's SEM micrograph. As seen in Fig. 5.7, a peak strain value of nearly 1.8% was observed, mostly in the ferrite grain areas. By contrast, minimal values were seen in the majority of the martensite regions, as predicted. Two martensite regions also recorded high localised strain values, due to their close proximity to ferrite areas with high localised strain values.

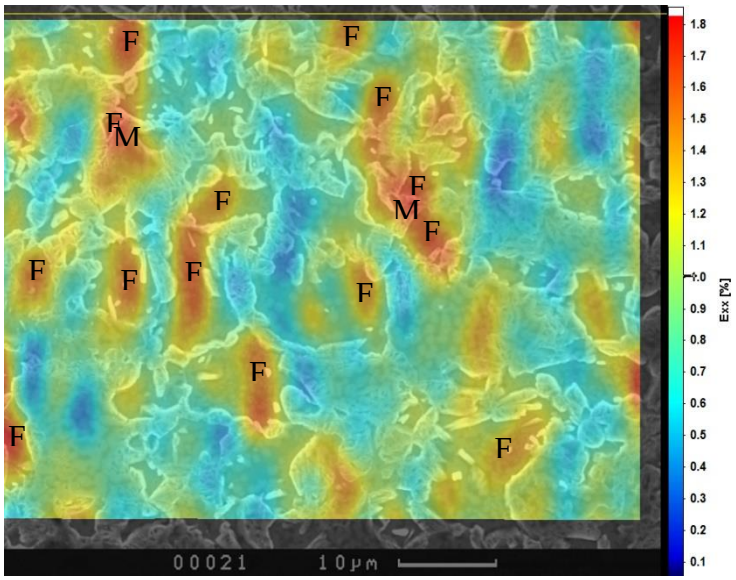

Fig. 5. 7 Strain distribution at the first point of plastic deformation.

Fig. 5.8 shows an example of the microstructure, and the deformation of DP1000 during the SEM tensile test, with the local tensile strain component (Exx) distribution measured using DIC at the UTS of 1053 MPa with an applied global strain value of 0.13. A high value for strain localisation is shown in areas 1 and 3 in Fig. 5.8. The strain values in the ferrite areas were generally higher than those in the martensite areas. In this figure, areas 1 and 3 are revealed to have the highest strain value, especially in the ferrite, and so it is anticipated that damage might have been initiated in areas 1 and 3. The highest localisation strain value was 31%, so it was interesting to follow the strain pattern before and after the UTS.

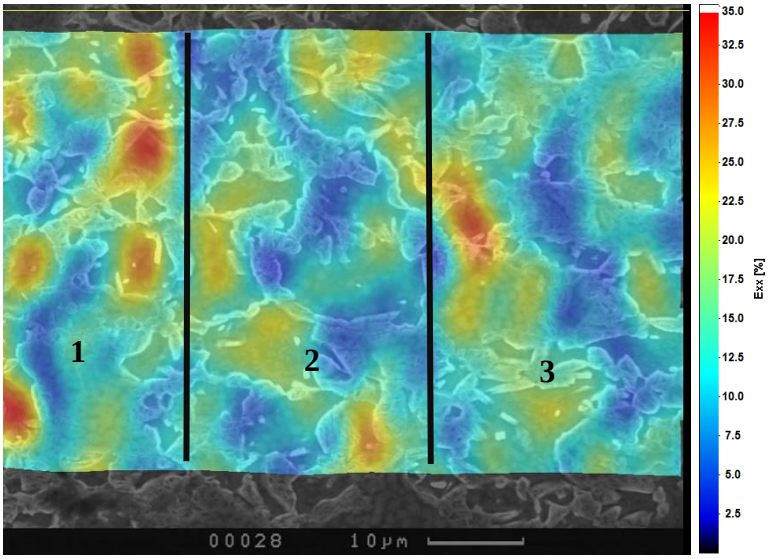

Fig. 5. 8 The deformed microstructure at UTS after the application of 0.13 global strain. The image shows the tensile strain component distribution measured with DIC.

The localisation of deformation that occurred within the microstructure can be observed clearly at the applied strain of 0.11 within a 45-degree deformation band (in the oval shape), as shown in Fig. 5.9. The rectangle shows the highest localised region, where it was expected that microcracks and voids may appear.

Fig. 5.10 shows the strain maps produced through DIC after the strains of 0.18 (a) and 0.33 (b) were applied. Fig. 5.10 also shows that the localised bands of deformation intensified as the applied strain increased to the end point of the test; the local strain values in the ferrite phase reached 55% at 0.18, and 250% before the final fracture. Strain values as low as 10% were recorded in both phases, with the majority occurring in the martensite. This finding also indicates significant heterogeneity of deformation within each phase. These bands were initiated within the ferrite before crossing the martensite islands as part of their development phase.

The largest strain to intensify the bands at the applied strain of 0.33 is depicted in the highlighted areas (values of up to 220% and, at the maximum, 230% localisation strain).

The rectangle on the DIC map shows the localisation of high strain, which started before the UTS was reached and remained until the final fracture. It is therefore anticipated that damage would form in that region.

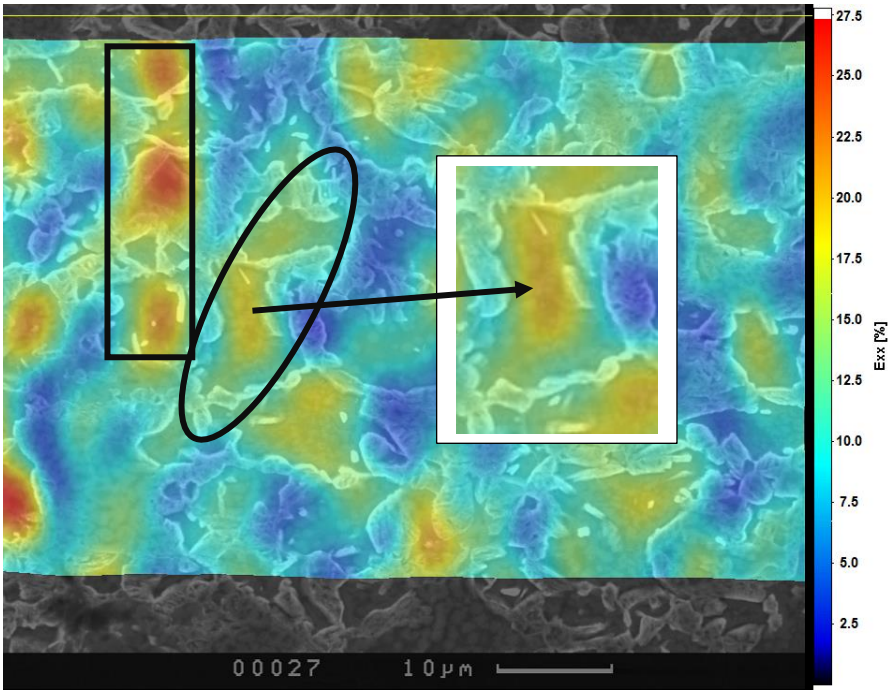

Fig. 5. 9 Map distribution for 0.11 global strain.

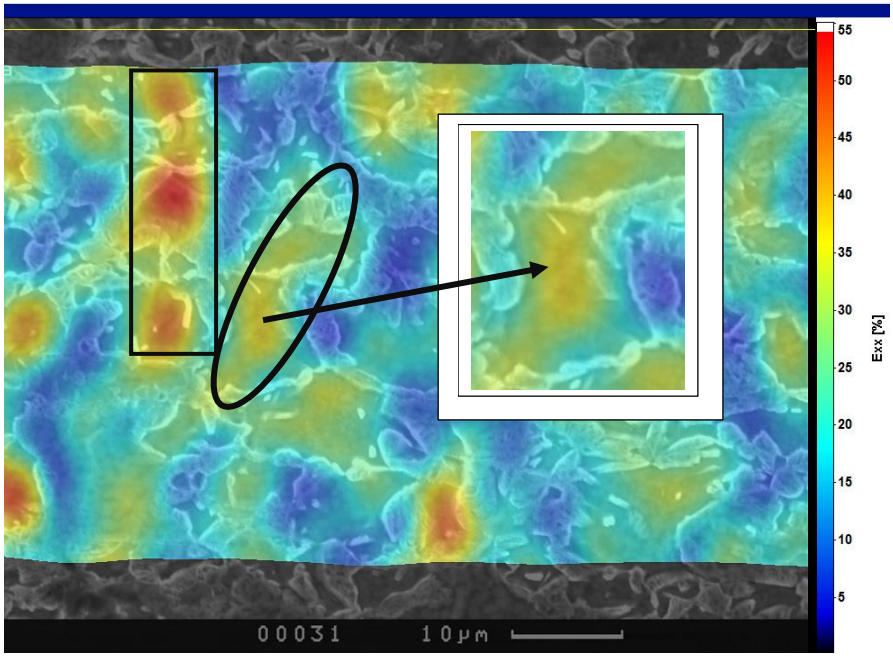

(a)

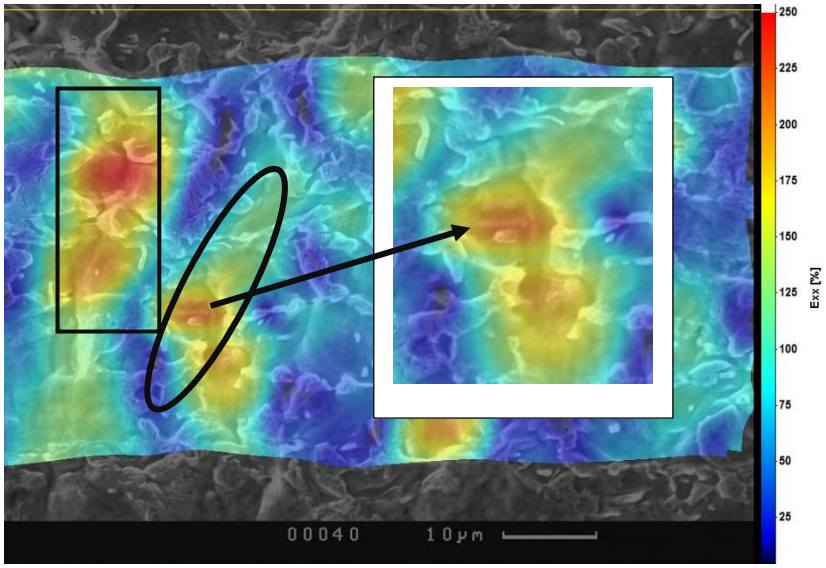

(b)

Fig. 5. 10 Distribution of microstructure strain: (a) 0.18 global strain; (b) 0.33 global strain.

With the frequency distribution of the strain values in these phases, Fig. 5.11 details the graph for the two phases separately. The strain distribution results were obtained at the UTS. This figure was obtained by combining the DIC results with finite element simulations at the UTS. The combination method was used to extract each item of data individually and separate the martensite and ferrite phases to determine the frequency distribution. DIC was used to draw the strain map on the microstructure. Two MATLAB scripts (Alharbi, 2015; Davis, 2010) were used to mesh the microstructure and map the DIC strain values onto this meshed microstructure, as explained in Fig.4.4. Then, a finite element (FE) simulation software (Abaqus) was used to deform the microstructure to extract details of the strain distribution. The ferrite and martensite properties were defined separately in the FE simulation according to the flow curve, as shown in the next chapter (Fig.6.11(a)). After this, the strain map results for the FE simulation were compared with the DIC strain distribution, as explained in the following chapter.

The data for each phase can now be determined by illustrating the frequency distribution. These findings are categorised according to the phase (martensite or ferrite). The histograms indicate that the martensite and ferrite deformed to similar levels, and the mean value for the ferrite (11%) was slightly higher than that for the martensite (10%). The histograms also indicate that these materials have a similar strain heterogeneity.

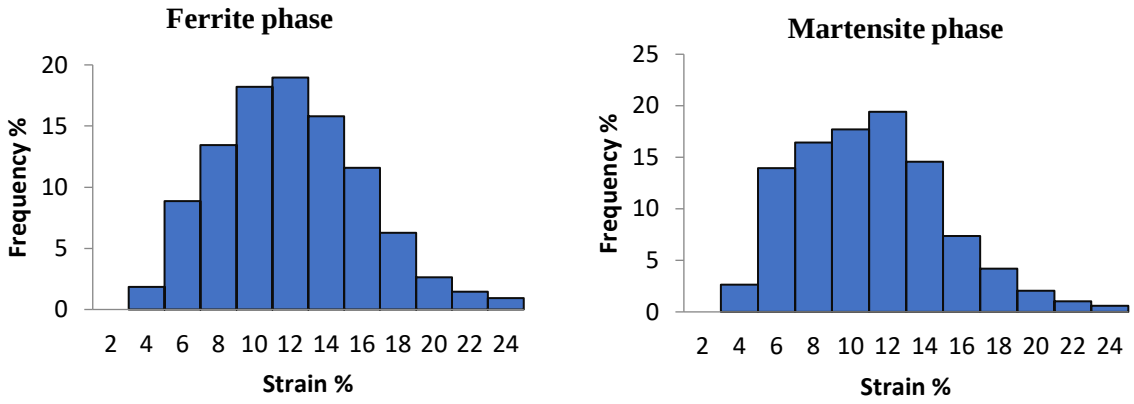

Fig. 5. 11 Comparative histograms for strain values for ferrite and martensite.

To quantify the evolution of strain distribution during the tensile test, further frequency distribution graphs were drawn before and after the UTS. The localised strain value reached 200% for the applied strain of 0.36 before the sample failed. Figure 5.12 show the average strain in both ferrite and martensite phases against the average strain calculated over the area of the microstructure analysed with DIC to study the evolution of strain partitioning before UTS, at UTS and after UTS. Results show similar strain partitioning between the two phases with slightly higher average strain recorded in the more ductile ferrite phase.

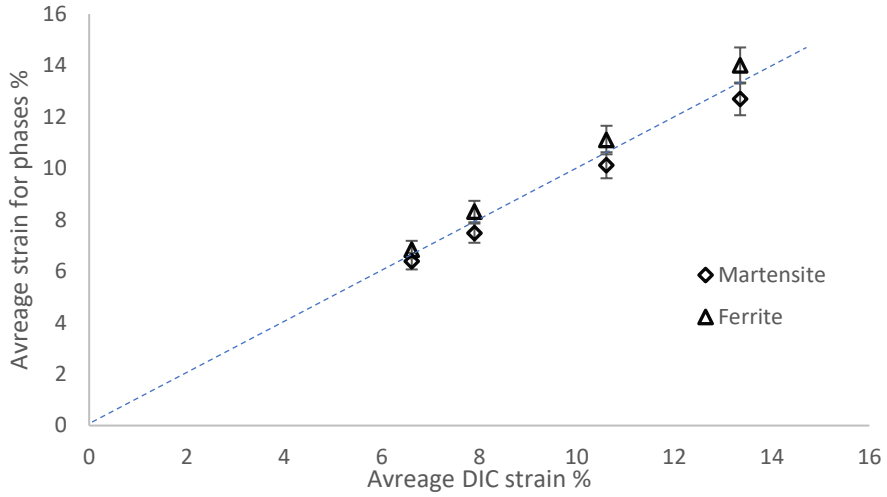

Fig. 5. 12 Evolution of strain partitioning between ferrite and martensite throughout an in-situ tensile test.

5.2.4 Strain analyses of the onset of martensite microcracking and ferrite void nucleation using DIC

The images were captured at high magnification in the SEM throughout the tensile test to advance understanding of the martensite cracking and ferrite void formation processes. In the previous section, the microcracks were analysed relative to the overall stress–strain curve. In this section, the DIC strain results were studied for insights into the deformability and damage mechanisms.

Table 5.3 shows strain distributions immediately prior to the martensite cracking. The first crack appeared when the martensite deformed with the local strain value of 8.8%, which was very close to the region experiencing the highest strain. The majority of the cracks happened as a result of ferrite deformation close to the ferrite martinsite interface; e.g., cracks 3, 5, 6, 7, 8, 11,12, and 13. The local strain value for crack 6 was 18%, which was close to the 20% strain value of crack 3. Cracks 5 and 7 also occurred close to the maximum ferrite strain value, with strain values of 31% and 48%, respectively. Crack 12 formed after a local strain value of 148%. Cracks 8 and 13 formed close to the maximum strain value, which was located on the ferrite.

Therefore, the maximum strain value for the ferrite phase could affect and cause fracture close to the martensite. The strain values for these cracks were 33% and 110%, respectively.

In cracks 2, 4, 9 and 10, the martensite fracture occurred when the strain localisation value was neither at its maximum nor at its smallest value, and cracks 2 and 4 appeared at strain values of 15% and 20%, respectively. Cracks 9 and 10 had 32% and 29% strain values, respectively, and were present before microcracking could be seen in the martensite.

In conclusion, the maximum strain value in the ferrite phase might have caused the martensite to crack, as it was very close to this ferrite area. Furthermore, even though the global strain continued to increase, the majority of the localised strain values resulting in cracking were between 15% and 33%.

Table 5. 3 Strain distributions in relation to the onset of the martensite cracking, as measured by DIC. Red arrows indicate the martensite fracture location. Black arrows indicate the DIC measurement strain localisation value before each crack appeared. Blue arrows indicate the maximum ferrite value located close to the martensite fracture.

Crack	Strain localization Exx measurement before martensite cracking
1	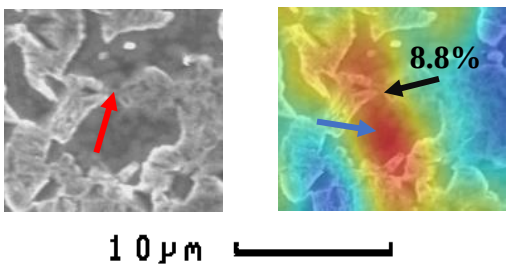
2	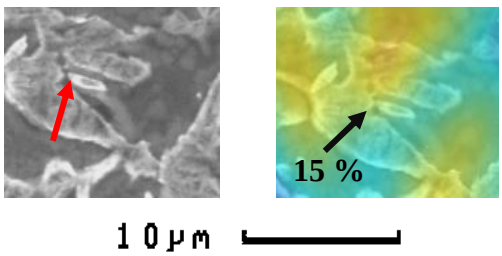

3	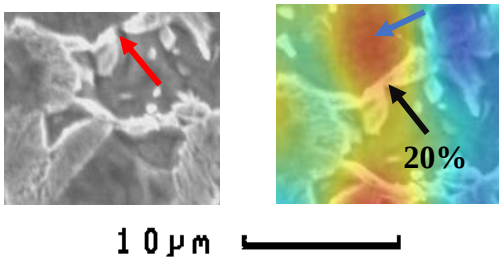
4	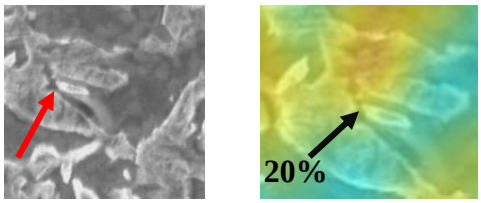
5	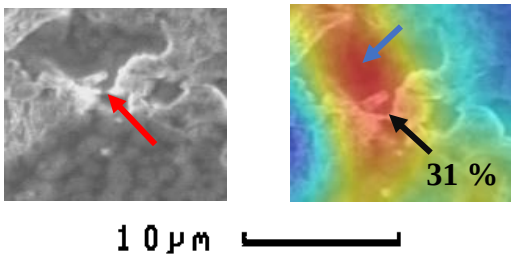
6	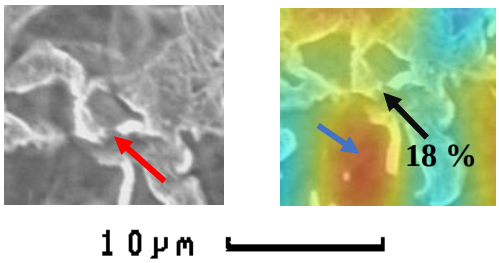
7 and 8	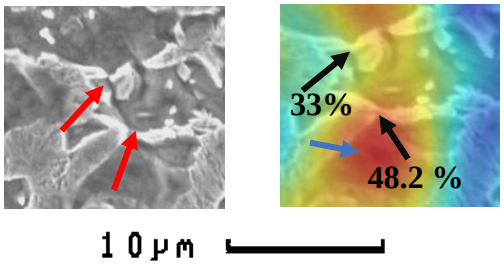

9	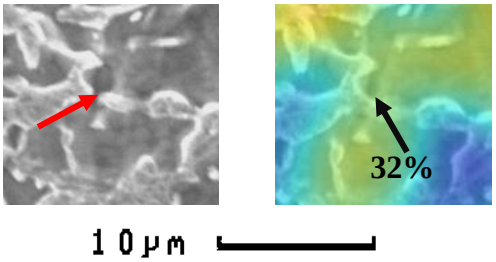
10	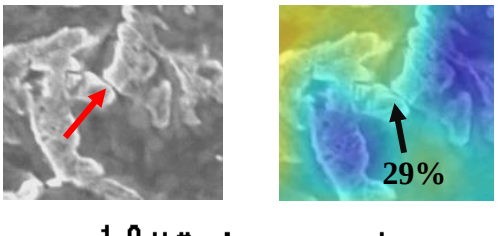
11	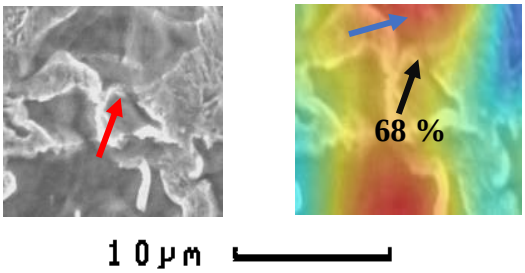
12	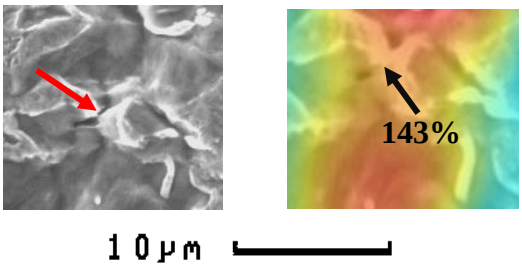
13	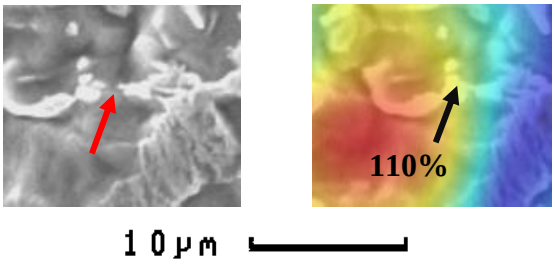

Strain distributions leading to ferrite void formation were also measured with DIC. Table 5.4 shows the local strain distributions just prior to void initiation in the ferrite region. Voids 1 and 2 were located in different regions, but had the same localisation strain value of 104%. Void 3 was initiated at the highest strain value, which was very close to the maximum localisation strain of about 141%. Voids 3 and 4 formed at a global strain value of 0.3, but the local strain value for the onset of void 4 formation was only 75%. It is noteworthy that, although the values were situated in the ferrite phase, they were extremely close to the interface, positioned alongside the martensite.

Table 5. 4 Ferrite voids measured by DIC. Red circles indicate the ferrite void location in the microstructure. Black arrows indicate the ferrite strain localisation value just prior to void formation.

	Localization strain void measurement
1	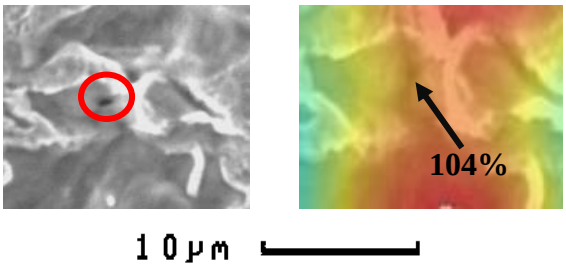
2	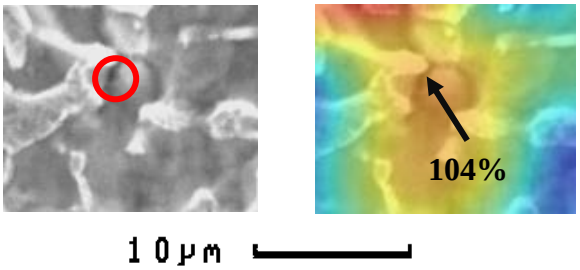

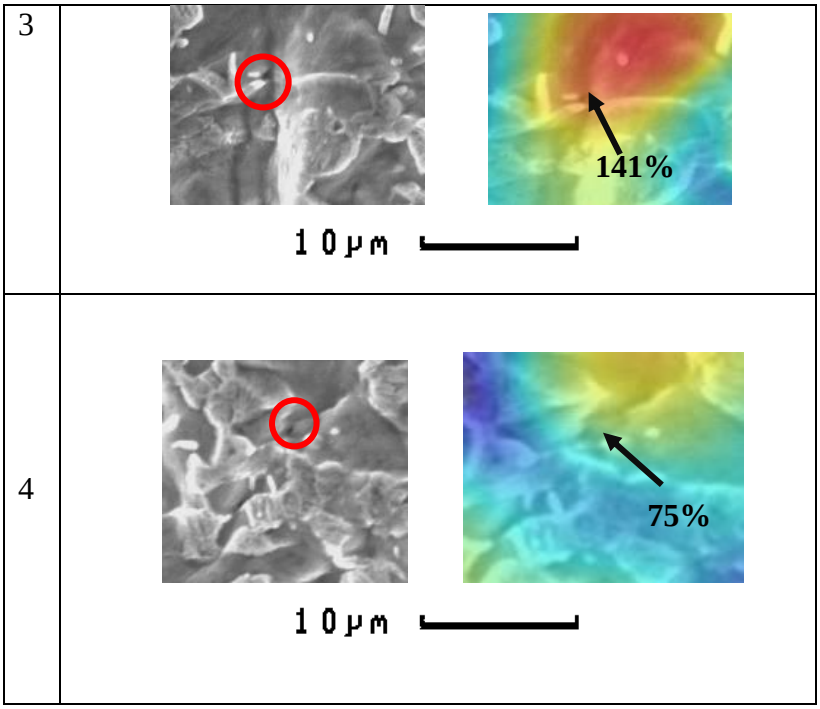

The strain maps in section 5.2.3 seem to show that the localised bands of deformation where strain values are maximum remained in a similar position throughout the test. The maximum strain values, therefore, do not seem to shift location. Eight of the twelve martensite fractures near the ferrite area were located at the point of maximum strain. The ferrite phase therefore affects the formation of cracks in the martensite islands as a result of plastic deformation.

Fig. 5.13 (left) shows that the majority of the local strain values at the onset of the martensite fracture increased with the global strain. The graph shows a clear correlation between the local and global strain values with most martensite cracking occurring within a global strain range that corresponded to the region around the UTS point in the stress strain curve. This is confirmed by the graph on the right-hand side. Fig. 5.13 (right) shows the graph for global stress as it corresponds to the martensite fracture values, and compared to the local DIC strain, in which the majority of the martensite's cracks were located around the UTS point.

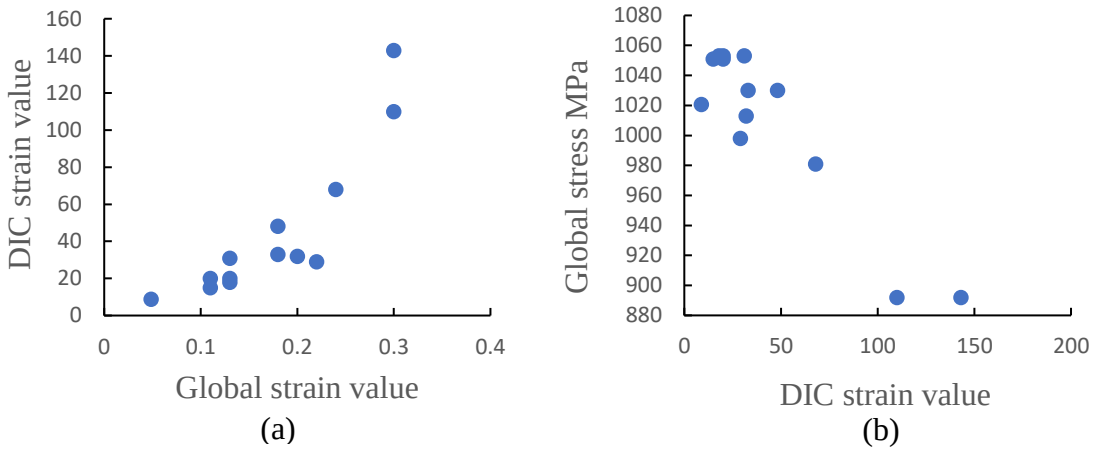

Fig. 5. 13 (a) shows the global strain value against local DIC strain values on the left curve and (b) the global stress value (MPa) against the local DIC strain value on the right curve.

5.3 Formability tests for DP1000

Due to the exceptionally limited amount of damage propagation observed at the surface of the specimen during the tensile test carried out in the SEM, punch tests were conducted to enhance understanding of the deformation and damage development in DP1000. An existing macro-punch test, which had previously been developed in the Department (see chapter 3) was conducted first, but limitations of this test in terms of the available microstructural observations led to the development of an SPT in this work. The results are presented in the following sections.

5.3.1 Punch test using optical 3D DIC

5.3.1.1 load displacement curve of punch test

The macro punch test was conducted using the 90-mm-diameter sample. The displacement control of the 100 KN Mayes machine was 1 mm per minute. The DIC recording commenced when the Mayes machine started operating, and the test stopped once the load curve had dropped. Fig. 5.14 (a) details the cracks observed on the sample at the end of the test. Fig. 5.14 (b) shows the average load–displacement curve in this sample. The maximum load was 25.6

KN, whereas the tool's displacement reached 11.2 mm before the sample failed. This test therefore achieved the aim of generating damage development in DP1000 up to the point of failure.

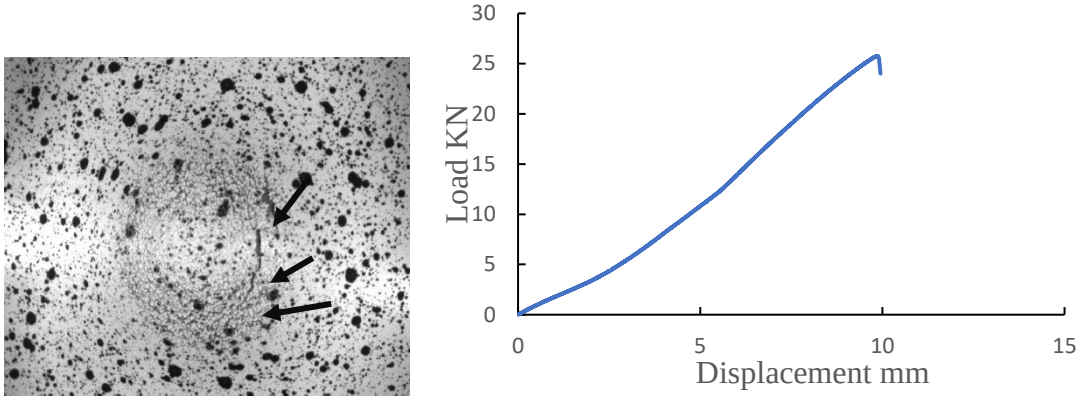

Fig. 5. 14 (a) Sample after failure, with black arrows indicating cracks; (b) load–displacement curve for the macro punch test.

5.3.1.2 3D DIC analysis of punch test

3D DIC, used in conjunction with the punch test, provides information about any deformation on the sample surface. Two 3D cameras were affixed to the rig of the punch test equipment to conduct the 3D DIC; these were focused on the centre of the sample. The cameras captured all the images throughout the test. The correlated solution VIC-3DIC DIC software then processed all the images to generate information about deformation and strain distribution for each sample.

Fig. 5.15 depicts the deformation results recorded using 3D DIC in the Z direction. Fig. 5.16 shows the maximum displacement in the Z direction. A comparison of the machine and the DIC Z-direction displacement reveals that applied machine displacement was higher than the DIC value, as measured on the top surface of the specimen, with the difference being

approximately 1.25 mm. These results emerged from our observations of the maximum displacement values before the cracks appeared on the surface.

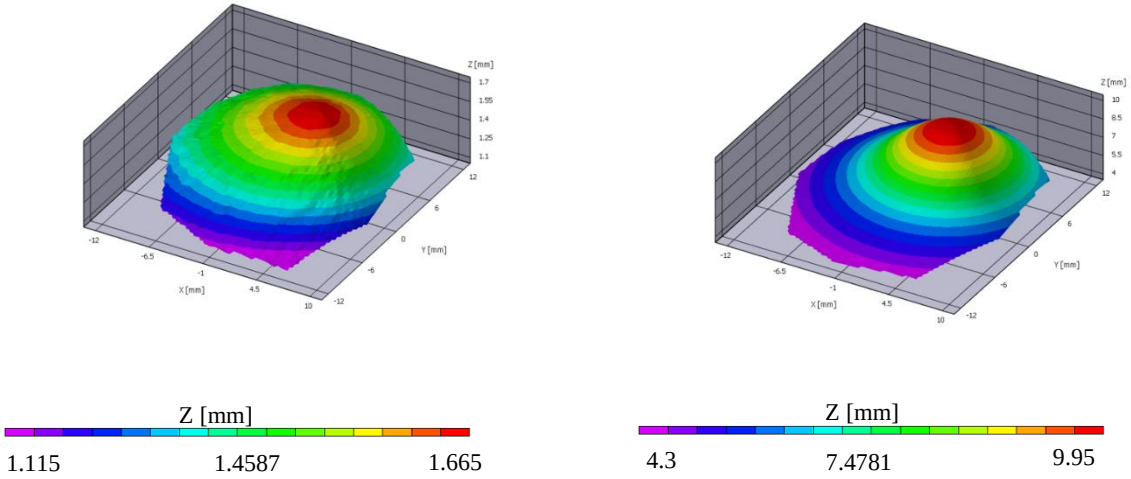

Fig. 5. 15 3D DIC results of the out-of-plane displacement in the Z direction, through the beginning of the deformation process and before the appearance of a crack.

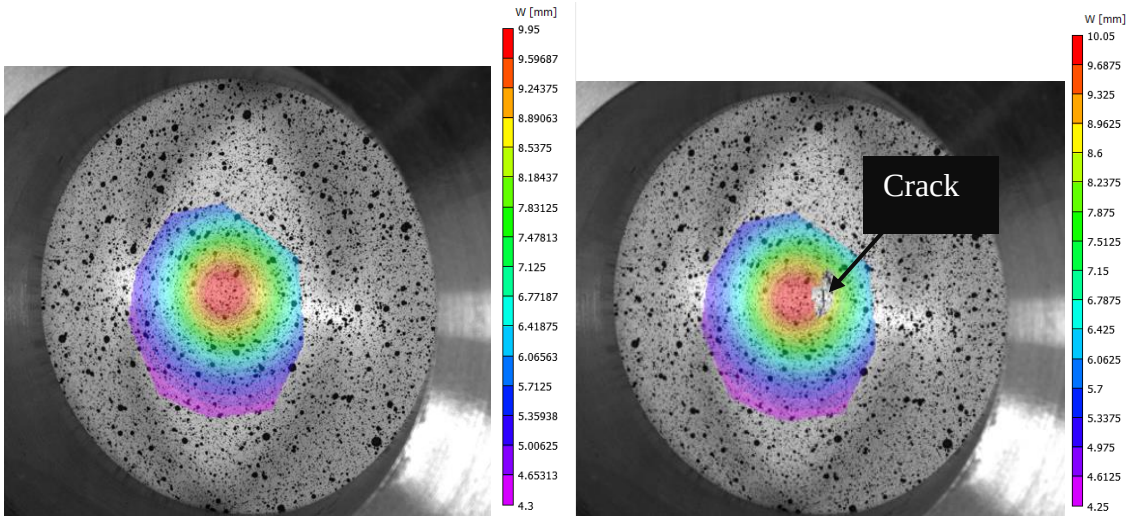

Fig. 5. 16 2D plot of maximum displacement in the Z direction, before and after the appearance of the crack on the surface.

Fig. 5.17 shows the evolution of strain Exx distributions at the surface of the sample, immediately before the crack appeared. The high strain values were concentrated uniformly around the centre of the specimen. As deformation increases in the two regions of high strain, the values move from the centre of the specimen to the side of the dome of deformation (see

Fig. 5.17). This image was captured before the fracture occurred in the region of highest strain values, where the maximum local strain value was 0.456.

The Appendix VIII figures VIII.1 (a) to (f) shows the results of the deformation of the punch test. From the first image onwards there was no contact between the sample and the punch tool. Plastic deformation started to occur as the tool began to contact the sample, but this was still not visible on the surface, where the local strain (Exx) value reached 0.0098. The load and strain distribution increased and deformation became more localised around the tool tip, producing a local strain value of 0.174.

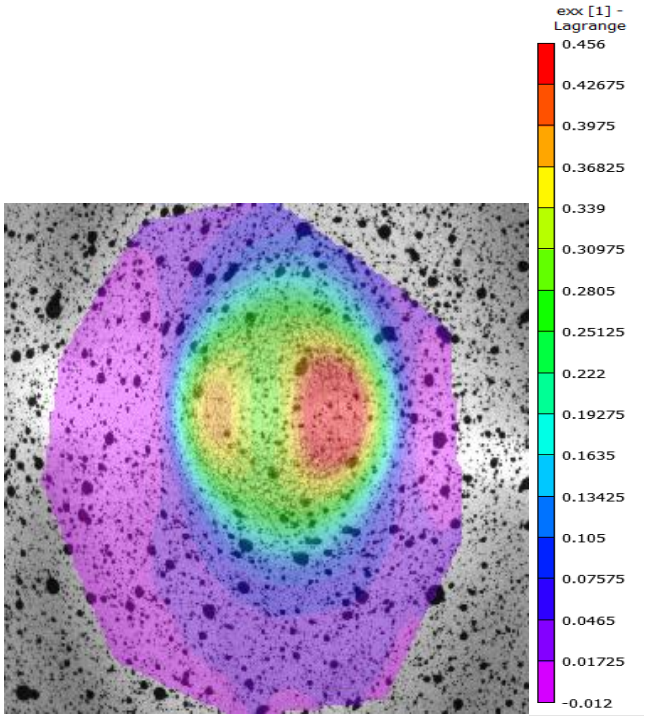

Fig. 5. 17 Lagrangian strain distribution results (Exx) for the punch test deformation.

The DIC software can output different strain results, namely, strain along the X direction (Exx), strain along the Y direction (Eyy), shear strain (Exy), and maximum and minimum principal strains (e1 and e2, respectively), as well as the equivalent von Mises strain. Fig. VIII.2 in the Appendix VIII shows all these results just prior to material failure. Table 5.5 shows the comparative strain results that were obtained.

Table 5. 5 Maximum Lagrangian strain results before surfacing of crack.

Exx (Strain along x axis)	Eyy (Strain along y axis)	Exy (Shear strain)	V.M. (Von Mises strain)	e1 (Maximum principal strain)	e2 (Minimum principal strain)
45.6%	43.2%	6.4%	43.6%	50%	30%

While the tensile test provided details of uniaxial loading, the punch test explains biaxial loading. For insights into the loading, Fig. 5.18 plots the maximum principal strain (e1) with respect to the minimum principal strain, and the resulting curve shows the punch test applies loading conditions that are close to equi-biaxial loading.

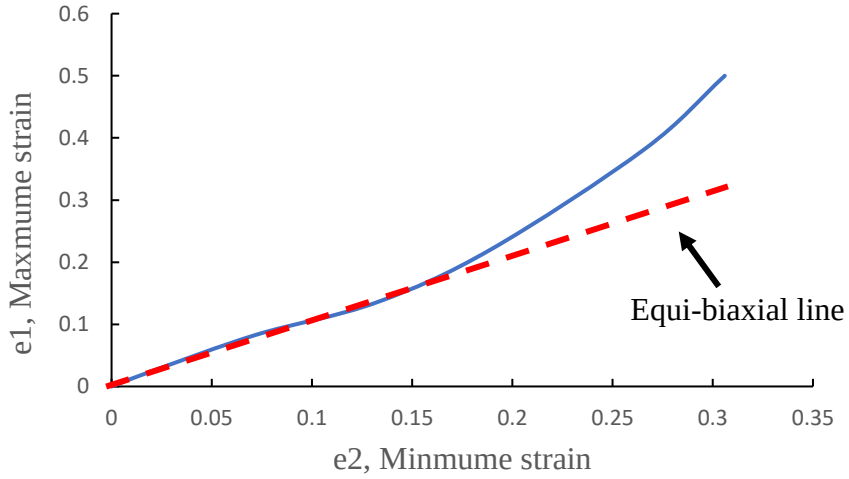

Fig. 5. 18 Maximum principal strain e1 against minimum principal strain, e2 showing biaxial loading as it applied during the punch test.

5.3.2 Small punch test analysis using micro scale SEM and 3D DIC

5.3.2.1 Microstructure deformation and damage

Although the macro-punch test provided the means to study the failure process as it affected DP1000 under loading conditions, these were more representative of forming operations than the uniaxial tensile test, and analysis of damage development leading to failure at the scale of the microstructure proved very difficult, due to the large specimen size.

A new small punch (SP) test was therefore designed and manufactured (see chapter 3) to study damage development in DP1000. The test was regularly interrupted, and the small specimen of 30 mm in diameter was transferred to the SEM chamber to observe the microstructure.

The SP test was conducted using a 100 kN Mayes machine, and the microstructure was observed using an inspect F SEM, as mentioned in Chapter 3. Fig. 5.19 shows the load–displacement curve for the test, and where the test was interrupted to photograph the microstructure. The test was interrupted twice; the first time was after 1.12 mm displacement was applied, and the second after the application of 2.6 mm displacement. Fig. IX.1 in Appendix IX shows the sample after the test was stopped for the second time. No crack was visible on the surface of the sample, but the microstructure had become totally deformed and damaged.

Table 5.6 shows examples of three microstructure locations that were damaged through the SEM SPT. Prior to the test, the sample was polished and etched to reveal the microstructure. The reference images in Table 5.6 show the undeformed microstructure located at the tip of the deformation dome centre of the red rectangle in fig.IX.1, as shown in the Appendix IX. After 1.12 mm displacement was applied to the specimen, two small cracks appeared in the ferrite area, as shown by the blue arrow in Case 1 in the table 5.6. Cases 2 and 3 in table 5.6 show the

ferrite deformation close to the ferrite martensite interface, leading to the martensite to crack. This mechanism agrees with the second mechanism in the situ tensile tests (see table 5. 1).

The third column in the table 5.6 shows the microstructure after 2.6 mm displacement was applied. This provides information about the deformation and damage in the microstructure before the macroscopic crack appeared on the surface of the sample. In case 1, the image shows evidence of the very large deformation of the microstructure at this point in the punch test. The crack propagated horizontally in the image (highlighted by the red rectangle), crossing martensite areas and continuing to spread. The complete images of the microstructure, highlighting damage in the ferrite and martensite, are reported in the Appendix IX figures IX.2 , IX.3, and IX.4.

The load–displacement curve (Fig. 5.19) shows the maximum displacement to failure for the SPT was less than that for the macro punch test. In accordance with the references (Abendroth & Kuna, 2003; Martínez-Pañeda, Cuesta, Peñuelas, Díaz, & Alegre, 2016; Simonovski et al., 2017) , the curves in Fig. 5.19 can be divided into three different areas according to the deflection of the material. Region I was defined as an elastic deformation area; II as a plastic deformation region; and III as plasticity and structural instability (fracture region). The graph demonstrates that considerable deformation happened before the crack appeared on the specimen's surface. Based on the observation of the sample, the crack appeared between the displacements of 2.7 and 3.8 mm in the fracture region (III). Large deformation of the microstructure and early damage to the ferrite began in phase II, with damage developing and leading to macroscopic cracks at the start of phase III. In addition, the cracks and high deformation is distinct on the microstructure between displacements of 1.12 and 2.6 mm in the plastic deformation region (II). Comparing the punch test extension value with that of the in situ tensile test, it becomes clear that much greater deformation can

be achieved prior to fracture when using the punch test. This test is therefore best suited to the study of damage development, leading to failure in DP 1000.

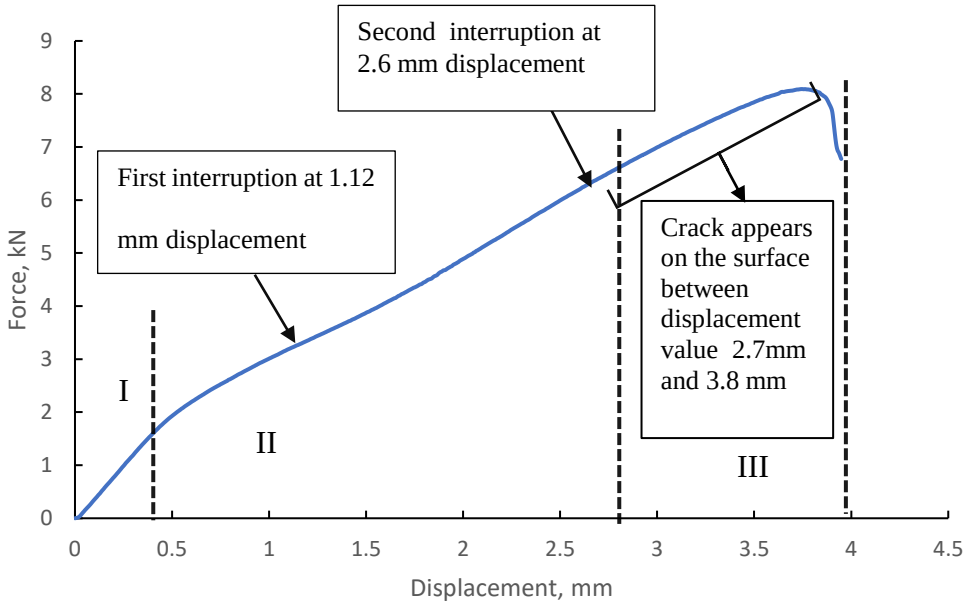

Fig. 5. 19 Load–displacement curve for SPT. Points of interruption during the test are shown.

Table 5. 6 Three locations of microstructures damaged through the SEM SPT.

Number of cases	Reference Image	First interrupted at 1.12 mm displacement	Second interrupted at 2.6 mm displacement
Case 1	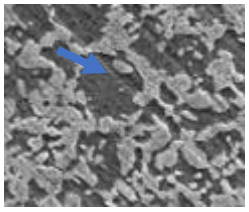	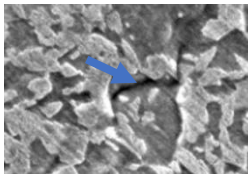	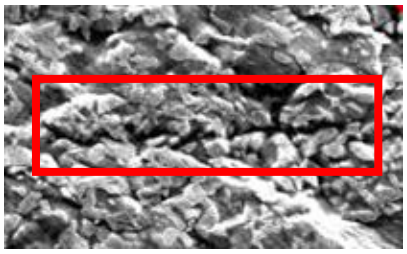
Case 2	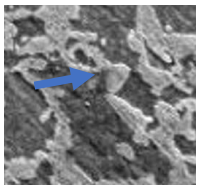	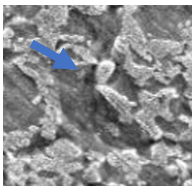	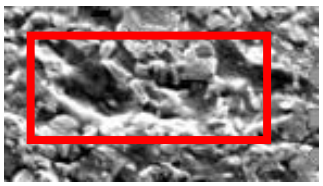
Case 3	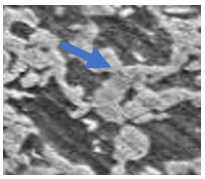	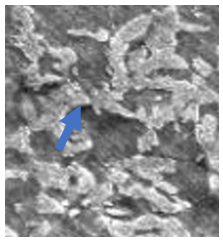	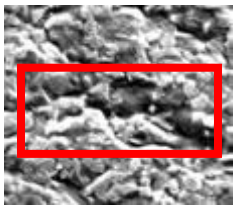

5.3.3 Small punch test study using 3D DIC

A new rig incorporating 3D DIC was designed and manufactured for the SPT (see chapter 3). The cameras used during the macro punch test were arranged in position, and the strain distributions processed by the same Correlated Solutions VIC-3D software.

Evolution of the out-of-plane displacement in the Z direction is shown in Fig. 5.20. The maximum displacement value before and after the sample failed was 2.59 mm, as shown in image (a) and (b). The results show the machine-applied displacement value of the tool was greater than that recorded by DIC on the upper surface of the sample, by about 1.4 mm. This

was because the DIC calculated the deformation results at the surface only, not throughout its depth.

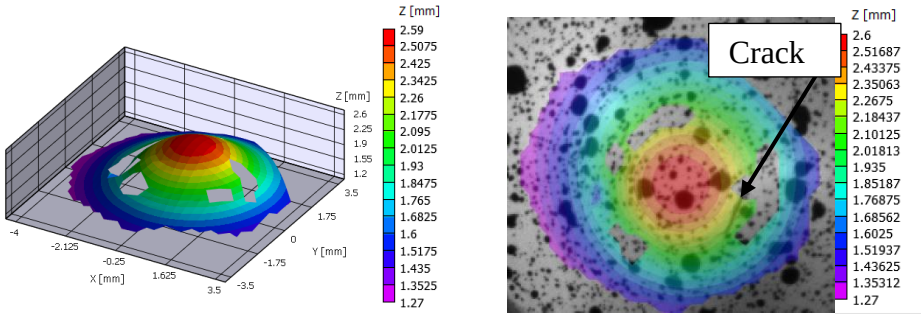

(a) (b)

Fig. 5. 20 (a) 3D DIC results of plan deformation before crack appearance test; (b) Maximum displacement in Z direction after the crack appearance on the surface.

Fig. 5.21 shows the maximum strain for the small sample before the appearance of the crack. The crack was located in the region of the sample where the strain value was around 0.17, which was less than the maximum value.

Additional results describe the undeformed sample prior to contact with the tool. Once the tool contacted the sample a local strain value of 0.00064 was given, as shown in the Appendix X figures X.1 (a) to (f). It also shows the maximum strain Exx value increased, because the deformation grew as a consequence of continual pushing by the punch tool, and the strain value grew from 0.0043 to 0.138. The load continued to increase, and the strain became more localised at the centre of the sample, where Exx was 0.234 just before the crack became visible at the surface.

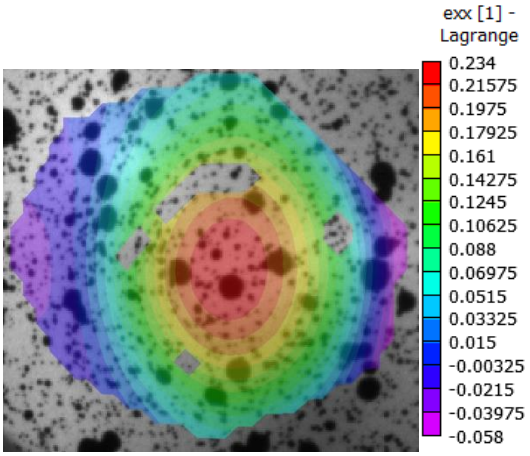

Fig. 5. 21 Strain results of SPT using 3D DIC, before the emergence of crack at the sample of the surface.

Other strain distribution results were for Eyy, e1, e2 and the von Mises strain (and table 5.7). The figures X.2 for all the results were shown in the Appendix X. The results did not show a significant difference in terms of strain distributions, because the deformation was localised at the centre of the specimen for all strain values. The SPT was a continuation of our study investigating deformation under biaxial loading, and as such provided further information about the damage.

Table 5. 7 Maximum Lagrangian strain results before the surfacing of cracks.

Exx (Strain along x axis)	Eyy (Strain along y axis)	V.M. (Von Mises strain)	e1 (Maximum principal strain)	e2 (Minimum principal strain)
23.4%	23.6%	23.35%	23.8%	23.2%

5.3.4 Small punch test using 3D DIC for crack propagation analysis

Crack development in the damaged region of the SPT sample, with DIC is studied by inspecting the thickness of the specimen in this section. First, the paint and speckled pattern resulting from the DIC test were removed, and the surface was then prepared for cutting. An area measuring 5 mm × 5 mm around the location of the damage to the sample was prepared using the Secotom-

-50 cutting machine. The sample was then cut along its centre line, and mounted using conductive backelite, as shown in Fig. 5.22. Subsequently, after being ground, polished and etched, the surface was inspected using inspect SEM.

Fig. 5.23 shows the cross section of the specimen. In the middle of the sample, secondary cracks formed from the main crack, as apparent in region 1. A further secondary crack was observed in region 1a, running mainly across the ferrite region, in between highly deformed martensite islands. Ferrite microcracks also formed below the surface, as shown in regions 2a, 3b, (Fig. 5.23), and (4a-1 and 4b-1 in the Appendix X figs. X.3). Ferrite voids were also found, as shown in regions 3c, 3f, and (4a-2 and 4b-2 In the Appendix X fig. X.3). Therefore, all these observations confirm the hypothesis that crack propagation in DP1000 happens predominantly in the ferrite phase, during the last stage of damage development after extensive deformation of the ferrite. Cracking could not have propagated through the martensite islands because propagation ceased once the martensite islands were initially fractured, as seen in regions 2b, 3d, (and 4b-3 and 5a in the Appendix X fig. X.3).

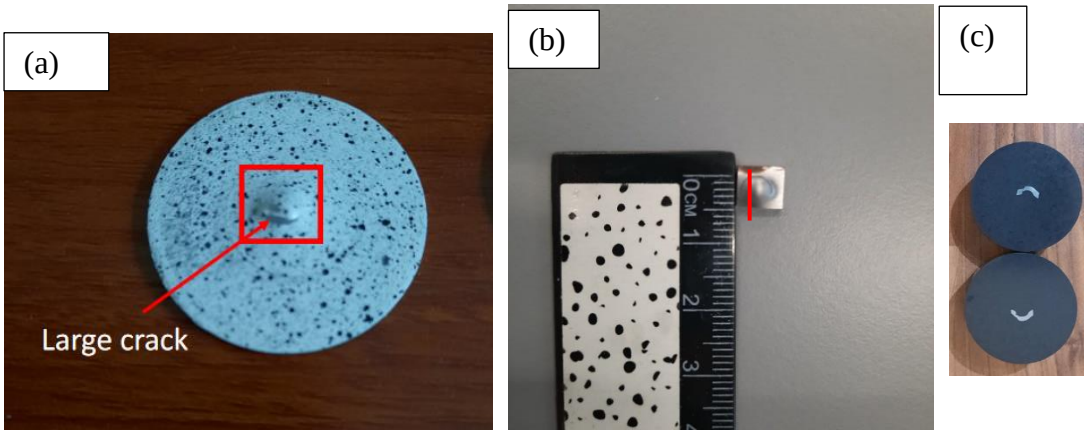

Fig. 5. 22 Images of (a) area cut around the crack, (b) second cut through the crack and (c) samples mounted after cutting for the purpose of observation using the inspect F SEM.

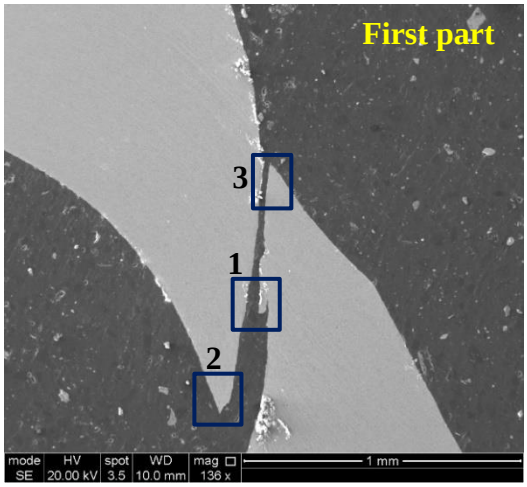
First part
3
1
2
mode SE
HV 20.00 kV
spot 3.5
WD 10.0 mm
mag 136 x
1 mm

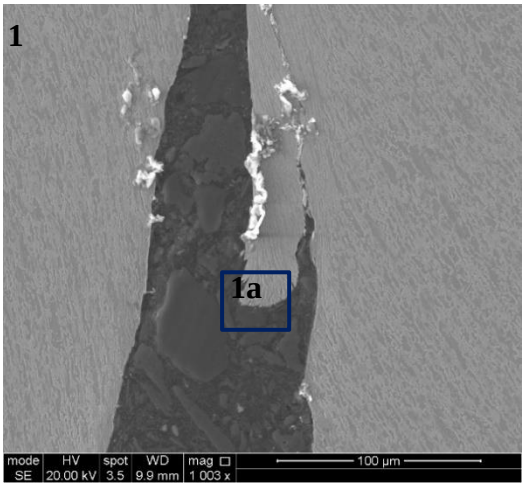
1
1a
mode SE
HV 20.00 kV
spot 3.5
WD 9.9 mm
mag 1 003 x
100 µm

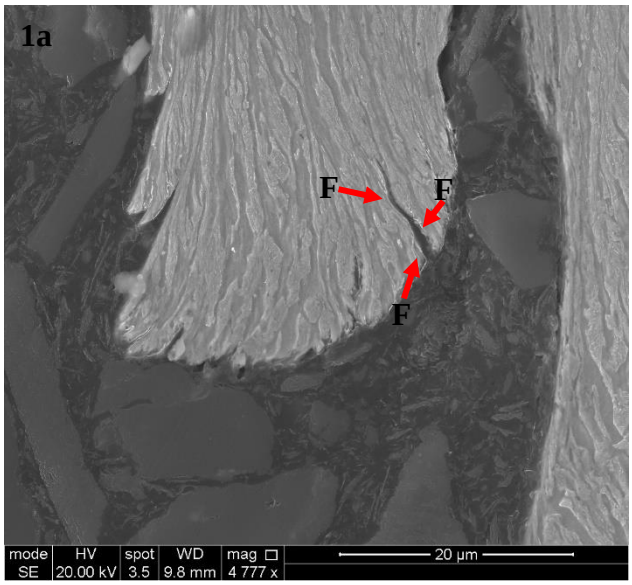
1a
F
F
F
mode SE
HV 20.00 kV
spot 3.5
WD 9.8 mm
mag 4 777 x
20 µm

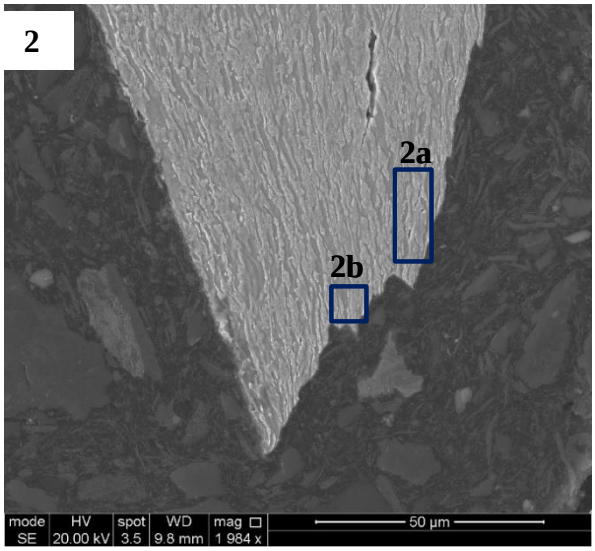
2
2a
2b
mode SE
HV 20.00 kV
spot 3.5
WD 9.8 mm
mag 1 984 x
50 µm

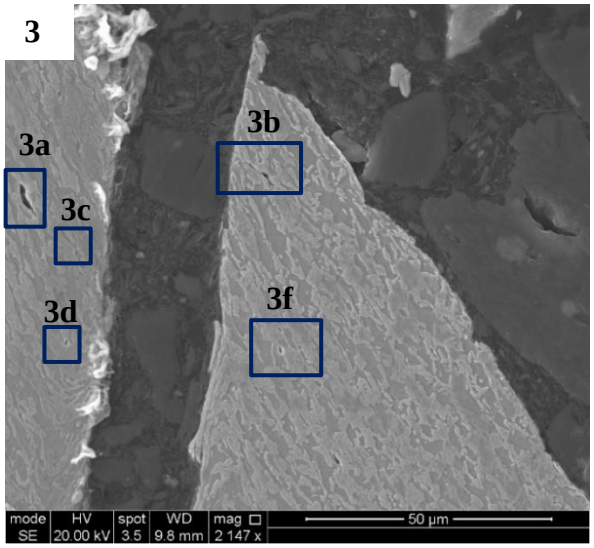
3
3a
3b
3c
3d
3f
mode SE
HV 20.00 kV
spot 3.5
WD 9.8 mm
mag 2 147 x
50 µm

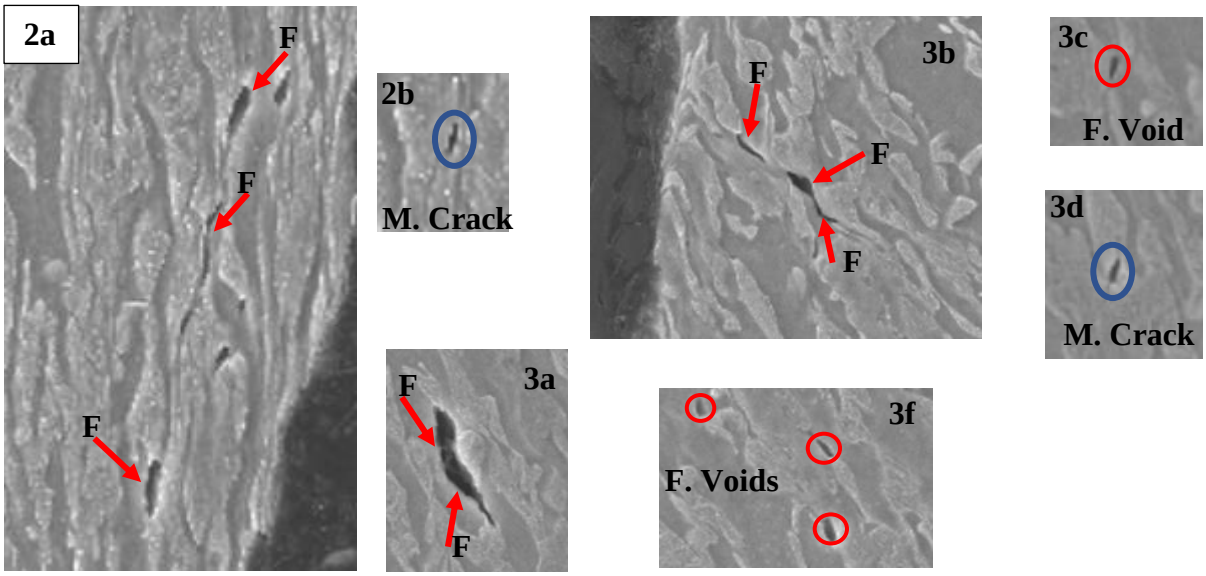

Fig. 5. 23 Results of crack inspection in the areas of the first of the SPT after the 3D DIC sample was fractured throughout its depth.

Images in Fig. 5.23 provide further evidence of the final stages of crack propagation, which resulted in the failure of the sample. The largest opening along the main crack reveals the crack was initiated at the surface in contact with the tool. It was then propagated through the thickness of the sample, and appeared at a later stage on t he upper surface where strains were measured using DIC.

5.4 Bending test of DP1000 using micro bending stage results

Due to the limitations of the punch test, as reported in the previous section in terms of studying the final stages of the failure of the specimen (final crack initiating below the top surface of observation and at the contact surface with the tool), a new bending test inside the SEM, which became available towards the end of the PhD research stage was considered. The three-point bending test geometry is shown in Fig. 5.24 (a). A bespoke specimen geometry (see chapter 3) was used to promote cracking at the surface, where SEM observation tales place (Fig. 5.24 (b), (c) and (d)). The bending test was conducted in a manner way to the in-situ tensile test, with regular interruptions to capture images, that could then be processed with the DIC to measure

strain distributions within the microstructure. The test was interrupted after every 0.25 mm change. Fig. 5.24 (a) shows a low-magnification image of the specimen after the appearance of cracks at the surface under maximum tensile stress (shown under higher magnification in Fig. 5.24 (b), (c) and (d)).

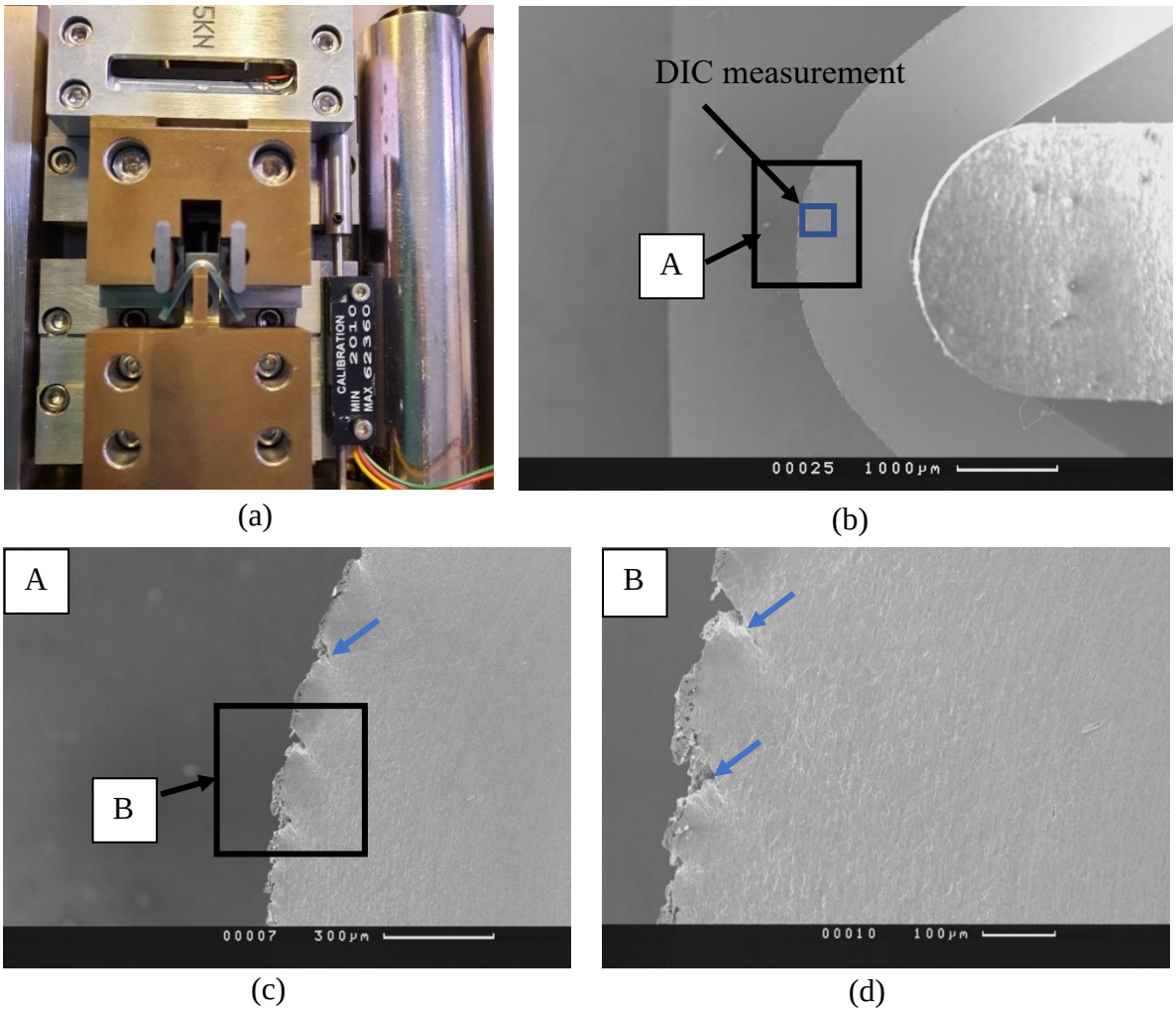

Fig. 5. 24 (a) Bending test geometry with (b), (c) and (d) cracks appearing following a large deformation. The black rectangle highlights the region where the cracks appeared (blue arrows), with the blue rectangle in (b) highlighting the region of the microstructure analysed using DIC.

A small region of the microstructure, as highlighted by the blue rectangle in Fig. 5.24 b was analysed using DIC to determine the process of damage development in relation to the distribution of strain across the microstructure. Fig. 5.25 a displays the original image of the

sample (before any loading was applied), with the dashed lines X and Y highlighting where the band of deformation would occur during the test (to be presented in section 5.4.1).

The circles outline in Fig. 5.25 a, c, and d details the area containing the ferrite deformation cracks. An area of martensite is also shown as a dashed-line curve on the black square in the image.

After the application of 1.5 mm displacement (Fig. 5.25 b), the ferrite deformation started appearing in the microstructure, as indicated by blue circles shown in Fig. 5.25 b. The initial non-uniform deformation can be seen in Fig. 5.25 b, in which two deformation bands started forming, with oval red shapes indicating where they were initiated. The ferrite deformed as a result of the ductile deformation of the DP1000, thus breaking down the martensite in the area indicated by the black square, and initiating the fracture of a cluster of martensite islands. With this increase in displacement, the deformation became more local, and the mechanism of damage started to emerge once displacement reached 1.75 mm (as shown in Fig. 5.25 c). The final deformation before the sample fractured can be seen in fig. 5.25 d.

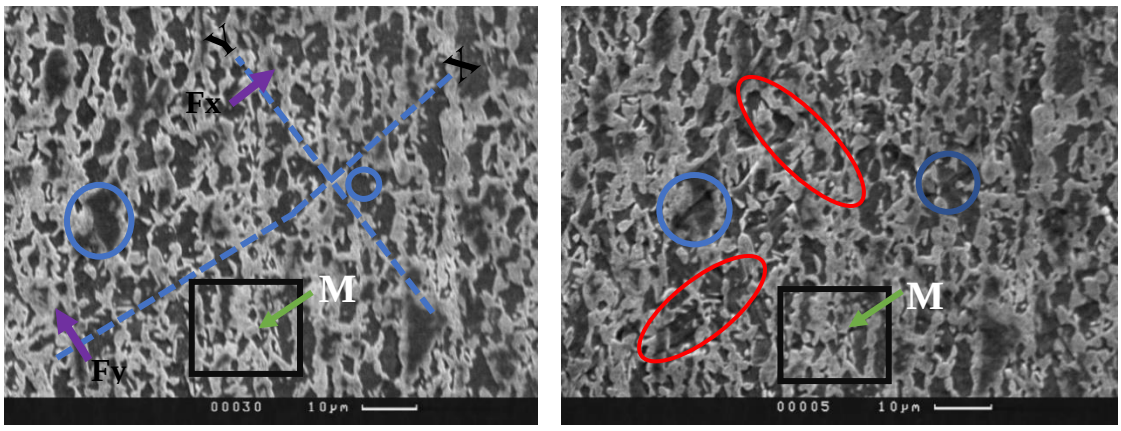

(a) (b)

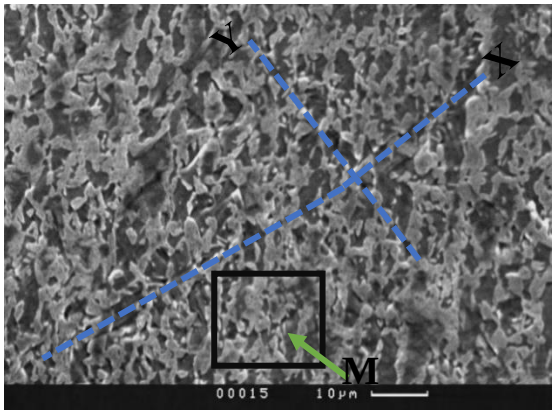

(c)

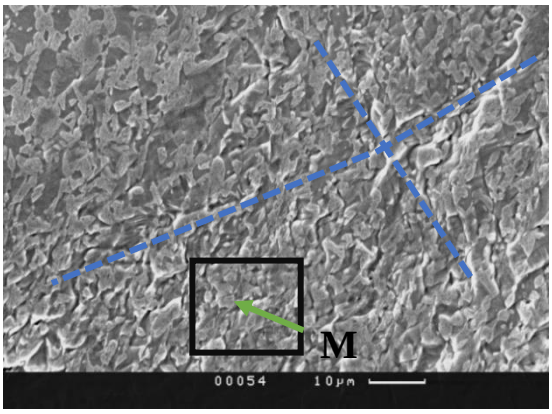

(d)

Fig. 5. 25 Micrographs showing (a) the expected deformation of lines X and Y; (b) initial deformation of both lines (black and red arrows), early deformation in the ferrite phase (blue rectangle and circles) and the continuation of deformation (black squares); (c) continuation of deformation mechanism; (d) stage prior to final fracture.

The dashed lines X and Y in Fig. 5.25 show intense deformation bands. The force of deformation pushed these dashed lines and cracked the martensite and ferrite close to, or at, line X. The ovals in Fig. 5.26 surround the localised lines of deformation and allow the deformation to be observed, without having to actually draw the lines.

The first micrographs show the formation and movement of the lines when the applied force value was 285 N at this level. Fig. 5.26 a shows the deformed lines within the ovals at the point of 3.00 mm displacement, and Fig. 5.4.3b analyses the force that pushed the two lines resulting in deformation. In this calculation, if a 30-degree angle is assumed to exist between forces, then the directional forces for lines X and Y will be:

$$Fx = F \cos(30) = 285 \cos(30) = 245.8 \text{ N.}$$

$$Fy = F \sin(30) = 285 \sin(30) = 142.5 \text{ N.}$$

The force that affected line Y was greater than the force affecting line X. This means the deformation in the X direction was more developed, and the martensite and ferrite present in this direction deformed and cracked more than the islands in the Y direction did, as shown in

Fig. 5.26 a, at the displacement point of 5.5 mm. The formation of additional martensite cracks and ferrite voids is explained in Table 5.8 and the subsequent paragraphs.

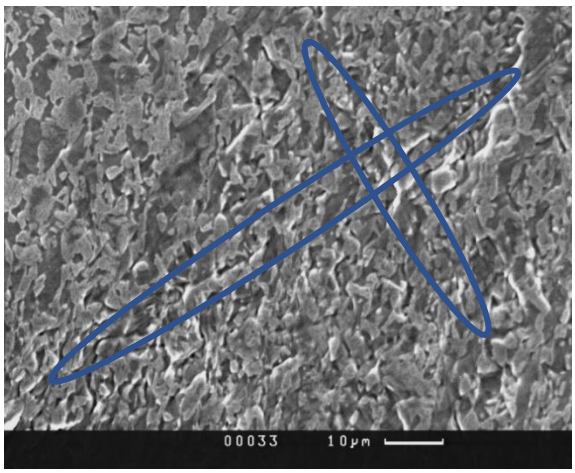

(a)

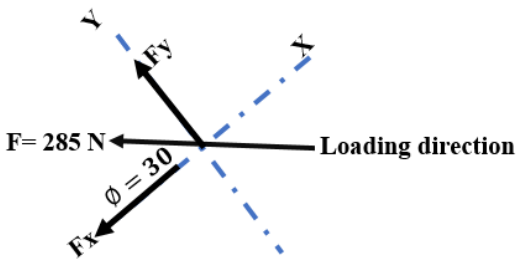

(b)

Fig. 5. 26 Images of the (a) deformation lines (indicated by ovals), and (b) force analysis of the deformation lines X and Y.

Analyses of the bending test showed that martensite cracks appeared at different locations within the same area as that analysed with DIC. These cracks could have occurred because of the high level of ferrite deformation close to the martensite, or directly in the martensite as a result of deformation. Table 5.8 explains the process of martensite cracking throughout the process of ductile deformation, and more details about table 5.8 are shown in the Appendix XI. Fig. 5.27. shows the load extension curve for the SEM bending test.

The first crack mechanism separated the martensite into two segments at 1.25 mm displacement. The crack occurred before the maximum point on the curve at 295 N, as shown in Fig. 5.27. The ferrite deformation which caused the martensite to crack was the second crack mechanism for numbers 2 and 3. The ferrite deformed close to the martensite at the 1.75 mm extension point for crack number 2, and the load was 298 N, as shown in Fig. 5.27. For crack number 3, the martensite fractured at 2 mm, where the load was 297 N. A microcrack formed in the ferrite after the martensite was damaged. For crack number 4, two ferrite areas deformed

and were then connected to create a microcrack after the martensite cracked. The displacement for this crack was 2.25 mm, and the load was 294N. A microcrack deformed the ferrite after the appearance of crack number 4, and this was then propagated fracturing the martensite for crack number 5 at the maximum point on the curve, where the extension value was 2.5 mm, and the load was 292 N. In the case of crack number 6, the martensite cracked directly as a result of the deformation occurring at the same level as in crack number 4. For crack number 7, the microcrack in the ferrite was also created after the maximum point on the curve, and was also propagated to the martensite at 3 mm, where the load was 285 N.

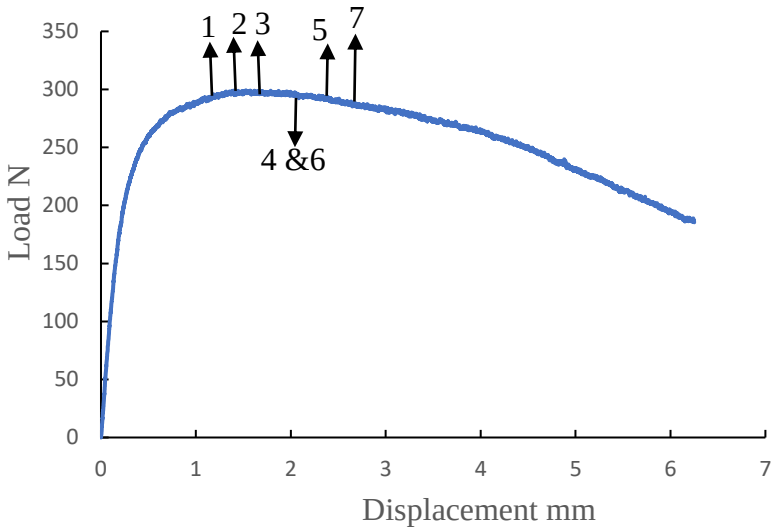

Fig. 5. 27 Load displacement curve from the bending test; the black numbered show the order in which the martensite cracks were initiated.

Table 5. 8 Martensite cracks and ferrite voids present throughout the deformation.

Crack number 1 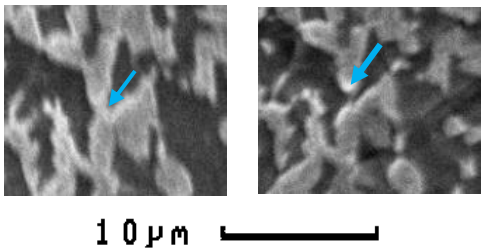 The blue arrows indicate the martensite fracture.	Crack number 2 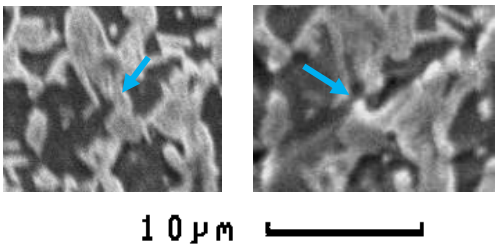 The blue arrows reveal the martensite fracture.
Crack number 3 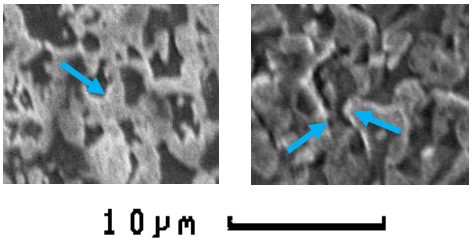 The blue arrows indicate the martensite fracture.	Crack numbers 4 and 5 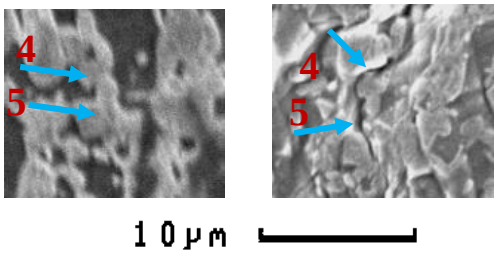 The blue arrows indicate the martensite cracks.
Crack number 6 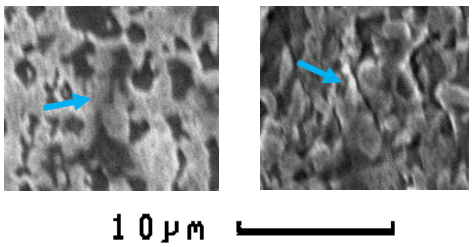 The blue arrows indicate the martensite fracture.	Crack number 7 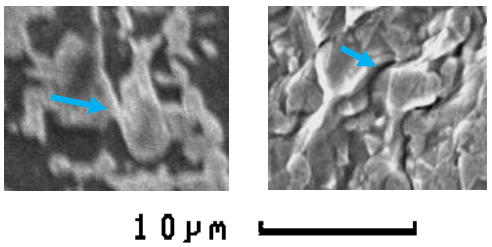 The blue arrows indicate the martensite cracks.

5.4.1 Bending test strain analysis using micro DIC

The damage and local deformation of the microstructure cited in the results of the bending test, were evaluated using DIC. The strain distribution was calculated in the Y direction, which was the direction of tension in the bending sample for the overall microstructure, and this will be described in this section.

Fig. 5.28 a shows the distribution map after the application of 1.5 mm displacement. The maximum localised strain value started to appear early in the ferrite phase, at 32%. In comparison, the minimum value was observed in the martensite islands. Localised deformation in the microstructure apparent at 1.75 mm in a group of microstructures that were located along lines X and Y, as shown in fig. 5.28 b. The arrows in Fig 5.28 b show the high strain values that were located along both lines. Martensite cracks and ferrite voids were expected to occur along or close to these lines, as shown in Table 5.9. The strain value peaked at about 48% in an area of local strain that was located on line X, very close to line Y in the ferrite phase. This area of high strain values in the ferrite phase appeared at the start of the deformation process, and remained at the same location throughout. The group of martensite cracks shown in the black square in Fig. 5.28 started deforming at the point of 9% local strain in ferrite, and increased to 35% before a microcrack appeared.

Fig. 5.28 c shows the strain map after a displacement value of 5.5 mm was applied prior to the final fracture. E_{YY} corresponds to the Lagrangian strain component along the Y axis, which appears as vertical in the images. The deformation along lines X and Y became more localised at 130% in the ferrite phase before damage appeared. The results clearly show that high strain localisation began in the ferrite phase and progressed to the point of final fracture. Therefore, ferrite is likely to control damage in DP1000.

The findings clearly show that high strain localisation started in the ferrite phase, and progressed to the point of final fracture. Therefore, the presence of ferrite is likely to limit damage in DP1000.

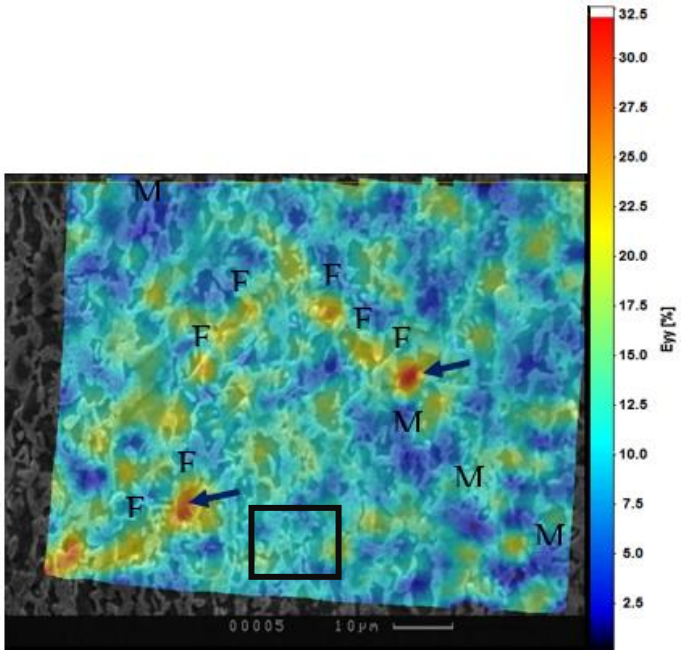

(a)

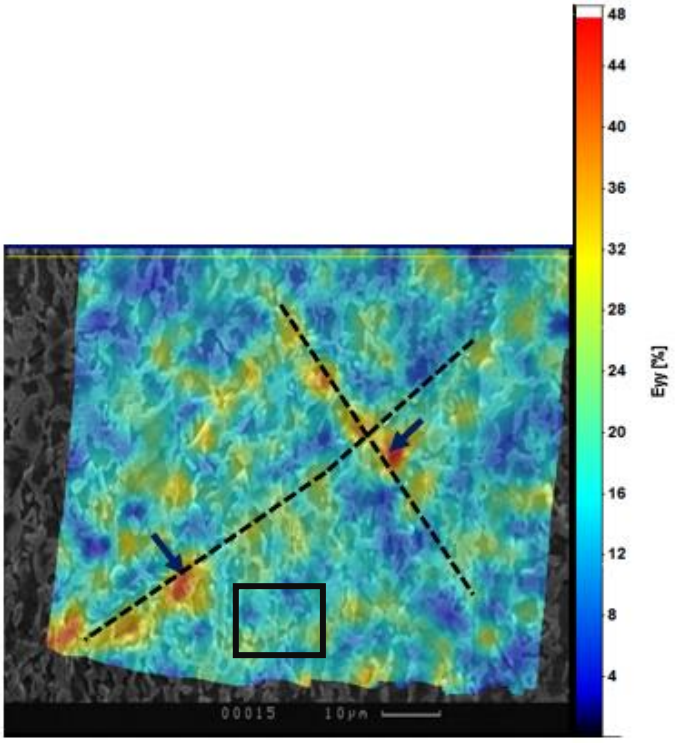

(b)

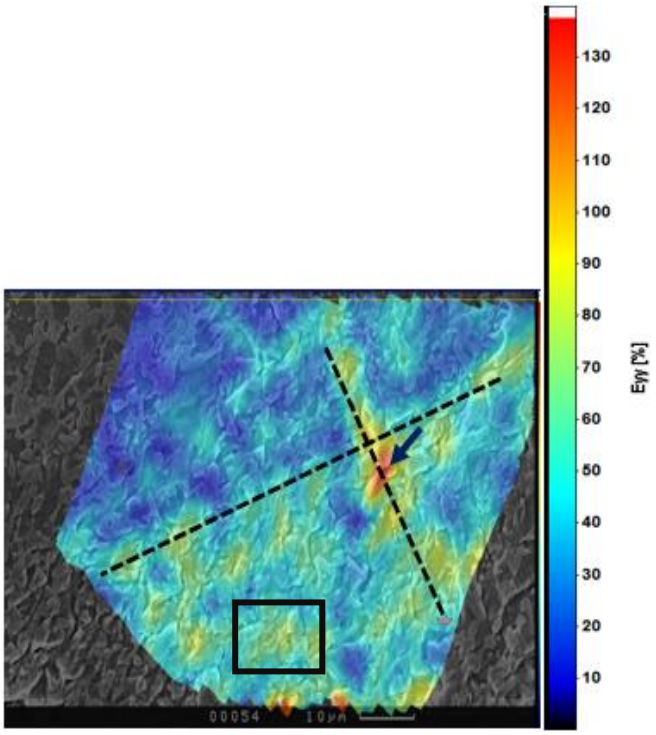

(c)

Fig. 5. 28 (a) the maximum strain value appeared early in the ferrite phase. The arrows point to the maximum value appearing along the deformation lines in the black ovals. (b) shows the maximum region was within the ferrite. (c) shows the most affected region is at the same location in the ferrite phase.

High-magnification SEM images were captured throughout the bending tests to help further understanding concerning the formation of martensite cracks and ferrite voids. Table 5.9 details local strain distributions in relation to fracture mechanisms. The first, second and third cracks were initiated when local strain values were 21%, 22.5% and 20%, respectively. Crack numbers 1 and 2 were very close to the maximum local strain values observed in the ferrite phase. Crack number 5 occurred at a global extension greater than that for crack number 4. The strain localisation of crack number 5 was 24.5%, which was less than the 35% value of crack number 4. For cracks number 6 and 7, the martensite fracture occurred when the local strain values reached 32.5% and 50%, respectively. Crack number 7 in the martensite phase might have been initiated under the effect of the microcrack in ferrite, which had a maximum local value of 80%.

Table 5. 9 Strain distributions measured by DIC in relation to the fracture mechanism in table 5.8.

Crack number 1 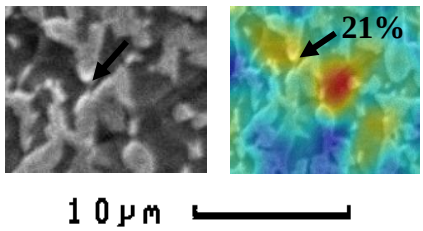	Crack number 2 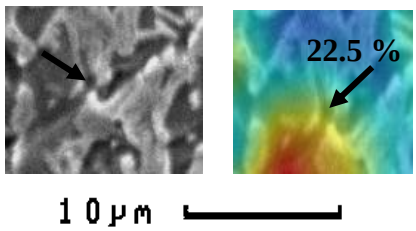
Crack number 3 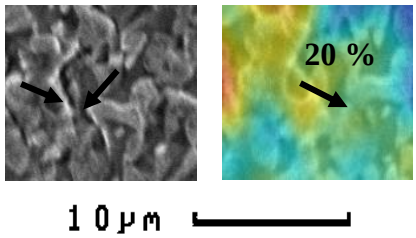	Crack numbers 4 and 5 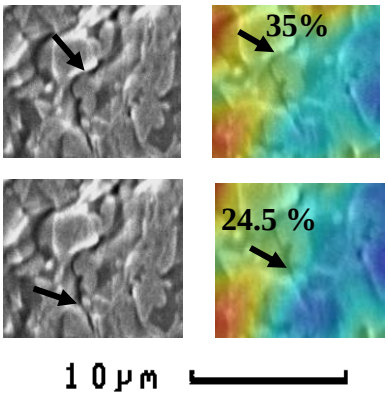
Crack number 6 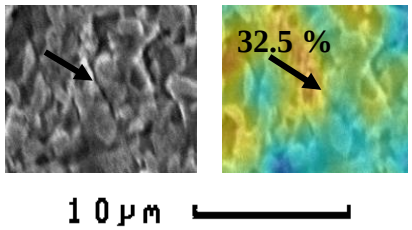	Crack number 7 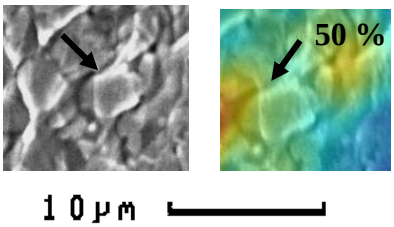

5.4.2 Bending test using micro bending stage to investigate Crack Propagation

Large crack propagation was analysed to determine the process of damage development in DP1000. Cracks were observed in two samples using in-situ bending tests under the SEM. The first specimen was the same sample as that used in the previous section to study local

deformation by means of DIC. The second sample was used to track large cracks throughout the bending test, from the moment of initiation to material fracture. The following sub-sections explain the cracking propagation mechanisms in depth.

5.4.2.1 Crack formation during first micro stage bending test

After characterising the local deformation in the specific area of the microstructure analysed with DIC in section 5.4.1, the damage and cracks that had appeared in other areas of the specimen were analysed. The major cracks are presented at low magnification in Fig. 5.29. They were initiated at the edge of the specimen, which experienced maximum tensile stress when subjected to bending, as shown in Figs. 5.30 a, 5.30 c and 5.30 e. Significant crack propagation occurred, as shown by the measurements of crack length. The SEM image was recorded at micrometre resolution. Using Photoshop (Andrews, 2013) software, the image was converted to pixels, which were then changed to millimetres using a measurement scale.

Fig. 5.30 b magnifies the crack present in Fig. 5.30 a, which showed a crack size of 0.04 mm. Figure 5.30 d shows magnification of a crack with a propagation length of 0.0168 mm, before changing direction over a length of 0.006 mm. A crack in Fig. 5.30 e was propagated in a different direction from the cracks in Figs. 5.30 b and 5.30 d; the size of this crack was 0.018 mm. Fig. 5.30 e shows an additional crack formed in the microstructure away from the edge of the point of maximum tensile stress in the sample.

Void formation was also visible, as shown in Figs. 5.30 a (blue circle), and 5.30 d (red arrow). A number of microcracks were also seen, as indicated by the blue arrows in Figs. 5.30 d. Additional examples and information concerning crack observation and measurement length have been added to the Appendix XII.

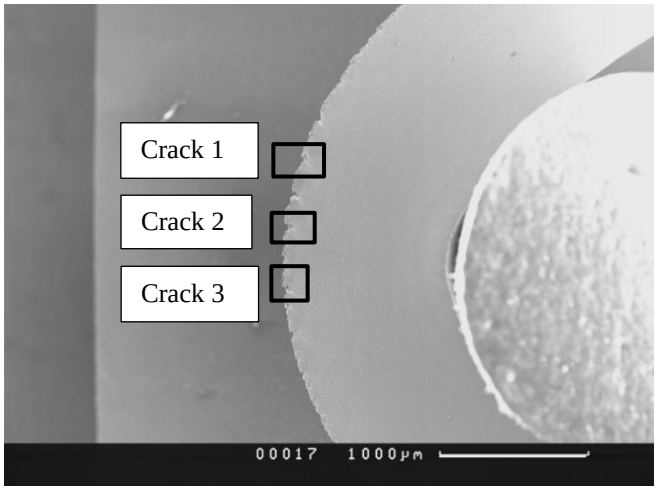

Fig. 5. 29 Location of large cracks in the sample, with details provided in Fig. 5.30.

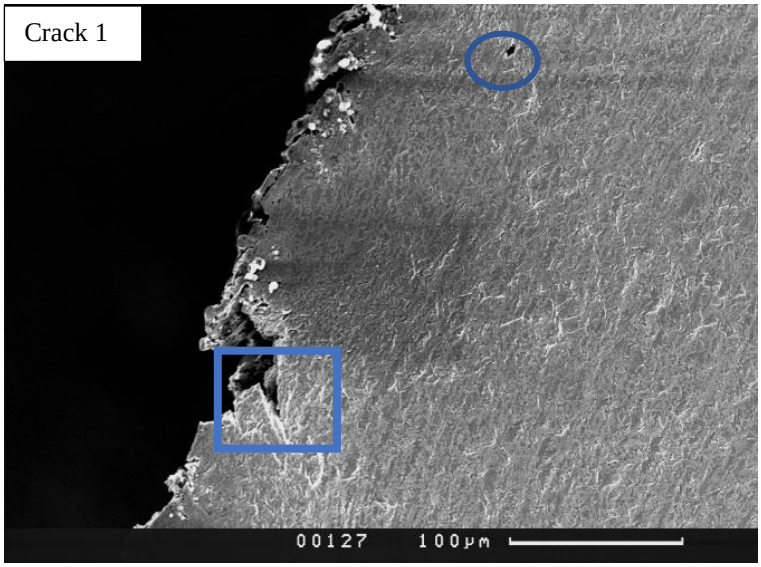

(a)

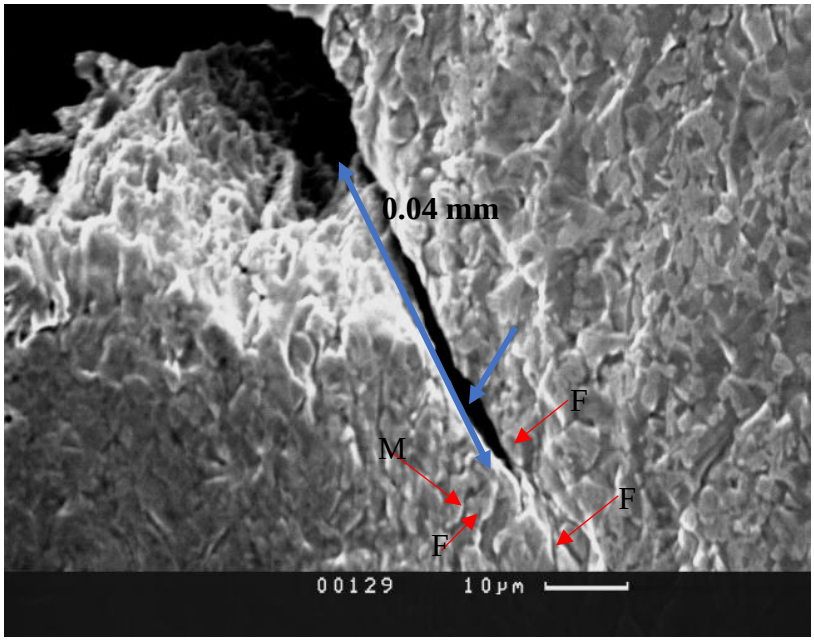
0.04 mm
F
M
F
F
00129 10µm

(b)

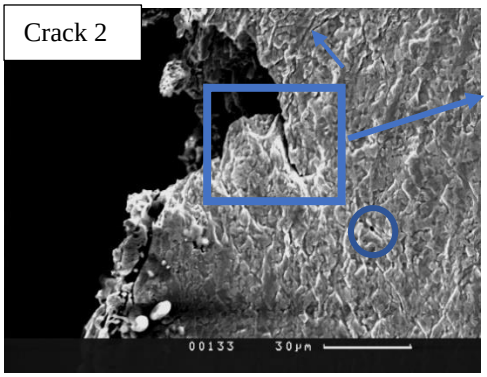
Crack 2
00133 30µm

(c)

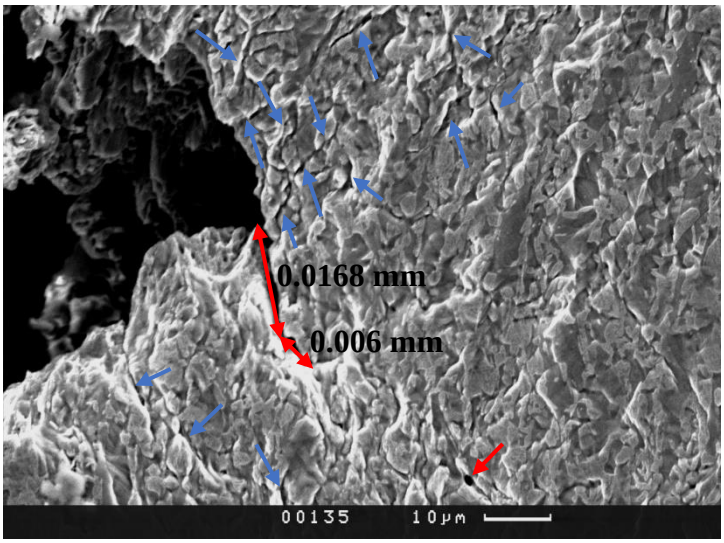
0.0168 mm
0.006 mm
00135 10µm

(d)

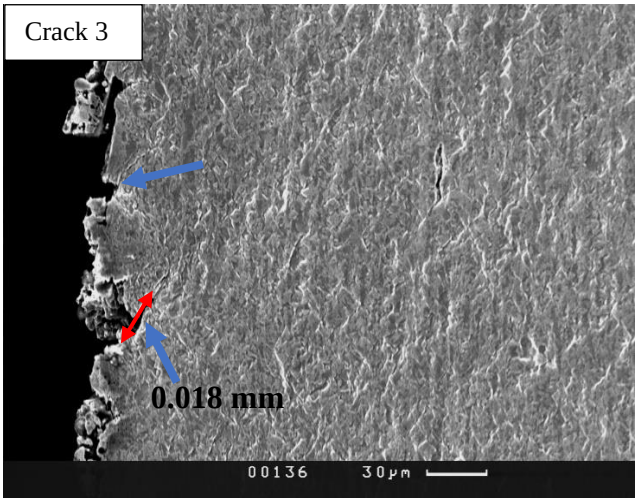

(e)

Fig. 5. 30 Cracks in the samples after the material became damaged; images b and d provide magnifications of images (see blue squares) a and c respectively.

It is evident from these results that this bespoke bending test successfully led to crack formation on the surface of observation in SEM with a significant quantity of propagation. However, initiation and propagation of these cracks was not closely followed in the first bending test, as the focus was on analysing strain distributions, as measured with DIC in a particular area of the microstructure. A second test was subsequently performed to follow the development of these cracks.

5.4.2.2 Second bending test analysis using micro stage bending test to investigate the track of crack propagation

Fig. 5.31 provides a low-magnification image detailing the cracks in the bending specimen at the conclusion of the test. Four major cracks are highlighted here by blue rectangles. The cracking mechanism for each crack in the figure was analysed in the following sub-sections. Cracks numbered 1 and 2 will be explained in this section. Cracks numbered 3 and 4 have been added to the appendix XIII.

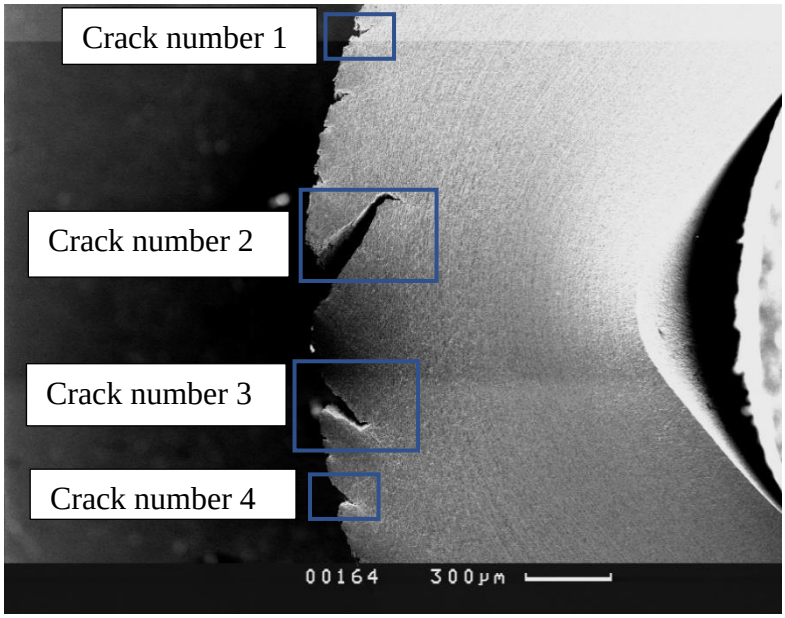

Fig. 5. 31 Bending sample after damage; the crack propagation is clearly visible.

5.4.2.2.1 Crack number 1

Examination of the propagation shows the ferrite started deforming at the 0.225 mm extension level, as detailed in Fig. 5.32 a. Figs. 5.32 b and 5.32 c highlight the crack path on the undamaged microstructure, with the red dashed line tracking the cracking; noting that the ferrite was deforming before damage started to propagate at the 2.027 mm extension level. The crack first became visible and appeared to grow as the ferrite continued to deform at 2.475 mm applied displacement, as shown in Fig. 5.32 d. The crack continued to grow, cracking a martensite island located in its path before once again propagating in the next ferrite phase, as shown in Fig. 5.32 e, at the displacement of 2.98 mm. The crack then met a cluster of martensite islands, which impeded its propagation, leading to extensive deformation of the microstructure located around the crack tip. This extensive deformation led to the formation of voids in the ferrite phase, as shown in Fig. 5.33 f, at the 3.504 mm displacement point. These voids eventually connected, leading to further crack propagation along a path with a different

orientation to the initial crack path (Fig. 5.32 g) at 4.041 mm. Fig. 5.32 h shows extension of the crack length by 0.09803 mm along this new direction.

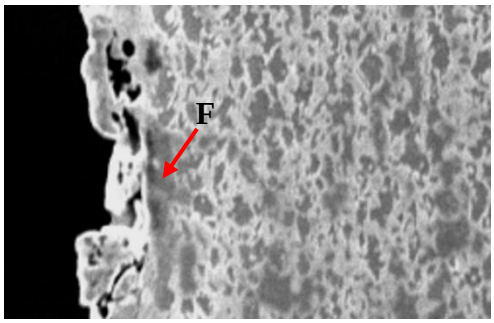

(a)

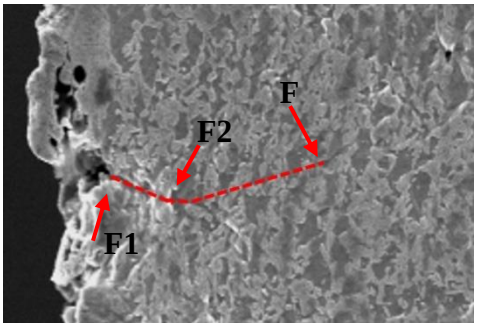

(b)

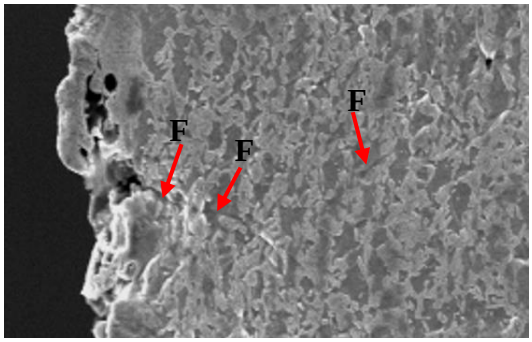

(c)

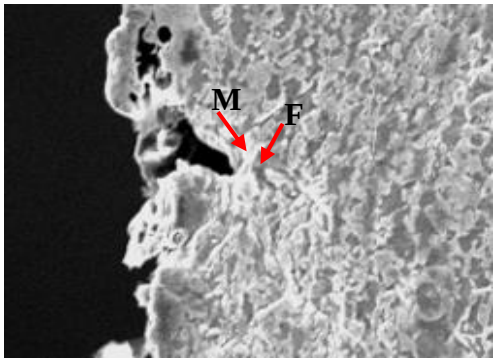

(d)

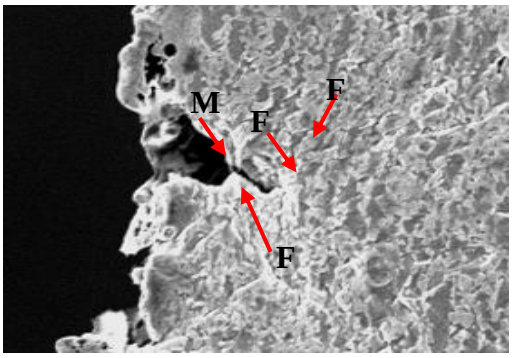

(e)

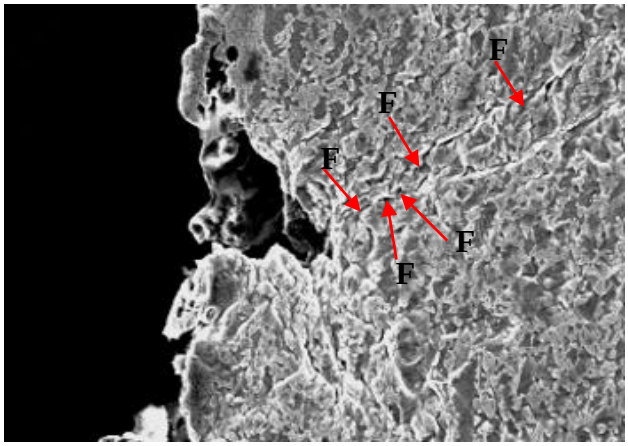

(f)

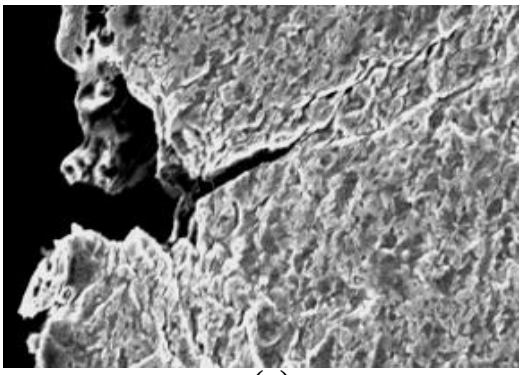

(g)

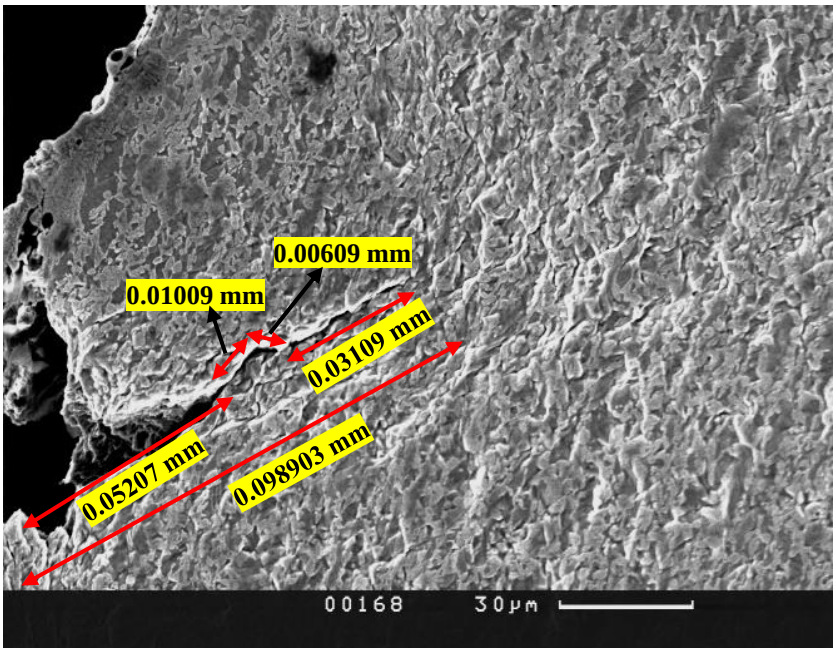

(h)

Fig. 5. 32 (a) to (h) results in the development of crack propagation. Figs. (a) and (b) show the crack pathway and early ferrite deformation, respectively. Displacement values for all images: fig. (a) at 0.225 mm, figs. (b) and (c) at 2.027 mm, fig. (d) at 2.475mm, fig.(e) at 2.98 mm, fig. (f) at 3.504 mm, and fig. (g) at 4.041 mm. (h) Measurement length of the crack once the sample has been damaged.

5.4.2.2.2 Crack number 2

Figs. 5.33 a and b depict the initiation of the propagation, with the red dashed line indicating the crack path over the undamaged microstructure. The ferrite microcrack was first observed at the displacement of 2.027 mm. In Fig. 5.33 c, the microcrack appeared in the ferrite close to the martensite at 2.475 mm; crack propagation is hindered by a cluster of martensite islands

leading to extensive deformation of the microstructure at the crack tip, as shown in Fig. 5.33 d, at the 2.98 mm displacement. This extensive deformation leads to damage to the ferrite, as well as martensite cracking around the crack tip, eventually leading to further crack extension at the 3.28 mm extension level, as shown in Fig. 5.33 e. Coalescence of damage created during extensive deformation then drives crack propagation along a crack path with a different orientation, as shown in Figs. 5.33 f and g, where the displacement is 3.504 mm and 3.685 mm, respectively. The crack continued propagating at 4.041 mm and 4.784 mm, with an orientation of about 45^{o} with respect to the horizontal axis, as shown in Figs. 5.33 h and i. Finally, the crack continued to propagate at the 5.03 mm extension, as shown in Fig. 5.33 j, with the direction of the crack changing again following an applied displacement of 5.515 mm, as shown in Fig. 5.33 k. The crack extension at 45^{o} orientation was 0.446 mm, with a further extension of 0.06888 mm after altering the orientation, as shown in Fig. 5.33 l.

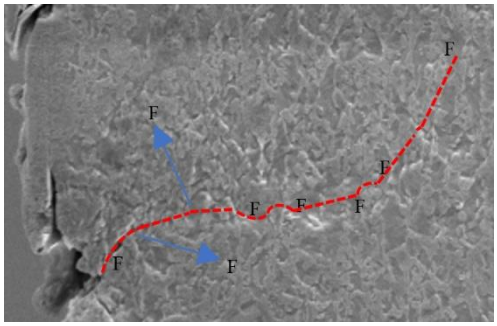

(a)

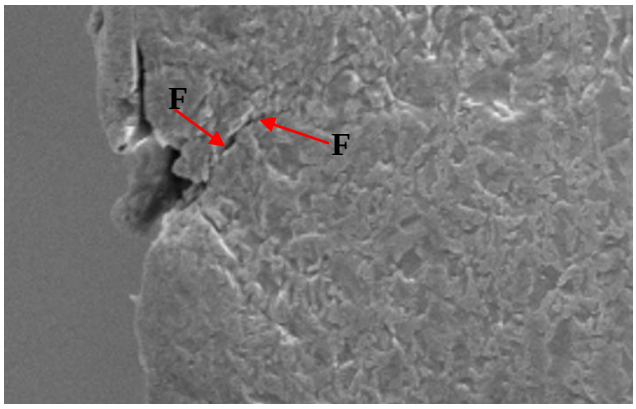

(b)

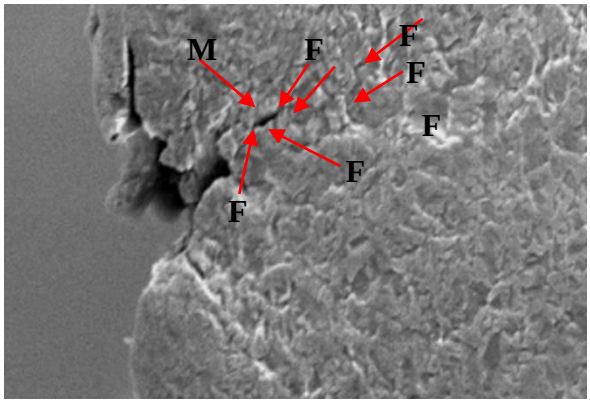

(c)

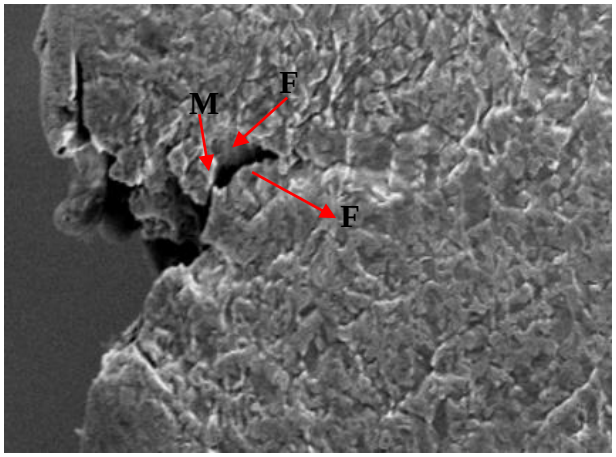

(d)

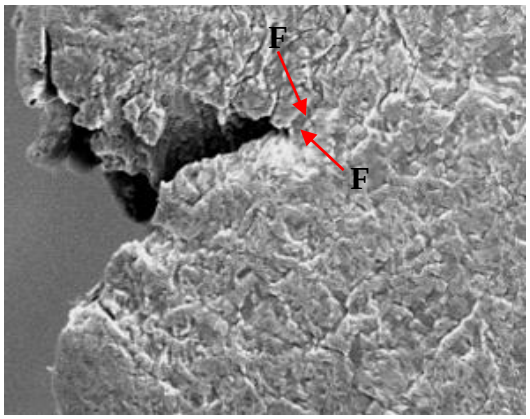

(e)

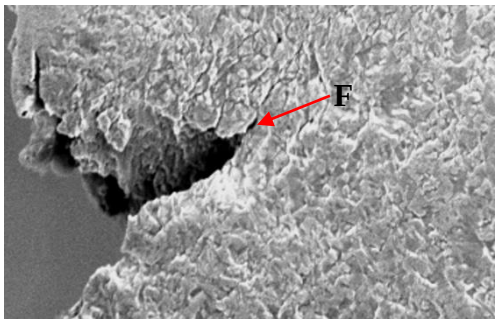

(f)

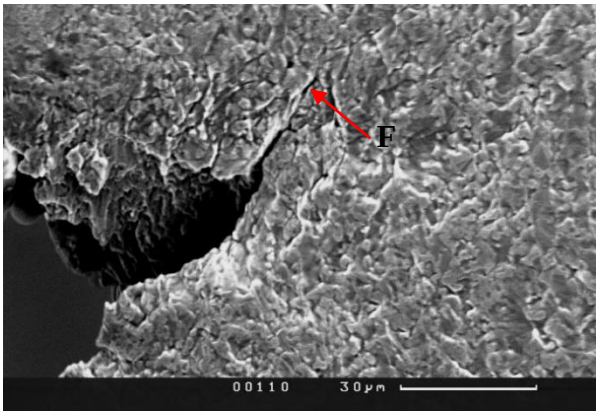

(g)

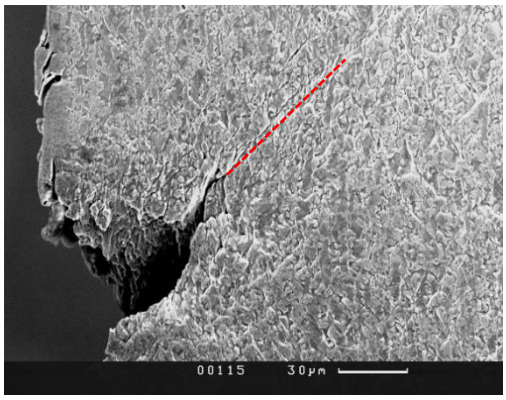

(h)

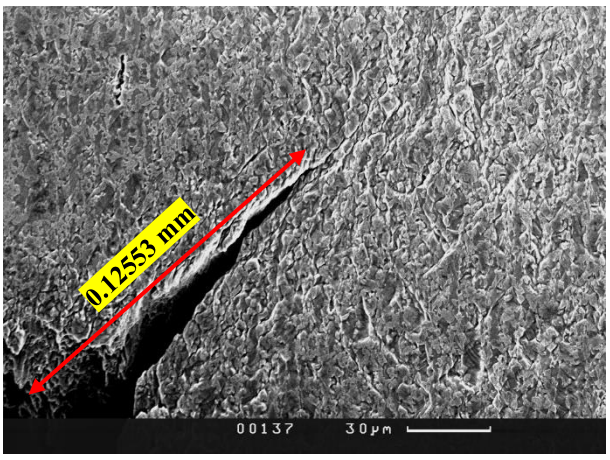

(i)

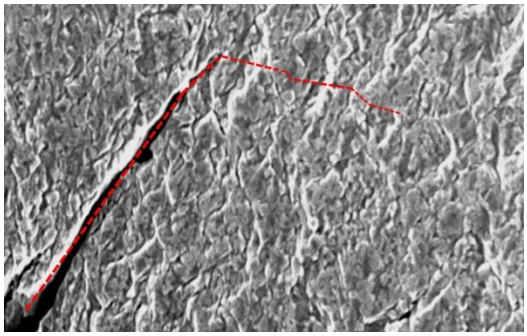

(j)

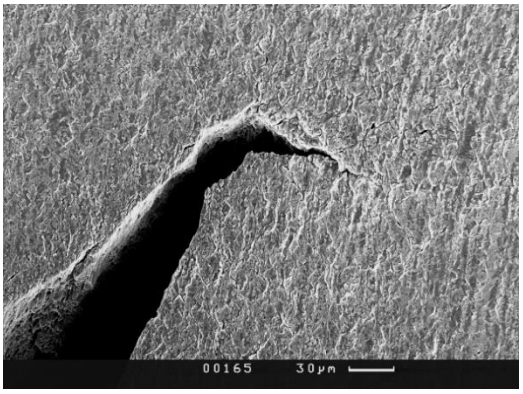

(k)

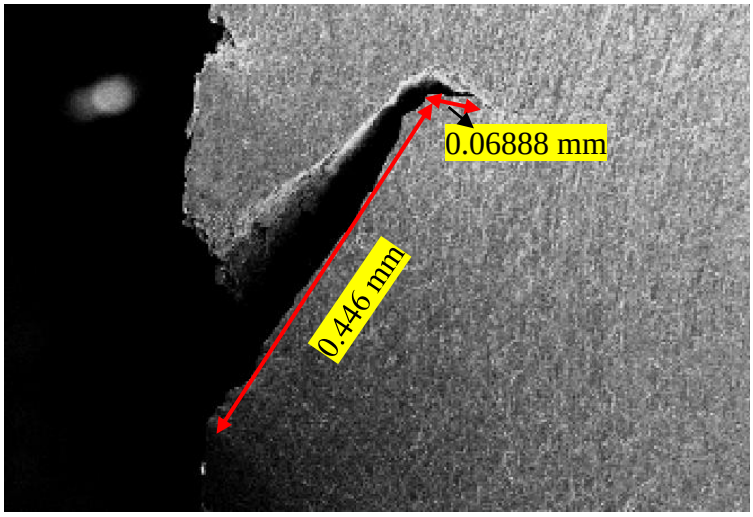

(l)

Fig. 5. 33 (a) to (l) shows crack number 2, from the start of the ferrite deformation until the final propagation. Displacement values for all images: fig. (a) and (b) at 2.027 mm, figs. (c) at 2.475 mm, fig.at (d) 2.98 mm, fig.(e) at 3.28 mm, figs (f) at 3.504 mm, (g) at 3.685mm, fig (h) at 4.041 mm, fig (i) at 4.784 mm, fig.(j) at 5.03 mm, and fig.(k) at 5.515 mm. (l) Measurement length of the crack after the sample was damaged.

5.5 Summary

This chapter reported new results and further understanding of damage initiation and propagation in DP1000 through the development of an original experimental procedure combining a series of tests enabling multi-scale analysis of the material deformed under either uniaxial or biaxial loading. In-situ tensile tests with DIC were characterised quantitatively, along with the initiation of damage in the martensite region when analysing a large number of

damage events, which were captured within the analysed area. Initially, the initiation of several voids in the ferrite could also be quantified in terms of the local strain values towards the end of the test. A novel SPT provided further insight into damage development in the microstructure of DP1000 under biaxial loading, which occurred closer to the forming operation, with the propagation and crack path controlled in the ferrite phase. Finally, a unique in-situ bending test setup provided novel results concerning large crack propagation in the material's microstructure. The results confirmed the final phase of damage development in DP1000 led to failure of the material, which was controlled in the ferrite phase, thereby providing new insight into the mechanisms responsible for the long elongation prior to failure and the formability of this material.

6. FE SIMULATION ANALYSIS OF DP1000

FE modelling combines the different scales presented in this chapter to clarify the deformation and damage behaviour of dual-phase steel in terms of multi-scale modelling. The first section addresses the results of the macroscale modelling, which was conducted using tensile tests with different specimen geometries. Damage modelling was conducted using the GTN model, with the model parameters calibrated using FE simulation notched specimen geometries. The first section also validates the model against in-situ tensile specimen geometry for the test conducted in SEM. Another section reports the microstructure simulation results using the strain measurements obtained with DIC to predict damage initiation in both martensite and ferrite for DP1000. Finally, the further section shows simulation results for the punch tests, and bending tests for the prediction of damage development at the scale of specimens, with validation provided through the 3D DIC measurements and experimental observations.

6.1 Continuum damage Modelling of DP1000

This section presents the results of the macroscale damage modelling for DP1000 using the Gurson model. The (GTN) model was commonly used to describe the damage behaviour of the ductile materials (Needleman & Tvergaard, 1984; Tvergaard, 1981, 1989; Tvergaard et al., 1981). Since this model is incorporated into Abaqus, it was also used here. The gradual growth of the voids resulted in a gradual decrease in the load required to deform the specimen beyond the ultimate tensile strength of the material. This was evident from the softening behaviour observed in the load-displacement curve. Consequently, the reduction of the load in the softening portion of the load-displacement curve can be modelled using the GTN model. The model includes eight parameters in total. Three parameters (ε_n, f_n, S_n) are used to model void nucleation, and two parameters (f_c, f_f) relate to the sudden drop in stress capacity that corresponds to damage coalescence, causing the specimen to fracture. These describe the

evolution of the void's growth, up to the point of coalescence and final failure. However, this aspect of the stress-strain curve is proposed as an area of future work associated with this project. Three parameters (q_1, q_2, q_3) characterise the yield behaviour of the material, with a direct effect from each parameter on the load-displacement curve, with ε_n controlling the beginning of the void's nucleation, and f_n controlling for the magnitude of the nucleation. S_n reported only a small or negligible effect on the load-displacement curve. The results of their effect on the load-displacement curves were compared with the experimental results, as detailed in the next subsection.

6.1.1 Tensile damage modelling: Effect of GTN parameters

This section describes the effect of the Gurson parameters, and their calibration by comparison with load-displacement curves recorded through the tensile testing of the notched specimens introduced in chapter 3. Validation is performed by comparing the model prediction against the load-displacement curve in the tensile test carried out in the SEM. The true stress-strain curve for DP1000 was obtained from tensile testing of a standard specimen as shown in Fig. 5.1 in chapter 5. It was first introduced into Abaqus to simulate the tensile deformation of notched specimens. Fig. 6.1 compares the simulation result and the experimental load-displacement curve for the first notched specimen (7.5 mm) before adjusting the Gurson model's parameters.

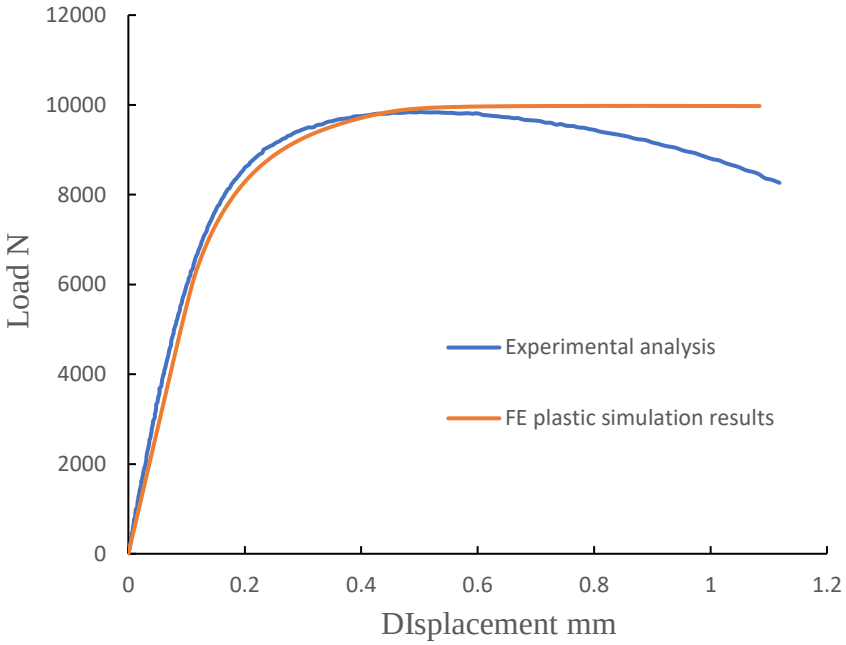

Fig. 6. 1 Modelled plastic deformation curve.

A study was conducted to analyse the effect of the Gurson model parameters on the prediction process, first reviewing the effect of the q parameters. The modelling of the notched specimen shown in Fig.4.1 was the first simulation performed to study the effect of these parameters on the load displacement curve. A graph comparing the simulation results with the experimental curve is shown in Fig. 6.2 for each of the different q parameters. The ranges for the q1 and q2 parameters of the GTN model, based on the literature, are 1 – 1.6 and 0.9 – 1.1, respectively. The curve approaches the experimental curve when q1 and q2 increase; thus, the best value for q1 was 1.6 and the best value for q2 was 1.1. The q3 parameter, as recommended in the literature, was the square of q1 (2.56).

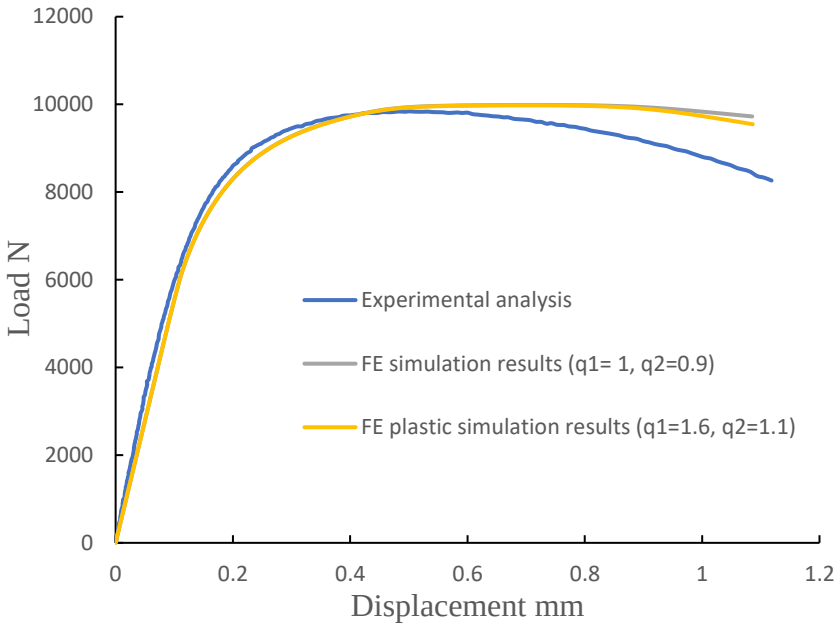

Fig. 6. 2 Effect of q parameters on curve.

The remaining parameters (ε_n, S_n, f_n) physically affect void nucleation, with the mean ε_n controlling for the beginning of the nucleation. Fig.6.3 shows the effect of the mean on the curve. The range of the mean, based on the GTN model, fell between 0.1 and 0.3. The mean started with the values 0.2 and 0.1. The results show the curve becomes close when the mean value is 0.1, thus, it is not necessary to test 0.3. The void volume fraction controlled the magnitude of void nucleation, and Fig.6.4 illustrates this effect. According to the literature review, standard deviation has a small effect on the curve, as can be clearly seen in Fig.6.5. The simulation curve could also be fitted against the experimental one through 'trial and error', without applying any optimisation procedure. The best fitted curve is shown in Fig. 6.6, corresponding to the following Gurson parameter values: q1 = 1.6, q2 = 1.1, q3 = 2.56, ε_n = 0.15, f_n = 0.05 and $S_n = 0.06$.

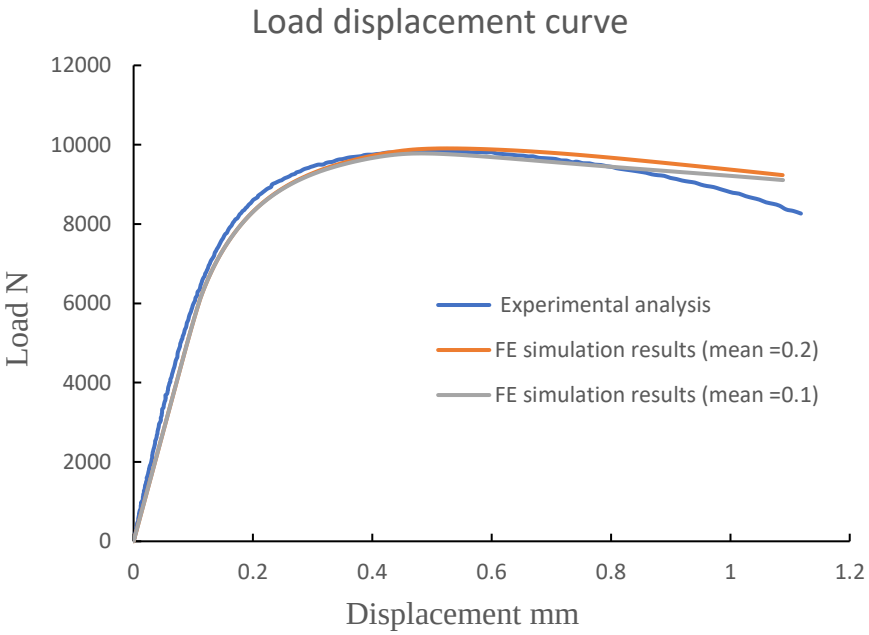

Fig. 6. 3 Void volume fraction effect on the simulation curve.

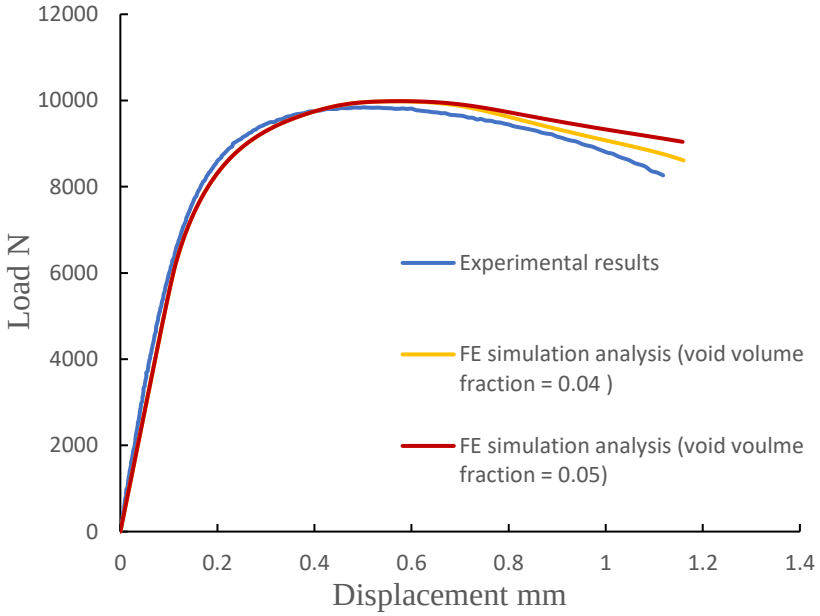

Fig. 6. 4 Influence of void volume fraction on the curve.

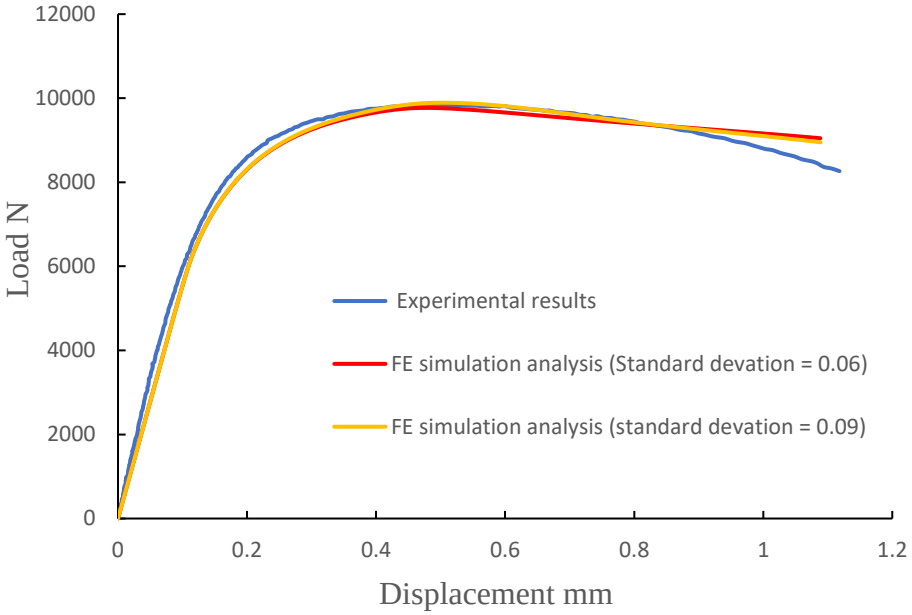

Fig. 6. 5 Influence of standard deviation on the curve.

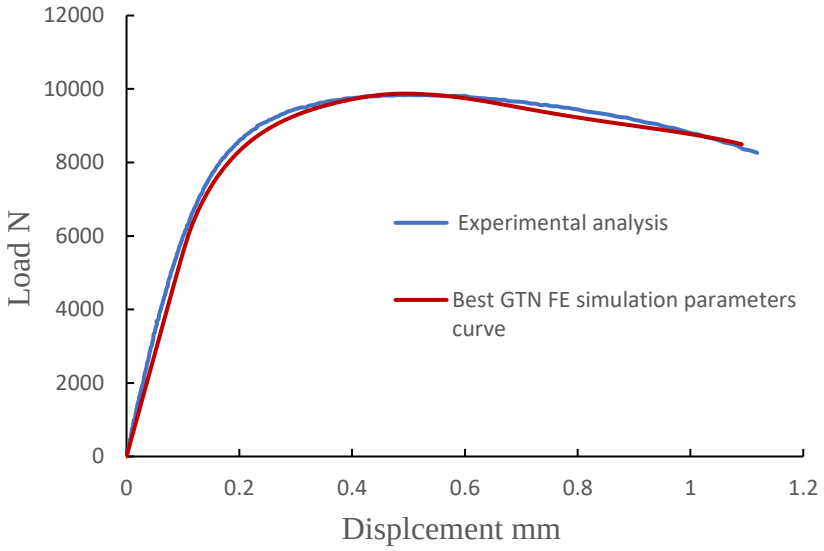

Fig. 6. 6 Best fitted simulation results compared to the experimental curve.

For further validation of these parameters, the second notched geometry (with a radius of 1.5 mm (see Fig. 3.2 (a) in chapter 3)) was tested by applying them directly within the simulation. The experimental load displacement curve was also closely fitted using the same parameters as those applied for the first notch geometry, as shown in Fig. 6.7.

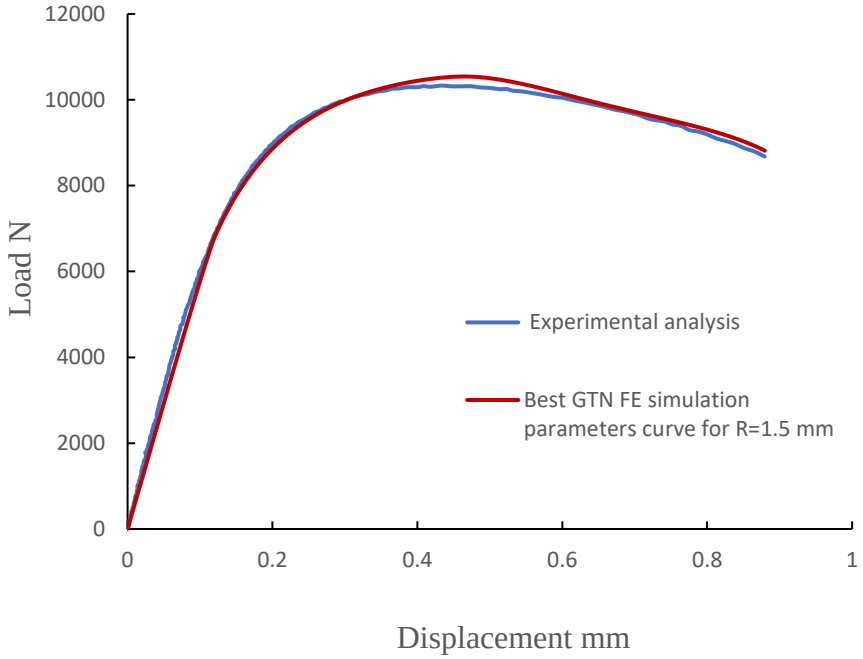

Fig. 6. 7 Load displacement curves for the second notch, with the same GTN parameters as those applied to first notch.

The predictability capacity of the Gurson model with q parameters calibrated with the 2 notch geometries was then tested for validation purposes against the load displacement curve recorded during the in-situ tensile test conducted inside the SEM. Fig. 6.8 (a) compares simulation and experimental results, and the blue line indicates the experimental results. The standard deviation and volume fraction for the three FE GTN simulations in fig.6.8 (a) are $S_n = 0.06$ and $f_n = 0.05$. The mean value varies in the three continuum GTN models, where the mean for the orange line is $\varepsilon_n = 0.3$, and the mean values for the grey and yellow lines are $\varepsilon_n = 0.15$ and $\varepsilon_n = 0.2$. Close agreement is observed here, thereby validating the previously identified parameters. Fig.6.8 (b) shows that an even closer match can be achieved when adjusting the value of the mean and volume fraction parameters while keeping the q parameter values constant, as the third row in table 6.1 shows.

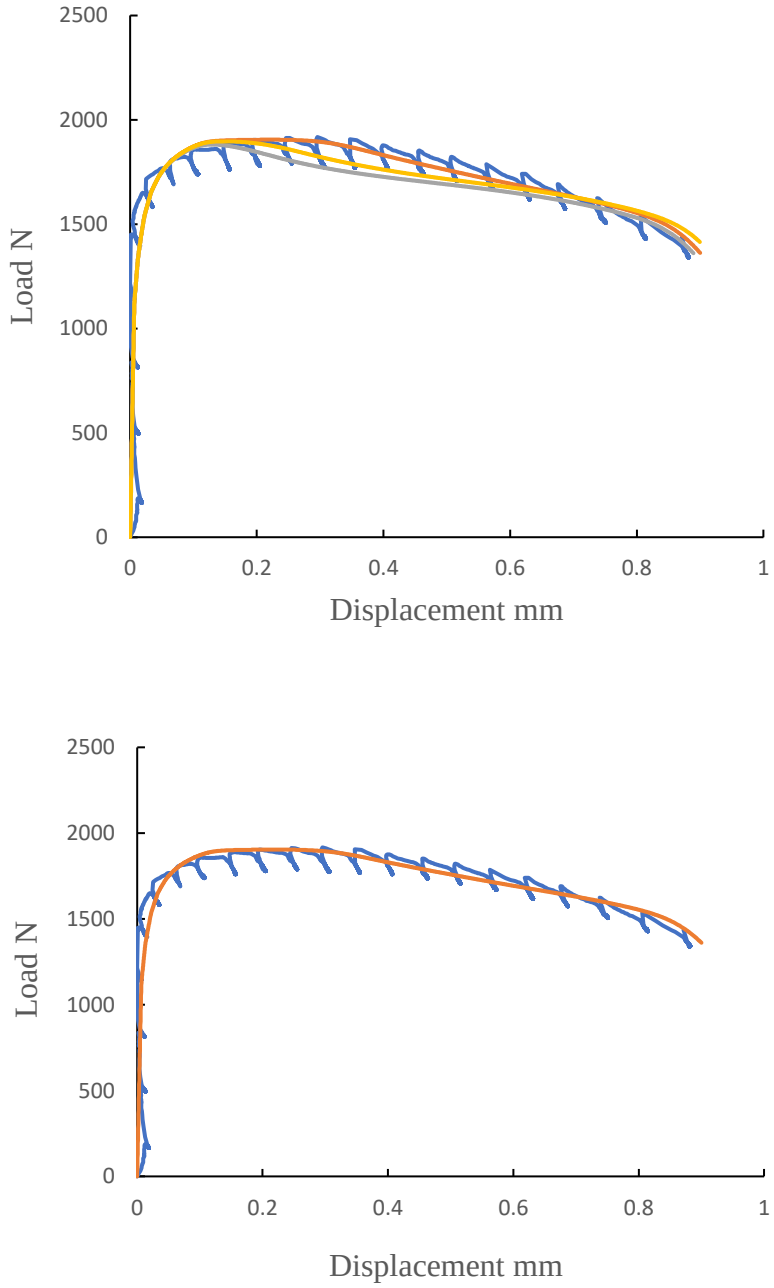

Fig. 6. 8 Simulation curve with GTN parameters compared with experimental results.

Table 6. 1 Show the damage parameters for all geometries.

Geometries/parameters	q1	q2	q3	ε_n	f_n	S_n
First notched	1.6	1.1	2.56	0.15	0.05	0.06
Second notched	1.6	1.1	2.56	0.15	0.05	0.06
SEM sample	1.6	1.1	2.56	0.3	0.06	0.06

6.2 Microstructure based modelling results of DP1000

The deformation and damage to DP1000 observed during the in-situ tensile test conducted under the SEM were analysed using multi-scale modelling. The full-field strain values measured using DIC as detailed in Chapter 5 were applied as boundary conditions for the finite element simulation for the deformation of the microstructure, as explained in Chapter 4.

Stress analysis was performed on the dual-phase (martensite and ferrite) steel sample (DP1000) using FE analysis, and the stress distribution (which could not be evaluated experimentally) then investigated using simulations conducted using Abaqus. This modelling was performed to investigate whether stress distributions control the initiation of damage in the microstructure.

The accuracy of the simulations is dependent on the mesh size, and corresponds to the subset (square) size used to discretise the SEM images (see chapter 4). It was therefore vital to study how the subset size affected the resolution of the geometry phases, as simulated in the finite element model, in particular how this would affect the microstructure simulation results. A fine mesh size would provide microstructure simulation results that would match the experimental results best. However, when the element size was small, the FE microstructure shape deformation was indeed very close to that included in the experimental results.

Figure 6.9 represents how changing the subset size discretising the SEM image affected the resolution of the image itself, and Fig. 6.10 details the resulting effect on the resolution of the phase geometry, as simulated in the finite element model. A mesh size corresponding to 1 pixel in the image was selected for this study.

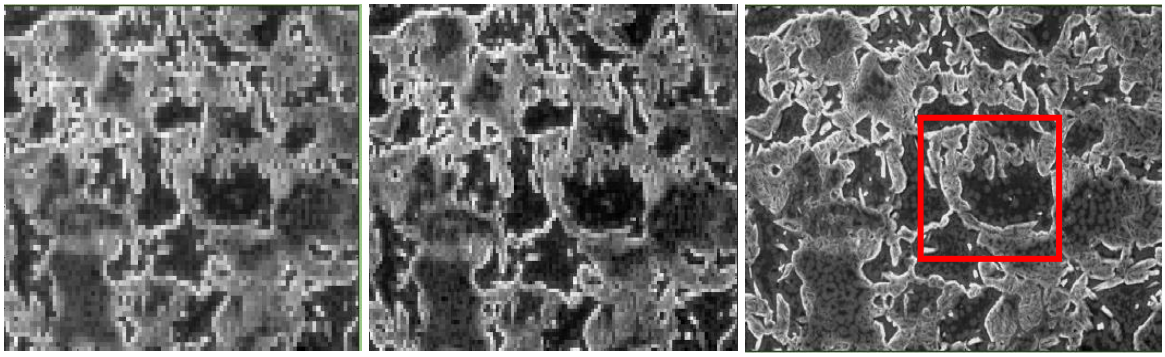

(a) (b) (c)

Fig. 6. 9 Effect of the subset size on the image resolution: (a) 8 x 8 pixels, (b) 5 x 5 pixels and (c) 1 square pixel.

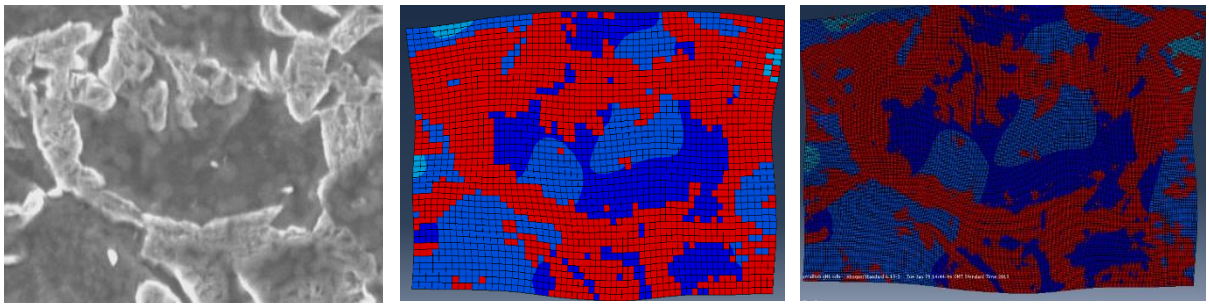

(a) (b) (c)

Fig. 6. 10 (a) Area of the microstructure highlighted by the red rectangle in Fig.6.9 (c), (b) Mesh corresponding to a 5 x 5 pixels subset size and (c) 1 pixel subset size.

The flow curves for the martensite and ferrite phases had to be adjusted to correspond to the literature, so as to minimise the error between the simulation and experimental results (Alharbi, 2015). Microstructure simulation was undertaken to calibrate the phase properties for this work. The Poisson ratio for both phases was 0.3, and the moduli for elasticity were 182 GPa for the martensite, and 198 GPa for the ferrite. The SEM image shown in Fig. 4.2 was used for the purposes of the simulation. Global strain values of 0.017, 0.032, and 0.048 were utilised because no damage was observed at the level of applied strain located before the UTS.

The flow curves for the martensite and ferrite were adjusted by minimising the difference between the computed (see chapter 4 for the computation of the average stress) and measured flow stress values (Alharbi, 2015). Fig.6.11 (a) details the curves adjusted for the ferrite and

martensite phases that resulted from this calibration procedure and Table 6.2 reports the error values between numerical and experimental flow stress values. The minimum error was found to be 1.08%.

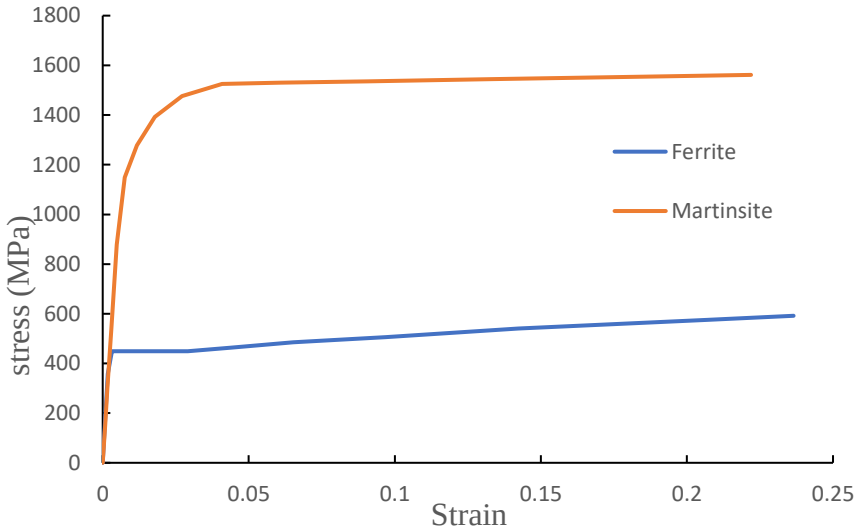

(a)

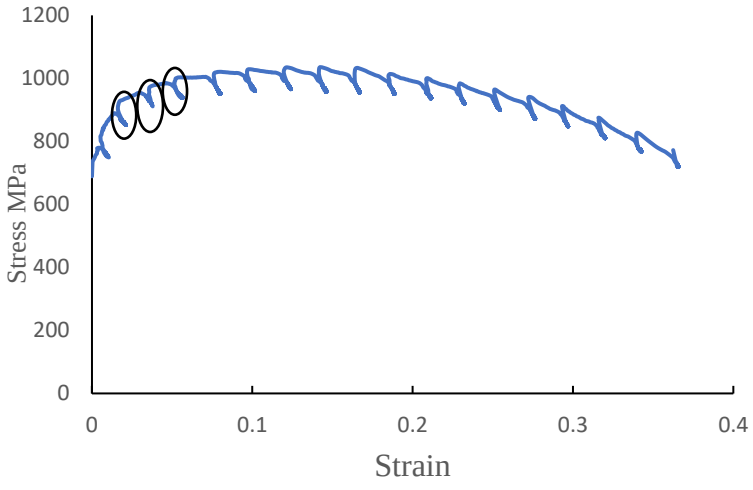

(b)

Fig. 6. 11 (a) Adjusted stress-strain curves for both phases from finite simulations of the microstructure, (b) Applied strain values selected for calculated errors reported in Table 6.2.

Table 6. 2 Percentage error between the experimental true stress and averaged simulation stress for applied displacements selected before the appearance of the first crack.

Applied strain	0.017	0.032	0.048
SEM true stress (MPa)	1110	1138	1170
Average simulation stress (MPa)	1098	1107	1133
Error %	1.08	2.7	3.16

The results in Table 6.2 reveal there is an acceptable error between the true experimental stress and the average stress from the simulation. The adjusted flow curves were therefore used in subsequent simulations to analyse stress distributions at the onset of damage to the microstructure. The next step concerning the microstructure simulations was to check that the displacement vectors measured through DIC were correctly transferred as boundary conditions for the finite element simulations describing the deformation of the microstructure aimed at analysing the onset of damage nucleation. Strain distributions were measured by DIC, and predicted with the finite element model and then compared. Fig. 6.12 shows this comparison, and Table 6.3 shows the error between the experimental DIC strain and the simulated strain values for particular locations on the maps. The level of error associated with the maximum strain value was 3.1%, which is considered acceptable.

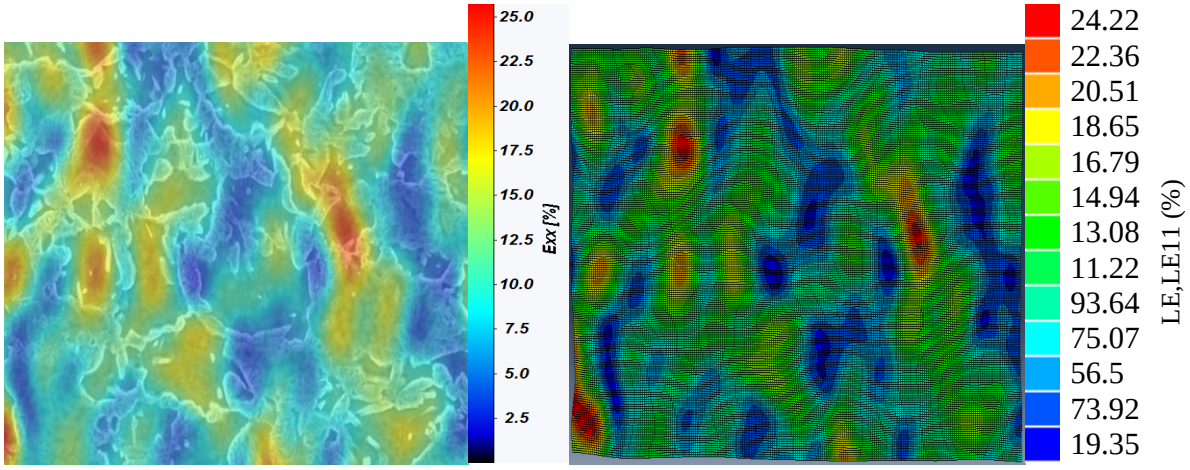

(a) (b)

Fig. 6. 12 Strain distributions for (a) experimental and (b) modelling result.

Table 6. 3 Error between experimental and simulation strain values

Experimental strain (DIC)	25	22.5	20	17.5	15	12.5
Simulation strain	24.22	21.74	19.2	16.79	14.31	11.84
Error (%)	3.11	3.35	3.65	4.04	4.55	5.27

After verification of the strain results, FE simulations were conducted to assess the stress distributions in the martensite and ferrite phases of DP1000. The aim of these simulations was to analyse the local stress resulting in damage to the microstructure.

The image selected for this study was captured prior to the appearance of the first, second and third cracks in the martensite. This made it possible to analyse the local stress values before the onset of the martensite cracking phase. The microstructure analysis corresponded to a global strain value of 0.048. The analyses then continued for a small area, including about six cracks within the martensite, as illustrated in Fig. 6.16.

Fig. 6.13 shows the FE simulation results, where the maximum principal stress was 1779 MPa prior to the commencement of cracking in the martensite. A high stress values occurred in the

martensite ranging from 629 MPa to 1779 MPa, with the stress values in the ferrite ranging from 52 MPa to 485 MPa.

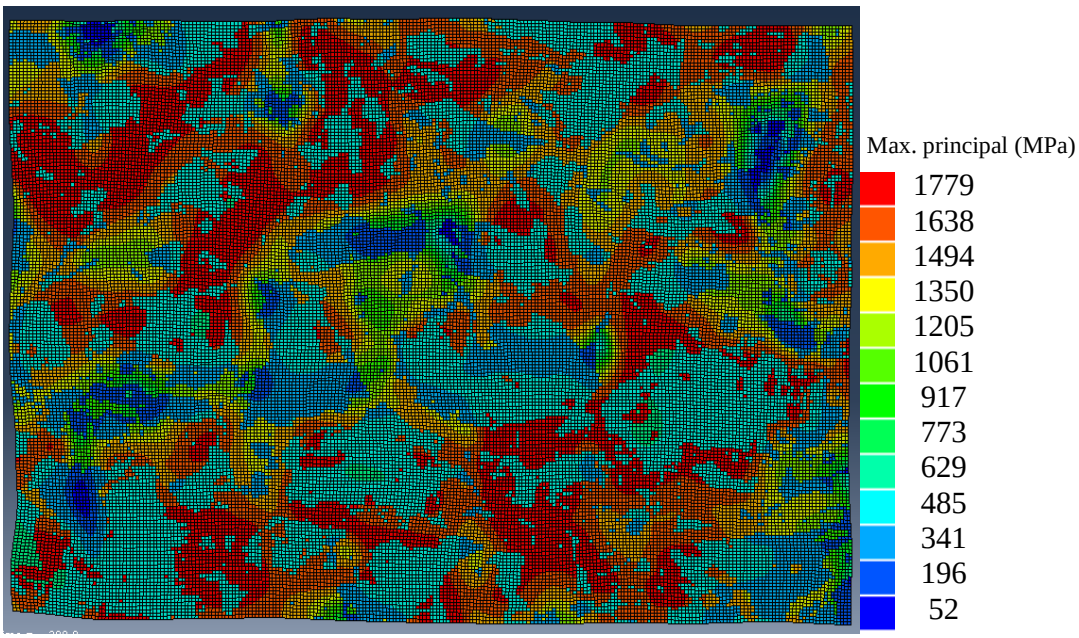

Fig. 6. 13 Maximum principal stress distribution in the two-phase microstructure (in MPa) at 0.048 global strain.

Fig.6.14 depicts the significant difference in the von Mises localised stress results between the ferrite and martensite regions. The maximum stress value in the ferrite was about three times that found in the martensite. Therefore, heterogeneous stress could be examined by studying the standard deviation between the ferrite and martensite.

Fig.6.15 shows the frequency distribution of von Mises stress in the ferrite and martensite phases. The mean value of the ferrite von Mises stress was 516 MPa; whereas, the stress affecting the martensite was 1539 MPa. The standard deviation in the martensite was 8, which was much smaller than the 27 found in the ferrite. Hence, the stress distribution of DP1000 in the ferrite phase exhibited greater heterogeneity.

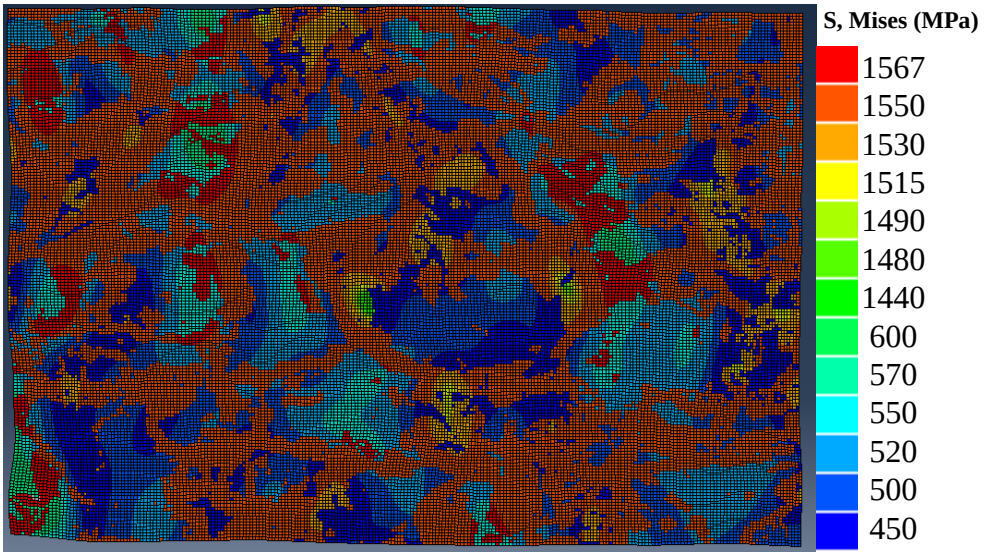

Fig. 6. 14 Results on von Mises stress distribution (in MPa).

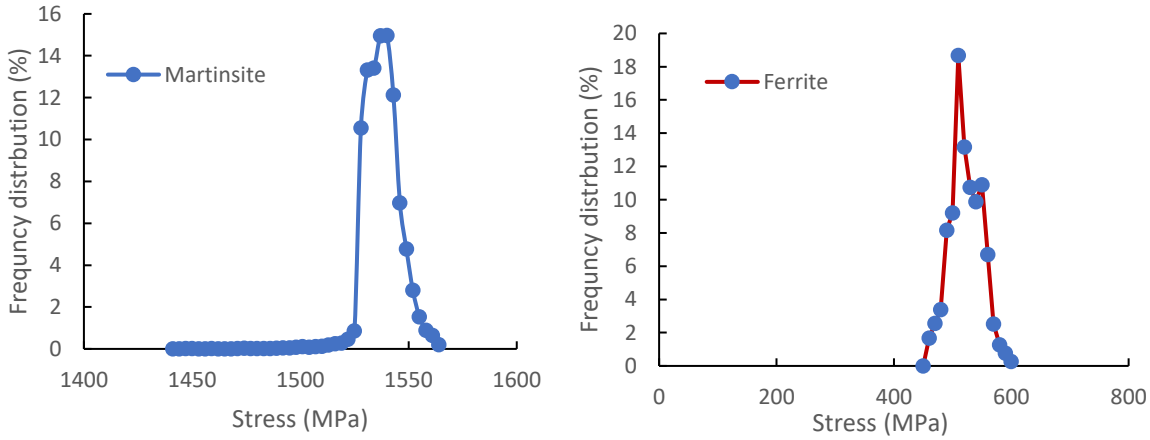

Fig. 6. 15 Results on von Mises stress frequency distribution for both martensite and ferrite.

Microstructure modelling was performed to investigate and study the onset of the damage caused by the cracking in the martensite, and the voids in the ferrite. Inspection for cracks in the SEM images revealed a small area in which six cracks occurred in the martensite phase during the test. This small area is depicted in Fig. 6.16.

The experimental results in chapter 5 revealed that some cracks had high strain values, and others were close to the maximum strain deformation value for the ferrite. Fig.6.16 shows the strain distribution in the image selected in the tensile test in the ‘X’ direction at 0.11 global

strain. The black lines in the image indicate the locations of the martensite cracking as reported in chapter 5.

Fig. 6.17 shows the FEA simulation results in terms of the distribution of maximum principal stress values in the microstructure. The black circles in Fig. 6.17 highlight locations with high stress values in the martensite. It is therefore evident from these results that cracks that appeared experimentally in the martensite were located in the regions of high stress values. However, there are also regions of high stress values that did not experience martensite cracking. The maximum principal stress value experienced in the martensite at the point where the cracks initiated was calculated as 1783 MPa. Additional details concerning fig.6.17 maximum principle stress is given in the Appendix XIV figs XIV.1 (a) and (b).

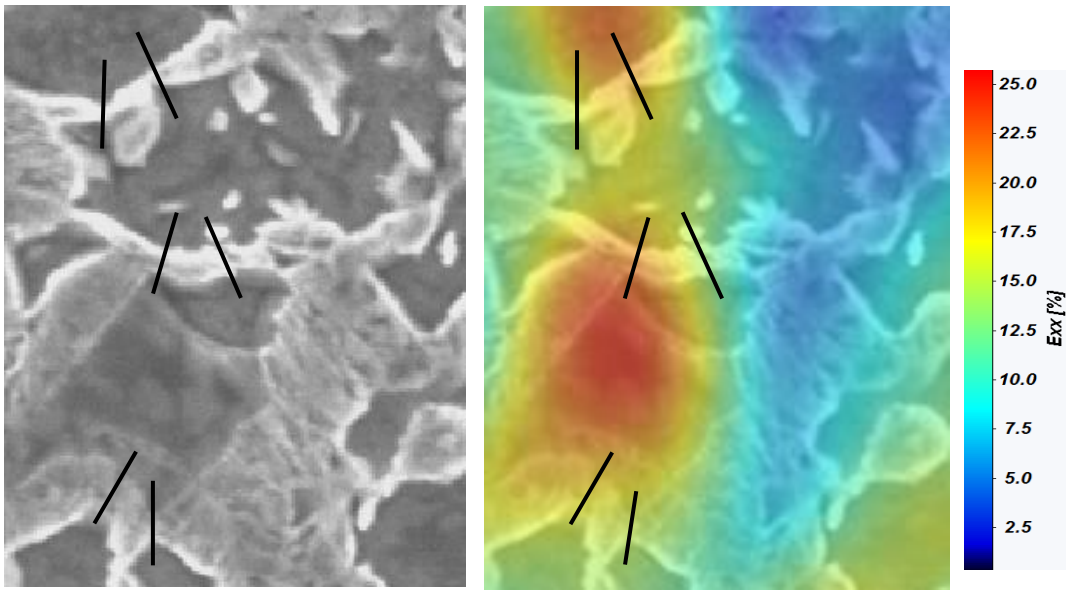

Fig. 6. 16 Strain results for the area where six cracks occurred in martensite. The black lines indicate their locations (the X direction is horizontal).

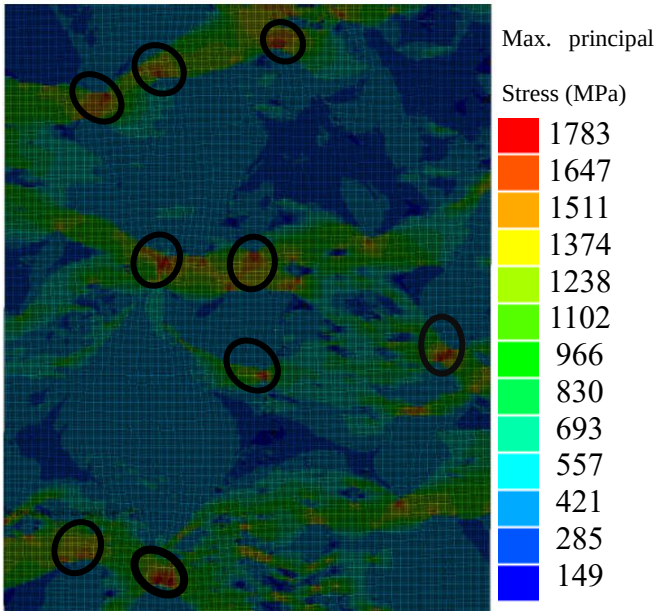

Fig. 6. 17 Maximum principal stress distribution (MPa) in the martensite phase. Highlights on martensite phase: black circles indicate maximum principal values located in crack region and other areas where cracks could occur.

The microstructure simulation was also used to investigate the nucleation of ferrite voids with regard to stress distribution. Experimentally, the ferrite voids were initiated under high global strain values of 0.26 and 0.3, as shown in table 5.1. The local strain value upon initiation for the first and second voids was 104%, while the local strain values for the third and fourth voids were 141% and 75% respectively (see Table 5.3).

Four microstructure images were selected to investigate stress distribution in the voids prior to damage initiation. Figure 6.18 shows the ferrite voids and the corresponding stress distribution values in the microstructure, just prior to when the voids appeared. The voids were highlighted by circles in the images, as initiated in high stress regions at maximum principal stress values of approximately 921 MPa for the first void (example shown in Figure 6.18). 923 MPa for the second void, 990 MPa for the third void and 915 MPa for the fourth void (see the Appendix

XV Figures XV.1, XV.2 ,and XV.3 for more details). The results are as summarised in Table 6.4.

Table 6. 4 Summary of results for ferrite voids initiation.

Void number	Global strain value	Local strain value	Local stress value (MPa)
1	0.26	104%	921
2	0.26	104%	923
3	0.3	141%	990
4	0.3	75%	915

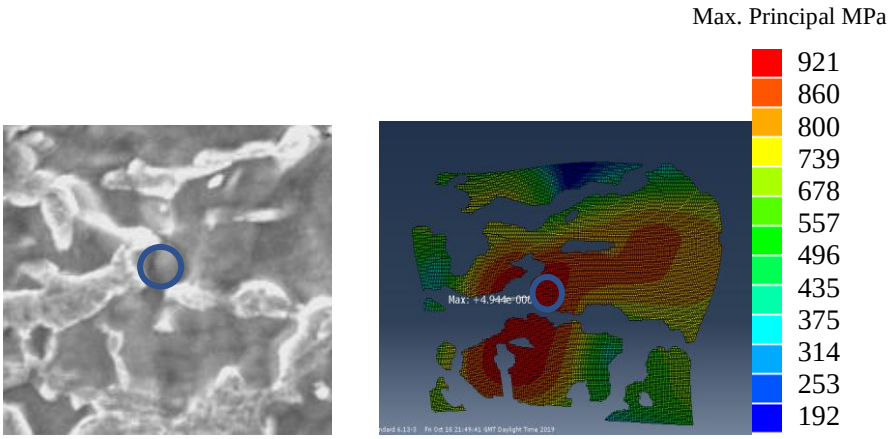

Fig. 6. 18 Maximum principal stress distribution before the first void appeared in the microstructure in the tensile test (0.26 global strain).

6.3 Macro-scale modelling to analysis the fracture of DP1000

Finite element modelling was conducted to simulate the deformation of DP1000 up to the point of fracture. Experimental strain measurements obtained through DIC and reported in chapter 5 were used to validate some of the simulation data. The following subsections report on the simulation of the macro punch test, the SPT, and the bending test.

6.3.1 Formability punch test FE simulation

Fig. 6.19 compares the finite element simulation of the deformation of DP1000 during the macro punch test and the experimental curve measured. It is worth noting that damage

modelling was not implemented in these simulations as the work was focused on developing the SPT. Reasonably good agreement could be obtained between the two curves. Fig. 6.20 shows the comparison for strain distributions in the specimen between simulation (LE11 and LE22) and the experimental (Exx and Eyy) results for an applied displacement of 9.95 mm prior to the appearance of a crack. The errors that occurred between the two results for maximum strain ‘exx’ and ‘eyy’ values were 2% and 3%, respectively, and these were considered acceptable.

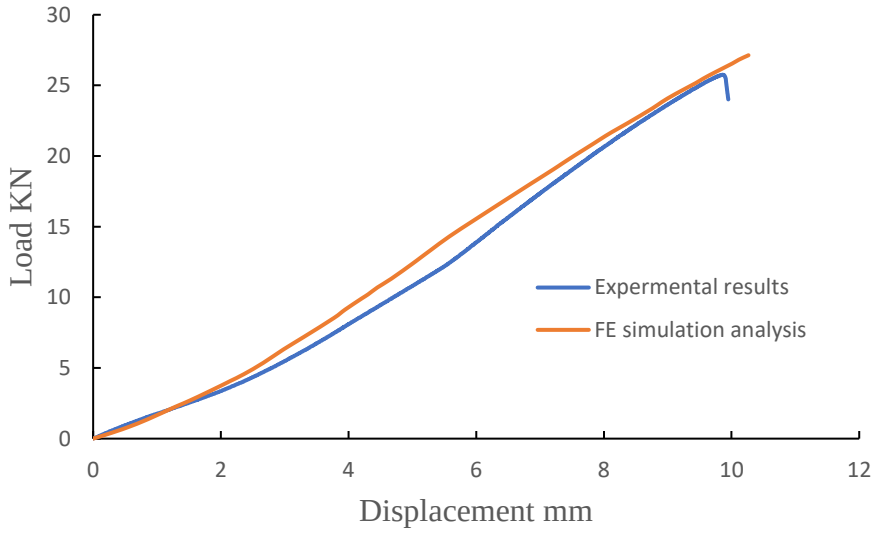

Fig. 6. 19 Load-displacement curves comparing the punch test experimental results with the FE punch simulation analyses.

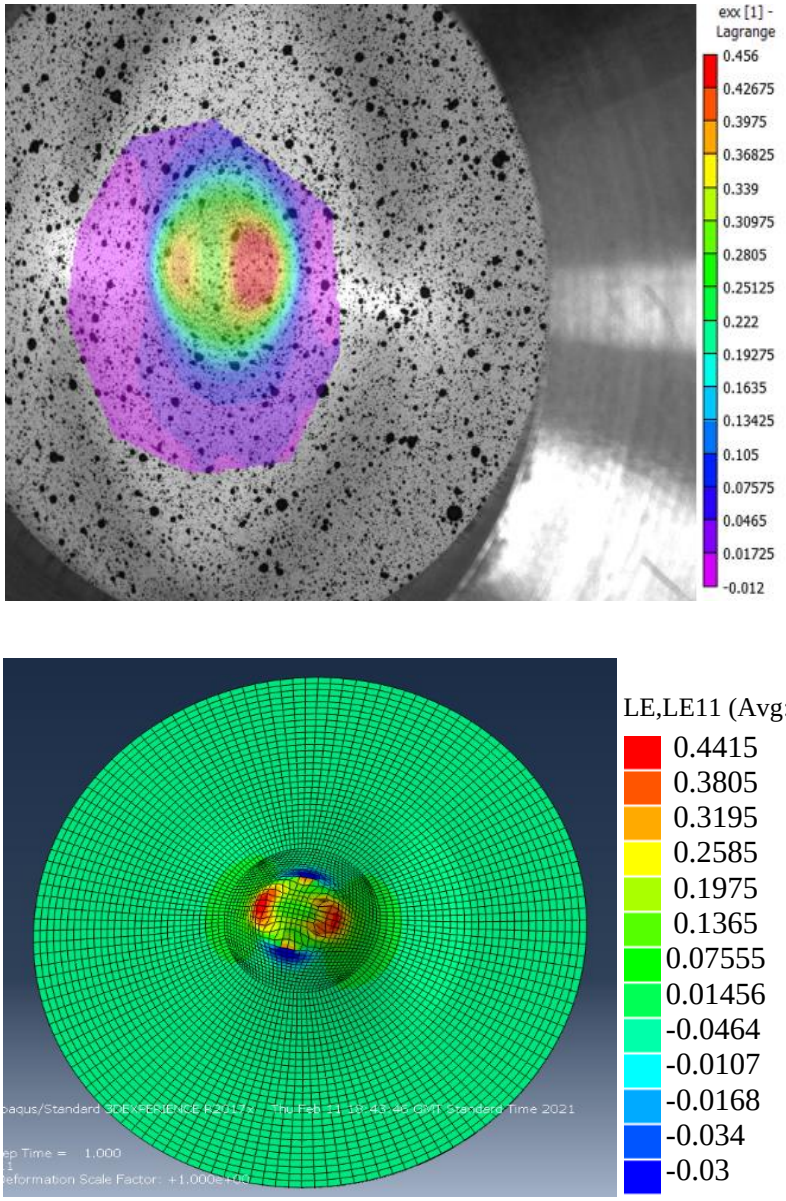
exx [1] -
Lagrange
0.456
0.42675
0.3975
0.36825
0.339
0.30975
0.2805
0.25125
0.222
0.19275
0.1635
0.13425
0.105
0.07575
0.0465
0.01725
-0.012

LE,LE11 (Avg:75%)
0.4415
0.3805
0.3195
0.2585
0.1975
0.1365
0.07555
0.01456
-0.0464
-0.0107
-0.0168
-0.034
-0.03

(a)

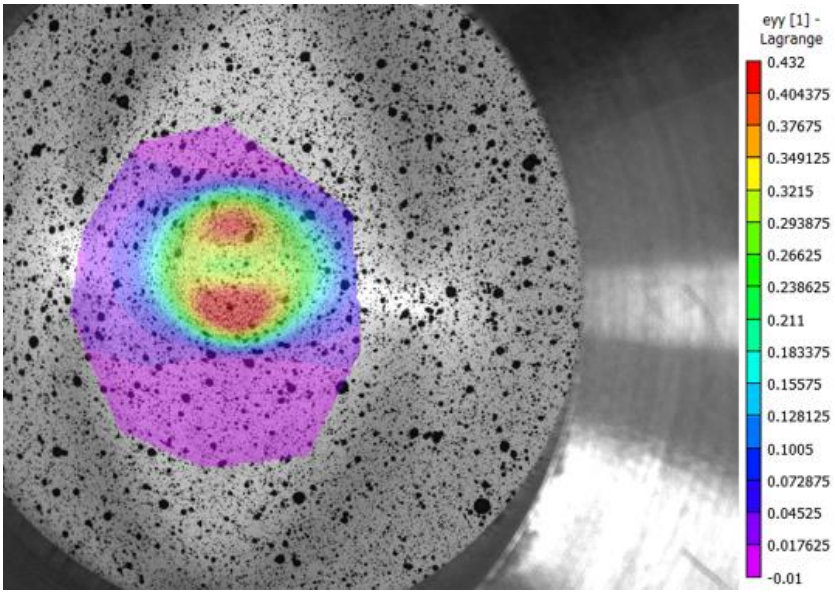

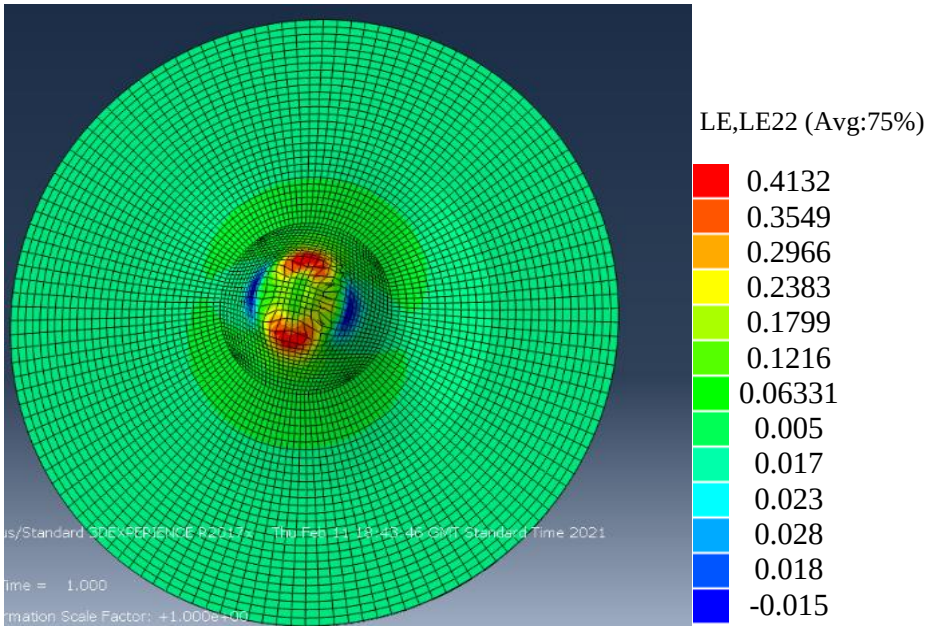

(b)

Fig. 6. 20 (a) comparison between LE11 strain distributions in the simulation and Exx in the experiment, at displacement of 9.95. (b) distribution of computed LE22 compared to experimental Eyy.

6.3.2 Small punch test

Strain distributions in the DP1000 specimen were analysed in greater detail in the SPT. A mesh refinement study was first conducted to assess whether the results attained were mesh independent. Four simulation models with different element sizes through thicknesses 2 to 8 (as shown in Fig.6.21) were generated. The graph compares the maximum strain values of Exx

and Eyy for element sizes 2, 4, 6 and 8, of which the best element size to achieve mesh independent results while minimising computing time was found to be 8.

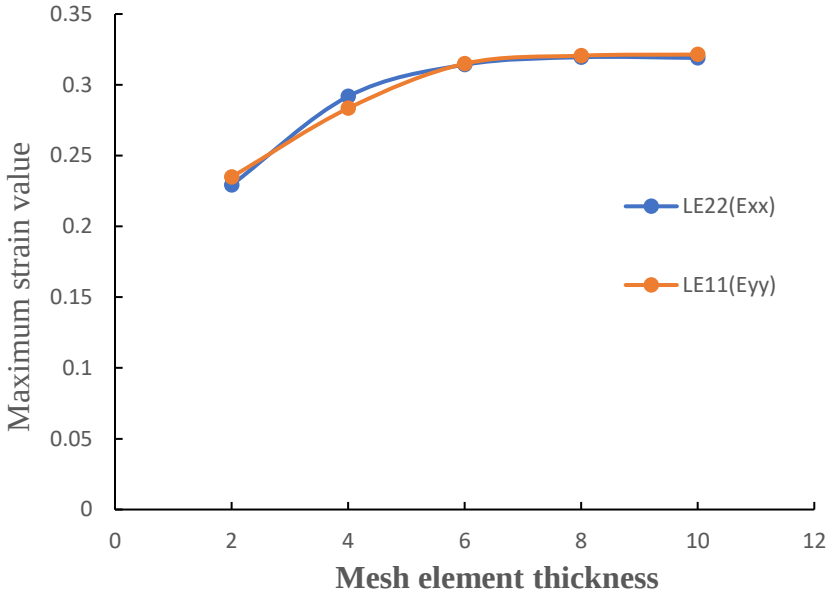

Fig. 6. 21 Maximum strain value obtained for small punch model with mesh element sizes 2, 4, 6 and 8.

As for the macro punch test, comparison between the load-displacement curve predicted by the model and the experimental curve is shown in Fig.6.22, not inclusive of damage modelling. Once again good agreement is observed between the two curves up to the point of maximum load. Comparison of the strain distributions between modelling and DIC results is shown in Fig. 6.23. As for the macro punch test, results show the plastic deformation of DP1000 prior to fracture of the specimen was predicted with reasonable accuracy in the model.

The damage was explored by analysing damage criteria, such as the equivalent plastic strain, as shown in Fig.6.24. Fig.6.24 (a) shows that at the beginning of the test the maximum equivalent strain value was located at the surface of the specimen in contact with the tool, with a maximum value of 7%. As deformation continued, the maximum strain value moved to the top surface of the specimen, with a maximum value of 8%, and remained there until the point

of final fracture. The maximum plastic strain value reached 66% when the crack appeared on the top surface of the small punch sample.

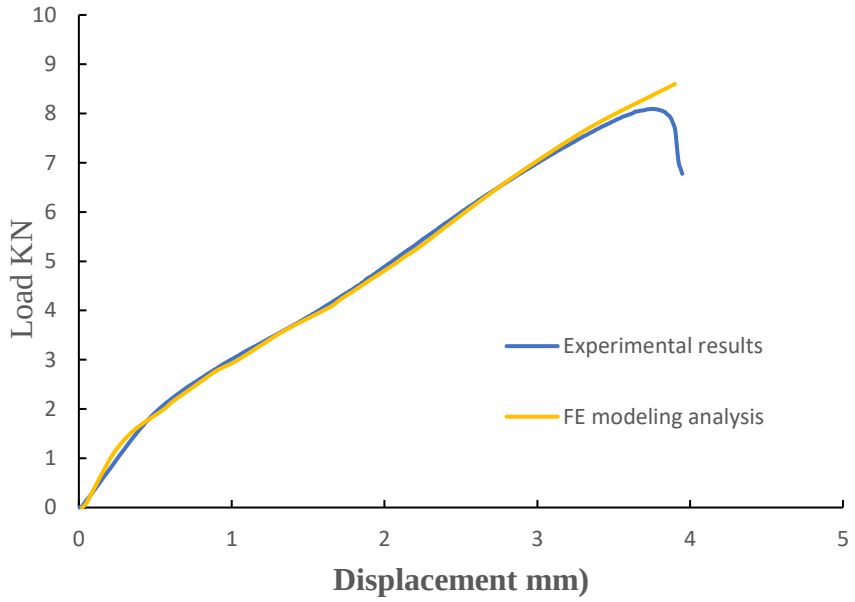

Fig. 6. 22 Experimental results compared with the results of the modelling.

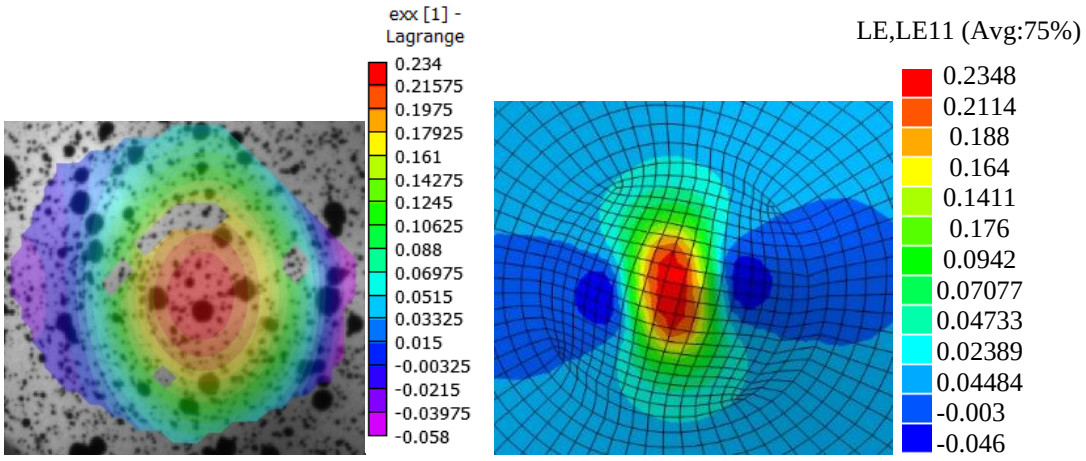

(a)

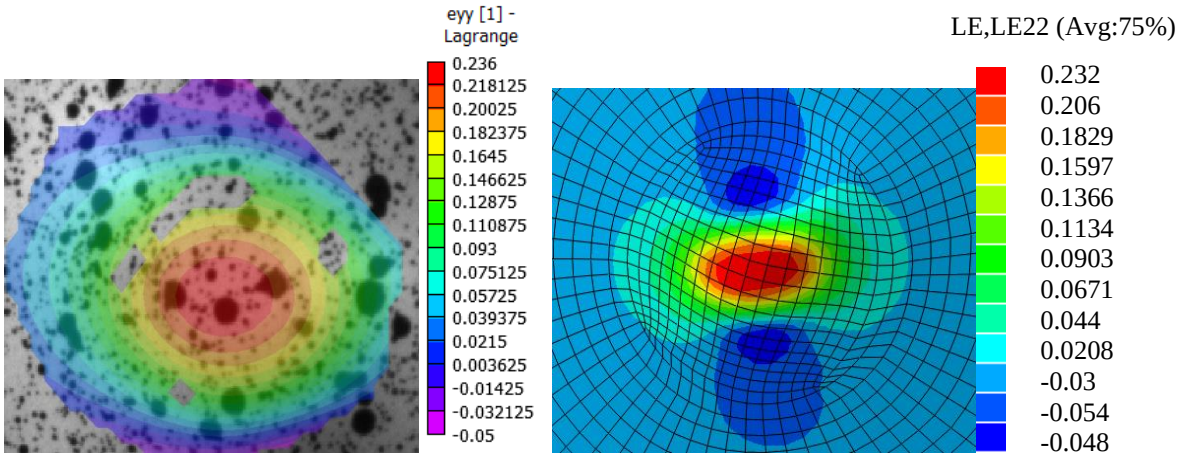

(b)

Fig. 6. 23 (a) and (b) LE11 and LE22 Strain distributions from Abaqus compared to Exx and Eyy experimental results respectively .

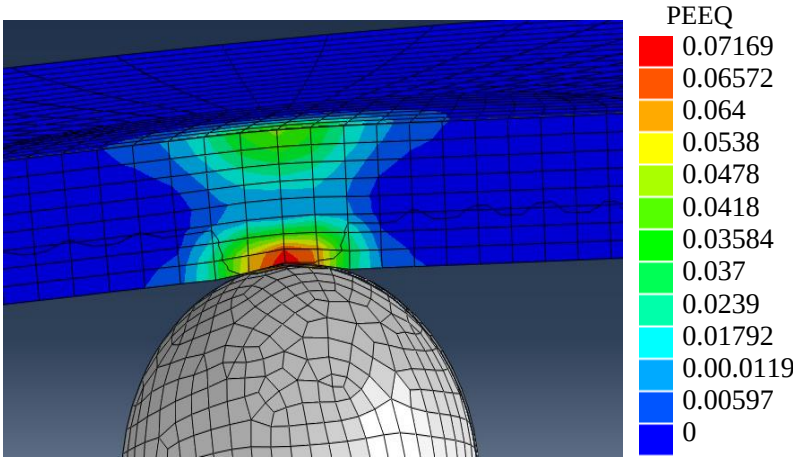

(a)

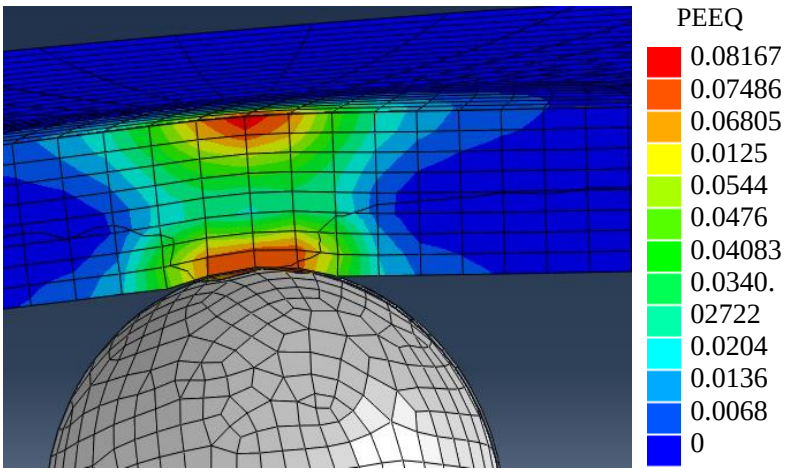

(b)

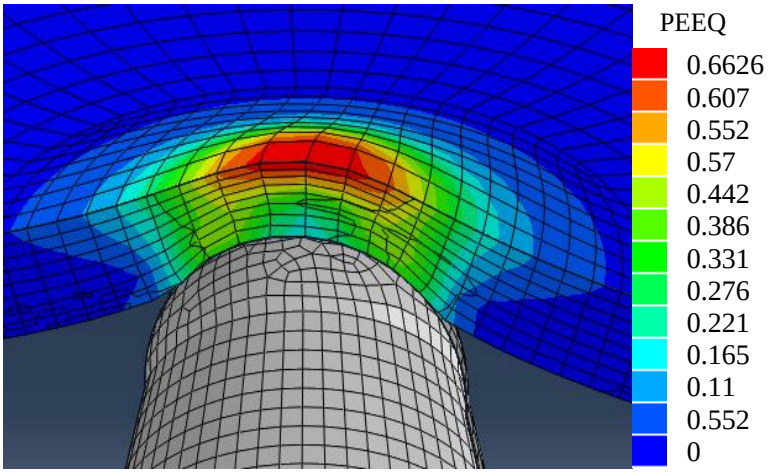

(c)

Fig. 6. 24 Equivalent plastic strain distributions through the thickness: (a) maximum value of about 7% at the surface in contact with the tool, (b) maximum value of about 8%, moving to the top surface of the sample, and (c) Prior to final fracture with a maximum value of 66%.

The GTN model was therefore also used in the SPT to check whether the parameters identified under tensile loading were also suited to this test geometry with biaxial loading. Fig. 6.25 compares the modelling results and the experimental curve. The same q parameters as those used present in the tensile tests were applied first (q1 = 1.6, q2 = 1.1, q3 = 2.56). Minimum values for the q parameters were also used (q1 = 1, q2 = 0.9, q3 = 1) to clarify the effect on the drop and curvature of the final part of the curve. However, as the results show, good agreement could not be obtained between the predicted curves and the experimental curve. As the experimental work changed direction and moved to the in-situ bending test at a later stage in the PhD, the applicability of the GTN model to more complex geometries was not explored further.

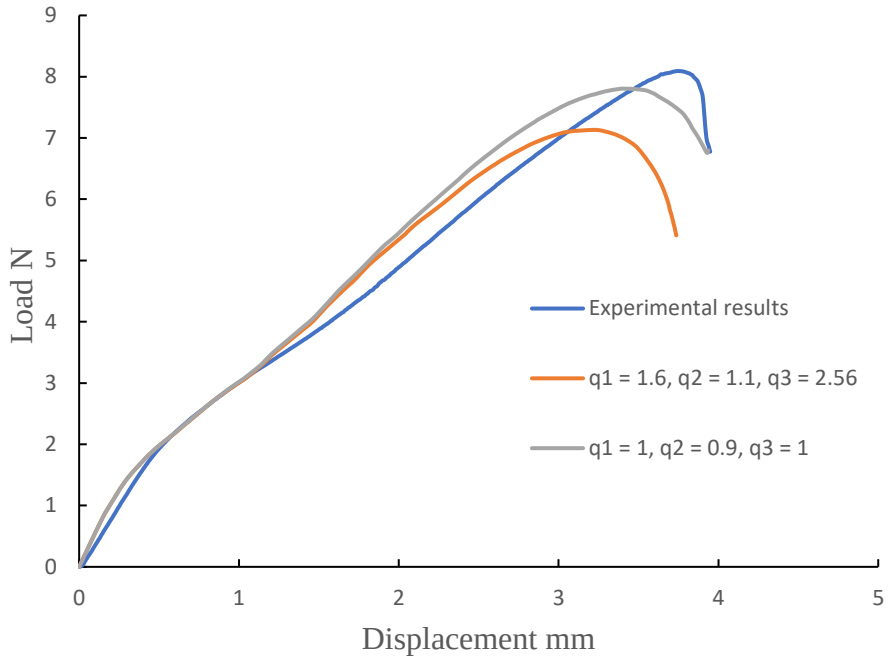

Fig. 6. 25 Comparison between GTN simulations with different q parameters and experimental results.

6.3.3 Bending Test

The three-point bending test was carried out inside the SEM, and was also simulated using Abaqus to understand the mechanical conditions leading to crack initiation at the edge of the sample (surface of observation in the SEM), on the tensile surface in the bespoke specimen geometry. Fig. 6.26 compares the load-displacement curves between the simulation and the experimental measurements. Although not perfect, the agreement between the simulation and experimental curves remains acceptable, with most discrepancies emerging in the part of the curve corresponding to damage development, as crack propagation was not simulated in the specimen . The agreement was better for the hardening part of the curve before the appearance of a crack, and Fig. 6.27 shows the equivalent strain distribution results for both the edge and the top surface of the specimen. These results show the bespoke geometry of the specimen used in the in-situ test led to a maximum equivalent strain value located at the surface of observation in the SEM, thereby making this test configuration well-suited to studying damage initiation

and propagation at the microstructure scale. Therefore, damage criterion can be estimated using the FE simulation. The first cracks were initiated at a maximum strain value of 43%, and were located on the tensile surface (where the crack started propagating) (see Fig.5.29).

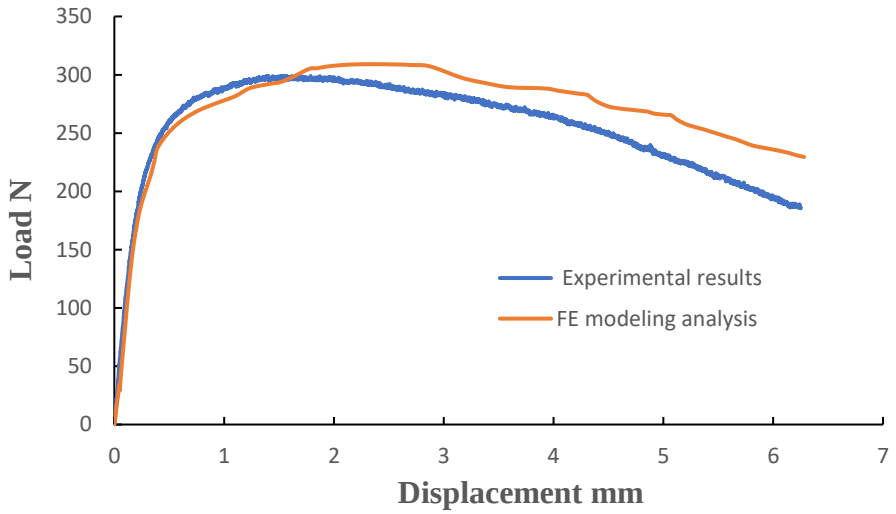

Fig. 6. 26 Load-displacement curve for experimental bending test compared to simulation results.

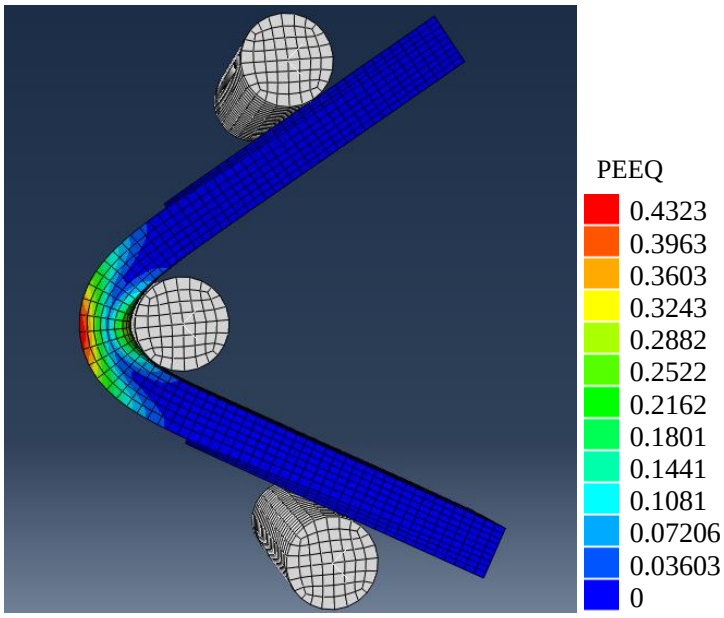

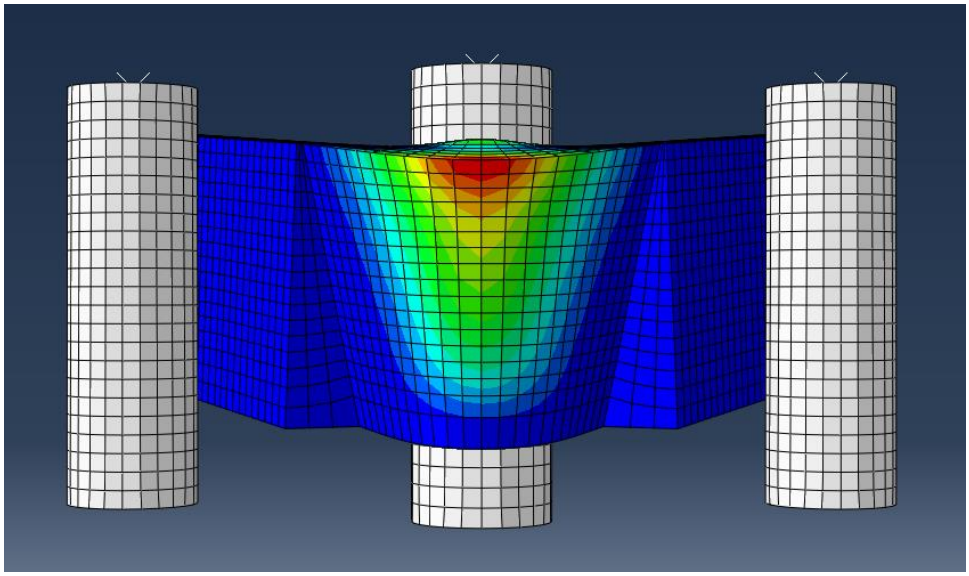

Fig. 6. 27 Top and front views of the equivalent plastic strain distribution on both the edge and the top surfaces of the specimen prior to the appearance of a crack.

6.4 Conclusion:

This chapter reported results the for the multi-scale modelling approach adopted to study the processes of deformability and damage development in DP1000. Modelling at the scale of the microstructure revealed that the original approach developed in this work as it applies to strain distributions, when measured by DIC as boundary conditions for finite element simulations. This enables a study of damage initiation in both the martensite and ferrite in relation to local strain and stress states. Damage development was also studied through a novel in-situ bending test, with modelling results showing that crack initiation started on the surface of the specimen, and was observed in the SEM at the location of the point of maximum equivalent strain. The nucleation strain could therefore be inferred from the modelling results. The simulation results for the punch tests showed very close agreement with experimental measurements, not only for the overall load-displacement curves, but also with the strain distributions measured with DIC. The maximum equivalent strain distributions throughout the thickness of the new SPT sample revealed how maximum strain moves from the surface in contact with the tool to the top surface

of the specimen throughout the test, making the analysis of failure more complex than in the case of the in-situ bending test. Experimental results were reported in Chapter 5, and confirmed crack initiation at the surface in contact with the tool. All the new modelling results obtained in this chapter can therefore be used to develop more advanced multi-scale models showing deformation and damage to DP1000, especially as the traditional GTN model portrayed key limitations transferring damage parameters, as calibrated against tensile testing, to more complex testing geometries that are representative of forming operations.

7. DISCUSSION

According to the results from the micro tensile test, the small punch and bending tests conducted on the DP1000 sample and reported in Chapter 5, damage occurs at the microstructure level following the localisation of plastic deformation, and then continues to develop until the specimen fractures. The following sections discuss and summarise the deformation, damage development and fracture mechanisms, affording new insights to explain the high formability of DP1000 and identifying predictive factors.

7.1 Plastic deformation

AHSS are used in the automotive industry, offering both high strength and high formability. The properties of DP1000 are of particular interest, as demonstrated by the tensile results shown in Fig. 5.1 for the standard specimen with UTS, and strain to failure values of 1109 MPa and 11%, respectively. Formability is most effectively assessed through a punch test with deformation conditions involving operations with maximum principal strain values of about 50%, as recorded during the macro punch test prior to failure (Table. 5.5).

Plastic deformation at the scale of the microstructure was clearly observed during the in-situ tensile and bending tests. Fig. 5.10 shows strain values as high as 250% were measured in the ferrite phase in the localised deformation bands, and 220% in the martensite phase prior to specimen failure for the in-situ tensile test. These high strain values are realistic, and in line with those reported by (Ghadbeigi et al., 2010) and (Rohaizat, 2018), contributing evidence to verify the high ductility of the martensite phase in DP1000. The results for the new bending test carried out in the SEM in this work also confirmed high strain values were experienced in the microstructure, with strain values of about 135% recorded in the ferrite and about 90% in the martensite (see Fig. 5.28). The frequency distribution of the strain values at the UTS point

in the tensile test (Fig. 5.11) further demonstrates the martensite and ferrite phases are very ductile, where the mean values for both phases is 10%, corresponding to (Rohaizat, 2018).

Regardless of the test geometry, plastic deformation in the microstructure of DP1000 began with localised deformation in the ferrite phase, apparent from the formation of local deformation bands (Fig. 5.4 and Fig. 5.25). This stage was then followed by the formation of large deformation bands connecting the ferrite areas at points where large deformation bands were concentrated (e.g., Fig. 5.9, Fig. 5.10 and Fig. 5.28). As these large deformation bands develop, they cross martensite islands in their path, promoting damage in the martensite phase.

7.2 Martensite damage

According to the results of the micro tensile, small punch and bending tests conducted on the DP1000, damage occurs at the microstructure level and develops until the specimen fractures. The most commonly observed first damage event corresponds to the cracking of some martensite islands, with initiation usually occurring around the UTS point in the stress-strain curve of the in-situ tensile test, and around the point of maximum force in the in-situ bending test (Table 5.1 and Fig. 5.13(b) for the in-situ tensile test, Fig. 5.27 and Table 5.4.1 for the in-situ bending test). It is important to note; however, that the cracking of martensite islands does continue throughout the test, although it is more frequently observed around the point of maximum force. Three mechanisms that appear to contribute to initiating martensite cracking have been observed. The first mechanism corresponds to martensite cracking without extensive noted deformation of the surrounding ferrite (Table 5.1 and Table 5.9). A more prominent mechanism corresponds to martensite cracking following significant deformation of the surrounding ferrite (Table 5.1 and Table 5.9). Finally, a third mechanism, which is not often observed, corresponds to martensite cracking following, and is void ferrite formation, which causes martensite cracking (Table 5.1 and Table 5.9). These initiation mechanisms eventually

result in martensite cracking, which is classified as an early form of damage in DP1000, as is also reported in (Alharbi, 2015; Ghadbeigi et al., 2010). Damage initiation, in martensite was further analysed using local strain measurements obtained through DIC. The initiation of thirteen martensite cracks was studied in the in-situ tensile test, and seven martensite cracks occurred in the bending test. The local strain value was measured just prior to the onset of the cracking of the martensite. Strain values ranging from 8.8% to 31% were recorded before the UTS, and from 33% to 143% after the UTS for the in-situ tensile test. In the case of the in-situ bending test, local strain values ranging from 20% to 50% were measured. Fig. 7.1 shows these results in the form of distribution graphs to allow a clearer comparison.

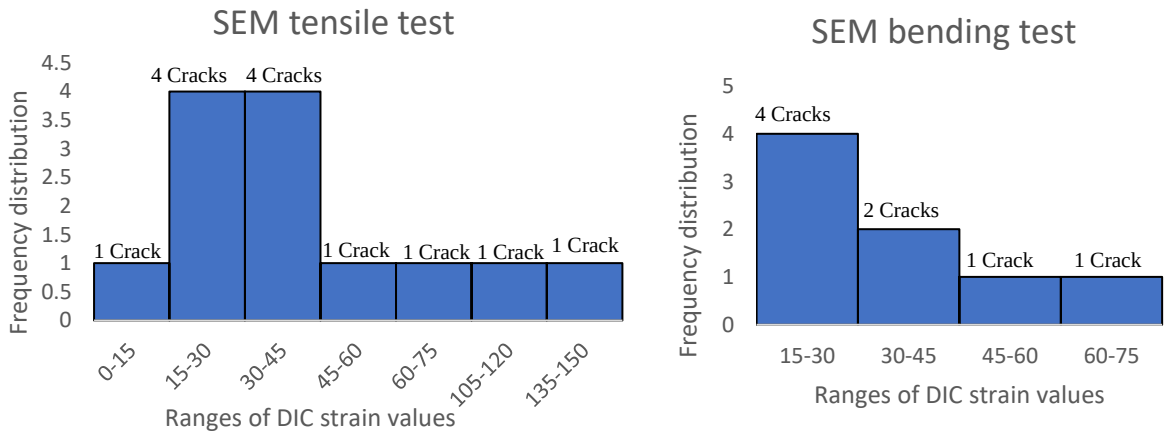

Fig. 7. 1 Distributions of strain values at the onset of the martensite cracking phase. Left: in-situ tensile test; and Right: in-situ bending test.

Despite the limited number of measurements, the results illustrate that statistically more martensite cracking occurs at local strain values ranging from 15% to 45%. These results show a greater range of strain values at the onset of martensite cracking than (Rohaizat, 2018). However, the results reported in (Rohaizat, 2018) were gathered from various DP1000 steels undergoing different heat treatments, and insufficient measurements were recorded for each heat-treated steel. Furthermore, damage initiation in martensite was further analysed here through finite element simulations, as reported in chapter 6. The results described the initiation

of martensite cracking in locations with high principal stress values, and in martensite islands with a local stress value of about 1783 MPa for the six martensite cracks analysed. These results therefore suggest martensite cracking initiation is more stress-controlled than strain-controlled, which aligns with results reported by (Alharbi et al., 2015), who only analysed 3 martensite cracks, and reported a principal stress value of 1700 MPa upon initiation. However, the finite element simulations reported in Fig. 6.17 also show that martensite regions of high principal stress values did not trigger crack initiation. Therefore, while statistically martensite cracking appears to typically initiate in response to the critical local stress value, the results also show that this conclusion can only be confirmed after analysing a large number of martensite cracking events.

Observations clearly show that damage to martensite is the first main damage event to occur during the deformation of DP1000. This was reported in several studies carried out on various DP steels (Avramovic-Cingara, Saleh, et al., 2009; Calcagnotto, Adachi, Ponge, & Raabe, 2011; Erdogan, 2002; Ghadbeigi et al., 2010; Rohaizat, 2018). Typically, following damage initiation in the martensite phase a crack normally forms, leading to complete cracking of the local martensite island with the crack stopping when it meets the next ferrite interface. For example, Fig. 5.5 shows that martensite cracks initiated around the UTS point but did not propagate into the ferrite phase after complete cracking of the local martensite islands. Damage in martensite therefore does not determine the fracturing of DP1000, where extensive deformation is recorded in the ferrite phase (e.g., Fig. 5.10) before damage nucleation in the ferrite appears.

7.3 Damage initiation in the Ferrite

Nucleation of voids in the ferrite phase was analysed in this work for the first time, in response to several void initiation events during the in-situ tensile test. The appearance of voids in ferrite

was observed towards the end of the test (Table 5.2) at the point close to final fracture, which is why this damage event is rarely reported in the literature after a tensile test (only one void has been reported on, in (Ghadbeigi et al., 2010)). The results reported in Chapter 5 confirmed that voids in ferrite are initiated after very large deformations occur, with local strain values ranging from 75% to 140%, as measured with DIC. These results correspond to the value of 120%, as reported in (Ghadbeigi et al., 2010). These high strain values, which are reported for void nucleation in the ferrite are also consistent with ductile damage models that include nucleation strain as it affects void formation. Local stress distributions around void nucleation sites in the ferrite were also investigated via finite element simulations, as detailed in chapter 6. Fig. 6.18 elucidates that although the voids in the ferrite occurred in regions with high local stress values ranging from 915 MPa to 990 MPa, they did not appear at locations of maximum stress, except for one void (Fig. 6.18), in which the ferrite phase was highly constrained by the surrounding martensite phases. From these results, it is apparent that voids in the ferrite are likely to form after significant and large deformations in the ferrite phase (strain values of the order of 120%), which also generated high stress values concerning the extent of the deformation.

Even though damage nucleation in ferrite has been be successfully observed and analysed in this work, damage propagation in the ferrite was not visible before fracture of the tensile specimen when loaded in the SEM. Damage propagation in the ferrite phase was therefore investigated using the small punch test (SPT) first, and then the bending test.

7.4 Damage propagation in DP1000

Initially, damage propagation leading to failure in DP1000 was investigated in this work through a macro punch test, with full-field strain measurements recorded using 3D DIC. The failure of DP1000 was observed to occur under bi-axial loading conditions (see Fig. 5.18),

which were more representative of an industrial forming operation than a uniaxial tensile test, although the appearance of a crack was as shown in Fig. 5.15. A local maximum principal strain value of 50% was measured with DIC, as reported in Table 5.5. This value is in line with values reported in (Rohaizat, 2018). Limitations constraining the macro punch test's capacity to study damage propagation in the microstructure DP1000 led to the development of a new SPT for this work, as reported in section 3.4.2. This original SPT was designed to: 1. accommodate 3D DIC for full-field strain measurements on the top surface of the specimen, and 2. enable the transfer of the specimen to and from the SEM chamber after each interruption of the test to conduct microstructural observations. Table 5.7 shows the local maximum principal strain value of 23.8% just prior to the appearance of the crack in the sample (e.g., Table 5.7). The lower load and strain to failure in the SPT (Fig. 5.19 and Fig. 5.21) compared to the same values in the macro punch test (Fig. 5.14 and Fig. 5.17) were due to the different test geometries, but could also be attributed to the different damage propagation processes. Cross-section results for the macro punch test, as reported in (Rohaizat, 2018) showed cracks were initiated either on the top surface of the specimen, or at the surface in contact with the tool. Meanwhile the results for the SPT showed the main crack occurred at the surface of the specimen in contact with the tool (Fig. 5.23).

There may have been defects in the material, or unique friction conditions affecting the tool that may have encouraged crack initiation at the contact surface. The simulation results reported in chapter 6 indeed indicate high equivalent strain levels moving rapidly to the top surface of the specimen during the test (Fig. 6.24), with high equivalent strain values promoting crack formation, as observed in the in-situ bending test (Fig. 6.27). Nevertheless, the SPT results provided very useful insights into the progress of damage development in DP1000 at the scale of the microstructure. Observations of the top surface of the specimen at the microstructure scale in the SEM revealed damage mechanisms generating crack propagation

not evident in the in-situ tensile test. Results for the interrupted SPT show martensite cracking early in the test (Table. 5.6 case 2 and 3), as predicted based on the results of the in-situ tensile test. Furthermore, the SEM image also reveals small cracks were located in the ferrite phase, and started to appear at about 25% of maximum displacement to failure, as applied during the test (Fig. 5.19). At that stage the small cracks only propagated through one ferrite island, demonstrating that very early crack propagation can be studied using the experimental procedure developed. The specimen could also be adequately re-positioned in the SPT rig after SEM observations to continue with the test. The second interruption was to demonstrate significant crack propagation in the microstructure prior to the failure of the specimen. This was successfully achieved, as shown in Fig. IX.2 (Appendix IX) after large deformation of the specimen but without any cracks apparent. The corresponding SEM image, shown in Table 5.6 third column provides evidence of large crack development in the microstructure at different orientations, with cracks crossing martensite islands that appear to be fragmented. However, the image shows that at the level of applied deformation during the test, the large volume of out-of-plane deformation in the microstructure makes it difficult to resolve the damage mechanisms in the material in detail. Further tests should therefore be carried out to optimise the number of test interruptions, and to produce a more progressive study of crack propagation in the microstructure. However, due to the restricted access to labs as a result of the Covid-19 situation, and the limitations affecting the results obtained with the SPT, this option was not pursued.

Cross sections of the failed specimen reported in Fig. 5.23 clearly showed the mechanisms of damage propagation leading to failure of the material. Multiple large voids and extended secondary cracks were visible in the ferrite phase after extensive deformation of the microstructure. These voids initially arose close to the interface with the martensite, which is consistent with the observations of damage initiation in the ferrite during the in-situ tensile test.

Cracks then propagated either at the interface or in between elongated martensite islands when the microstructure was favourably orientated. Close observations of Fig. 5.23 reveal the main crack eventually crossed the martensite islands located in the path of the propagating crack, which began at the contact surface with the tool. Further tests should be carried out to confirm whether crack initiation always appears at the surface in contact with the tool in the SPT. This was not pursued once the more promising in-situ bend test became available.

Limitations on the SPT in terms of the analysis of damage propagation in the microstructure of DP1000 led to the characterisation of damage during the in-situ bending test. The test rig became available at a late stage in the PhD, but was instrumental in studying and analysing damage propagation, which was the primary aim of this work. Results from the in-situ tensile test revealed the limitations associated with characterising damage at the surface of the specimen in the SEM with damage initiating at mid-thickness and propagating towards the surface, leading to sudden failure of the specimen. In consideration of this, a bespoke specimen geometry was designed with a slanted top surface (Fig. 3.23) to bring the maximum equivalent strain value at the surface of the specimen, as observed within the SEM. Fig. 6.27 shows the finite element results highlighting the location of the maximum equivalent strain at the edge of the specimen, and along the line of maximum tensile stress in bending. Fig. 5.24 confirms the assumption made in terms of cracks initiating at the location of maximum equivalent strain in the specimen, with several cracks appearing along the line of maximum tensile stress at the observation surface in the SEM following a large bending deformation. It is noteworthy that some significant crack propagation could also be observed away from the fibres undergoing maximum tensile stress (see Fig. 5.30 e); however, propagation remained limited in comparison to the main cracks initiating where the equivalent strain was maximum. A large number of the latter type of cracks were analysed to clarify the mechanisms for initiation and propagation.

All the figures in section 5.4.2.2 provide evidence of crack initiation in the ferrite phase, which is in line with observations reported for the SPT.

Further evidence of this initiation mechanism can also be observed away from the edge of the surface of observation, with large voids observed in the ferrite in Fig. XII.2 (k) (Appendix XII) in a region of the microstructure not subject to the edge effect. The propagation pathway of the main cracks is then apparently influenced by the local microstructure, with propagation often impeded when the pathway encounters a cluster of martensite islands. These serve as obstacles generating a large amount of deformation ahead of the crack tip, as the amount of applied bending deformation is increased, leading to small cracks in the surrounding ferrite islands which eventually join up with the main crack as progressive failure continues. After a large proportion of propagation at about 45^{o} with respect to the loading axis, and through repetition of the previous mechanism, the main crack branches out of its original pathway after a propagation over about 0.5 mm (as shown in Fig. 5.33 in section 5.4.2.2). This sudden change in the crack path at the macroscopic level might relate to changes in the stress/strain fields in the specimen due to the presence of a large crack. The initial orientation at 45^{o} seems to indicate that the crack propagates through a shear mechanism.

The results from the FE simulations (Fig. 6.27) indicate that cracks are initiated in the specimen at a continuum strain value of about 43%. It would be interesting to conduct further bending tests in the SEM with the aim of analysing crack initiation at the scale of the microstructure, in relation to local strain distributions. Thus, it is supposed that there is a compromise to be found between the magnification used to capture images in the SEM such that they can be processed successfully by the DIC software, and the magnification required to ensure that a crack will appear within the captured image. Unfortunately, such trial-and-error processes could not be conducted here due to time constraints and the restricted lab access arising from the Covid-19 situation.

Significantly, a key limitation of this work is that the results only inspect damage leading to the final failure at the specimen surface using SEM observations. It is likely that damage might also be occurring below the surface during deformation. It was not possible to capture such damage events in this work but future work could involve X-ray computed tomography (CT) measurements to inspect damage below the surface in a non-destructive manner.

7.5 Damage modelling

Chapter 6 of this work reported results concerning damage modelling carried out to predict the mechanical response of DP1000 under uniaxial or biaxial loading. The GTN model, which is commonly used to simulate the damage of ductile materials, was also applied to DP steels in the literature (Alharbi, 2015; Corigliano et al., 2000; Kim et al., 2004). The GTN model was therefore selected for this work as it had been successfully applied to DP1000 previously (Alharbi, 2015). Calibration of the damage parameters is commonly performed using tensile notched specimens with validation carried out using different test geometries. Figs. 6.6 and 6. 7 showed the model can provide a very good match with the experimental curves by adjusting the model parameters reported in Table 6.1. The model was successfully validated against the load-displacement curve recorded during the in-situ tensile test with a specimen geometry designed to highly concentrate stresses in a very small gauge length to facilitate damage observations in the SEM, while ensuring compatibility with the maximum load capacity of the in-situ tensile stage.

The results reported in Fig. 6.8 show the GTN model was able to simulate the response of DP1000 under uniaxial loading with acceptable accuracy. This result is in line with the results reported in (Alharbi, 2015). However, application of the GTN model to the punch test (Fig. 6.25) showed the limitations of the application of the model to biaxial loading conditions, with the modelling curves unable to simulate the sharp drop observed in the experimental load-

displacement curve, corresponding to damage development in the material, regardless of the parameter values employed. It therefore became evident that physical understanding of the damage process should be a priority when developing more advanced damage models for DP1000. The experimental work was therefore further developed using the novel results reported in previous sections, so as to bring new insight into the deformability and damage development mechanisms in DP1000. Such results clarify the reasons behind the exceptional properties of AHSSs, and provide the means for the development of more advanced multi-scale models aimed at predicting the overall mechanical response to the material, under either uniaxial or multi-axial loading. An approach based on Representative Volume Elements could be envisaged in the future to improve the modelling predictive capability. As previously mentioned SEM-based observations would have to be complemented by X-ray CT measurements for a full 3D characterisation of damage in the material in order to minimise modelling errors.

8. CONCLUSION AND FUTURE WORK

8.1 Conclusion

This research aimed to improve the physical understanding of the deformability and damage propagation mechanisms in DP1000 microstructures deformed under uniaxial and biaxial loading. Particular attention was paid to the issue of damage propagation, and the literature review highlighted a lack of information regarding the mechanisms leading to the final failure of the material. These mechanisms therefore control the deformation to failure of the material, which is of particular interest in the case of industrial forming operations.

Novel experimental procedures were developed in this work to provide new insights based on analysis provided through multi-scale modelling. An in-situ tensile test and a new in-situ bending test, with a bespoke specimen geometry, were conducted inside a SEM, in combination with full-field strain measurements using DIC to analyse plastic deformation localisation, damage initiation in both martensite and ferrite as well as damage propagation in DP1000. A small punch test (SPT) with 3D DIC was also developed to study damage development in microstructures subject to biaxial loading.

Martensite cracking did not lead to propagation in the ferrite phase, which deformed heavily before voids in the ferrite could be observed towards the end of the in-situ tensile test. Several voids in the ferrite were observed for the first time, and the same analysis as that performed for martensite could therefore also be applied to ferrite. The results from the finite element model showed that although the stress values were relatively high at damage initiation sites, the highest stress values were commonly observed at other locations in the ferrite phase. Given the very large strain values recorded before a void in the ferrite could be observed, it is suggested that damage affecting the ferrite is strain-controlled, with the relatively wide range of recorded strain values, possibly due to the lack of statistical results.

Damage propagation in the case of the scale of the microstructure was first observed in the SPT through interruptions to the test, and the transfer of the specimen to and from SEM. Early crack propagation in the ferrite phase was captured successfully by this new experimental procedure, which also showed further development of cracks throughout the test.

Unfortunately, the large deformation steps applied between the successive interruptions did not allow for local strain distributions to be measured at this scale, while macroscopic DIC measurements recorded the strain to fracture of the specimen at about 23%. This value differed significantly from the 50% measured value recorded in a macro-punch test. It is understood that this difference might be due to the fracture mechanism, which might have varied between the two tests. Inspection of the cross section after the test revealed that a crack was initiated at the surface in contact with the tool during the SPT, while cracking at the top surface of the specimen was reported in a previous study. Damage propagation mechanisms could however be observed through the inspection of the cross section of the specimen, and the results revealed that cracks were propagated mainly in the ferrite phase, but also occasionally traversed the martensite islands located on their path. These damage propagation mechanisms were further confirmed by the results obtained during the new in-situ bending test, which successfully led to crack initiation at the surface of the specimen observed in the SEM, and at the location of maximum equivalent strain with a value of 43% calculated by a finite element simulation. Extensive crack development was recorded with initiation in the ferrite phase, and propagation was sometimes hindered by clusters of martensite islands along their path, but eventually continuing in the ferrite phase.

Damage modelling using the GTN model was also tested during this work. Although the model was performed when predicting the mechanical response of DP1000 under tensile loading, the results clearly showed the limitations of the model under biaxial loading. It is therefore believed that better physically based models of damage development in DP1000 need to be developed

in the future in response to the novel experimental insight and analysis generated in this work. Such models would indeed help the steel industry design optimal microstructures to develop next generation automotive steels.

8.2 Future work

Various avenues for future work exist based on the results obtained in this study. Further bending tests with DIC should be conducted to analyse crack initiation and propagation in relation to local strain measurements, with the aim of identifying criteria for damage development. Further SPTs should be carried out to first assess the repeatability of the current results and to refine the novel experimental procedure developed in this work, so as to study damage development in the AHSSs microstructure under deformation conditions that are closer to those experienced in industrial forming operations. By optimising the amount of deformation between two successive interruptions of the test, it is believed that full-field strain measurements could be achieved using DIC. X-ray CT measurements could also be conducted to characterise damage in 3D and therefore address the limitations of SEM observations.

More advanced multi-scale models of deformability and damage of DP1000 also need to be developed, as the current work has shown the limitations of the commonly used GTN model. Microstructure-based models of damage propagation could be envisaged with Representative Volume Element based models, developed to link the scale of the microstructure to the scale of the specimen. Multi-scale experimental results could therefore be used to inform and validate these models and enhance their predictability.

REFERENCES

. (!!! INVALID CITATION !!!).

Abbasi, M., Ketabchi, M., Izadkhah, H., Fatmehsaria, D., & Aghbash, A. (2011). Identification of GTN model parameters by application of response surface methodology. *Procedia engineering, 10*, 415-420.

Abendroth, M., & Kuna, M. (2003). Determination of deformation and failure properties of ductile materials by means of the small punch test and neural networks. *computational materials Science, 28*(3-4), 633-644.

Abid, N. H., Al-Rub, R. K. A., & Palazotto, A. N. (2015). Computational modeling of the effect of equiaxed heterogeneous microstructures on strength and ductility of dual phase steels. *Computational Materials Science, 103*, 20-37.

Achouri, M., Germain, G., Dal Santo, P., & Saidane, D. (2013). Experimental characterization and numerical modeling of micromechanical damage under different stress states. *Materials & design, 50*, 207-222.

Alaie, A., Kadkhodapour, J., Rad, S. Z., Asadabad, M. A., & Schmauder, S. (2015). Formation and coalescence of strain localized regions in ferrite phase of DP600 steels under uniaxial tensile deformation. *Materials Science and Engineering: A, 623*, 133-144.

Alaie, A., Rad, S. Z., Kadkhodapour, J., Jafari, M., Asadabad, M. A., & Schmauder, S. (2015). Effect of microstructure pattern on the strain localization in DP600 steels analyzed using combined in-situ experimental test and numerical simulation. *Materials Science and Engineering: A, 638*, 251-261.

Alharbi, K. (2015). *Damage Investigation in Dual-Phase 1000 Steel and Behaviour Prediction Using Microstructure Based Modelling*. University of Sheffield,

Alharbi, K., Ghadbeigi, H., Efthymiadis, P., Zanganeh, M., Celotto, S., Dashwood, R., & Pinna, C. (2015). Damage in dual phase steel DP1000 investigated using digital image correlation and microstructure simulation. *Modelling and Simulation in Materials Science and Engineering, 23*(8), 085005.

Altstadt, E., Ge, H., Kuksenko, V., Serrano, M., Houska, M., Lasan, M., . . . Dai, Y. (2016). Critical evaluation of the small punch test as a screening procedure for mechanical properties. *Journal of Nuclear Materials, 472*, 186-195.

Andrews, P. (2013). *Adobe Photoshop CS3 AZ: Tools and features illustrated ready reference*: CRC Press.

ASTM. (2015). E643 -15 Standard Test Method for Ball Punch Deformation of Metallic Sheet Material. *ASTM*, 4. Retrieved from http://www.astm.org/cgi-bin/resolver.cgi?E643-15

Avramovic-Cingara, G., Ososkov, Y., Jain, M., & Wilkinson, D. (2009). Effect of martensite distribution on damage behaviour in DP600 dual phase steels. *Materials Science and Engineering: A, 516*(1), 7-16.

Avramovic-Cingara, G., Saleh, C. A., Jain, M., & Wilkinson, D. (2009). Void nucleation and growth in dual-phase steel 600 during uniaxial tensile testing. *Metallurgical and Materials Transactions A, 40*(13), 3117.

Azuma, M., Goutianos, S., Hansen, N., Winther, G., & Huang, X. (2012). Effect of hardness of martensite and ferrite on void formation in dual phase steel. *Materials Science and Technology, 28*(9-10), 1092-1100.

Azushima, A., Kopp, R., Korhonen, A., Yang, D.-Y., Micari, F., Lahoti, G., . . . Rosochowski, A. (2008). Severe plastic deformation (SPD) processes for metals. *CIRP annals, 57*(2), 716-735.

Besson, J. (2009). Continuum models of ductile fracture: a review. *International Journal of Damage Mechanics*.

Bruchhausen, M., Austin, T., Holmström, S., Altstadt, E., Dymacek, P., Jeffs, S., . . . Petzová, J. (2017). *European standard on small punch testing of metallic materials.* Paper presented at the Pressure Vessels and Piping Conference.

Brumovsky, M., & Kopriva, R. (2018). *Interlaboratory Study for Small Punch Testing Preliminary Results.* Paper presented at the Pressure Vessels and Piping Conference.

Calcagnotto, M., Adachi, Y., Ponge, D., & Raabe, D. (2011). Deformation and fracture mechanisms in fine-and ultrafine-grained ferrite/martensite dual-phase steels and the effect of aging. *Acta Materialia, 59*(2), 658-670.

Callister, W. D., & Rethwisch, D. G. (2007). *Materials science and engineering: an introduction* (Vol. 7): Wiley New York.

Chalon, I. (2004). Modelling of the microstructural deformation of duplex stainless steel during plane strain compression. *IMMPETUS, The University of Sheffield, UK*.

Corigliano, A., Mariani, S., & Orsatti, B. (2000). Identification of Gurson–Tvergaard material model parameters via Kalman filtering technique. I. Theory. *International journal of fracture, 104*(4), 349-373.

Cuesta, I., Rodríguez, C., García, T., & Alegre, J. (2015). Effect of confinement level on mechanical behaviour using the small punch test. *Engineering Failure Analysis, 58*, 206-211.

Davis, T. A. (2010). *MATLAB primer*: CRC press.

Dowding, R., Pinna, C., Ghadbeigi, H., & Farrugia, D. (2020). Analyzing the properties promoting shear bands and damage initiation in 3-point bending of ultra-high strength steel. *Procedia Manufacturing, 50*, 570-573.

Erdogan, M. (2002). The effect of new ferrite content on the tensile fracture behaviour of dual phase steels. *Journal of Materials Science, 37*(17), 3623-3630.

Estrin, Y., & Mecking, H. (1984). A unified phenomenological description of work hardening and creep based on one-parameter models. *Acta Metallurgica, 32*(1), 57-70.

Ghadbeigi, H., Pinna, C., & Celotto, S. (2013). Failure mechanisms in DP600 steel: initiation, evolution and fracture. *Materials Science and Engineering: A, 588*, 420-431.

Ghadbeigi, H., Pinna, C., Celotto, S., & Yates, J. (2010). Local plastic strain evolution in a high strength dual-phase steel. *Materials Science and Engineering: A, 527*(18), 5026-5032.

Ghassemi-Armaki, H., Maaß, R., Bhat, S., Sriram, S., Greer, J., & Kumar, K. (2014). Deformation response of ferrite and martensite in a dual-phase steel. *Acta Materialia, 62*, 197-211.

Gurson, A. L. (1977). Continuum theory of ductile rupture by void nucleation and growth: Part I—Yield criteria and flow rules for porous ductile media. *Journal of engineering materials and technology, 99*(1), 2-15.

Ha, J., Lee, J., Kim, J. H., Lee, M.-G., & Barlat, F. (2017). Investigation of plastic strain rate under strain path changes in dual-phase steel using microstructure-based modeling. *International Journal of Plasticity, 93*, 89-111.

Habibi, S., Ziadi, A., & Megueni, A. (2014). Modeling a Small Punch Testing Device. *Engineering, Technology & Applied Science Research, 4*(2), 612-617.

Hosford, W. F., & Caddell, R. M. (2011). *Metal forming: mechanics and metallurgy*: Cambridge university press.

Hosseini-Toudeshky, H., Anbarlooie, B., Kadkhodapour, J., & Shadalooyi, G. (2014). Microstructural deformation pattern and mechanical behavior analyses of DP600 dual phase steel. *Materials Science and Engineering: A, 600*, 108-121.

ISO, D. (2008). Metallic materials-Sheet and strip-Determination of forming-limit curves-Part 2: Determination of forming-limit curves in the laboratory. *ISO*.

Kadkhodapour, J., Butz, A., & Rad, S. Z. (2011). Mechanisms of void formation during tensile testing in a commercial, dual-phase steel. *Acta Materialia, 59*(7), 2575-2588.

Kamikawa, N., & Morino, H. (2019). Quantitative Analysis of Load–Displacement Curves in Erichsen Cupping Test for Low Carbon Steel Sheet. *Metallurgical and Materials Transactions A, 50*(11), 5023-5037.

Kang, J., Ososkov, Y., Embury, J. D., & Wilkinson, D. S. (2007). Digital image correlation studies for microscopic strain distribution and damage in dual phase steels. *Scripta Materialia, 56*(11), 999-1002.

Keeler, S., & Kimchi, M. (2015). *Advanced high-strength steels application guidelines V5*: WorldAutoSteel.

Kim, J., Gao, X., & Srivatsan, T. S. (2004). Modeling of void growth in ductile solids: effects of stress triaxiality and initial porosity. *Engineering Fracture Mechanics, 71*(3), 379-400.

Livatyali, H., Firat, M., Gurler, B., & Ozsoy, M. (2010). An experimental analysis of drawing characteristics of a dual-phase steel through a round drawbead. *Materials & Design, 31*(3), 1639-1643.

Lucas, G. (1983). The development of small specimen mechanical test techniques. *Journal of Nuclear Materials, 117*, 327-339.

Mansouri, L. Z., Chalal, H., & Abed-Meraim, F. (2014). Ductility limit prediction using a GTN damage model coupled with localization bifurcation analysis. *Mechanics of Materials, 76*, 64-92.

Manual, A. U. s. Version 6.10, 2010. *Dassault Systèmes Simulia Corp., Providence, RI, USA*.

Martínez-Pañeda, E., Cuesta, I. I., Peñuelas, I., Díaz, A., & Alegre, J. M. (2016). Damage modeling in small punch test specimens. *Theoretical and applied fracture mechanics, 86*, 51-60.

Matocha, K. (2015). Small-punch testing for tensile and fracture behavior: experiences and way forward. In *Small Specimen Test Techniques: 6th Volume*: ASTM International.

Needleman, A., & Tvergaard, V. (1984). An analysis of ductile rupture in notched bars. *Journal of the Mechanics and Physics of Solids, 32*(6), 461-490.

Nicolaou, P., & Semiatin, S. (2001). The effect of stress triaxiality on tensile behavior of cavitating specimens. *Journal of Materials Science, 36*(21), 5155-5159.

Ososkov, Y., Wilkinson, D. S., Jain, M., & Simpson, T. (2007). In-situ measurement of local strain partitioning in a commercial dual-phase steel. *International Journal of Materials Research, 98*(8), 664-673.

Park, K., Nishiyama, M., Nakada, N., Tsuchiyama, T., & Takaki, S. (2014). Effect of the martensite distribution on the strain hardening and ductile fracture behaviors in dual-phase steel. *Materials Science and Engineering: A, 604*, 135-141.

Paul, S. K. (2012). Micromechanics based modeling of Dual Phase steels: Prediction of ductility and failure modes. *Computational Materials Science, 56*, 34-42.

Paul, S. K. (2013). Effect of martensite volume fraction on stress triaxiality and deformation behavior of dual phase steel. *Materials & Design, 50*, 782-789.

Perzyński, K., Wrożyna, A., Kuziak, R., Legwand, A., & Madej, L. (2017). Development and validation of multi scale failure model for dual phase steels. *Finite Elements in Analysis and Design, 124*, 7-21.

Rahimi, F., & Eivani, A. (2015). A new severe plastic deformation technique based on pure shear. *Materials Science and Engineering: A, 626*, 423-431.

Ramazani, A., Ebrahimi, Z., & Prahl, U. (2014). Study the effect of martensite banding on the failure initiation in dual-phase steel. *Computational materials science, 87*, 241-247.

Ramazani, A., Mukherjee, K., Prahl, U., & Bleck, W. (2012). Modelling the effect of microstructural banding on the flow curve behaviour of dual-phase (DP) steels. *Computational Materials Science, 52*(1), 46-54.

Rashid, M. (1981). Dual phase steels. *Annual Review of Materials Science, 11*(1), 245-266.

Rodríguez, C., Cárdenas, E., Belzunce, F., & Betegón, C. (2013). Fracture characterization of steels by means of the small punch test. *Experimental Mechanics, 53*(3), 385-392.

Rohaizat, N. I. (2018). *Fracture of automotive high strength steels.* University of Sheffield,

Saeidi, N., Ashrafizadeh, F., Niroumand, B., Forouzan, M., & Barlat, F. (2014). Damage mechanism and modeling of void nucleation process in a ferrite–martensite dual phase steel. *Engineering Fracture Mechanics, 127*, 97-103.

Sarwar, M., & Priestner, R. (1996). Influence of ferrite-martensite microstructural morphology on tensile properties of dual-phase steel. *Journal of materials science, 31*(8), 2091-2095.

Segal, V. (2002). Severe plastic deformation: simple shear versus pure shear. *Materials Science and Engineering: A, 338*(1-2), 331-344.

Simonovski, I., Holmström, S., & Bruchhausen, M. (2017). Small punch tensile testing of curved specimens: Finite element analysis and experiment. *International Journal of Mechanical Sciences, 120*, 204-213.

Simulia, D. (2010). ABAQUS 6.10/CAE User's Manual. *Abaqus, 6*, 1174.

Smith, M. (2009). ABAQUS/Standard User's Manual, Version 6.9.

Tasan, C. C., Diehl, M., Yan, D., Bechtold, M., Roters, F., Schemmann, L., . . . Koyama, M. (2015). An overview of dual-phase steels: advances in microstructure-oriented processing and micromechanically guided design. *Annual Review of Materials Research, 45*, 391-431.

Testing, A. S. f., & Materials. (1990). *ASTM Standard E399-83, Annual Book of ASTM Standards, Section 3*.

Tvergaard, V. (1981). Influence of voids on shear band instabilities under plane strain conditions. *International Journal of fracture, 17*(4), 389-407.

Tvergaard, V. (1982). On localization in ductile materials containing spherical voids. *International Journal of Fracture, 18*(4), 237-252.

Tvergaard, V. (1989). Material failure by void growth to coalescence. *Advances in applied Mechanics, 27*, 83-151.

Tvergaard, V., Needleman, A., & Lo, K. K. (1981). Flow localization in the plane strain tensile test. *Journal of the Mechanics and Physics of Solids, 29*(2), 115-142.

Uthaisangsuk, V., Prahl, U., & Bleck, W. (2008). Micromechanical modelling of damage behaviour of multiphase steels. *Computational Materials Science, 43*(1), 27-35.

Wagoner, R., Wang, W., & Sriram, S. (1994). Development of OSU formability test and OSU friction test. *Journal of materials processing technology, 45*(1-4), 13-18.

Wang, C., Daniel, W. J., Lu, H., Liu, S., & Meehan, P. A. (2017). FEM Investigation of Ductile Fracture Prediction in Two-Point Incremental Sheet Metal Forming process. *Procedia engineering, 207*, 836-841.

Wcislik, W. (2016). Experimental determination of critical void volume fraction f F for the Gurson Tvergaard Needleman (GTN) model. *Procedia Structural Integrity, 2*, 1676-1683.

Yoon, J.-H., Cazacu, O., Yoon, J. W., & Dick, R. E. (2010). Earing predictions for strongly textured aluminum sheets. *International journal of mechanical sciences, 52*(12), 1563-1578.

Yue, Z. (2014). *Ductile damage prediction in sheet metal forming processes.* Troyes,

Zhao, Z., Tong, T., Liang, J., Yin, H., Zhao, A., & Tang, D. (2014). Microstructure, mechanical properties and fracture behavior of ultra-high strength dual-phase steel. *Materials Science and Engineering: A, 618*, 182-188.

APPENDICES

Appendix I

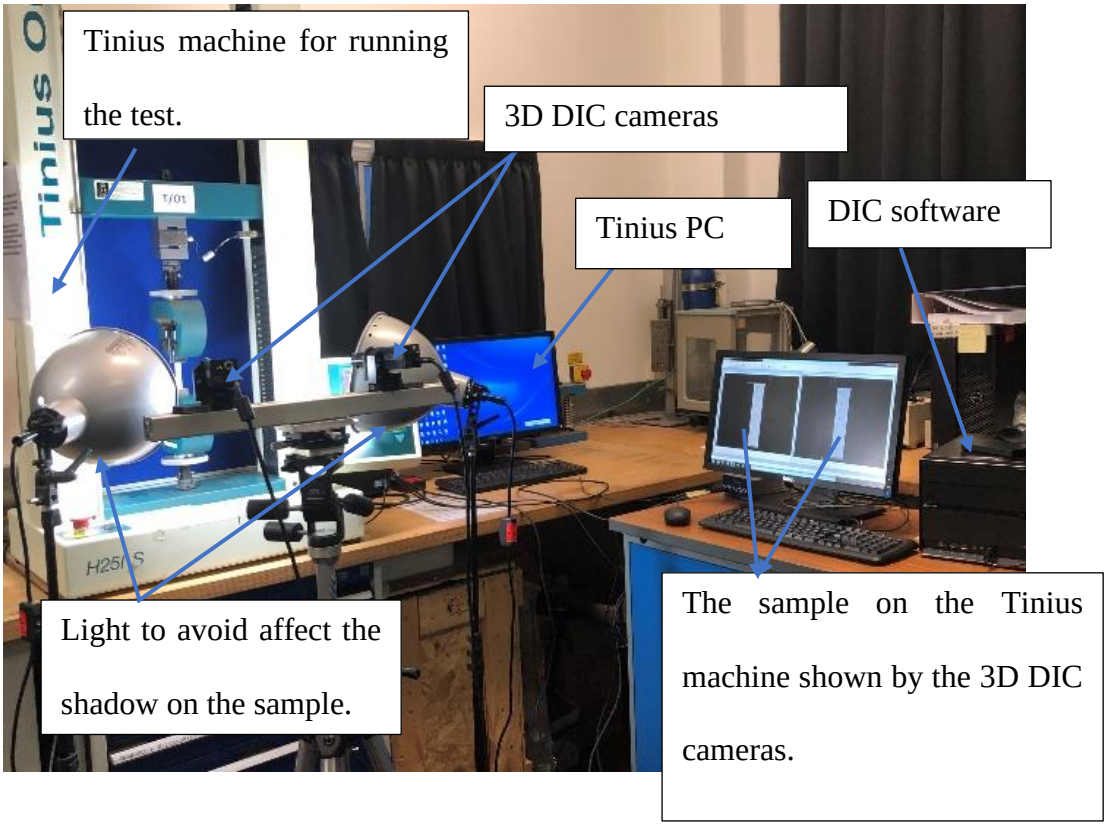

Fig. I. 1 More details for setup of tensile test with 3D

Appendix II

Fig. II. 1 Specimen on die

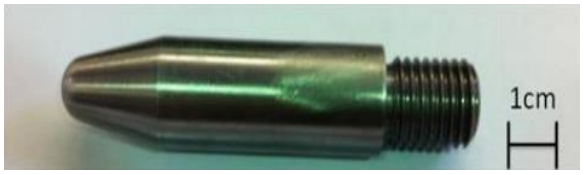

Fig. II. 2 Macro punch tool

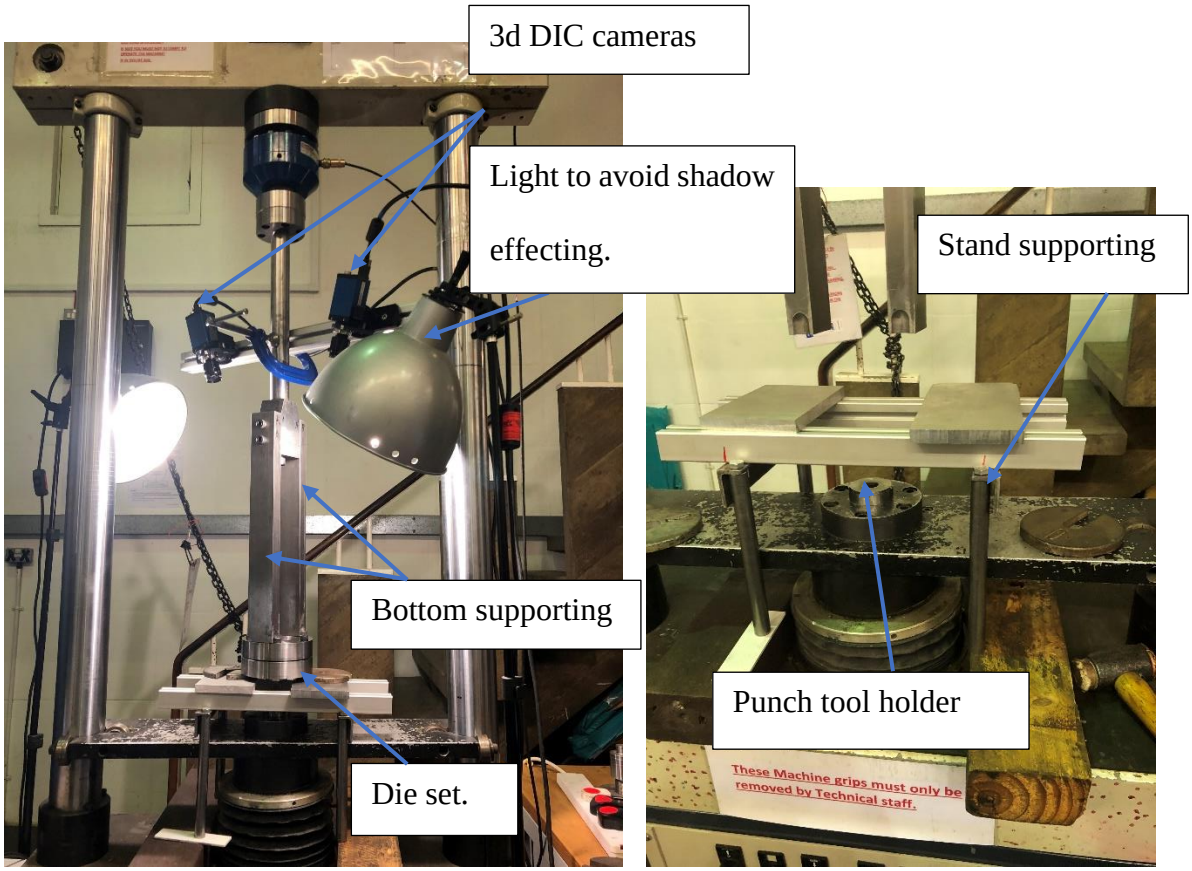

Fig. II. 3 3D DIC setting with punch rig for experiment.

Appendix III

Fig. III. 1 Top and bottom views of top die.

Appendix IV

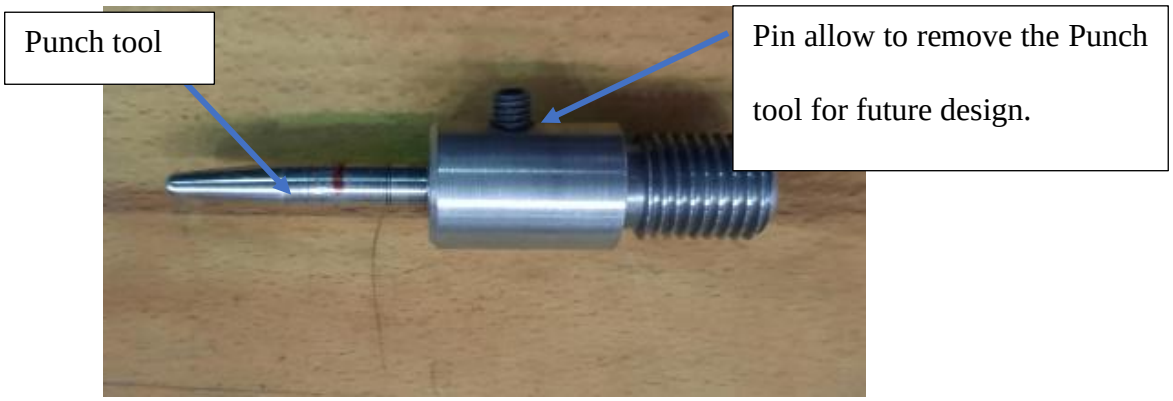

Fig. IV. 1 New punch design.

Appendix V

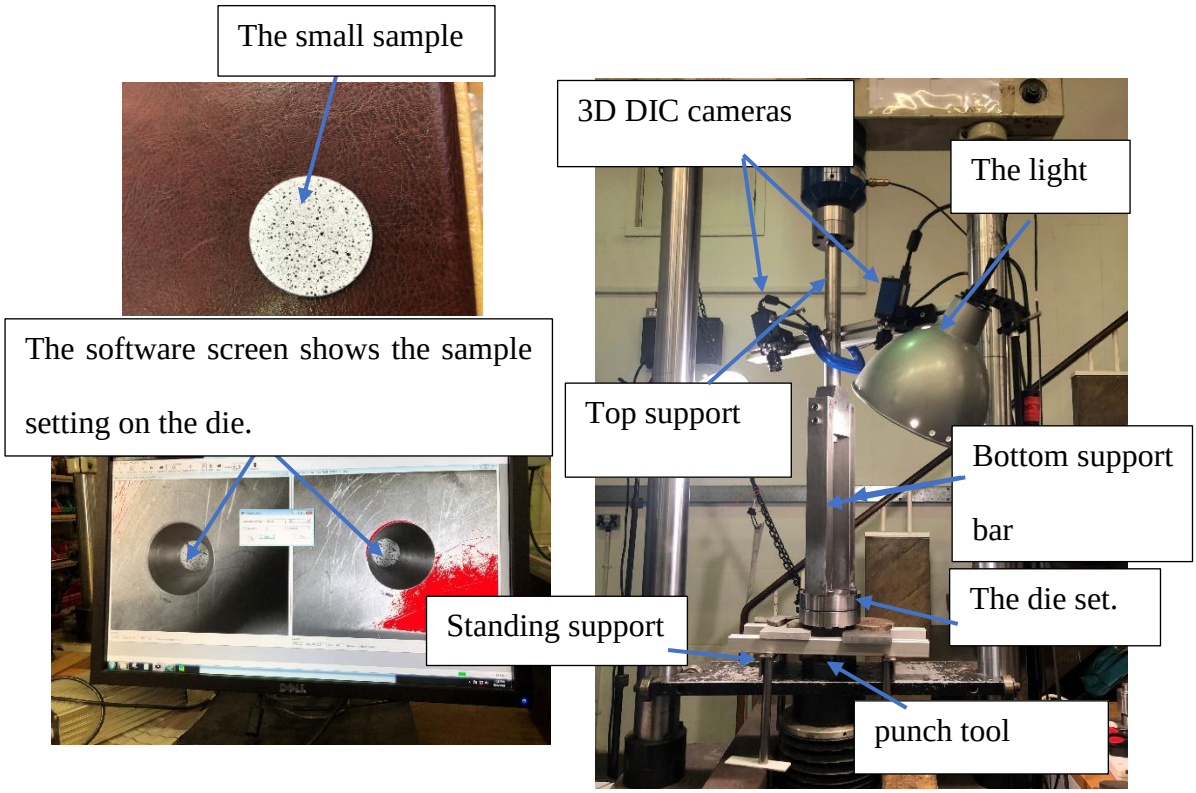

Fig. V. 1 Sample with rig of SP test with 3D DIC.

Appendix VI

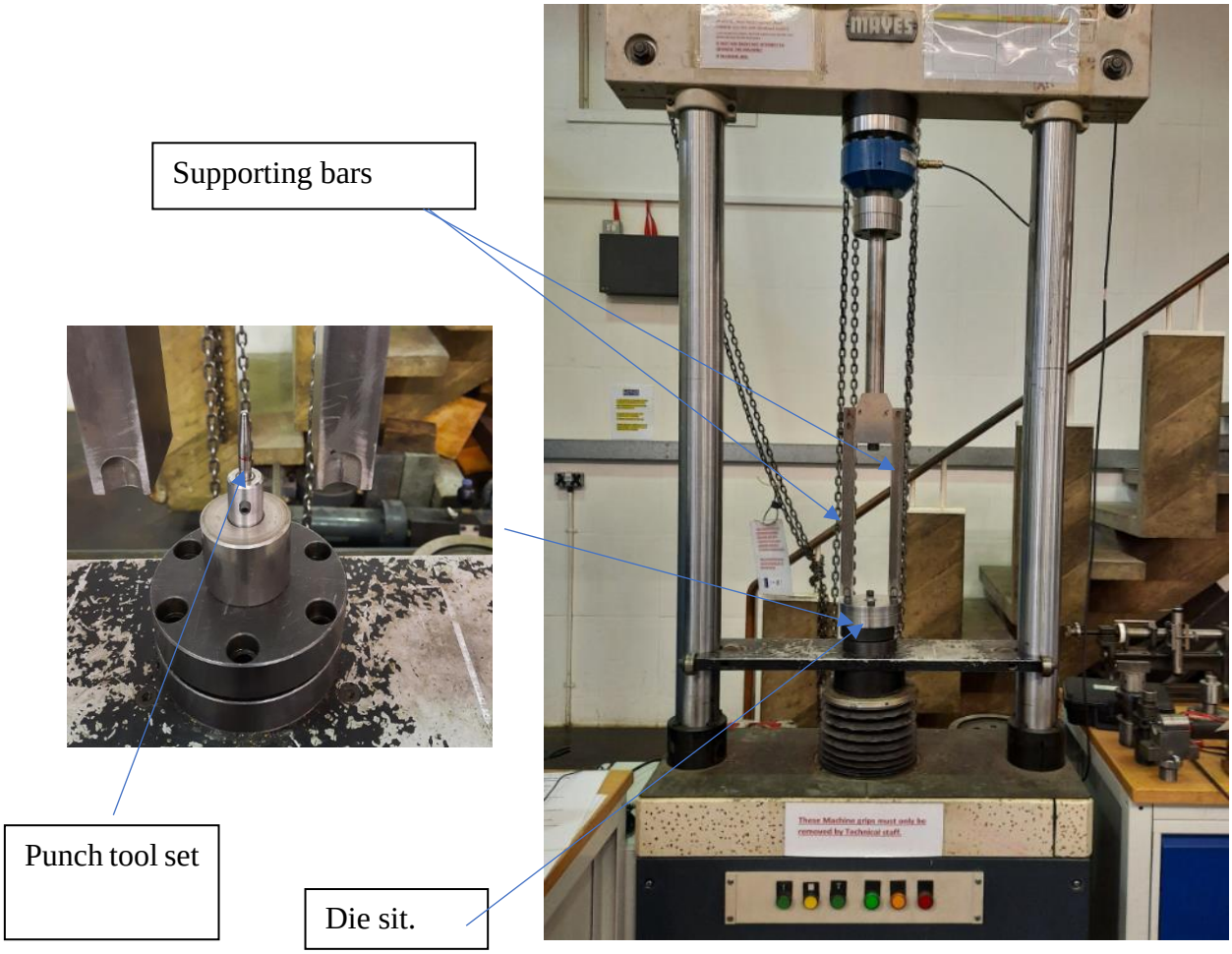

Fig. VI. 1 Setup of punch rig.

APPENDIX VII

Load displacement data for conventional tensile and Punch test.

Standards samples:

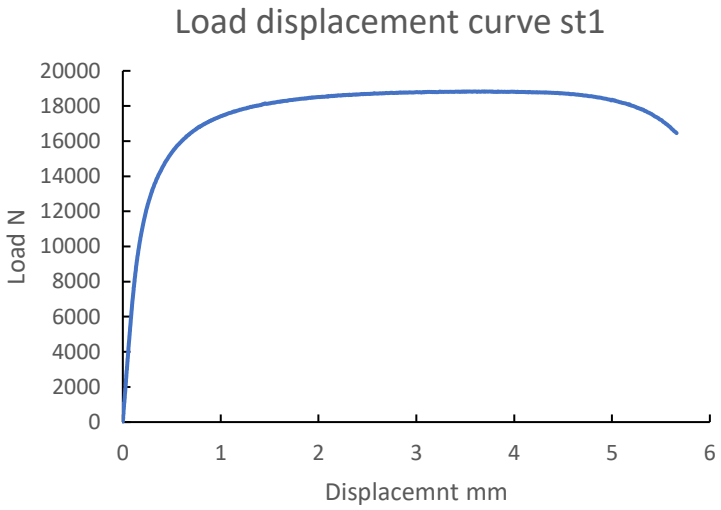

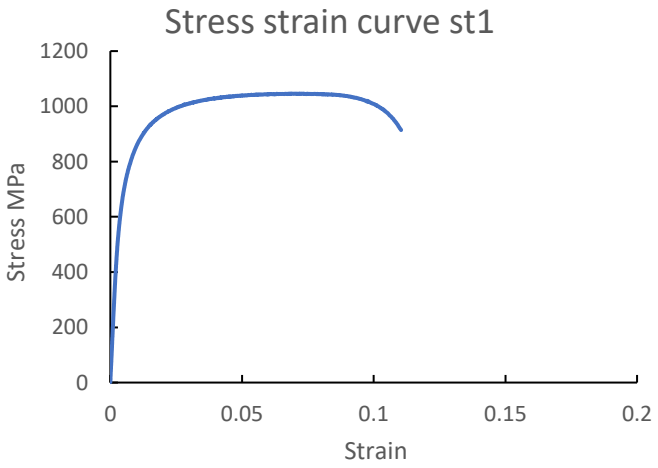

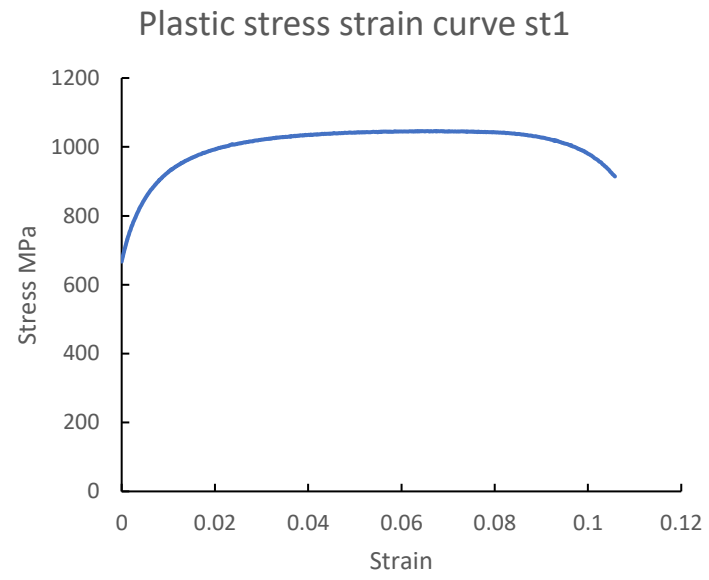
Plastic stress strain curve st1
Stress MPa
1200
1000
800
600
400
200
0
0
0.02
0.04
0.06
0.08
0.1
0.12
Strain

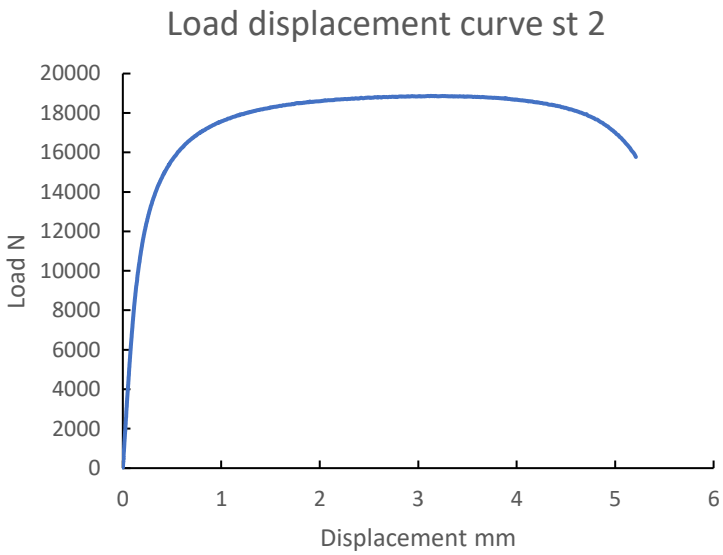
Load displacement curve st 2
Load N
20000
18000
16000
14000
12000
10000
8000
6000
4000
2000
0
0
1
2
3
4
5
6
Displacement mm

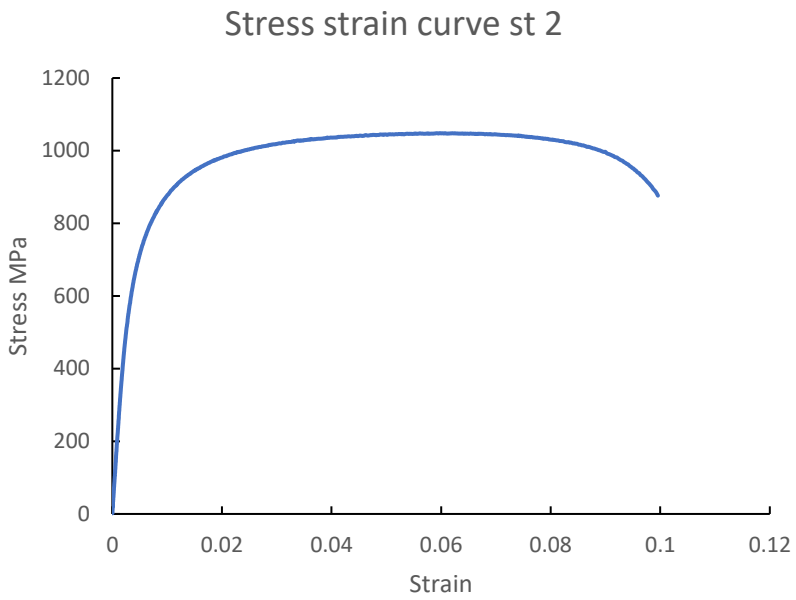
Stress strain curve st 2
1200
1000
800
600
400
200
0
Stress MPa
0
0.02
0.04
0.06
0.08
0.1
0.12
Strain

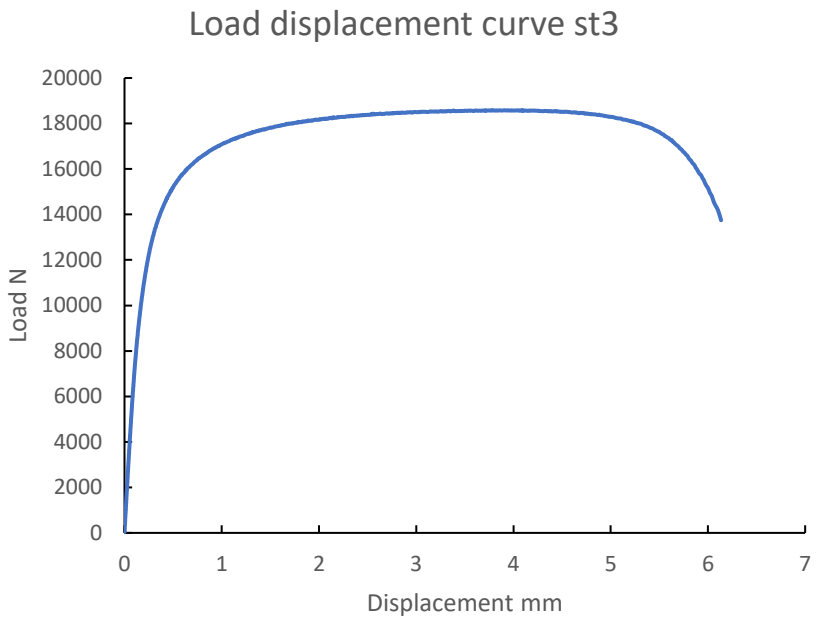
Load displacement curve st3
Load N
20000
18000
16000
14000
12000
10000
8000
6000
4000
2000
0
0
1
2
3
4
5
6
7
Displacement mm

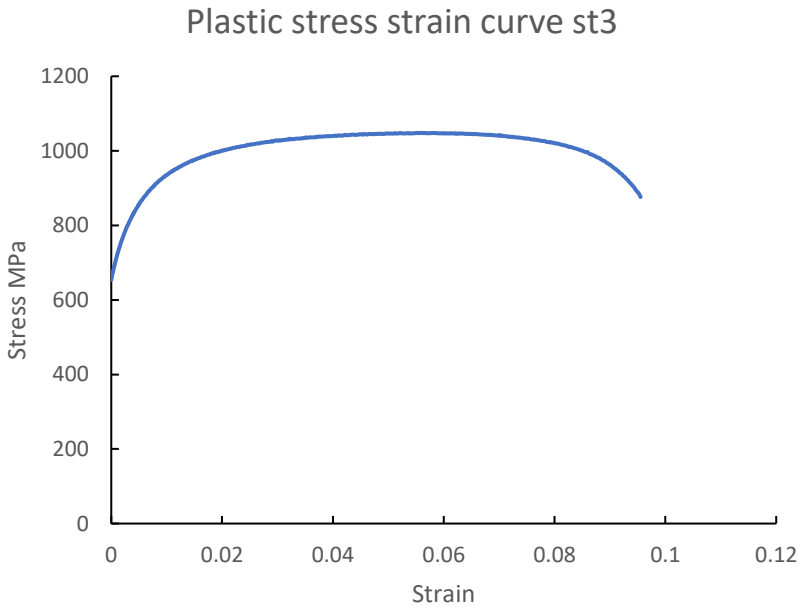
Plastic stress strain curve st3
Stress MPa
1200
1000
800
600
400
200
0
0
0.02
0.04
0.06
0.08
0.1
0.12
Strain

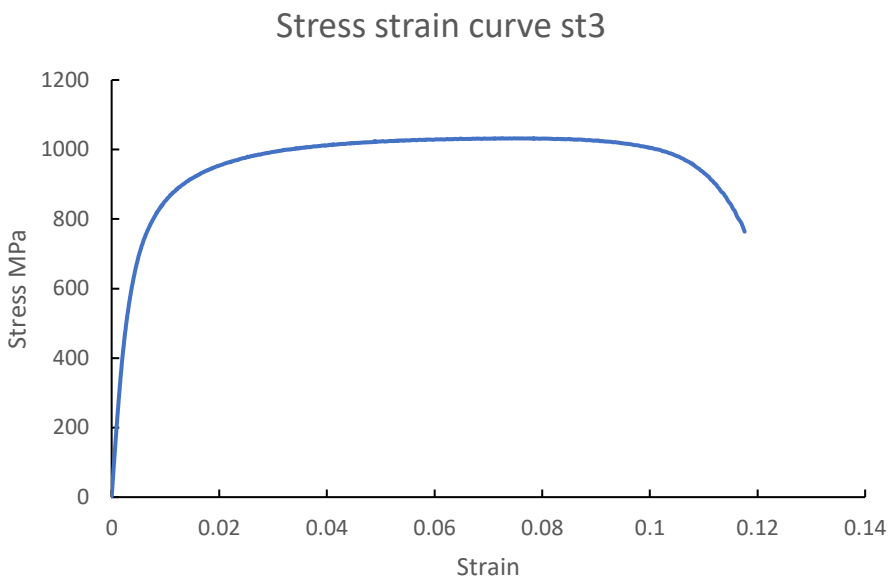

Notched samples:

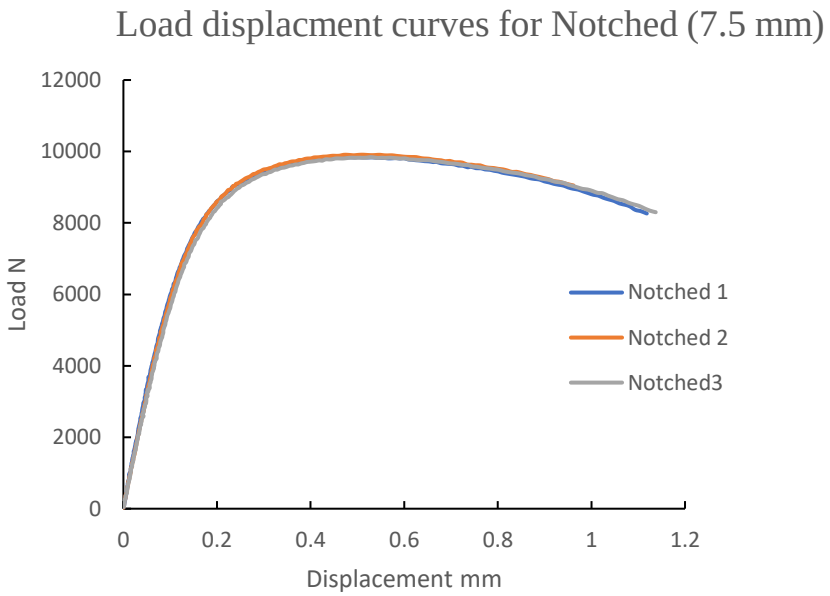

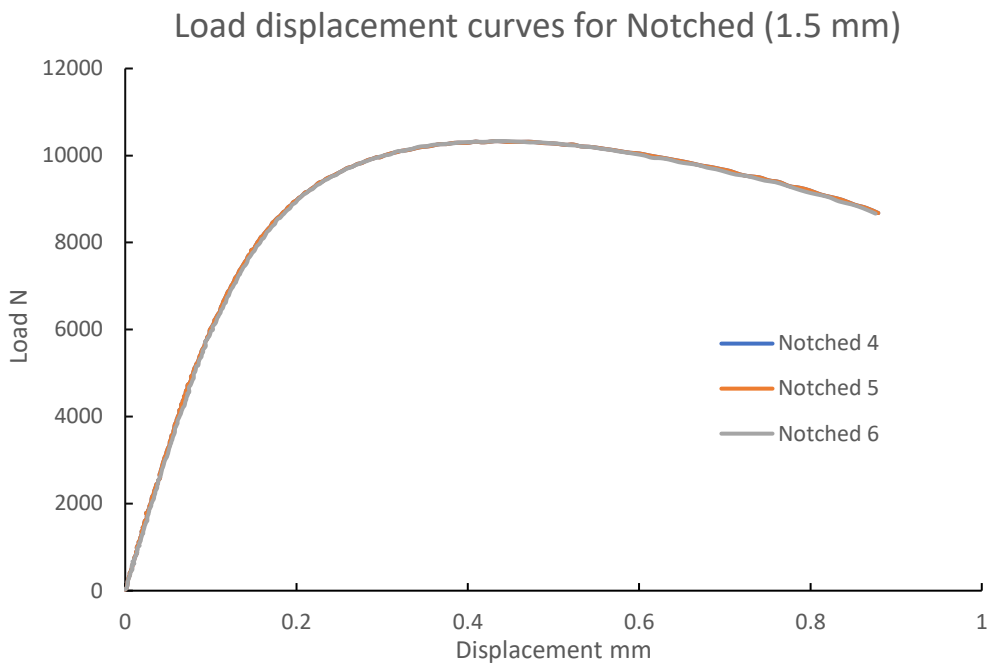

Punch samples:

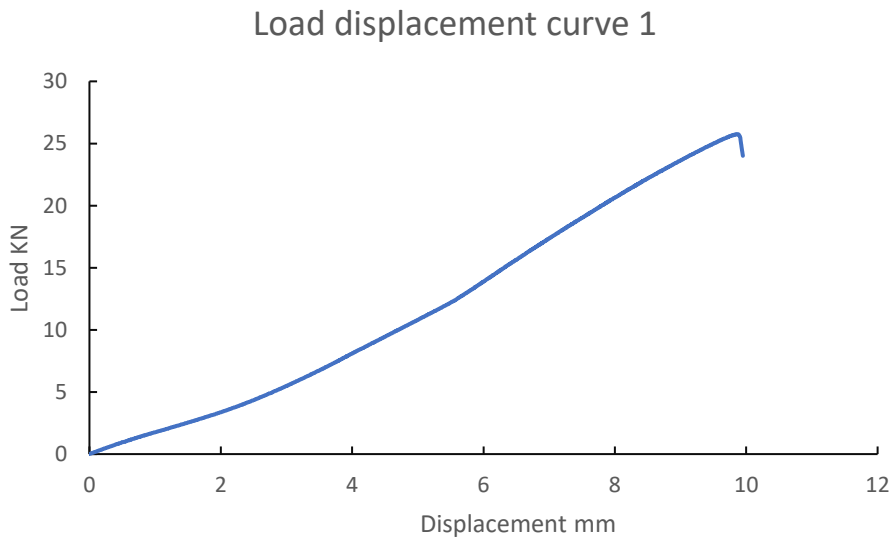

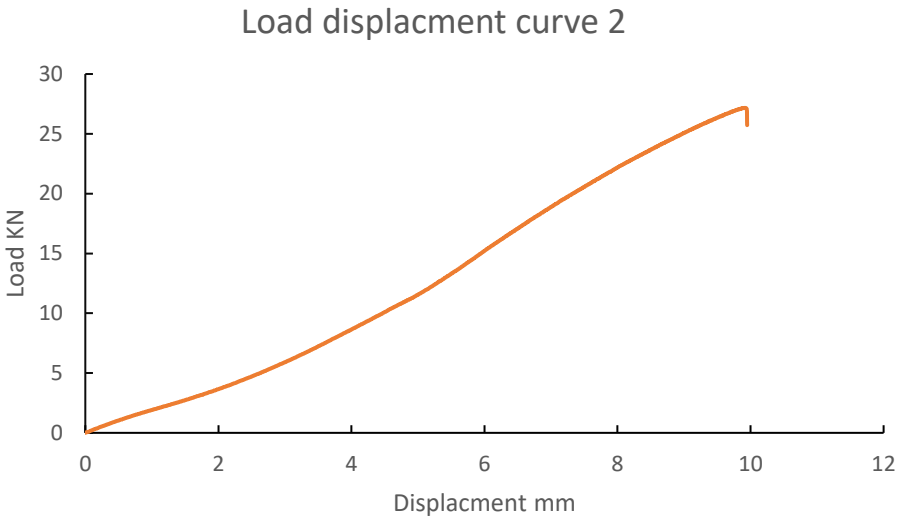

Appendix VIII

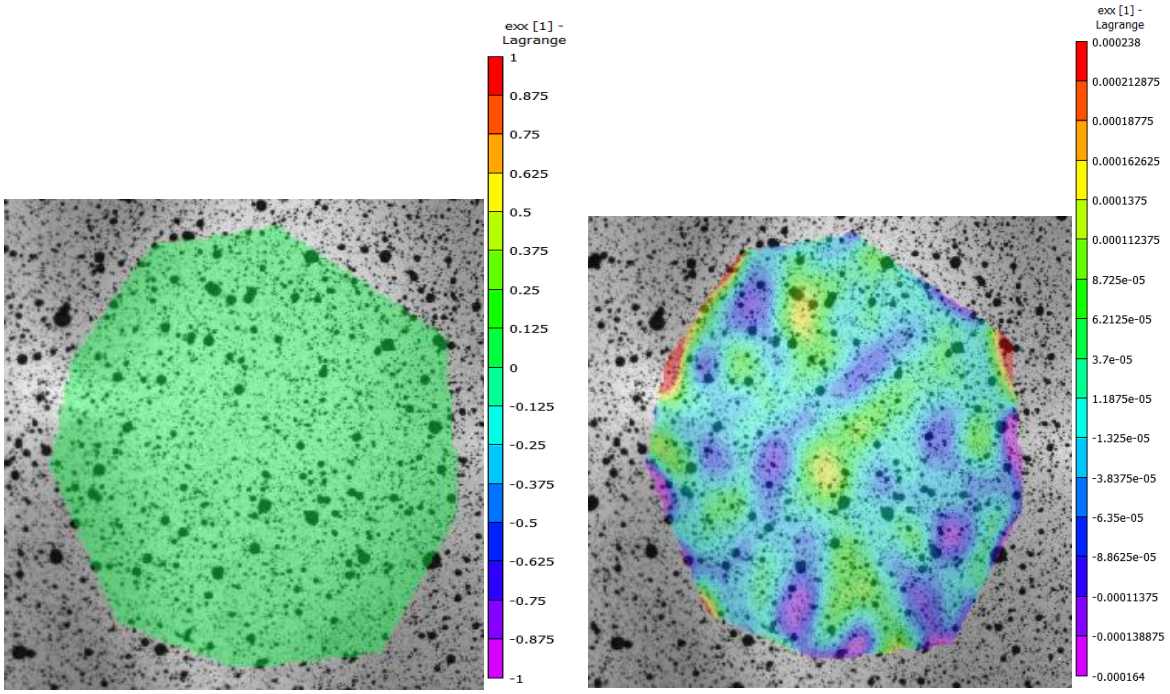

(a) (b)

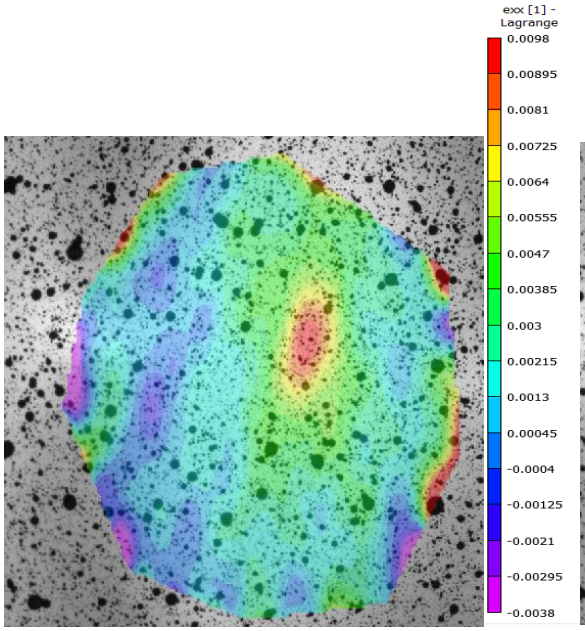

(c)

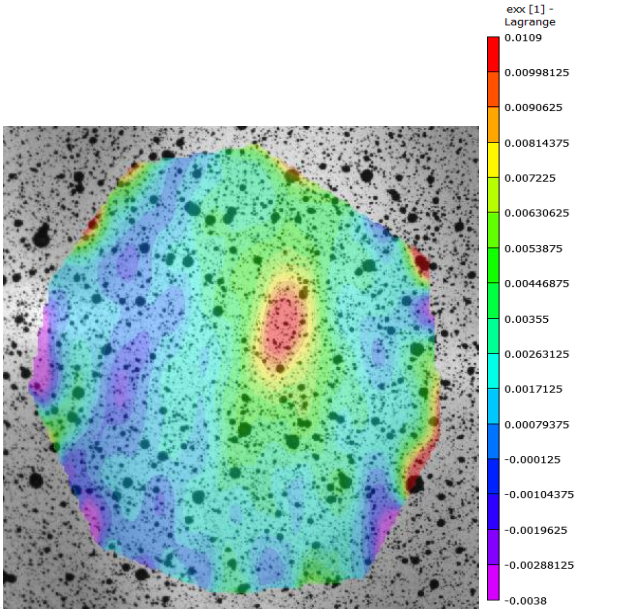

(d)

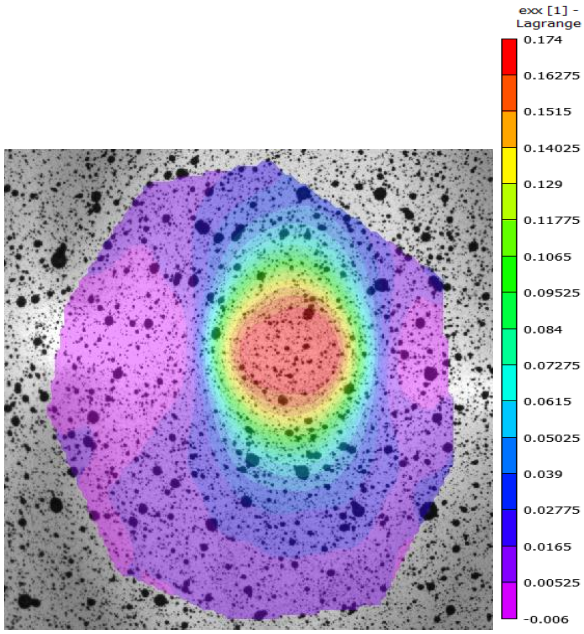

(e)

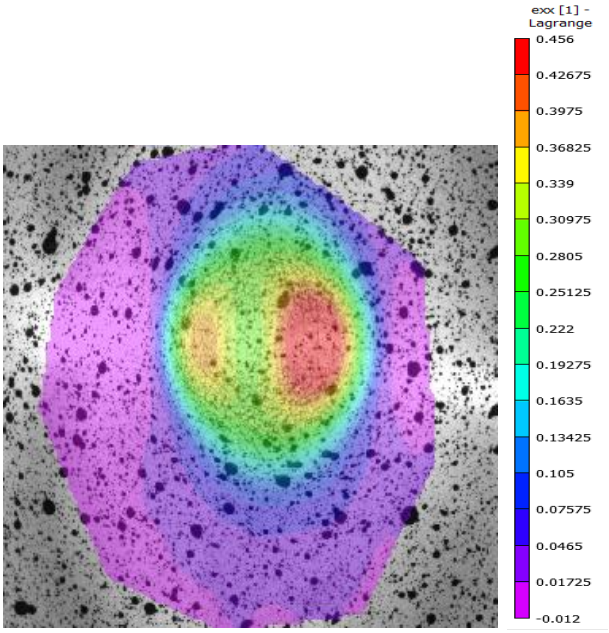

(f)

Figs. VIII. 1 Figures (a) to (f) explain Lagrangian strain distribution results (Exx) of punch test deformation

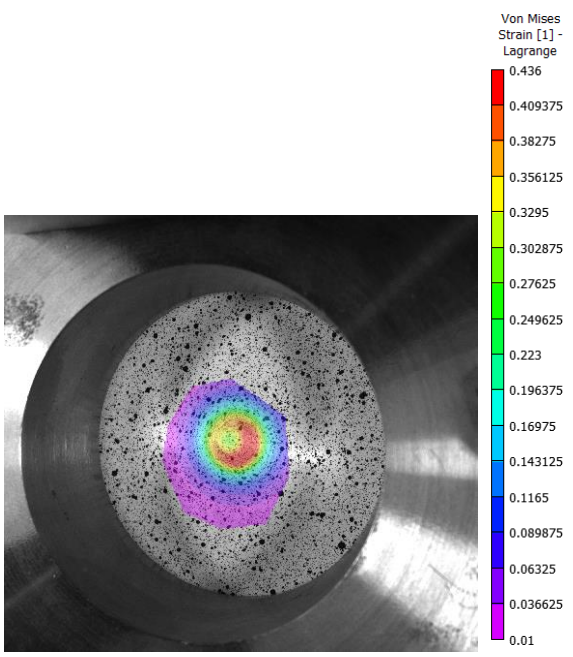
Von Mises Strain [1] - Lagrange
0.436
0.409375
0.38275
0.356125
0.3295
0.302875
0.27625
0.249625
0.223
0.196375
0.16975
0.143125
0.1165
0.089875
0.06325
0.036625
0.01

(a)

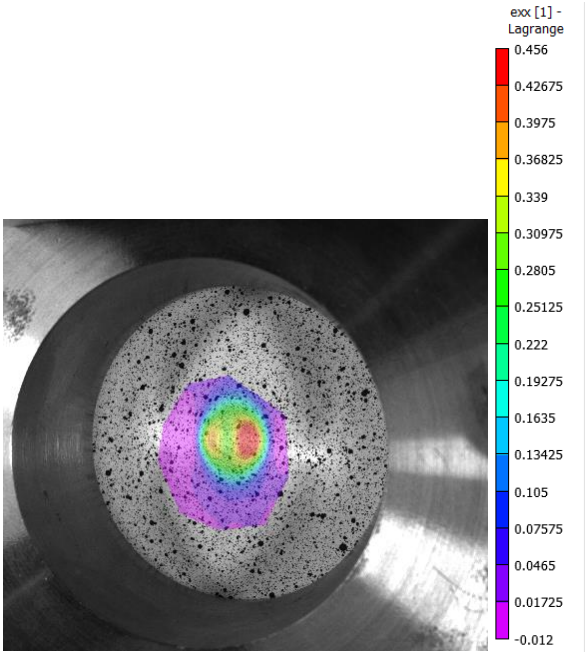
exx [1] - Lagrange
0.456
0.42675
0.3975
0.36825
0.339
0.30975
0.2805
0.25125
0.222
0.19275
0.1635
0.13425
0.105
0.07575
0.0465
0.01725
-0.012

(b)

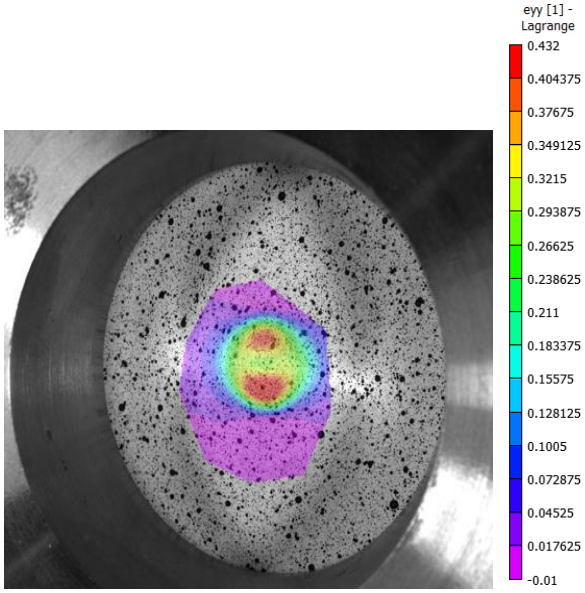
eyy [1] - Lagrange
0.432
0.404375
0.37675
0.349125
0.3215
0.293875
0.26625
0.238625
0.211
0.183375
0.15575
0.128125
0.1005
0.072875
0.04525
0.017625
-0.01

(c)

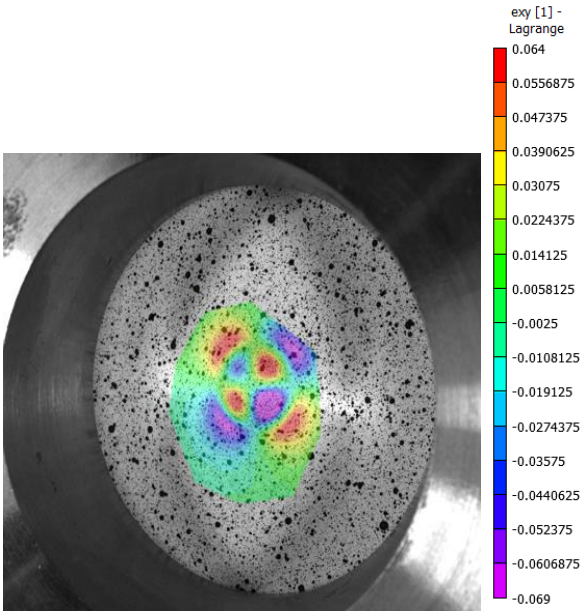
exy [1] - Lagrange
0.064
0.0556875
0.047375
0.0390625
0.03075
0.0224375
0.014125
0.0058125
-0.0025
-0.0108125
-0.019125
-0.0274375
-0.03575
-0.0440625
-0.052375
-0.0606875
-0.069

(d)

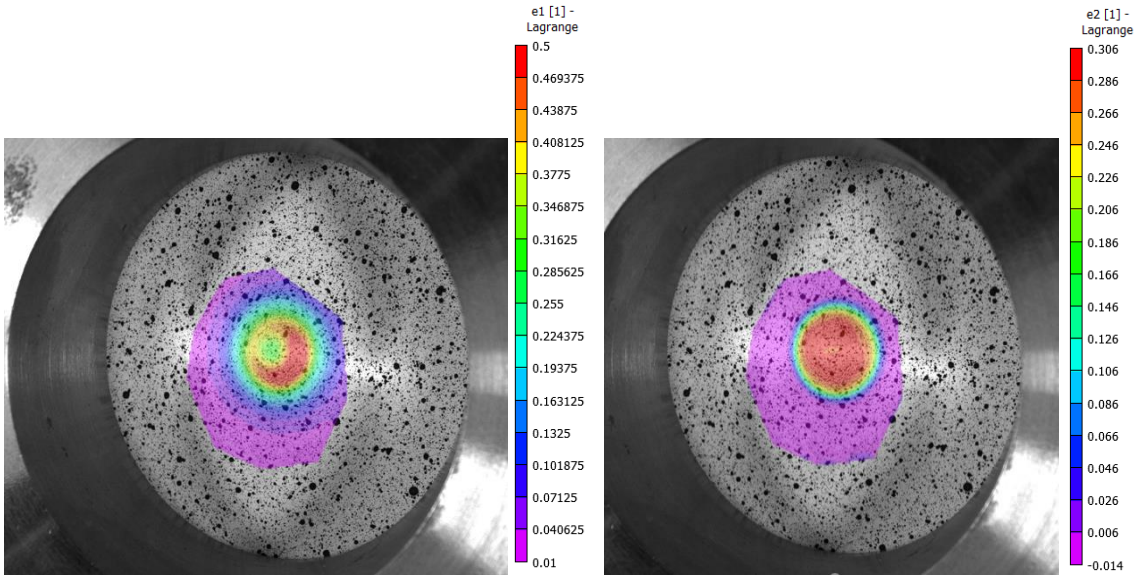

(e) (f)

Figs. VIII. 2 Figures (a) to (f) Clarify strain distribution results before crack appearance.

Appendix IX

Fig. IX. 1 Sample after application of 2.6 mm displacement. Red square shows lack of visible crack on surface.

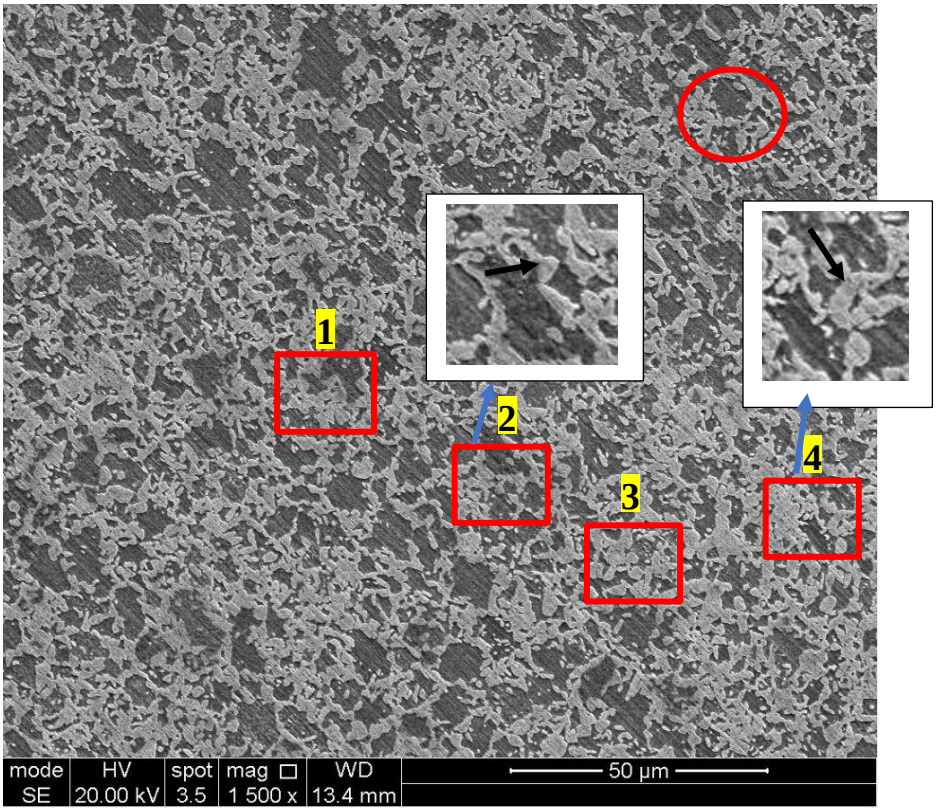

Fig. IX. 2 First image of microstructure before application of load in small punch test.

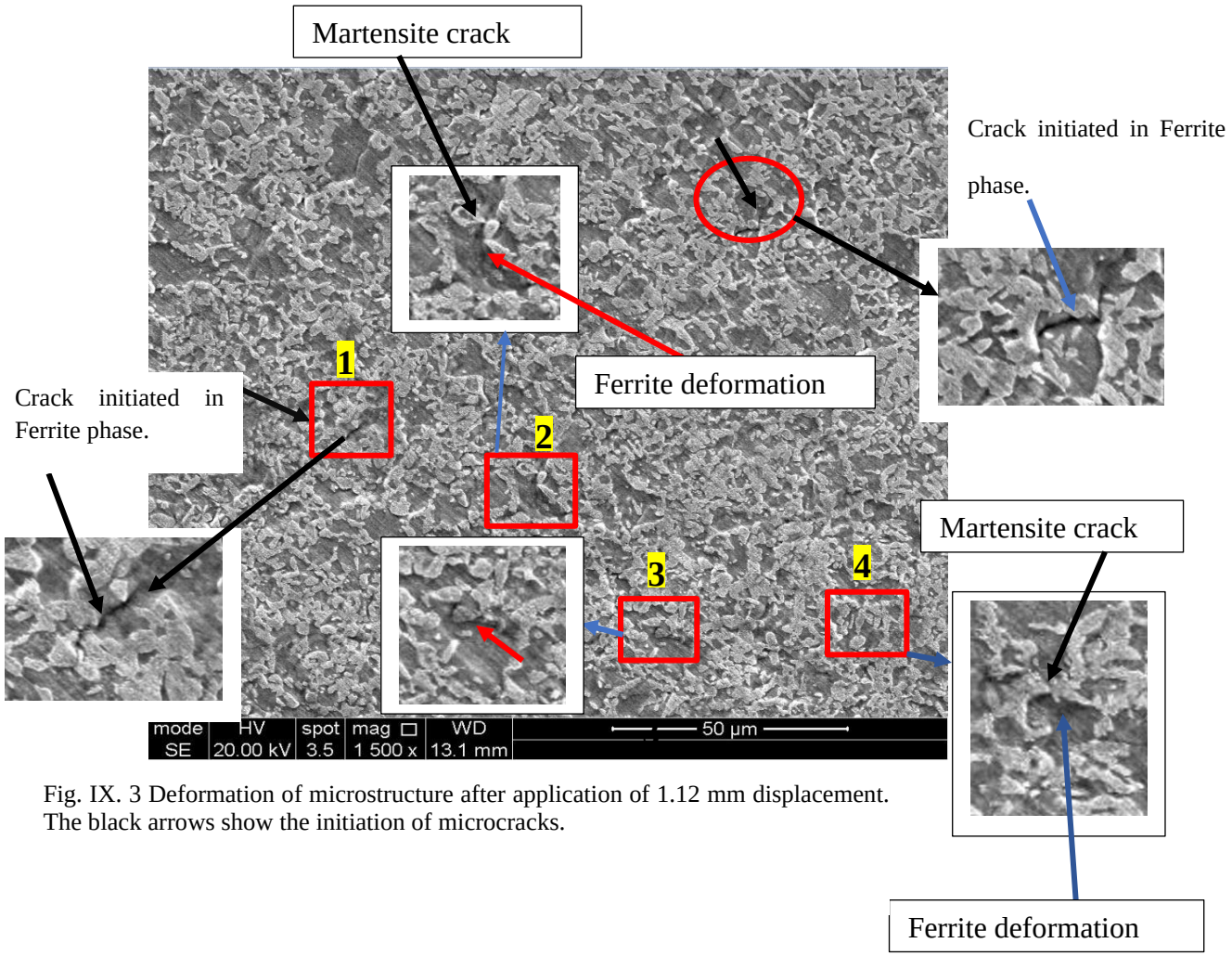

Fig. IX. 3 Deformation of microstructure after application of 1.12 mm displacement. The black arrows show the initiation of microcracks.

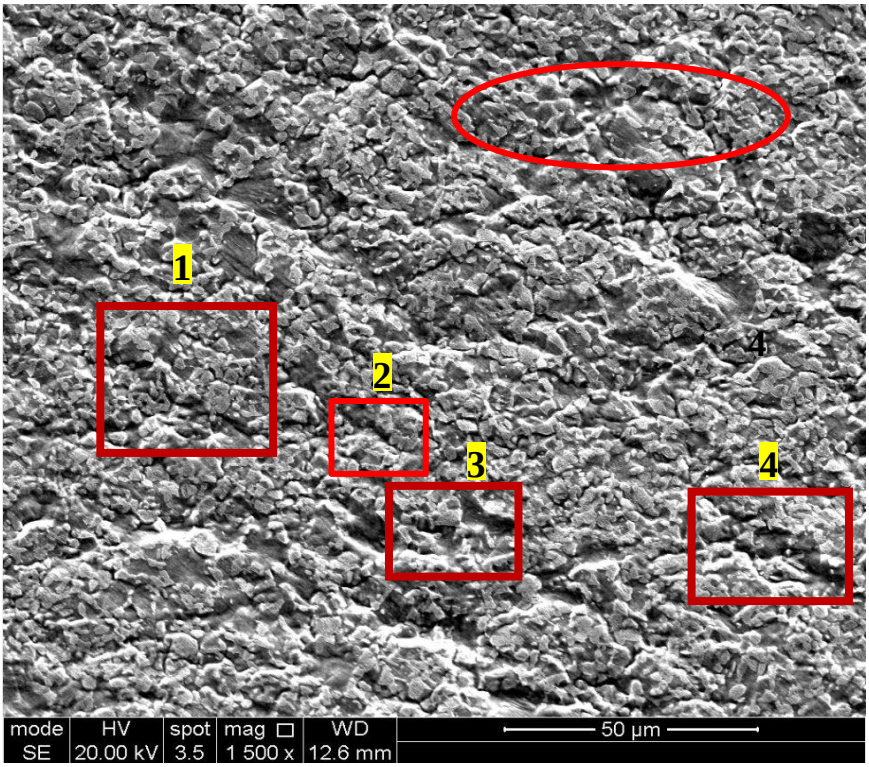

Fig. IX. 4 Microstructure damage before appearance of crack on surface

Appendix X

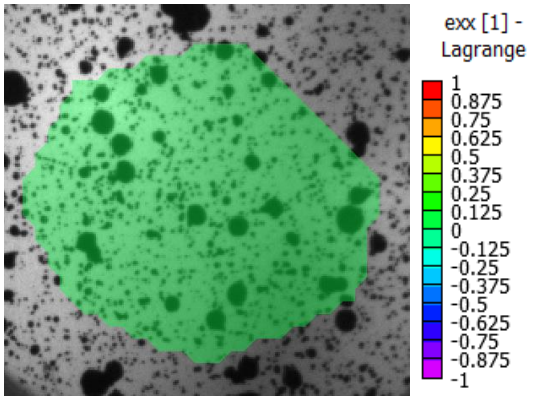

(a)

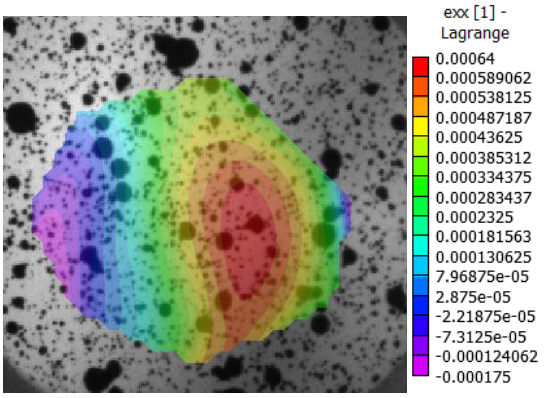

(b)

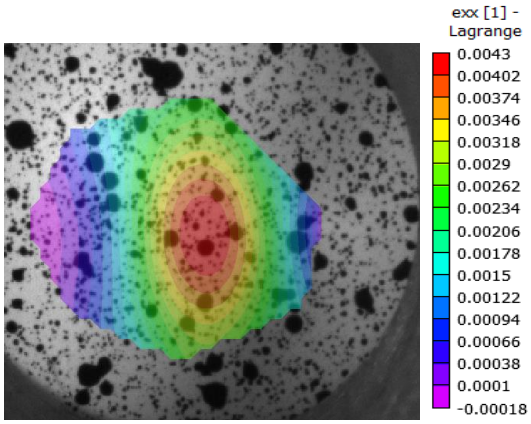

(c)

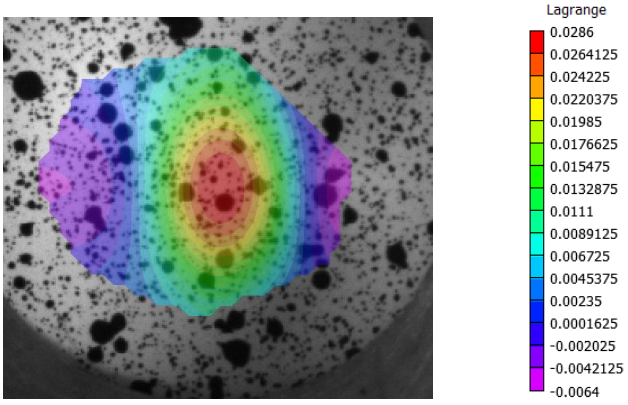

(d)

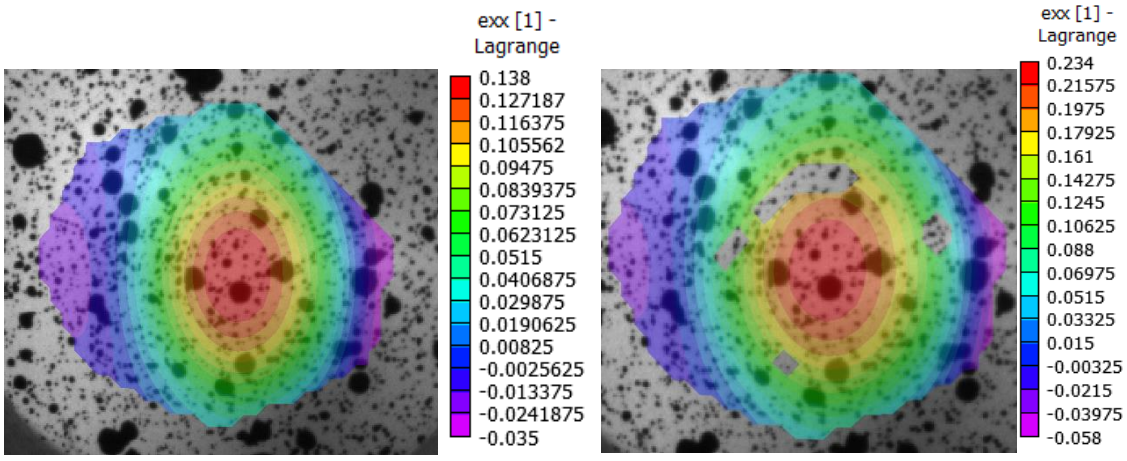

(e) (f)

Fig. X. 1 (a) to (f) Strain Exx results of micro punch test with 3D DIC, from beginning of test until before emergence of crack.

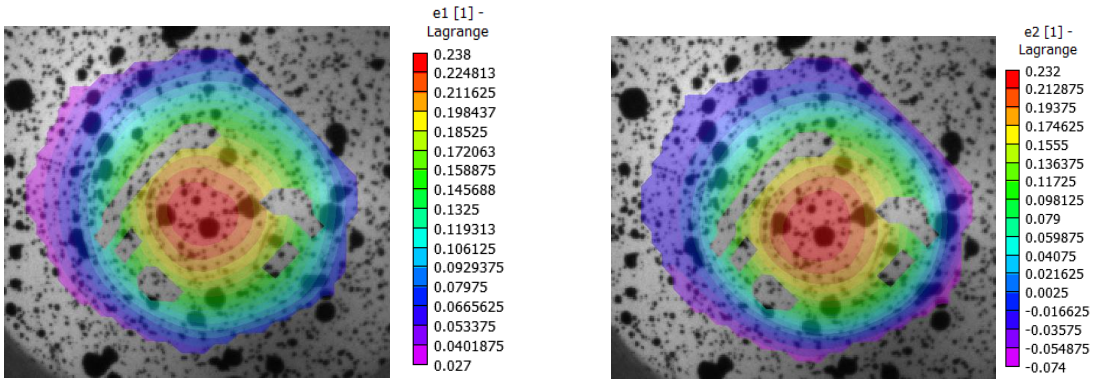

(a) (b)

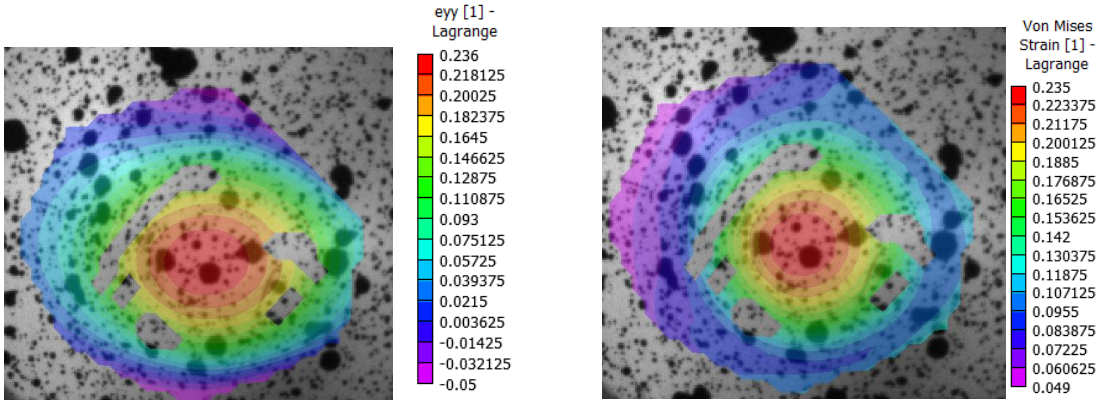

(c) (d)

Fig. X. 2 Strain distribution results before development of crack.

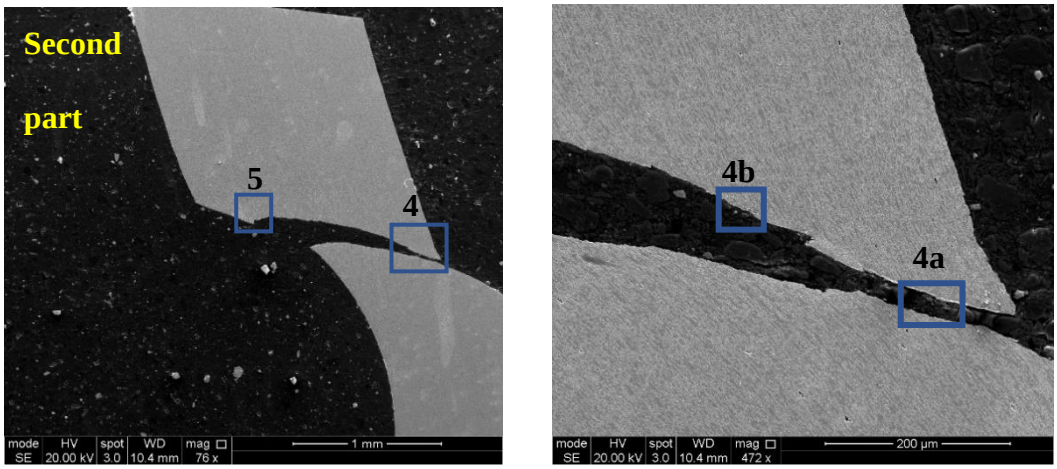

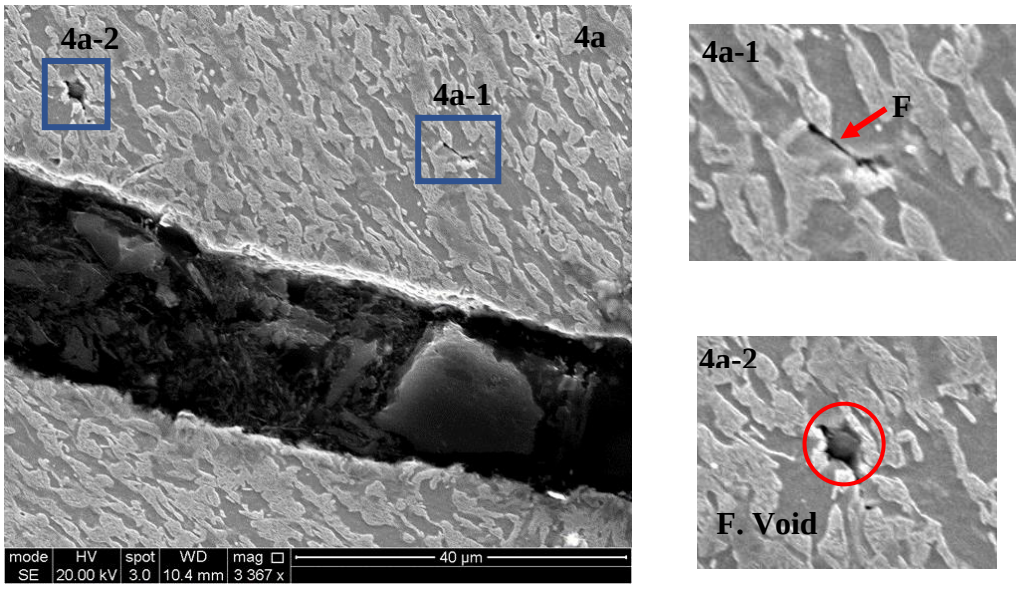

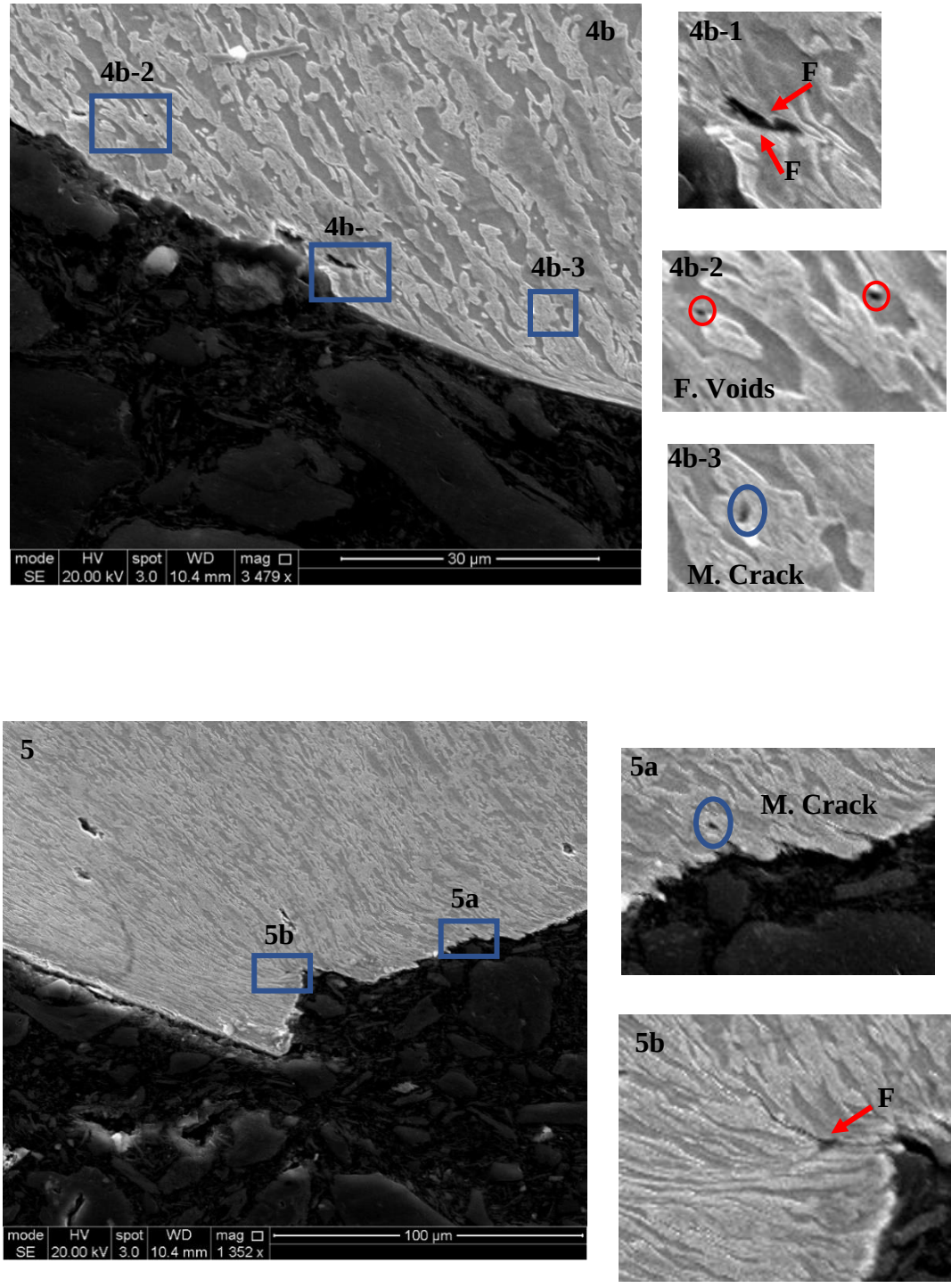

Fig. X. 3 Results of crack inspection in the areas of the first and second parts of the small punch test after the 3D DIC sample was fractured through its thickness.

Appendix XI

Table XI. 1 Martensite cracks and ferrite voids throughout the deformation.

<table>
<tr>
<td>Crack number 1
 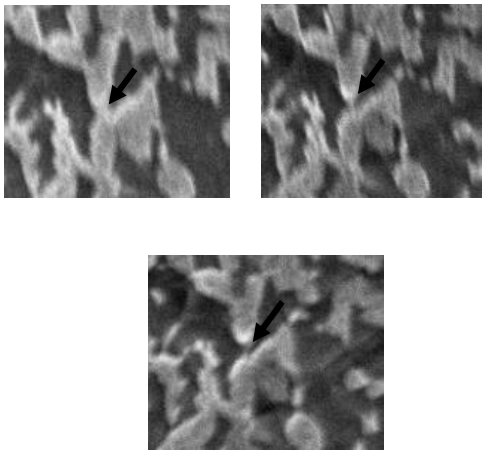
The black arrows indicate the martensite fracture.</td>
<td>Crack number 2
 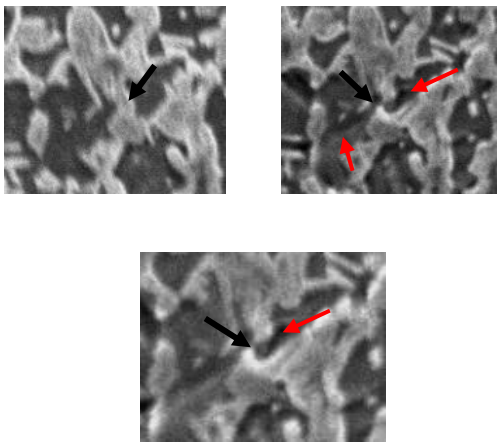
The black arrows reveal the martensite fracture. The red arrows show the ferrite deformation before the martensite cracked.</td>
</tr>
<tr>
<td>Crack number 3
 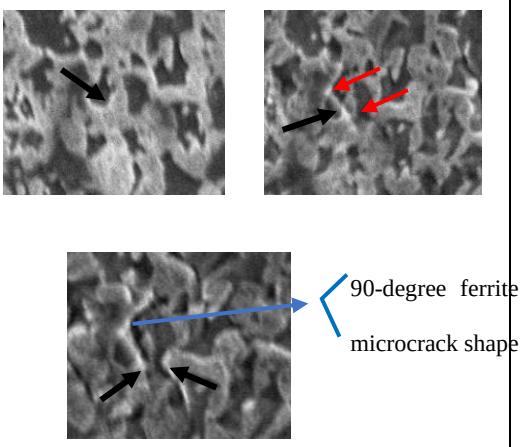

The black arrows point to the martensite fracture. The red arrows</td>
<td>Crack numbers 4 and 5
 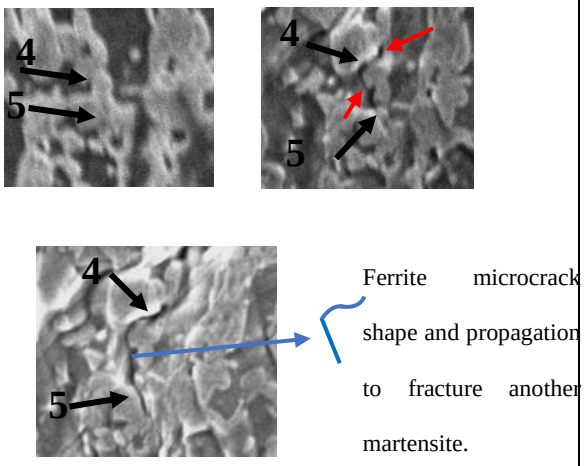

The black arrows point to the martensite cracks. The red arrows clarify the ferrite deformation.</td>
</tr>
</table>

show the ferrite deformation before the martensite cracked.	
Crack number 6 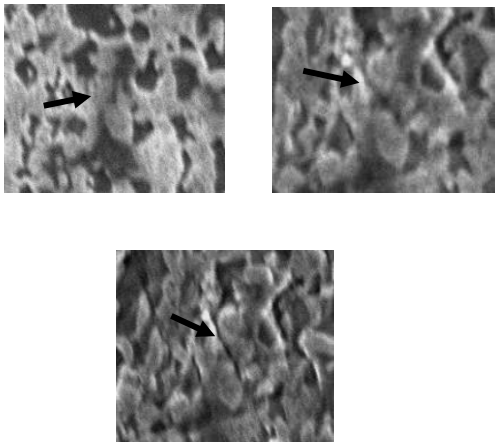 The black arrows point to the martensite fracture.	Crack number 7 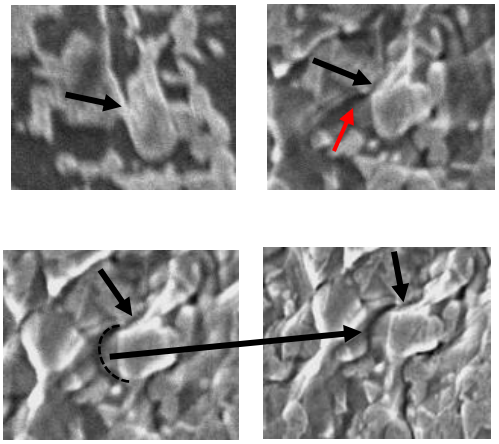 The black arrows point to the martensite cracks. The red arrows clarify the ferrite deformation. The dashed-line curve shows how the ferrite cracked before the martensite fractured.

Appendix XII

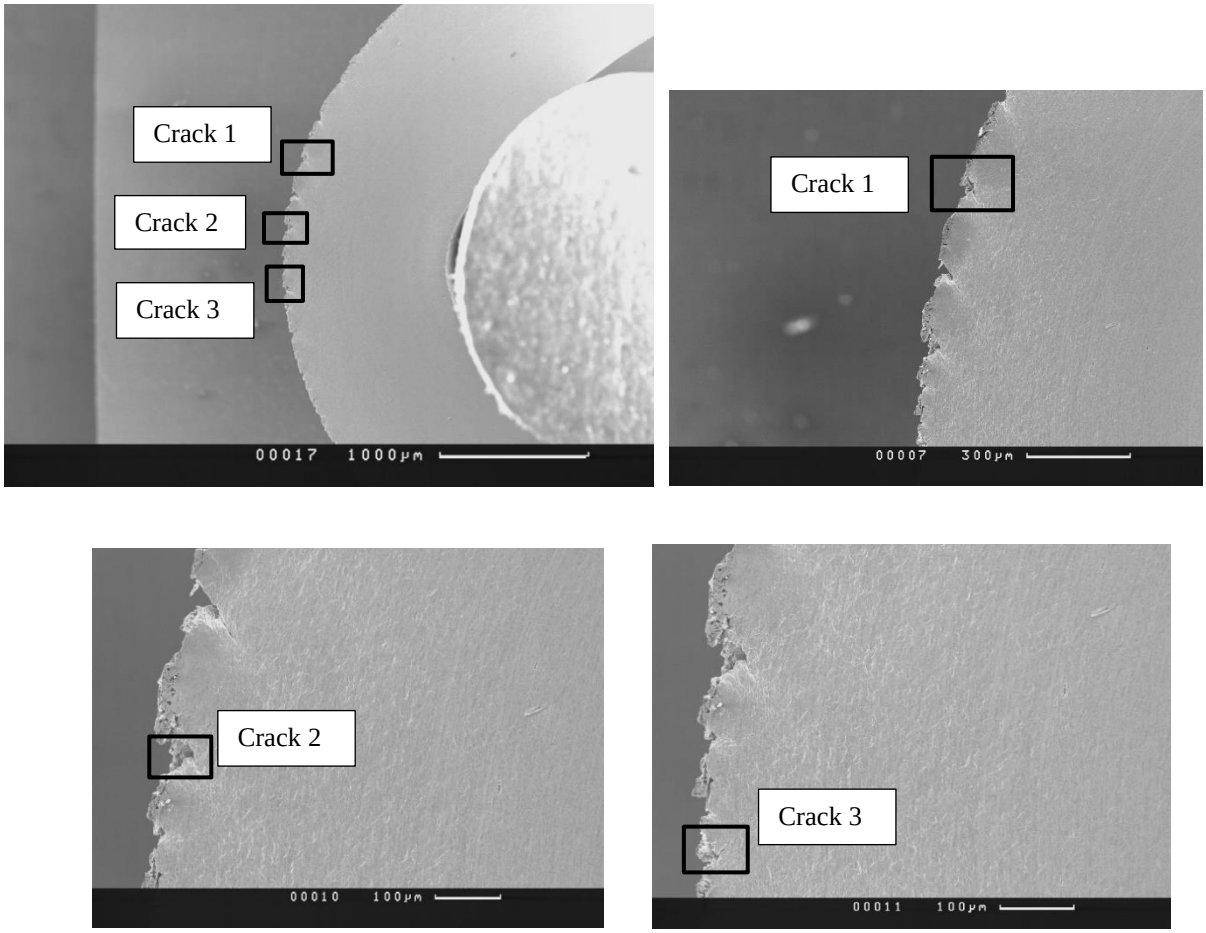

Fig. XII. 1 Location of large cracks in the sample, which are explained in detail Fig. (5.30) is section 5.4.2.1.

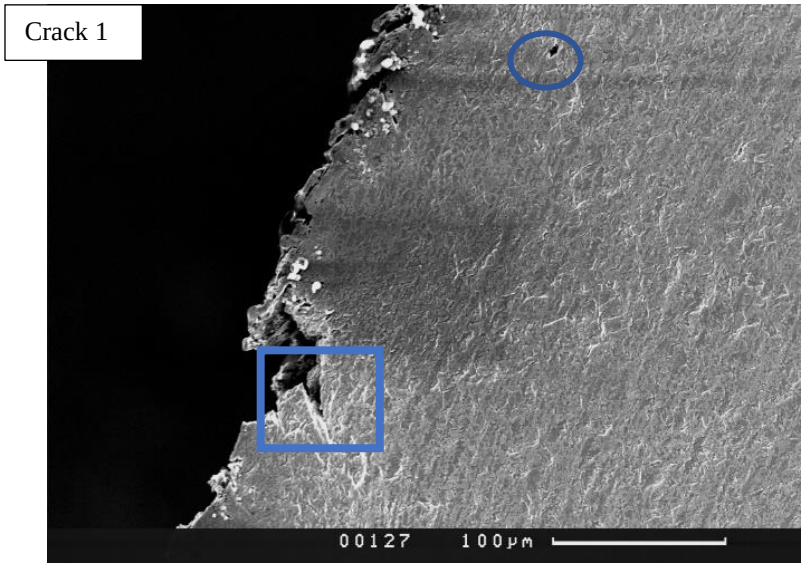

(b)

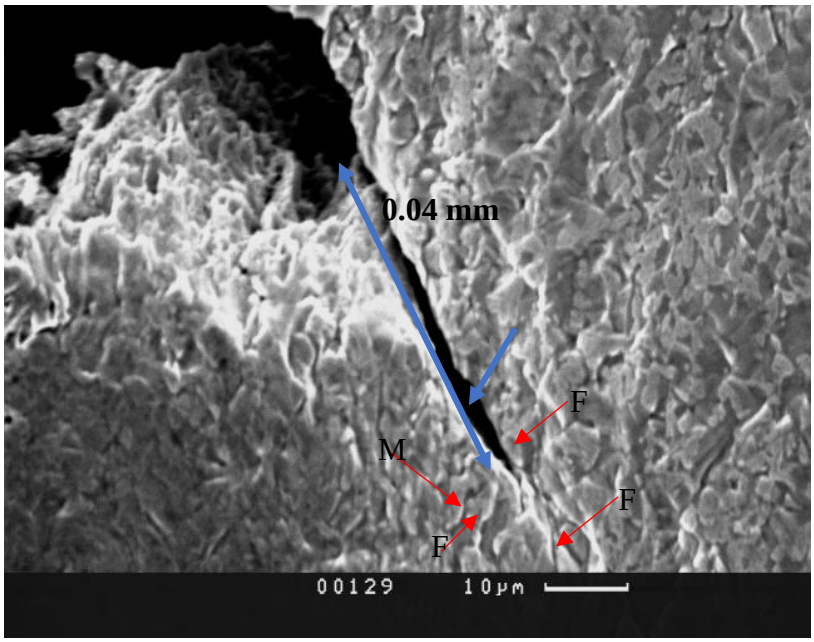
0.04 mm
F
M
F
F
00129 10µm

(c)

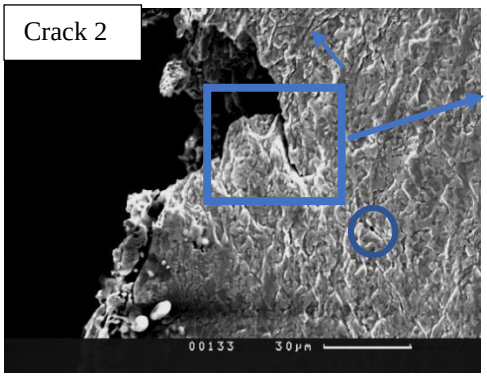
Crack 2
00133 30µm

(d)

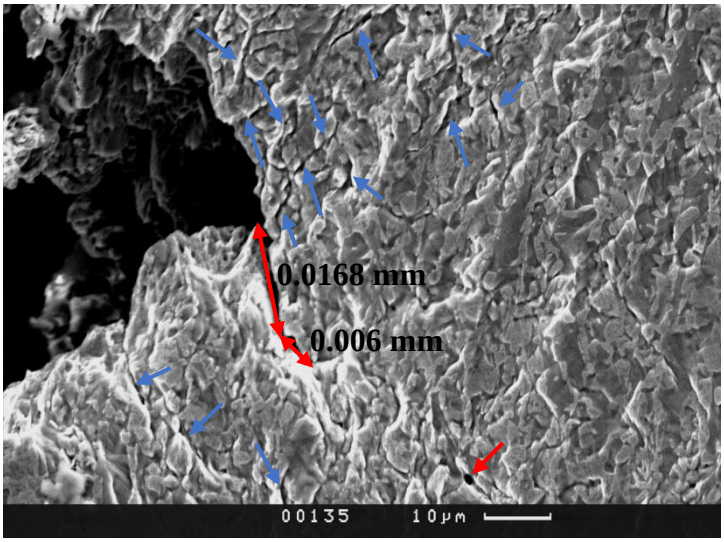
0.0168 mm
0.006 mm
00135 10µm

(e)

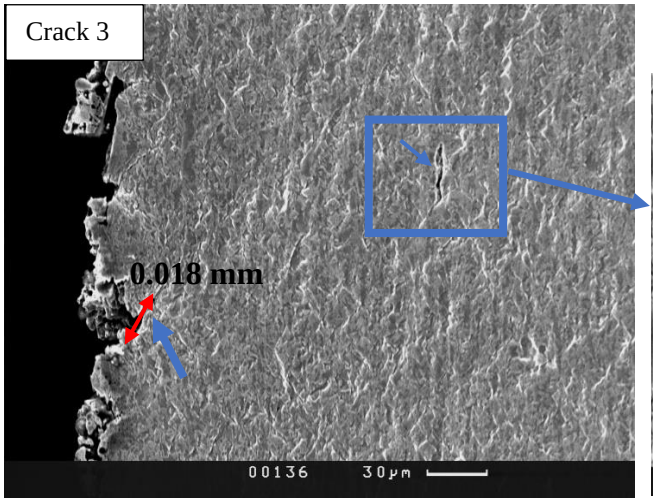

(f)

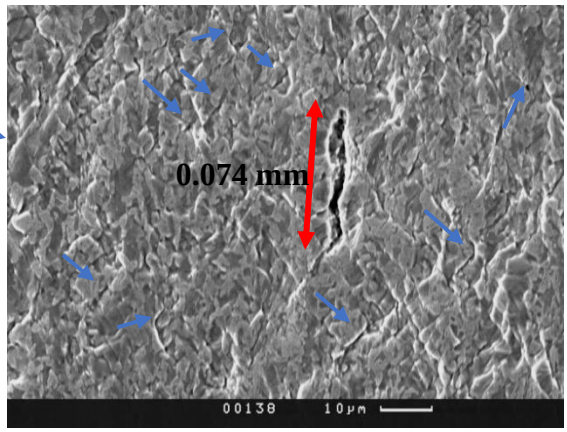

(g)

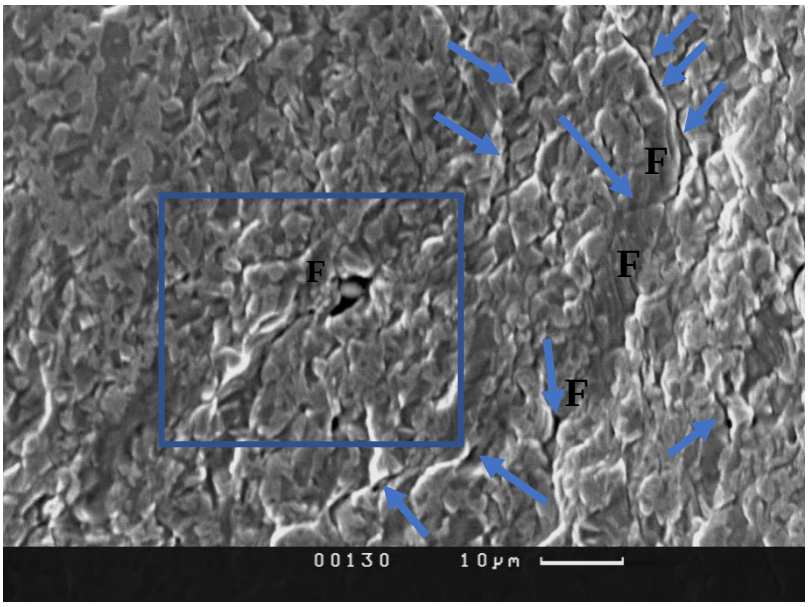

(h)

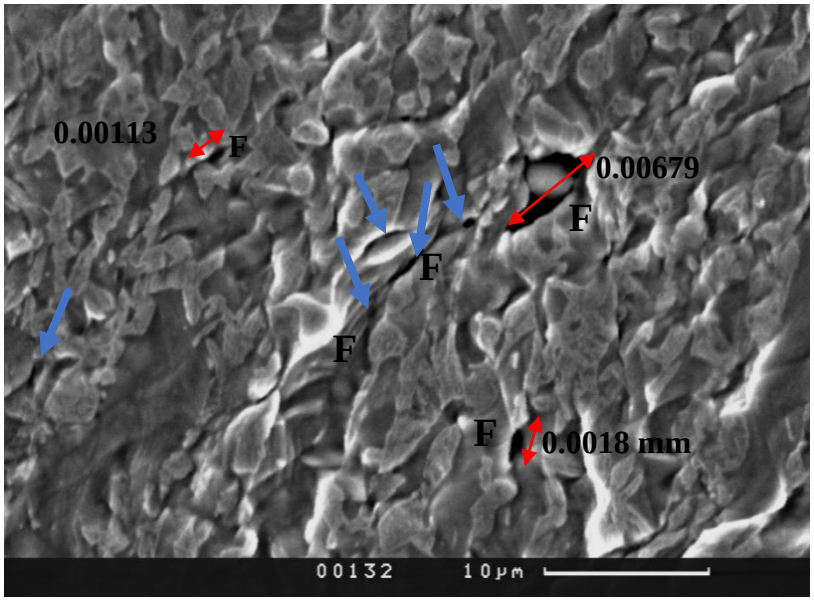

(K)

Fig. XII. 2 (b) to (k) explain cracks in samples after the material became damaged; images (c), (f), (g), and (k) are magnifications of images (see blue squares) (b),(d), (f), and (h), respectively.

Appendix XIII

Crack 3

A void appeared in the ferrite at the 0.976 mm extension level with the final crack path highlighted with the red dashed line on the undamaged microstructure, as shown in Fig. (a). The ferrite deformed opening the crack at the 2.027 mm extension level, as indicated in Fig. (b). As the crack met martensite islands on its path, extensive deformation is observed around the crack tip leading to damage ahead of the crack tip with voids in the ferrite highlighted by red arrows. These voids eventually join up leading to crack propagation at 45^{o} highlighted by the red arrows in Fig. (c) for an applied displacement of 2.475 mm. These microcracks connected together, thereby propagating the crack at the 3.504 mm extension level, as shown in Fig. (d). The increase in displacement made the crack further propagate at the displacement of 4.041 mm, as shown in Fig. (e). The direction of the crack then changed to form a small curve at the extension of 4.25 mm, as shown in Fig. (f). Then, the crack propagated to form a straight line again at the 4.784 mm extension level, as depicted in Fig. (g). Fig. (h) shows the crack after the 5.936 mm extension level was applied with a sharp change in direction; the initial crack propagated over a length of 0.11465 mm before changing direction and extending by a further 0.02585 mm up until the end of the test.

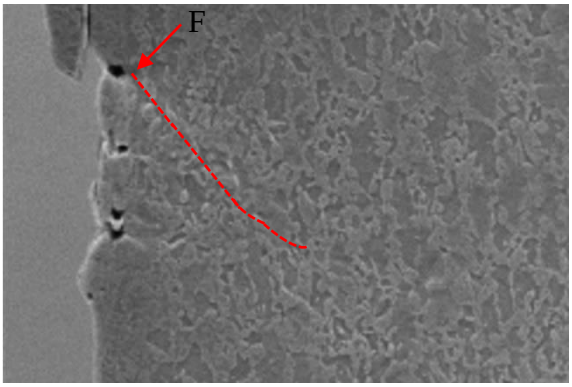

(a)

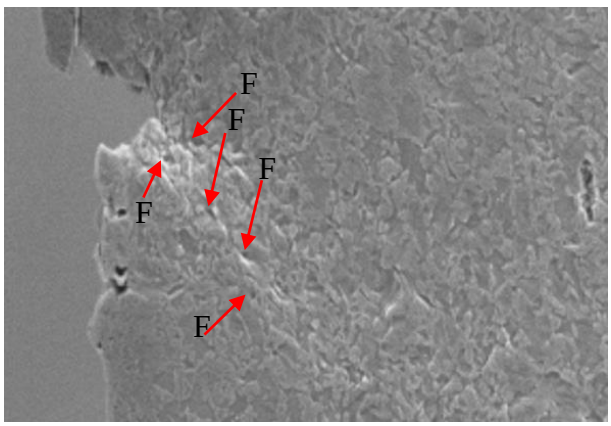

(b)

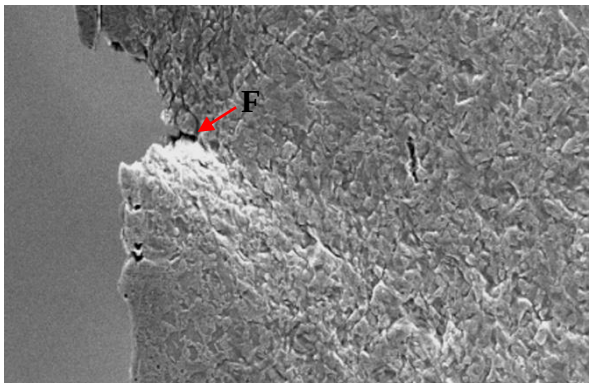

(c)

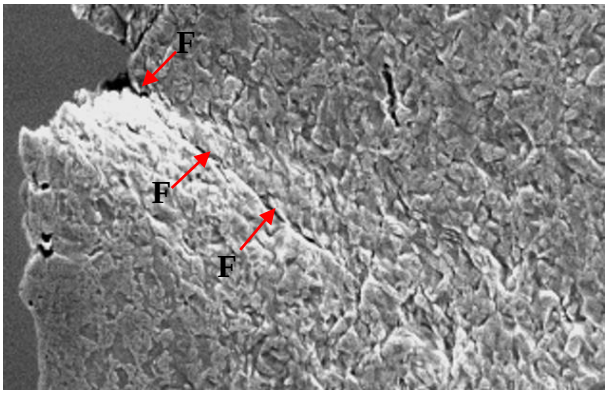

(d)

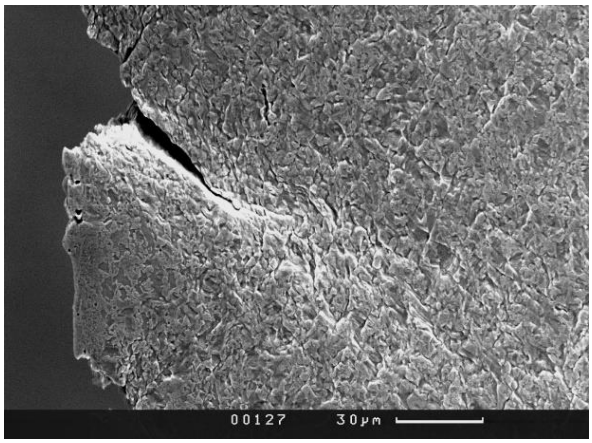

(e)

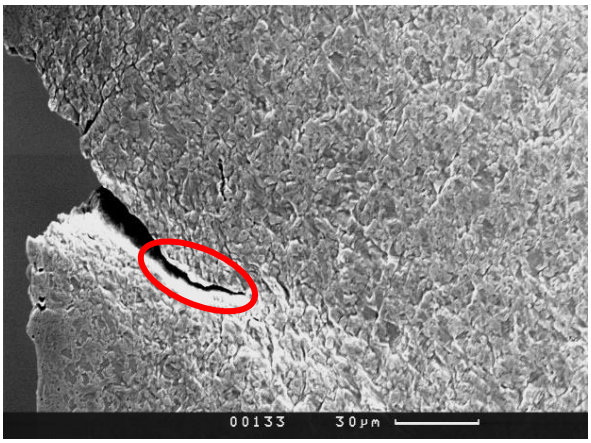

(f)

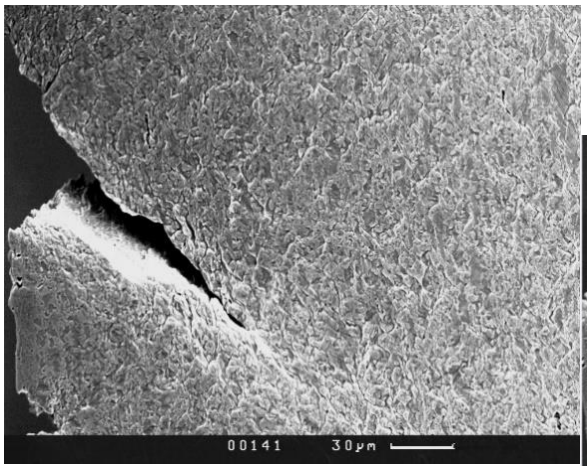

(g)

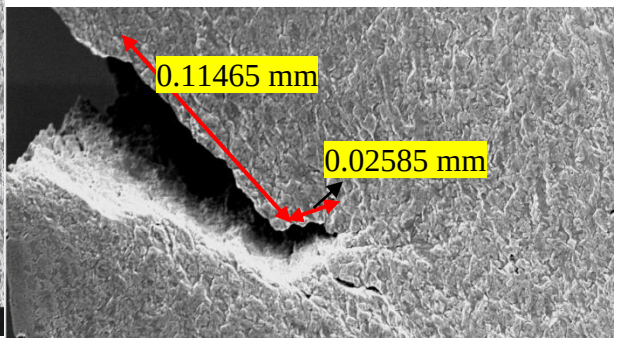

(h)

Figs. XIII. 1 (a) to (h) Propagation and crack path of crack number 3 from initiation to the end of the test. Displacement values for all images: fig.(a) at 0.976 mm, (b) at 2.027 mm, fig. (c) at 2.475 mm, fig.(d) at 3.504 mm, (e) at 4.041 mm, (f) at 4.25 mm, fig.(g) at 4.784, and fig.(h) at 5.936 mm.

Crack 4

Initially, the ferrite deformed at 0.225 mm applied displacement; Figs. (a) and (b) show the track of the crack propagation, with the red dashed line tracing the path, over the undamaged microstructure, fig. (b) located at 2.027 mm. Once again, the ferrite started to deform until a crack appeared in the ferrite phase. The crack opened due to deformation until it met a large martensite island on its path, leading to extensive deformation in the microstructure ahead of the crack tip at 2.98 mm, 2.475 mm and 3.504 mm extensions, as shown in Figs. (c), (d), and (e), respectively. Voids in the ferrite eventually join up leading to further crack propagation at 45 degree at the displacement value of 4.041 mm as shown in Fig. (f); the size of the crack was 0.07044 mm at the end of the test.

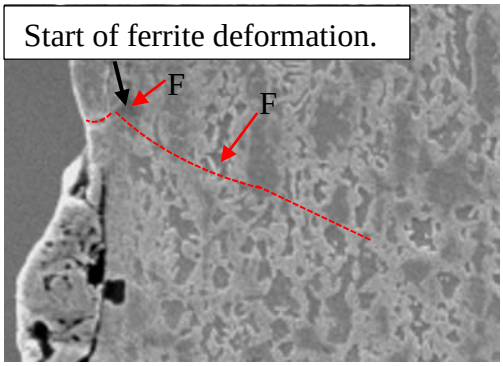

(a)

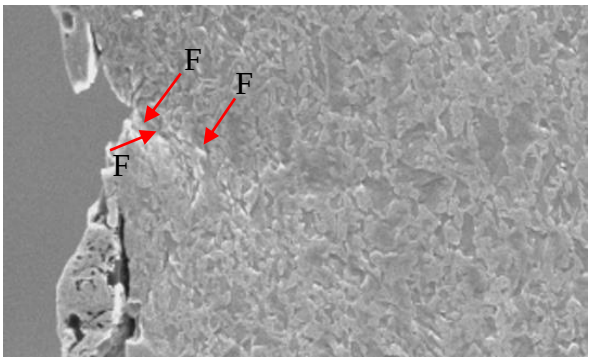

(b)

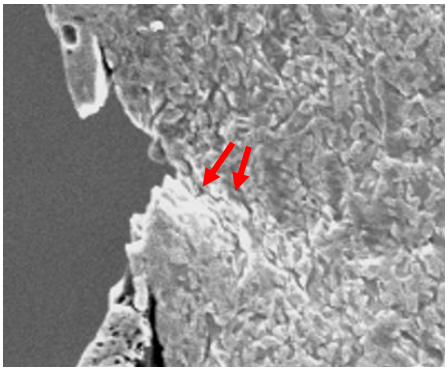

(c)

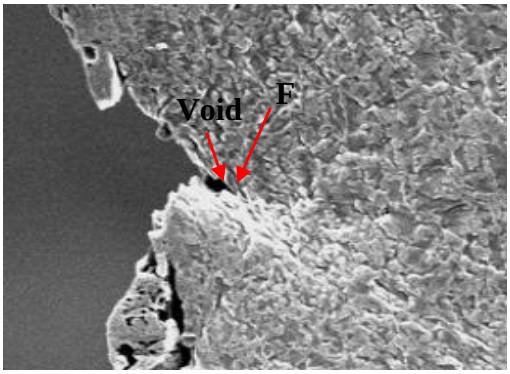

(d)

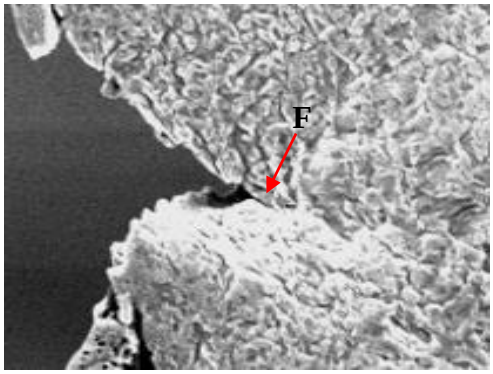

(e)

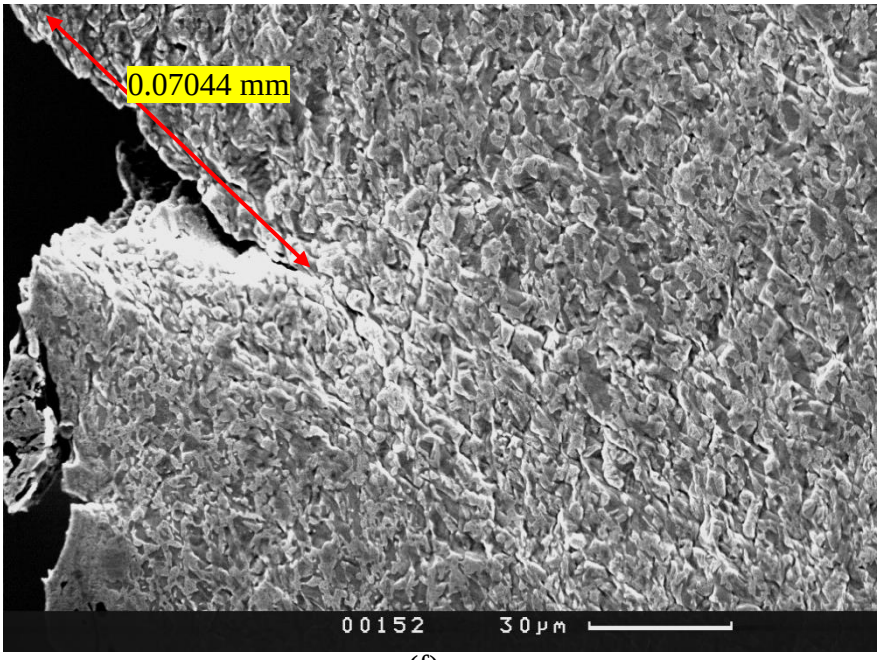

(f)

Figs. XIII. 2 (a) to (f) Propagation and path of crack number 4 from its initiation until the end of the test. Displacement value for all images: fig.(a) at 0.225 mm, fig.(b) at 2.027 mm, fig.(c) at 2.98 mm, fig. (d) at 2.475 mm, fig. (e) at 3.504 mm, and fig. (f) at 4.041 mm.

Appendix XIV

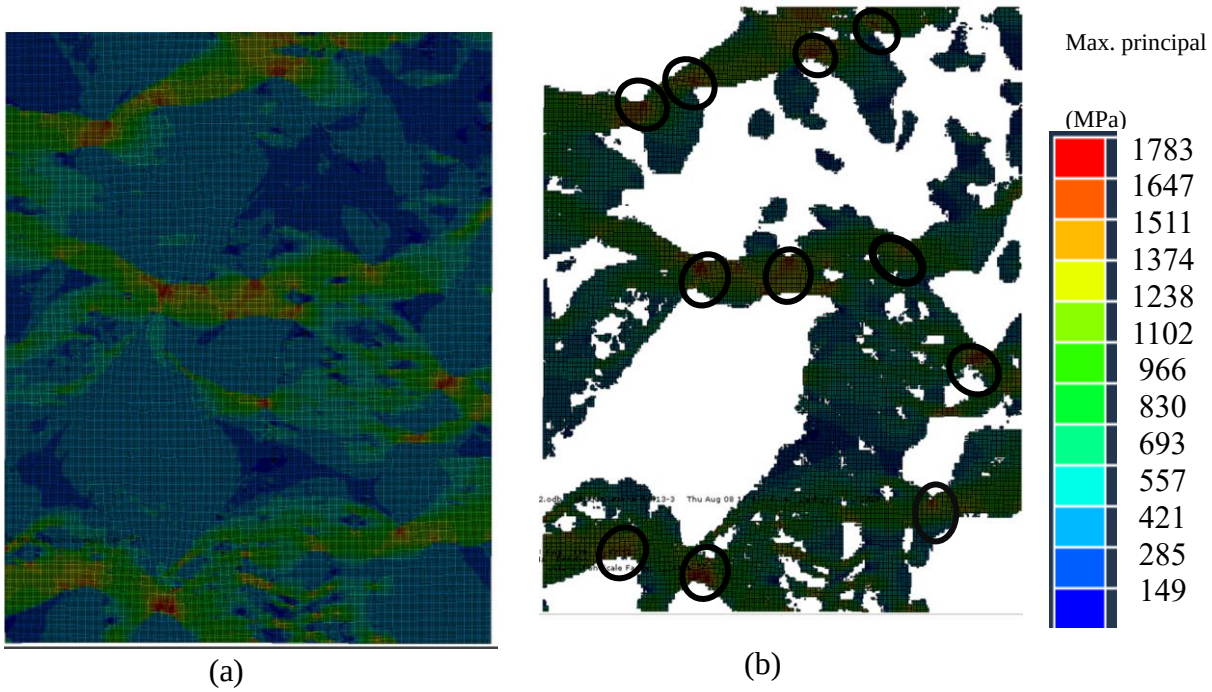

Figs. XIV. 1 (a) Maximum principal stress distribution in the martensite phase, and (b) Highlights on martensite phase; black circles indicate maximum principal values located in crack region and other areas where cracks could occur.

Appendix XV

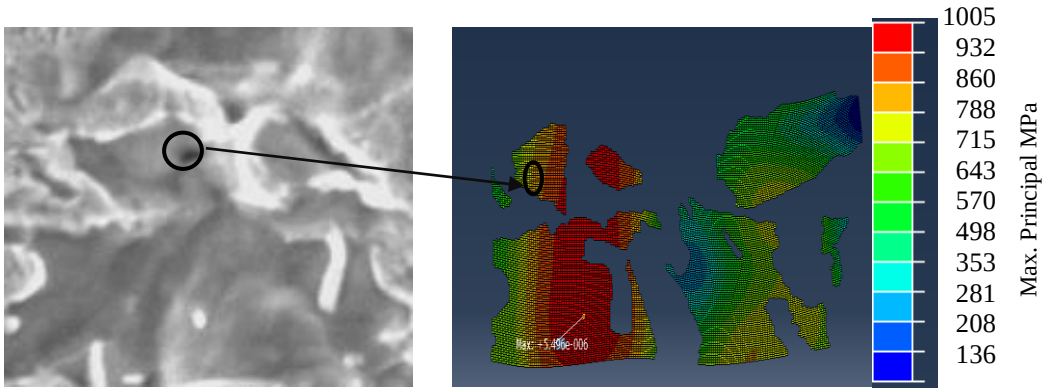

Fig. XV. 1 Max. principal stress distribution before the second void appeared in the ferrite phase (0.26 global strain).

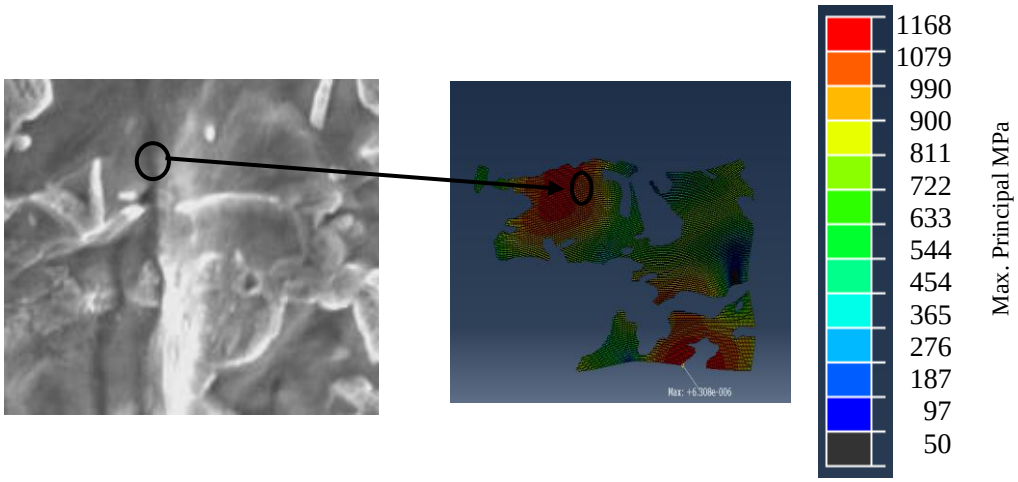

Fig. XV. 2 Max. principal stress distribution before the third ferrite void formed (0.3 global strain).

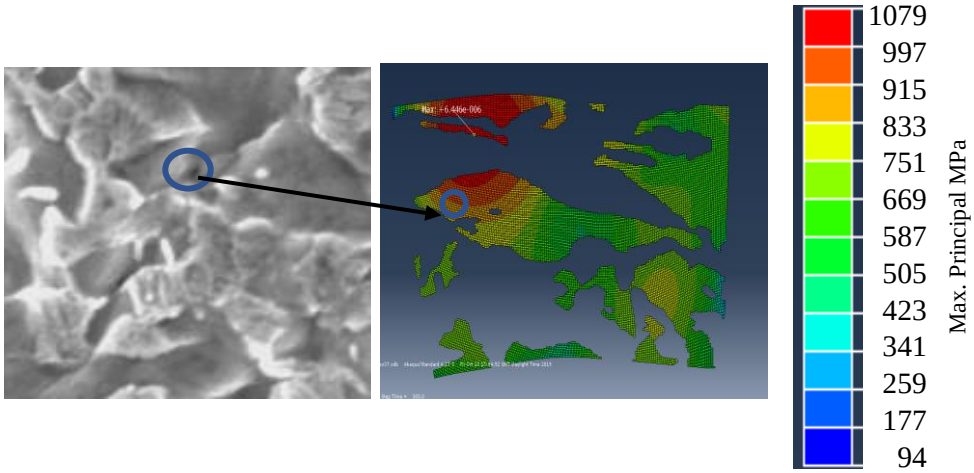

Fig. XV. 3 Max. principal stress distribution before the fourth ferrite void appeared (0.3 global strain).